

Selected Papers in the Hydrologic Sciences 1985

May 1985

- Preliminary modeling of an aquifer thermal-energy storage system
By R. T. Miller
- Low-level radioactive ground-water contamination from a cold scrap
recovery operation, Wood River Junction, Rhode Island
By B. J. Ryan and K. L. Kipp, Jr.
- An electromagnetic method for delineating ground-water contamination,
Wood River Junction, Rhode Island
By P. M. Barlow and B. J. Ryan
- Three-dimensional simulation of free-surface aquifers by finite-element
method
By T. J. Durbin and Charles Berenbrock
- Measurement of reaeration in the Wabash River near Lafayette and Terre
Haute, Indiana, by the modified tracer technique
By C. G. Crawford
- Performance of sodium as a transport tracer-experimental and simulation
analysis
By K. E. Bencala
- Uptake and regeneration of nitrate-by epilithic communities in a nearly
pristine environment
By F. J. Triska, V. C. Kennedy, and R. J. Avanzino
- Streambed oxygen demand versus benthic oxygen demand
By J. E. Terry and E. E. Morris
- The rate of ferrous iron oxidation in a stream receiving acid mine
effluent
By D. K. Nordstrom

United States
Geological
Survey
Water-Supply
Paper 2270



Selected Papers in the Hydrologic Sciences 1985

Edited by Seymour Subitzky

May 1985

Preliminary modeling of an aquifer thermal-energy storage system
By R. T. Miller

Low-level radioactive ground-water contamination from a cold scrap
recovery operation, Wood River Junction, Rhode Island
By B. J. Ryan and K. L. Kipp, Jr.

An electromagnetic method for delineating ground-water contamination,
Wood River Junction, Rhode Island
By P. M. Barlow and B. J. Ryan

Three-dimensional simulation of free-surface aquifers by finite-element
method
By T. J. Durbin and Charles Berenbrock

Measurement of reaeration in the Wabash River near Lafayette and Terre
Haute, Indiana, by the modified tracer technique
By C. G. Crawford

Performance of sodium as a transport tracer-experimental and simulation
analysis
By K. E. Bencala

Uptake and regeneration of nitrate-by epilithic communities in a nearly
pristine environment
By F. J. Triska, V. C. Kennedy, and R. J. Avanzino

Streambed oxygen demand versus benthic oxygen demand
By J. E. Terry and E. E. Morris

The rate of ferrous iron oxidation in a stream receiving acid mine
effluent
By D. K. Nordstrom

U.S. GEOLOGICAL SURVEY WATER-SUPPLY PAPER 2270

DEPARTMENT OF THE INTERIOR
DONALD PAUL HODEL, Secretary

U.S. GEOLOGICAL SURVEY
Dallas L. Peck, Director



UNITED STATES GOVERNMENT PRINTING OFFICE: 1985

For sale by the Superintendent of Documents,
U.S. Government Printing Office,
Washington, DC 20402

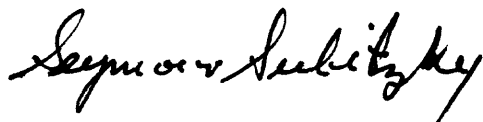
Library of Congress Catalog-card No. 84-600177

PREFACE

Selected Papers in the Hydrologic Sciences is a new journal-type publication aimed at meeting widespread public and professional interests of the hydrologic community for timely results on hydrologic studies derived from the Federal research program, and the Federal-State cooperative program of the U.S. Geological Survey. Also included will be results of some studies done on behalf of other Federal agencies.

This second volume of the *Selected Papers* series, comprising nine topical papers, addresses an array of topics including model simulation of ground- and surface-water systems, hydrogeochemistry, biochemistry of aquatic environments, and selected physical and chemical techniques on hydrologic studies.

Dialogue between readers and authors is encouraged, and a discussion section for reader's comments and author's replies will be included. Such dialogue, which will relate to papers published in the first volume (July 1984) and this volume, will be open for discussion until September 1985. Address comments to Editor, *Selected Papers in the Hydrologic Sciences*, U.S. Geological Survey, 423 National Center, Reston, Virginia 22092.

A handwritten signature in black ink, reading "Seymour Subitzky". The signature is written in a cursive style with a large, sweeping initial 'S'.

Seymour Subitzky
Editor

SI and Inch-Pound Unit Equivalents

International System of Units (SI), a modernized metric system of measurement. All values have been rounded to four significant digits. Use of hectare (ha) as an alternative name for square hectometer (hm²) is restricted to measurement of land or water areas. Use of liter (L) as a special name for cubic decimeter (dm³) is restricted to the measurement of liquids and gases.

Multiply SI units	By	To obtain inch-pound units
Length		
micrometer (μm)	0.000 039 37	inch (in)
millimeter (mm)	0.039 37	inch (in)
centimeter (cm)	0.393 7	inch (in)
meter (m)	3.281	foot (ft)
	1.094	yard (yd)
kilometer (km)	0.621 4	mile (mi)
Area		
centimeter ² (cm ²)	0.155 0	inch ² (in ²)
meter ² (m ²)	10.76	foot ² (ft ²)
	1.196	yard ² (yd ²)
	0.000 247 1	acre
hectometer ² (hm ²)	2.471	acre
kilometer ² (km ²)	0.386 1	mile ² (mi ²)
Volume		
centimeter ³ (cm ³)	0.061 02	inch ³ (in ³)
milliliter (mL)		
liter (L)	61.02	inch ³ (in ³)
	1.057	quart (qt)
	0.264 2	gallon (gal)
	0.035 31	foot ³ (ft ³)
	33.82	ounce, fluid (oz)
	2.113	pint (pt)
	1.057	quart (qt)
	0.264 2	gallon (gal)
meter ³ (m ³)	35.31	foot ³ (ft ³)
	1.308	yard ³ (yd ³)
	264.2	gallon (gal)
	0.000 810 7	acre-foot (acre-ft)
kilometer ³ (km ³)	0.239 9	mile ³ (mi ³)
Volume per unit time (includes flow)		
gram per minute (g/min)	0.035 27	ounce (avoirdupois) per minute (oz/min)
milliliter per minute (mL/min)	0.033 82	ounce (fluid) per minute (oz/min)
liter per second (L/s)	0.035 31	foot ³ per second (ft ³ /s)
	15.85	gallon per minute (gal/min)

Multiply SI units	By	To obtain inch-pound units
Volume per unit time (includes flow) Continued		
meter per second (m/s)	3.281	foot per second (ft/s)
meter per day (m/d)	3.281	foot per day (ft/d)
meter ² per day (m ² /d)	10.76	foot ² per day (ft ² /d)
meter ³ per second (m ³ /s)	35.31	foot ³ per second (ft ³ /s)
	15.850	gallon per minute (gal/min)
Mass		
microgram (μg)	0.000 00 154 3	grain (gr)
gram (g)	0.035 27	ounce, avoirdupois (oz avdp)
kilogram	0.002 205	pound, avoirdupois (lb avdp)
Mass per unit volume		
microgram per liter (μg/L)	0.000 058 41	grain per gallon (gr/gal)
milligram per liter (mg/L)	0.058 41	grain per gallon (gr/gal)
Temperature		
degree Celsius (°C)	Temp °F = 1.8 temp °C + 32	degree Fahrenheit (°F)
Specific conductance		
microsiemens per centimeter at 25 degrees Celsius (μS/cm at 25°C)	1.000	micromho per centimeter at 25 degrees Celsius (μmho/cm at 25°C)
millisiemens per meter at 25 degrees Celsius (mS/m at 25°C)	1.000	millimho per meter at 25 degrees Celsius (mmho/m at 25°C)
Heat		
Joule per meter day degree Celsius (J/md°C)	0.000 159 1	British thermal unit per foot day degree Fahrenheit Btu/ftd°F
Joule per cubic meter degree Celsius (J/m ³ °C)	0.000 014 92	British thermal unit per cubic foot degree Fahrenheit Btu/ft ³ °F

Any use of trade names and trademarks in this publication is for descriptive purposes only and does not constitute endorsement by the U.S. Geological Survey.

CONTENTS

Preface **iii**

SI and inch-pound unit equivalents **iv**

Preliminary modeling of an aquifer thermal-energy storage system
By R. T. Miller **1**

Low-level radioactive ground-water contamination from a cold-scrap
recovery operation, Wood River Junction, Rhode Island
By B. J. Ryan and K. L. Kipp, Jr. **21**

An electromagnetic method for delineating ground-water contamination, Wood
River Junction, Rhode Island
By P. M. Barlow and B. J. Ryan **35**

Three-dimensional simulation of free-surface aquifers by finite-element
method
By T. J. Durbin and Charles Berenbrock **51**

Measurement of reaeration by the modified tracer technique
in the Wabash River near Lafayette and Terre Haute, Indiana
By C. G. Crawford **69**

Performance of sodium as a transport tracer—experimental and simulation
analysis
By K. E. Bencala **83**

Uptake and regeneration of nitrate by epilithic communities in a nearly pristine
lotic environment
By F. J. Triska, V. C. Kennedy, and R. J. Avanzino **91**

Streambed oxygen demand versus benthic oxygen demand
By J. E. Terry and E. E. Morris **99**

The rate of ferrous iron oxidation in a stream receiving acid mine effluent
By D. K. Nordstrom **113**

Preliminary Modeling of an Aquifer Thermal-Energy Storage System

By Robert T. Miller

Abstract

The University of Minnesota, the Minnesota Geological Survey, and the U.S. Geological Survey are studying the feasibility of storing water at a temperature of 150 degrees Celsius in the Franconia-Ironton-Galesville aquifer. The Aquifer Thermal-Energy Storage project has a doublet-well design with a well spacing of approximately 250 meters. One well will be used for cool-water supply, and, the other, for hot-water injection.

The U.S. Geological Survey is constructing a model of ground-water flow and thermal-energy transport to aid in determining the efficiency of the Aquifer Thermal-Energy Storage system. A preliminary model of radial flow and thermal-energy transport was constructed, based on hydraulic and thermal properties of the Franconia-Ironton-Galesville aquifer determined in previous studies. The model was used to investigate the sensitivity of model results to various hydraulic and thermal properties and to study the potential for buoyancy flow within the aquifer and the effect of various cyclic injection-withdrawal schemes on the relative thermal efficiency of the aquifer.

Sensitivity analysis was performed assuming 8 days of injection of 150-degree-Celsius water at 18.9 liters per second, 8 days of storage, and 8 days of withdrawal of hot water at 18.9 liters per second. The analysis indicates that, for practical ranges of hydraulic and thermal properties, rock-heat capacity is the least important property and thermal dispersivity is the most important property used to compute temperature and aquifer thermal efficiency.

The amount of buoyancy flow was examined for several values of hydraulic conductivity and ratios of horizontal to vertical hydraulic conductivities. For the assumed base values of hydraulic and thermal properties, buoyancy flow was negligible. The greatest simulated buoyancy flow resulted from simulations in which horizontal hydraulic conductivity was increased to 10 times the base value, and the vertical hydraulic conductivity was set equal to the horizontal hydraulic conductivity.

The effects of various injection-withdrawal rates and durations on computed values of aquifer relative thermal efficiency and final well-bore temperature were studied for five 1-year hypothetical test cycles of injection and withdrawal. The least efficient scheme was 8 months injection of 150-degree-Celsius water and 4 months of withdrawal of hot water at 18.9 liters per second. The

most efficient scheme was obtained with 6 months of injection of 150-degree-Celsius water at 18.9 liters per second and 6 months of withdrawal of hot water at 37.8 liters per second. The hypothetical simulations indicate that the subsequent calibrated model of the doublet-well system will be a valuable tool in determining the most efficient system operation.

INTRODUCTION

In May 1980, the University of Minnesota, the Minnesota Geological Survey, and the U.S. Geological Survey began a cooperative study to evaluate the feasibility of storing water heated to 150°C in the deep (180-240 m) Franconia-Ironton-Galesville aquifer and later recovering it for space heating. High-temperature water from the cooling system for the University's electrical-generation facilities would supply heat for injection. The Aquifer Thermal-Energy Storage (ATES) site and doublet-well system design are shown diagrammatically in figure 1. The injection-withdrawal wells are approximately 250 m apart. Water is pumped from one of the wells through a heat exchanger where heat is added or removed. Water then is injected back to the aquifer through the other well. The experiment planned for testing the ATES system includes a series of hot-water injection, storage, and withdrawal cycles. Each cycle will be 24 days long, and the length of each injection, storage, and withdrawal step of the cycle will be 8 days.

The U.S. Geological Survey is constructing a ground-water-flow and thermal-energy-transport model for evaluating the efficiency of the ATES system. This paper describes sensitivity analyses for individual preliminary model-input properties, the potential for buoyancy-flow effects, and hypothetical simulations of aquifer relative thermal efficiency.

HYDRAULIC AND THERMAL PROPERTIES

The Franconia-Ironton-Galesville aquifer is a consolidated sandstone, approximately 60 m thick;

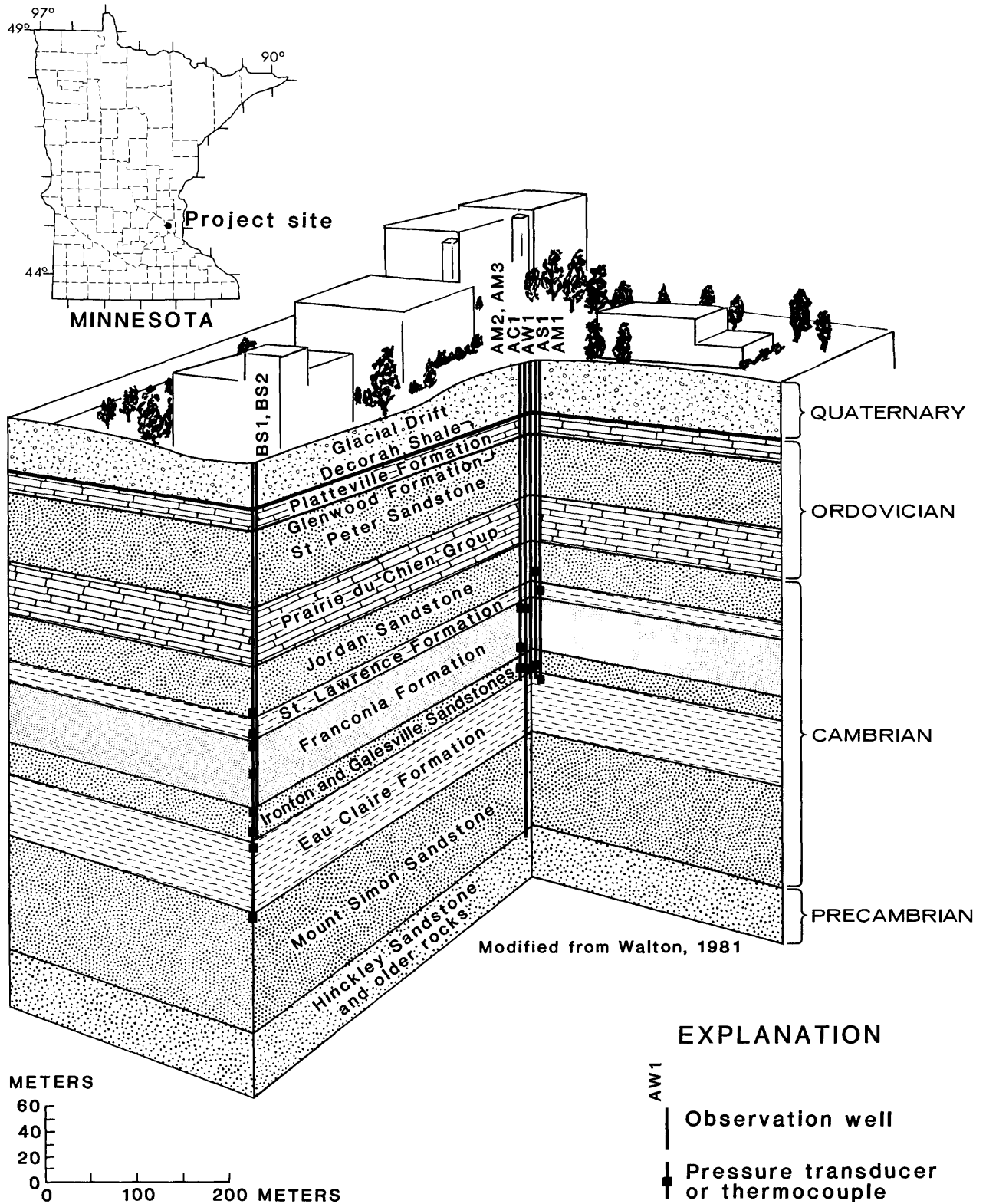


Figure 1. Location and block diagram of the Aquifer Thermal-Energy Storage site.

the top is approximately 180 m below land surface. It is confined above by the St. Lawrence Formation, which is an 8-m-thick dolomitic sandstone, and be-

low by the Eau Claire Formation, which is a 30-m-thick shale (fig. 1). Initial hydraulic testing with inflatable packers indicates that the aquifer has four

hydraulic zones with distinctly different values of hydraulic conductivity. The thickness and location of each zone were determined by correlating data from bore-hole geophysical logs, core samples, and the inflatable-packer tests. The stratigraphic relations of the hydraulic zones, their thicknesses, and horizontal hydraulic conductivities determined from these data are shown in table 1.

Table 1. Hydraulic zonation, thickness, and horizontal hydraulic conductivity determined from bore-hole geophysical logs, core samples, and inflatable-packer test data

Hydraulic zone	Thickness (m)	Horizontal hydraulic conductivity (m/d)
Franconia Formation:		
Upper	14	0.6
Lower	25	.03
Ironton Sandstone	15	1.2
Galesville Sandstone	6	.3

The average porosity for the Franconia-Ironton-Galesville aquifer is approximately 25 percent (Norvitch and others, 1973), and the average storage coefficient is 3.6×10^{-5} (Miller, 1983).

Values of rock thermal conductivity and rock-heat capacity are given in table 2 and represent averages from values given by Clark (1966) for different sandstones and shales that are similar in composition to the Franconia-Ironton-Galesville aquifer and the confining beds, St. Lawrence and Eau Claire Formations. Thermal dispersivity was estimated from the results of heat-storage testing by Sauty and others (1979).

Table 2. Summary of relevant system thermal properties

Rock thermal conductivity (aquifer and confining beds)	= 2.20×10^6	joules per meter per day per degree Celsius
Thermal dispersivity	= 3	meters
Rock-heat capacity	= 1.81×10^6	joules per cubic meter per degree Celsius

NUMERICAL MODEL AND MATHEMATICAL FORMULATION

Early in the study, a preliminary two-dimensional, radial-flow, anisotropic, nonisothermal, ground-water-flow and thermal-energy-transport model was constructed. Sensitivity analyses were made for a range of selected hydraulic and thermal properties that are known or assumed to be charac-

teristic of the aquifer. The preliminary model also was used for examining the relative efficiency of the aquifer for thermal-energy storage for different injection and withdrawal rates and duration.

The numerical model code was developed for the U.S. Geological Survey for calculating the effects of liquid waste disposal in deep saline aquifers (Intercomp, 1976). The model uses finite-difference techniques to solve simultaneously the equations of fluid and energy transport. The mathematical formulation of the model for radial flow is summarized below.

The equation of ground-water flow (continuity equation) for a fluid of variable density and viscosity, such as water at varying pressure and temperature, can be expressed as

$$\nabla \cdot \left[\rho \frac{k}{u} (\nabla_p - \rho g \nabla z) \right] - q' = \frac{\partial}{\partial t} (n\rho), \quad (1)$$

where p is pressure, k is intrinsic permeability, ρ is density, u is viscosity, g is gravitational acceleration, n is porosity, q' is mass rate of flow per unit volume from sources or sinks (the injection rate for this experiment), z is the spatial dimension in the direction of g , and t is the time dimension. The ∇ operator for an axially symmetric cylindrical coordinate system is $(1/r)(\partial/\partial r) + (\partial/\partial z)$, where r is the radial dimension.

The equation describing the transport of thermal energy in ground-water system is

$$\nabla \cdot \left[\rho \frac{k}{u} H(\nabla_p - \rho g \nabla z) \right] + \nabla \cdot K \cdot \nabla T - q_L - q'H = \frac{\partial}{\partial t} [n\rho U + (1-n)(\rho C_p)_R T], \quad (2)$$

where H is enthalpy, K is hydrodynamic thermal dispersivity (thermal conductivity plus hydrodynamic dispersivity), T is temperature, q_L is rate of heat loss across boundaries, U is internal energy, and $(\rho C_p)_R$ is the heat capacity of the aquifer matrix (a product of its density and specific heat); all other terms are as defined in equation 1. Boundary conditions for this equation are (1) specified flux of heat at the well radius, associated with the source-sink term q' , (2) heat convection at the model lateral boundary, and (3) heat conduction across the confining beds (Papadopoulos and Larson, 1978).

The radial-flow model simulates the St. Lawrence, Franconia, Ironton, Galesville, and the Eau Claire Formations. It consists of 16 variable-width node spacings in the vertical direction and 21 logarithmically increasing-width node spacings in the radial direction. The vertical spacings range from approximately 5 to 10 m. The smallest radial spacing is 0.18 m, and the largest is 26.8 m. The lateral model boundary represents one-half of the distance between

production wells A and B (125 m) and is simulated as a constant head.

Injection and withdrawal of heated water is through 12 vertical nodes, which, when combined represent the Franconia-Ironton-Galesville aquifer. Radially, the nodes represent the diameter of the well bore (0.18 m). Injection and withdrawal at the well bore into and out of each horizontal layer is based upon the layer mobility alone. Mobility is proportional to the relative layer permeability-thickness product divided by the total well-bore interval permeability thickness (Intercomp, 1976).

The confining beds, the St. Lawrence and Eau Claire Formations, are simulated by two nodes each. Energy transport is by convection and conduction at the respective inner boundaries of these confining beds with the Franconia-Ironton-Galesville aquifer and by conduction at their respective boundaries opposite the aquifer. Energy transport at the model's lateral boundary is by conduction and convection.

The regional gradient within the study area for the Franconia-Ironton-Galesville aquifer is estimated to be approximately 0.0002 with a natural pore velocity of 0.005 m/d (Roman Kanivetsky, Minnesota Geological Survey, written commun., 1980). This low regional flow rate will not impact seriously results of the sensitivity analyses because of the short term of the simulations or modeling of the hypothetical long-term relative efficiency because storage periods are not simulated. Therefore, the natural flow system is not simulated by the model.

As described above, the ATEs system will operate with a doublet-well system. The steady-state flowfield for a doublet-well system with well spacing equal to that of the ATEs system (250 m) is shown in figure 2. The equipotential lines indicate that the preliminary model assumption of radial flow is less exact with increasing distance from the center of either well bore. The interpretation of the preliminary model results, in terms of representing the ATEs doublet-well system, will be related to the radial distance that heat will move away from the well for the period of simulation; that is, the farther the heat moves away from the well, the less exact the assumption of radial flow. For the preliminary model simulations described in this report, all the heat was maintained within the boxed area around the injection well shown in figure 2. Figure 2 also shows the location of the preliminary model lateral boundary in relation to the doublet-well flowfield.

SENSITIVITY ANALYSIS

Sensitivity analyses were made on the preliminary model for the hydraulic properties of hydraulic

conductivity, porosity, and vertical anisotropy and on the thermal properties of rock thermal conductivity, rock-heat capacity, and thermal dispersivity. A radial-flow base model was constructed with data obtained from bore-hole geophysical logs, analysis of core samples, and inflatable-packer tests and from previous studies and laboratory values reported in text books. Base-model hydraulic and thermal characteristics are described in tables 1 and 2, respectively.

The purpose of the sensitivity analysis was to determine the relative importance of individual hydraulic and thermal characteristics in the computation of temperatures and aquifer thermal efficiency in relation to the preliminary radial-flow model. This information then could be used to guide data collection and the adjustment of model-input properties during calibration of subsequent models with data from the 24-day test cycles. Therefore, the simulation used in sensitivity analysis consisted of 8 days of injection of water at a rate of 18.9 L/s and a temperature of 150°C, 8 days of storage, and 8 days of withdrawal at a rate of 18.9 L/s comprising the 24-day test cycle.

The majority of injected heat calculated by the preliminary model during sensitivity-analysis simulations was concentrated within a radial distance of approximately 14 m from the injection well. None of the sensitivity-analysis simulations calculated movement of injected heat beyond approximately 17 m. The 17- and 14-m radial distances from the well are shown in figure 3, which is an enlargement of the boxed area shown in figure 2. Comparison of the equipotential lines for the doublet-well system and the 17-m model-computed radial extent of heat movement indicates that the preliminary model radial-flow assumption is fairly accurate for the sensitivity-analysis simulations. However, as indicated in the discussion of "Buoyancy Flow," the sensitivity of certain properties may change with longer term cycles (greater than 60 days).

To determine the relative sensitivity of the model simulation to different values of selected properties, temperature versus time plots were constructed from model results and compared with similar plots for the base-model simulation. The temperatures represent a point within the Ironton-Galesville Formation at a radial distance of approximately 6.5 m from the production well. Aquifer thermal efficiency was calculated as a percentage by dividing the total heat produced during recovery by the total heat injected. The aquifer thermal efficiency of the base simulation is 51.0 percent. The following discussion of individual properties is ordered from least to most sensitive in the model simulation.

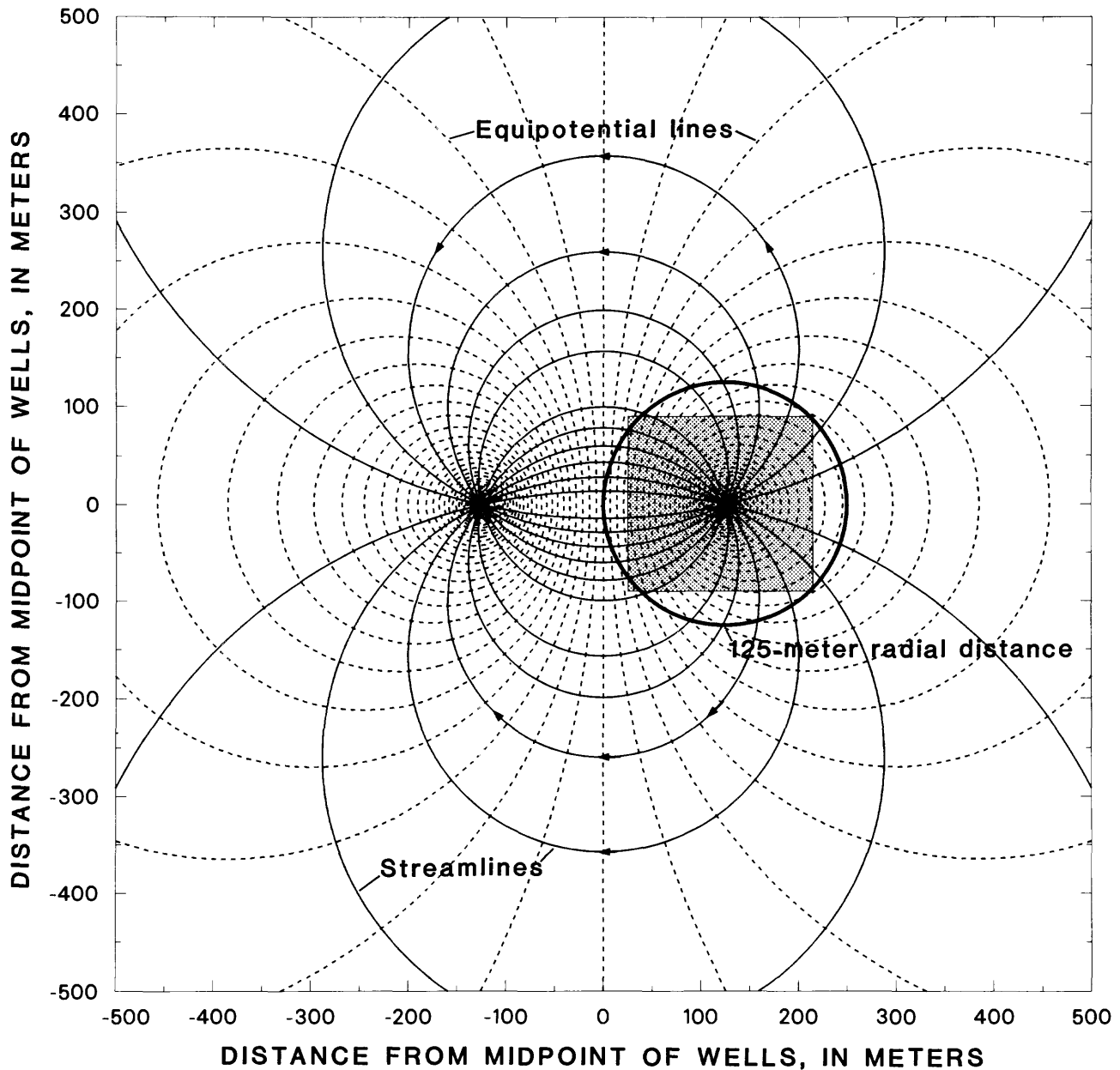


Figure 2. Flowfield showing a doublet-well system similar to the Aquifer Thermal-Energy Storage.

Hydraulic and Thermal Properties

Ratio of Horizontal to Vertical Hydraulic Conductivity

In the radial-flow model, horizontal hydraulic conductivity (K_H) is equal in all horizontal directions. Therefore, the only anisotropy that can be simulated is the ratio of horizontal to vertical hydraulic conductivity (K_V).

The ratio of K_H to K_V was varied from an isotropic condition ($K_H/K_V = 1$) to K_H/K_V equal to 100. The base value of K_H/K_V is assumed to be 10

(Norvitch and others, 1973). Figure 4 shows that simulation of different values of K_H/K_V had negligible effect on model-computed temperatures. The calculated aquifer efficiencies are 50.7 percent for K_H/K_V equal to 1 and 50.9 percent for K_H/K_V equal to 100. Model insensitivity to K_H/K_V is probably due to the relatively low values of hydraulic conductivity. The ratio of K_H to K_V will be shown to be more important in the simulation of heat convection at the thermal front due to density differences between the warm injection water and the cooler ground water. The relation between K_H/K_V and water-density differences is described in the section "Buoyancy Flow."

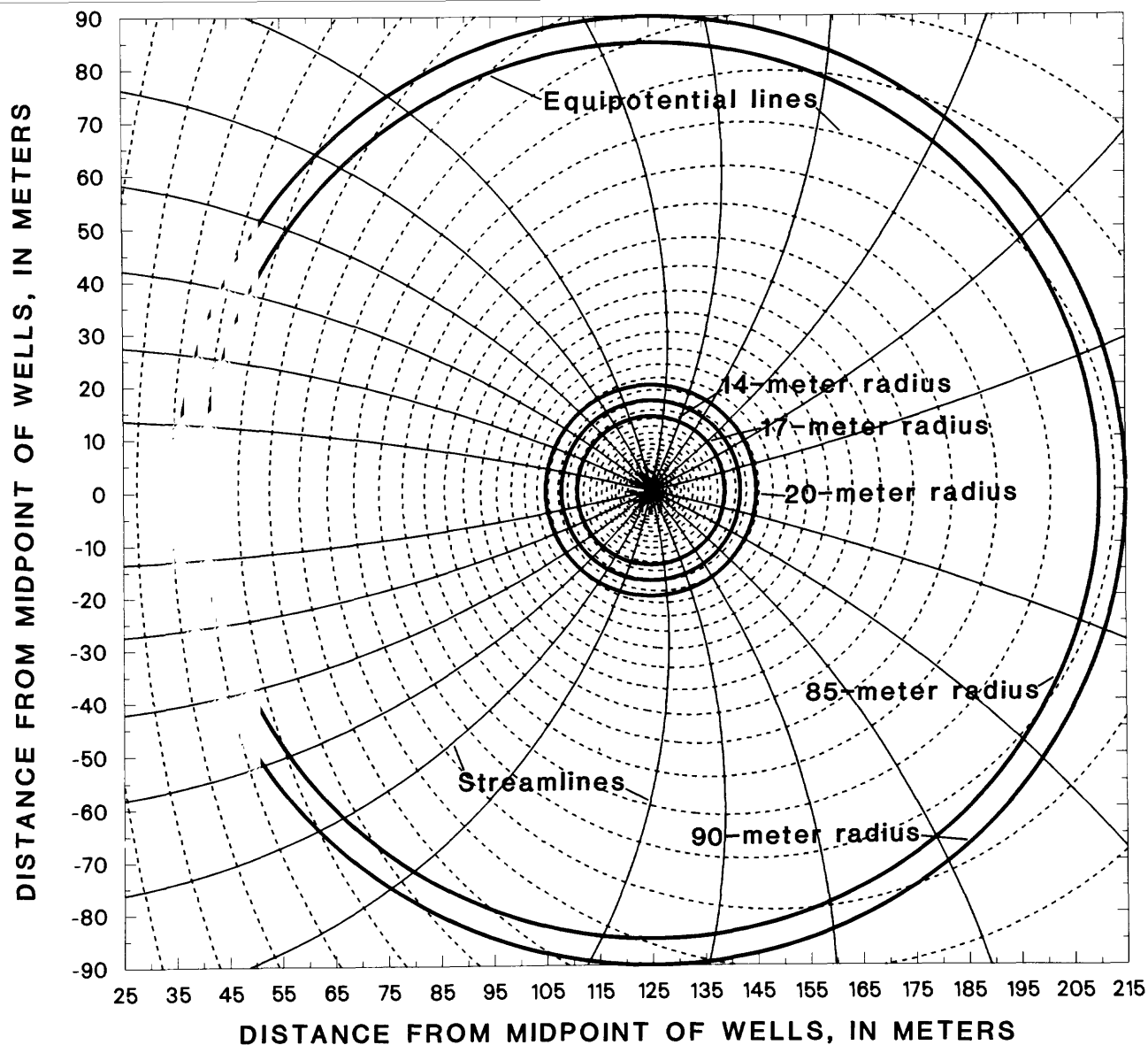


Figure 3. Flowfield showing an area near the injection well of a doublet-well system similar to the Aquifer Thermal-Efficiency Storage system.

Rock Thermal Conductivity

The values of rock thermal conductivity were varied in the model according to the approximate values given in Clark (1966) for sandstones comparable in composition to those in the Franconia-Ironton-Galesville aquifer. The reduction of rock thermal conductivity with temperature increase, as reported by Birch and Clark (1940), Sommerton and others (1965), and Clark (1966), is not accounted for in the computer code. This should not be a problem because the reduction of rock thermal conductivity described by these authors is small for the injection temperature (150°C), is within the range described for sandstone aquifers (Clark, 1966), and is used in

the sensitivity analysis. Figure 5 shows the computed temperatures for different values of rock thermal conductivity. The plots indicate a small divergence in the computed temperatures during storage, which is reflected in their aquifer thermal efficiencies of 51.8 and 50.3 percent for rock thermal conductivities of 1.25×10^{-5} and 3.14×10^{-5} J/md°C, respectively. This divergence probably is due to the effects of the rock thermal conductivity which are small in comparison to the effects of heat convection in the moving ground water during injection. Therefore, the simulated effects of thermal conductivity are not observed until the storage period and remain constant through withdrawal.

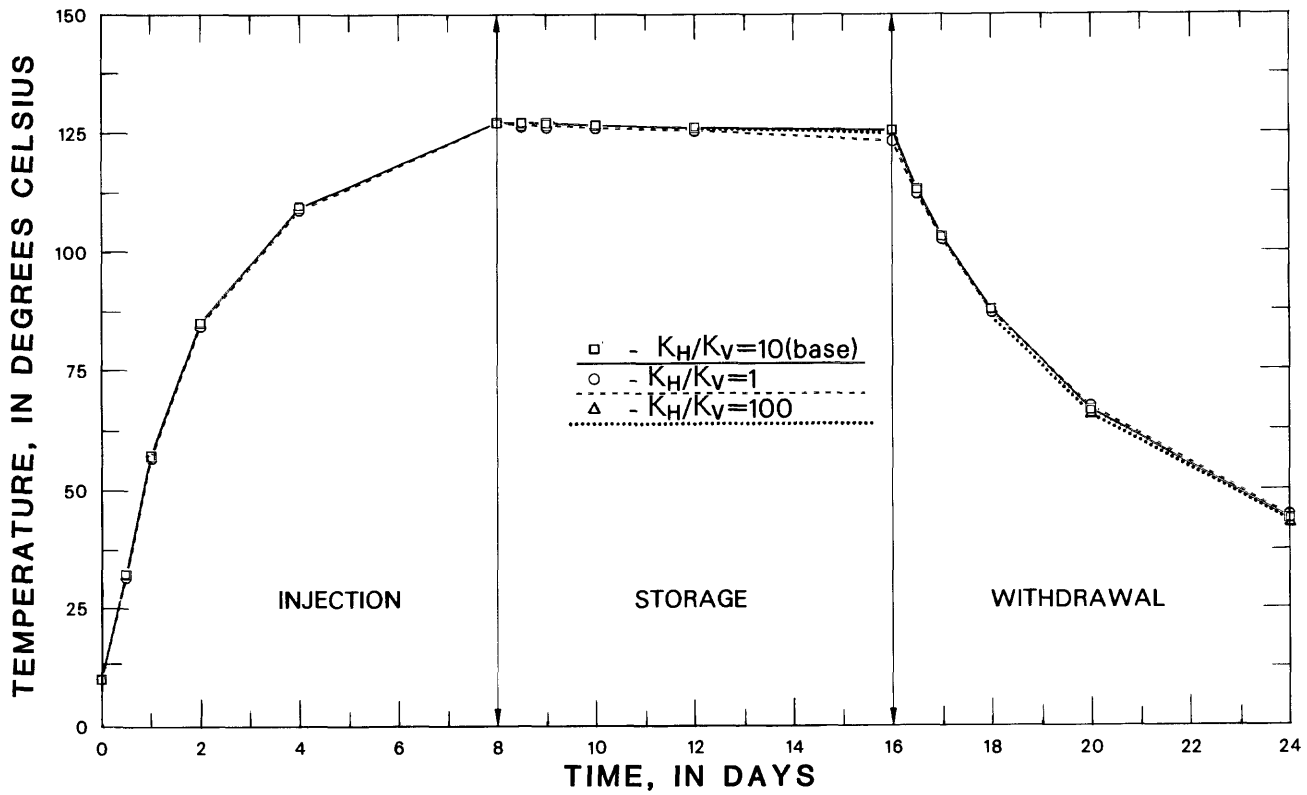


Figure 4. Model-computed temperatures for different values of the ratio of K_H/K_V .

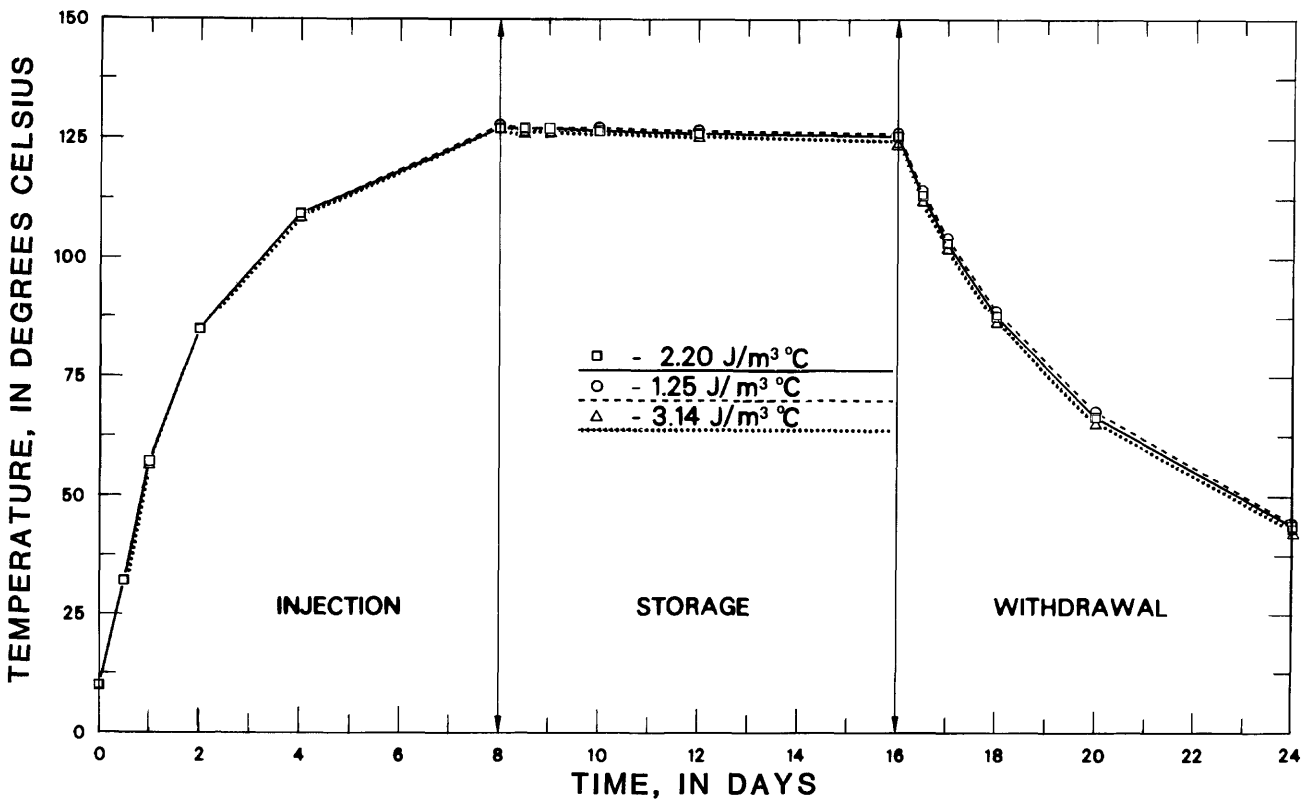


Figure 5. Model-computed temperatures for different values of rock thermal conductivity times 10^{-5} .

Horizontal Hydraulic Conductivity

Values of horizontal hydraulic conductivity (fig. 6) that are an order of magnitude greater than and less than the assumed base values (table 1) were simulated in the model; the ratio of K_H to K_V was set equal to 10. The order of magnitude less than the value resulted in computed temperatures and an aquifer thermal efficiency that differed only slightly from the base simulation. The order of magnitude more than the value of hydraulic conductivity resulted in lower computed temperatures during storage and a calculated aquifer thermal efficiency of 49.5 percent (base value equals 51.0 percent). This probably is due to vertical convection resulting from the temperature-induced density differences between the natural and injected ground water. This effect is discussed in more detail in the section "Buoyancy Flow." In brief, the density differences between the warmer injected water and the cooler water in the aquifer causes hot water to move to the top of the aquifer where heat can be lost to the upper confining layer or to move laterally away from the production well.

Porosity

A range of porosity values was selected from published data (Clark, 1966; Norvitch and others,

1973); the laboratory analysis of core samples; natural gamma, gamma-gamma, and neutron borehole geophysical data; and analyses of cores of the Franconia and Ironton and Galesville Formations in southern Minnesota (Minnesota Gas Co., oral commun., 1980). The values ranged from 0.10 to 0.40. The median value, 0.25, was assumed to be the base value. Differences in model-calculated temperature (fig. 7) for the values of simulated porosity were greatest during the injection period. This probably is due to the inverse proportionality of porosity to ground-water velocity. During injection-withdrawal, convection of heat by the moving ground water is the major mechanism of energy transport near the well where, for this analysis, the observation point is located. The greater the porosity the slower the heat front will move and, thus, the lower the temperature calculated at the observation point. Model-calculated aquifer efficiencies for the porosities of 0.10 and 0.40 were 51.5 and 50.1 percent, respectively.

Rock-Heat Capacity

Rock-heat capacity is the product of rock density and rock specific heat and is the ability of the rock to store heat. Ranges of heat capacity were obtained from Sommerton and others (1965) and were calculated by using data from Sommerton and others (1965), Clark (1966), Hellgeson and others (1978),

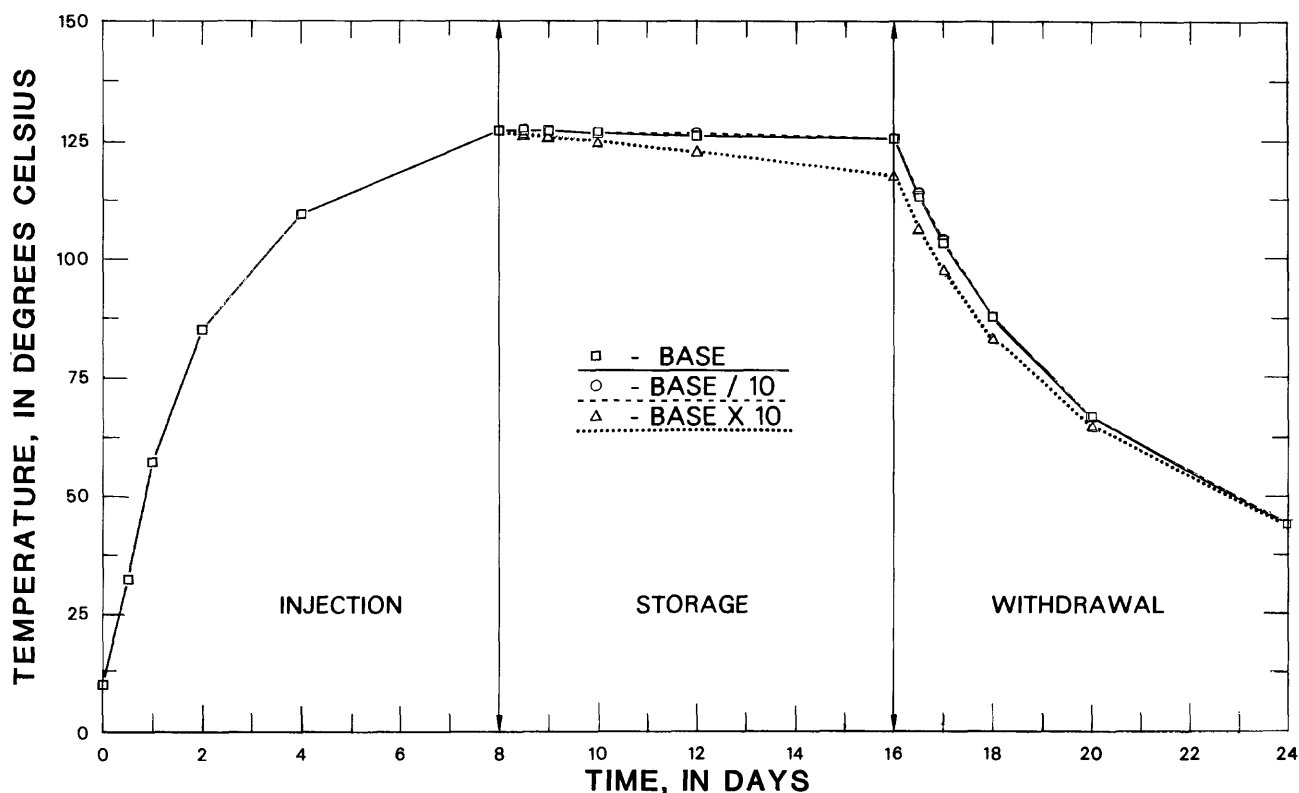


Figure 6. Model-computed temperatures for different values of horizontal hydraulic conductivity.



Figure 7. Model-computed temperatures for different values of aquifer porosity.

and Robie and others (1978) and from methods described by Martin and Dew (1965). The base value for rock-heat capacity represents a sandstone with a composition similar to sandstones in the Franconia-Ironton-Galesville aquifer. The low value of rock-heat capacity represents a quartz-rich sandstone, and the high value represents a clay-rich sandstone. The denser the rock, or the higher the specific heat, the greater the energy required to heat the rock. This is reflected in the model-computed temperatures in figure 8 for different values of rock-heat capacity. Lower temperatures are calculated for higher values of rock-heat capacity because of the amount of energy required to heat the rock. Calculated aquifer thermal efficiencies for rock heat capacities of 1.00×10^{-6} and $2.68 \times 10^{-6} \text{ J/m}^3\text{ }^\circ\text{C}$ are 51.7 and 50.3 percent, respectively.

Thermal Dispersivity

The model was most sensitive to thermal dispersivity which, unfortunately, is the most difficult property to measure in the ground-water-flow system. Although the body of data is not large, Sauty and others (1979) concluded from heat-injection tracer tests and model studies that thermal dispersivity is probably of the same order of magnitude as dispersivities measured by means of chemical trac-

ers. Sauty and others (1979) also described thermal dispersivity as a function of scale, suggesting a value of 0.1 m for a heat-storage radius of 10 m in isotropic aquifers. A base value of 3 m was assumed for sensitivity analysis.

In general, thermal dispersivity may be visualized as the dispersion of the thermal front, which is due to the length of the path a particle might take in going from one point in the aquifer to another point in the aquifer, and as a function of the properties of the aquifer. The thermal front, defined for this report, is the transition zone between the warm injected water and the cooler water in the aquifer. Figure 9 shows a plan view of a hypothetical thermal front. It is important to note that the relative width of the thermal front can vary from point to point within the aquifer. Where the particle path is more direct, the thermal dispersivity is smaller, the thermal front is thinner, and hotter water moves past a relative point faster. Where the path is longer, the dispersivity is larger, the thermal front is wider, and hotter water moves past a relative point slower. This is apparent in the very high temperature computed by the model early in the injection period, shown in figure 10, for a thermal dispersivity of 0.0 m and in the much lower temperature computed for a thermal dispersivity of 6.0 m.

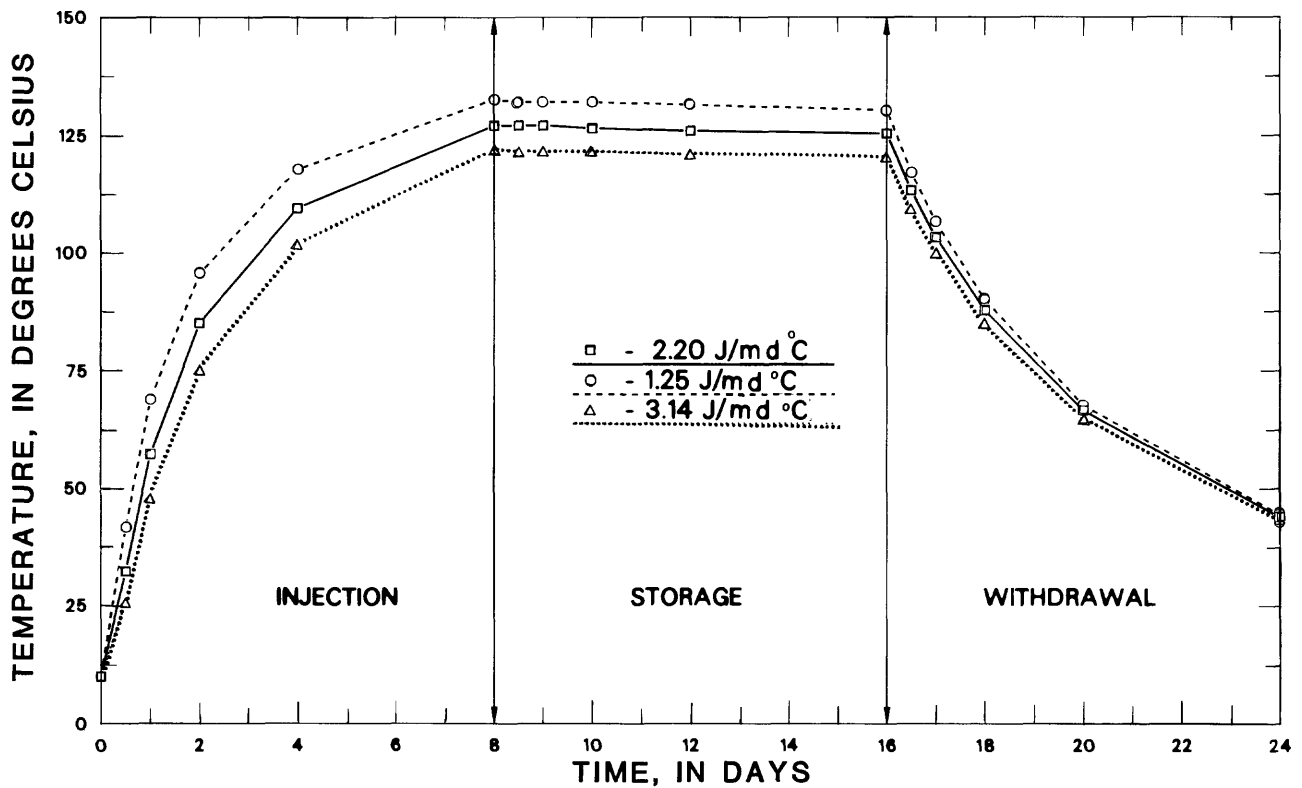


Figure 8. Model-computed temperatures for different values of rock-heat capacity.

Thermal dispersivity also has the greatest effect on the model-computed aquifer thermal efficiencies. A dispersivity of 0.0 m results in an efficiency of 66.8 percent, and a dispersivity of 6.0 m results in an efficiency of 43.4 percent.

Buoyancy Flow

Hellstrom and others (1979) described the effects of thermal convection, or buoyancy flow, which were due to the differences in density of the injected hot water and the cooler water in the aquifer. Their work was related to heat storage in shallow glacio-luvial aquifers, which generally have permeabilities

higher than values reported for the Franconia-Ironton-Galesville aquifer. Figure 11 illustrates the effects of buoyancy flow. During early injection, the thermal front (transition zone between the hotter injected water and colder aquifer water) is approximately vertical. The thermal front is unstable because the hotter, lower density water tends to rise convectively above the more dense cold water, resulting in thermal stratification in the aquifer and tilting of the thermal front. Heat losses from the aquifer to the confining units is roughly proportional to the areas of the upper and lower surfaces of the warm water region (fig. 11) (Hellstrom and others, 1979). Because buoyancy flow tends to increase in this region, it also increases the potential for heat loss. Excessive buoyancy flow may reduce seriously the efficiency of aquifer thermal storage.

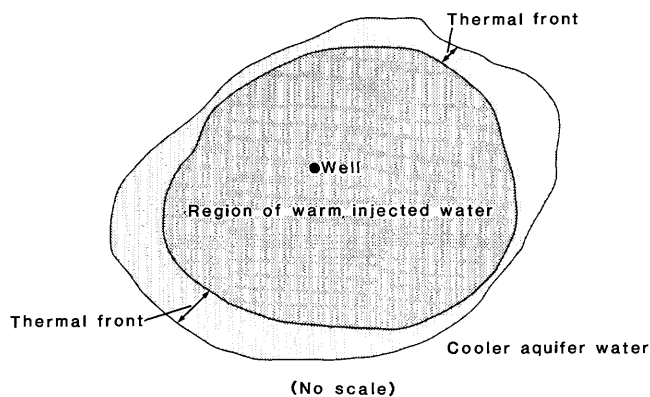


Figure 9. Plan view of hypothetical thermal front.

To examine the potential for buoyancy flow and its possible effect on the thermal efficiency of the Franconia-Ironton-Galesville aquifer, the preliminary nonisothermal, radial-flow, energy-transport model was used to simulate the 24-day test cycle from which temperature versus depth plots were constructed for selected values of K_H and K_H/K_V . As in previous simulations, the observation point for model-computed temperatures is 6.5 m radially from the injection well. The 24-day test cycle was simulated in the same way as in the sensitivity analysis with 8

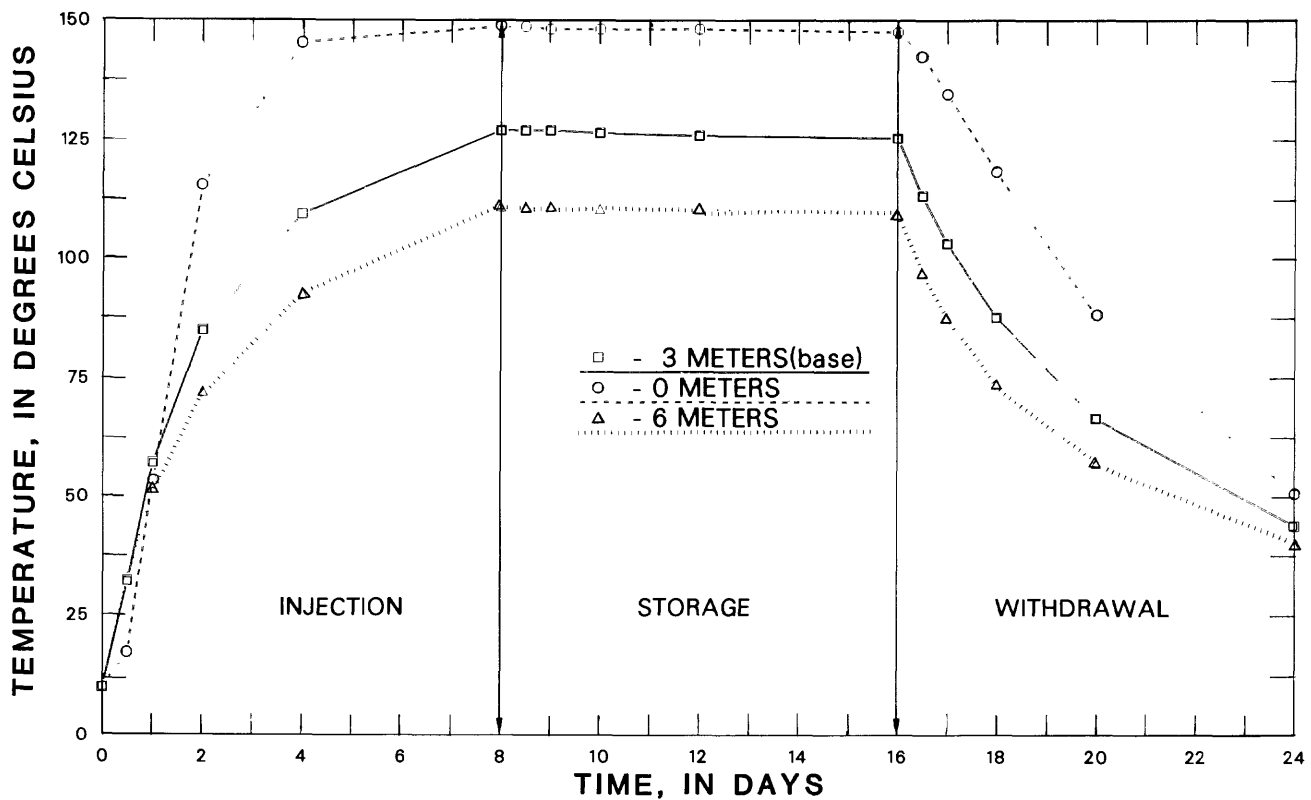


Figure 10. Model-computed temperatures for different values of thermal dispersivity.

days of injection of water at 18.9 L/s of 150°C water and followed by 8 days of storage and 8 days of withdrawal at 18.9 L/s. To examine the effect of buoyancy flow due to natural convection and due to forced convection during injection and withdrawal, vertical temperature profiles were constructed for the end of simulated injection, storage, and withdrawal periods.

Figure 12 illustrates the temperature profile at a radial distance of 6.5 m from the injection well for the base conditions (tables 1, 2) used in the sensitivity analysis and with K_H/K_V equal to 10. At the end of the simulated injection, little evidence of buoyancy flow remains. The temperature profile illustrates vertical heat losses to the upper and lower confining

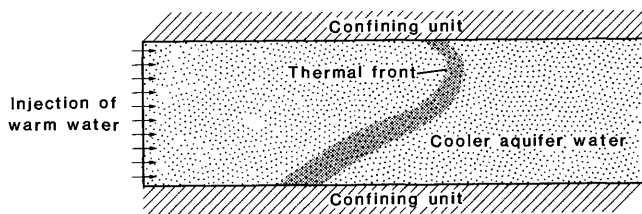


Figure 11. Horizontal injection of warmer water in an aquifer with excessive thermal stratification illustrating tilting of the thermal front, or buoyancy flow (Hellstrom and others, 1979).

layers and to the lower part of the Franconia Formation. The vertical and horizontal heat losses are apparent after the storage period, but tilting of the thermal front is small. At the end of withdrawal, thermal tilting is not apparent. It should be noted that some vertical convection can be observed by comparing the model-computed temperatures within the confining layers. At the end of the withdrawal period, the temperature in the upper confining layer, the St. Lawrence Formation, is warmer than the temperature in the lower confining layer, the Eau Claire Formation, even though the temperature in the Iron-ton-Galesville Formation is hotter than the temperature in the upper part of the Franconia Formation. It also should be noted that temperatures in the lower part of the Franconia Formation continued to increase during withdrawal, indicating that heat conduction from above and below is greater than forced convection from pumping into or out of this part of the formation. If heat injected or conducted to the lower part of the Franconia Formation is not recoverable, then the efficiency of the aquifer thermal-storage system could be reduced significantly.

Figure 13 illustrates the model-computed temperature profile for conditions similar to those in figure 10 except that horizontal and vertical hydraulic conductivities are equal. The computed tempera-

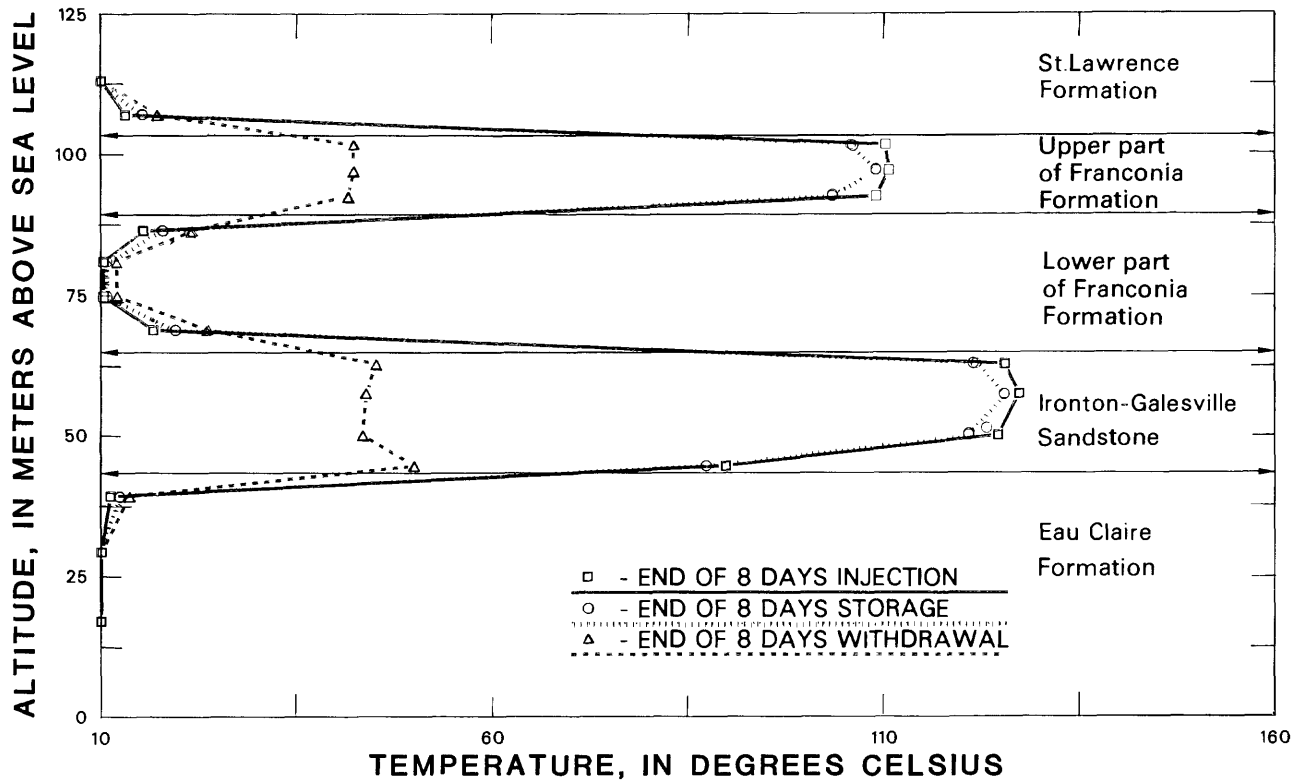


Figure 12. Model-computed temperature profiles at the end of simulated injection, storage, and withdrawal for assumed base conditions.

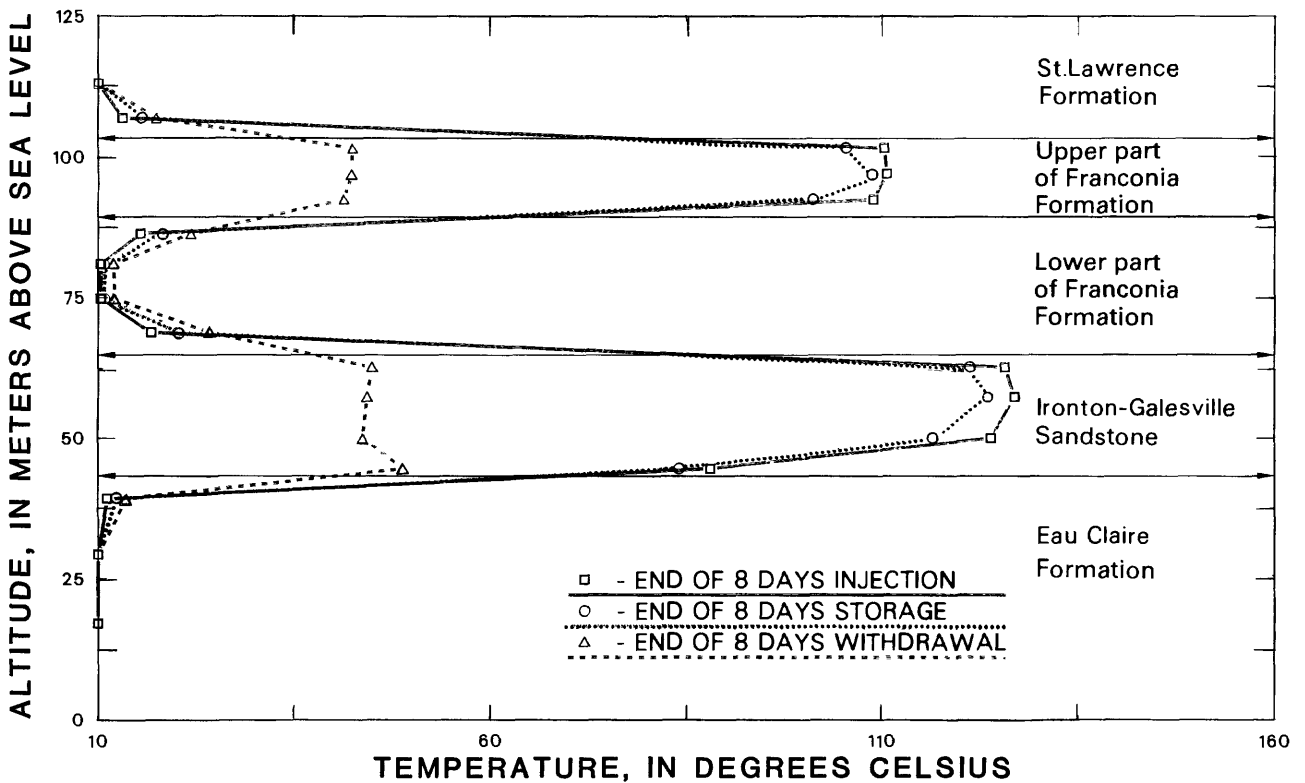


Figure 13. Model-computed temperature profiles at the end of simulated injection, storage, and withdrawal for base conditions and K_h equal to K_v .

ture profiles in figure 13 are similar to figure 10 except for a slightly larger tilt in the thermal front after the storage period and slightly higher temperatures in the upper confining layer (St. Lawrence Formation) and the lowermost point (lower Franconia Formation). This is because simulation of a larger vertical hydraulic conductivity allowed for easier vertical heat conduction, which resulted in greater thermal stratification and buoyancy flow. The small amount of heat lost due to greater buoyancy was reflected in a calculated aquifer thermal efficiency that was 0.2 percent lower than the aquifer thermal efficiency calculated for base conditions.

To further examine the effects of buoyancy flow within the possible range of hydraulic conductivity for the aquifer, hydraulic conductivity was simulated as 10 times the base value with K_H/K_V equal to 10 (fig. 14). The computed temperature profiles at the end of the storage period are similar to those in figures 12 and 13 except in the Ironton-Galesville aquifer, where the thermal front is moderately tilted. Also, computed temperatures are higher in the upper part of the Ironton-Galesville aquifer during the withdrawal period than in the previous simulation. This resulted in greater heat loss to the lower part of the Franconia Formation and an aquifer thermal efficiency that was 1.3 percent lower than in the base simulation.

Figure 15 illustrates model-computed temperature profiles for hydraulic conductivities 10 times the base values and K_V equal to K_H . The buoyancy flow is evident in the thermal tilting produced in the upper part of the Franconia and the Ironton and Galesville Formations at the end of the storage and withdrawal periods. The greater buoyancy flow resulted in an aquifer thermal efficiency that was 2.9 percent lower than in the base simulation.

It is important to note that the temperature in the lower Franconia Formation continued to increase throughout the simulated test cycle for each of the assumed conditions. As stated earlier, losses to the lower part of the Franconia Formation may result in a significantly lower thermal efficiency of the formation. A method for possible reduction of heat loss to this part of the aquifer may be screening only the permeable parts of the upper part of the Franconia and the Ironton and Galesville Formations and, thus, not injecting hot water directly into the lower part of the Franconia Formation.

Finally, it must be noted that in simulations used to investigate buoyancy flow and tilting of the thermal front, only horizontal and vertical hydraulic

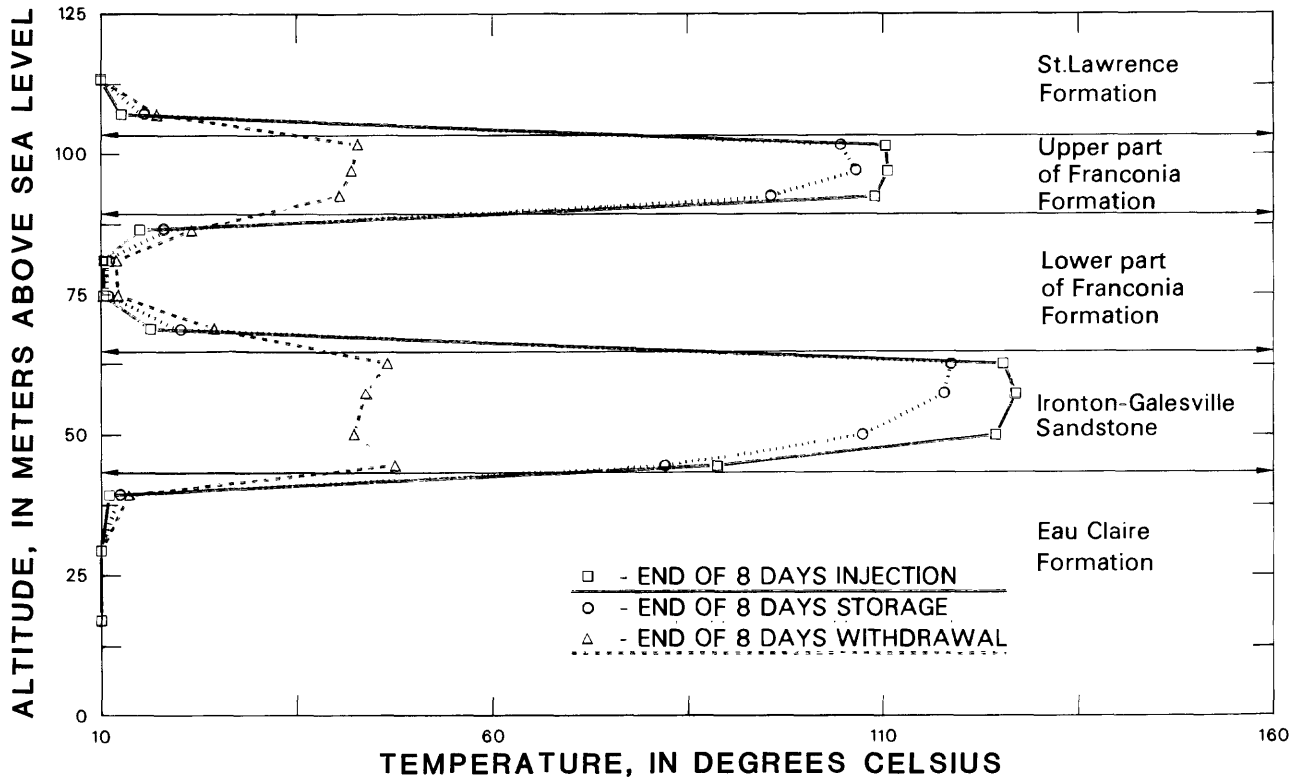


Figure 14. Model-computed temperature profiles at the end of simulated injection, storage, and withdrawal for hydraulic conductivities equal to 10 times the base value.

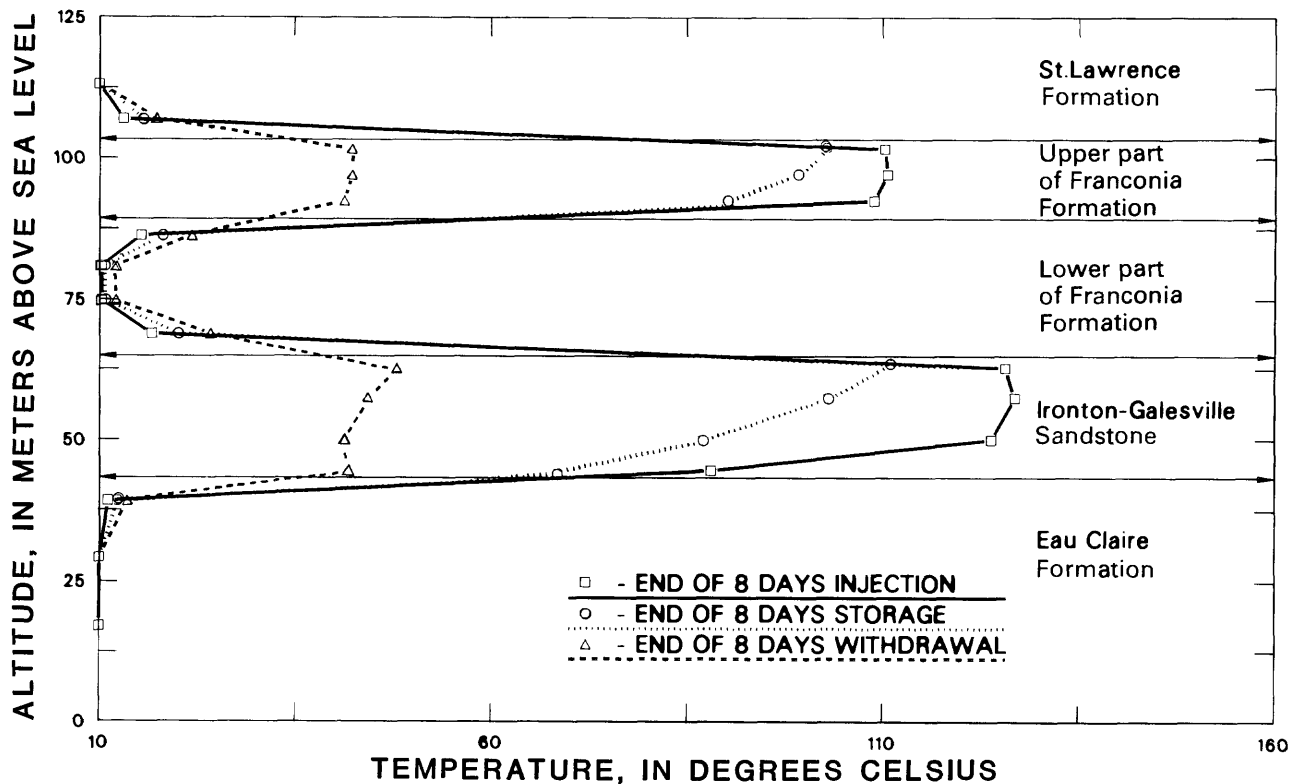


Figure 15. Model-computed temperature profiles at the end of simulated injection, storage, and withdrawal for horizontal hydraulic conductivities equal to 10 times the base value and K_v equal to K_H .

conductivity were varied while other hydraulic and thermal properties were not. It is possible that for other values of porosity, thermal dispersivity, rock-heat capacity, and thermal conductivity different results may be obtained for simulations of buoyancy flow.

AQUIFER THERMAL EFFICIENCY

The feasibility and success of an ATEs system are determined by the amount of thermal energy that can be stored in and recovered from the aquifer. Aquifer thermal efficiency, expressed as a percentage, was calculated as the total energy withdrawn divided by the total energy injected. For base values of hydraulic and thermal properties, the flow and energy-transport model calculated a thermal efficiency of 51 percent for simulation of short-term test cycles. Although the model is sensitive to values of certain hydraulic and thermal characteristics in terms of calculated temperature, simulation of different values of the properties resulted in only small differences in calculated thermal efficiency. Generally, these differences were less than 2 percent, except for thermal dispersivity where values were approximately 7 percent. In terms of estimating aquifer thermal efficien-

cy, the model sensitivity analysis only indicates the possible range of thermal efficiency based on the possible range of values of hydraulic and thermal properties. Better definition of these properties will improve model estimates of efficiency.

The sensitivity analysis indicates the properties that need to be defined more precisely to make the model estimate as accurate as possible. However, in addition to the physical properties of the aquifer system, operational factors also will affect the thermal efficiency of the ATEs system. These factors include temperature of injected water, rate of injection and withdrawal, and duration of injection, storage, and withdrawal. To test the effects of these factors on thermal efficiency, a series of model simulations were performed in which these factors were varied, and the results were compared. Base values of hydraulic and thermal properties were used in all these simulations.

As described above, the ability of the preliminary radial-flow model to simulate the ATEs doublet-well system is related to the radial distance that heat will move away from the well for the period of simulation. Model computed temperatures for the short-term cycle simulations (fig. 16) indicate that injected heat was contained within a radial distance

of approximately 20 m. This radial distance is shown in figure 3. Comparison of the equipotential lines for the doublet-well system and the 20-m, model-computed radial extent of heat indicates that the short-term cycle simulations are fairly representative of the doublet-well system.

Longer term simulations indicate that heat will be contained within an 85-m radial distance for the 6-month injection periods and a 90-m radial distance for the 8-month injection periods (figs. 17–20). These two radial distances are plotted on figure 3. A comparison of the 85- and 90-m radial distances with the equipotential lines for the doublet-well system indicates that the preliminary model radial-flow assumption may not represent adequately the doublet-well system for the longer term cycles. However, the usefulness of the results of the preliminary model long-term simulations is not affected because the purpose of the simulations is to describe how the operational factors of injection and withdrawal rates and duration can affect the aquifer efficiency. The aquifer efficiencies obtained from the long-term simulations are termed relative. Although they may not exactly represent efficiencies that would be obtained from the working ATES doublet-well system, they are comparable to each other and, thus, serve the intended purpose.

For purposes of this study, short-term testing cycles were defined as 8 days of injection at 18.9 L/s of 150°C water, 8 days of storage, and 8 days of withdrawal at 18.9 L/s for a total of 24 days. Figure 16 shows a plot of model-computed well-bore temperatures as a function of time for five sequential 24-day cycles as simulated by the base radial-flow model. Also indicated at the end of each 24-day cycle is the aquifer thermal efficiency. The plot indicates that, for the short-term uniform cycles, the aquifer thermal efficiency tends to increase with successive cycles. This is because injected water must heat up the aquifer from its initial ambient temperature of approximately 10°C. At the beginning of subsequent injections, the aquifer is warmer due to residual heat that was not completely recovered from the previous cycle. The graph also indicates that the aquifer thermal efficiency will approach a maximum value after several cycles. For the simulation depicted in figure 16, the maximum aquifer efficiency probably will be between 60 and 65 percent.

A working ATES system would not operate on the short-term (24-day) test cycles but rather on yearly cycles based on seasonal thermal-energy surplus and demand. Figure 17 shows model-computed well-bore temperatures and relative thermal efficiencies for five continuous 1-year cycles of 8 months of injection.

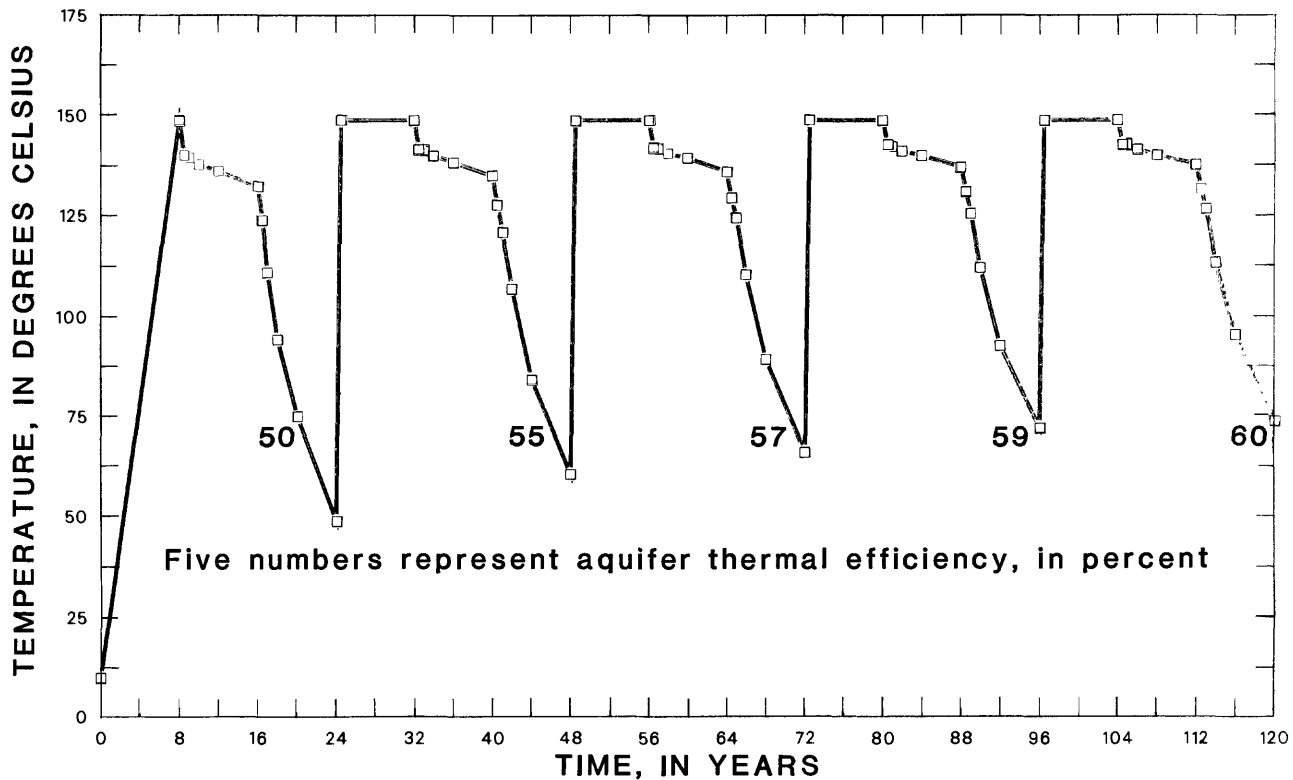


Figure 16. Model-computed well-bore temperatures and aquifer thermal efficiencies for five sequential 24-day test cycles.

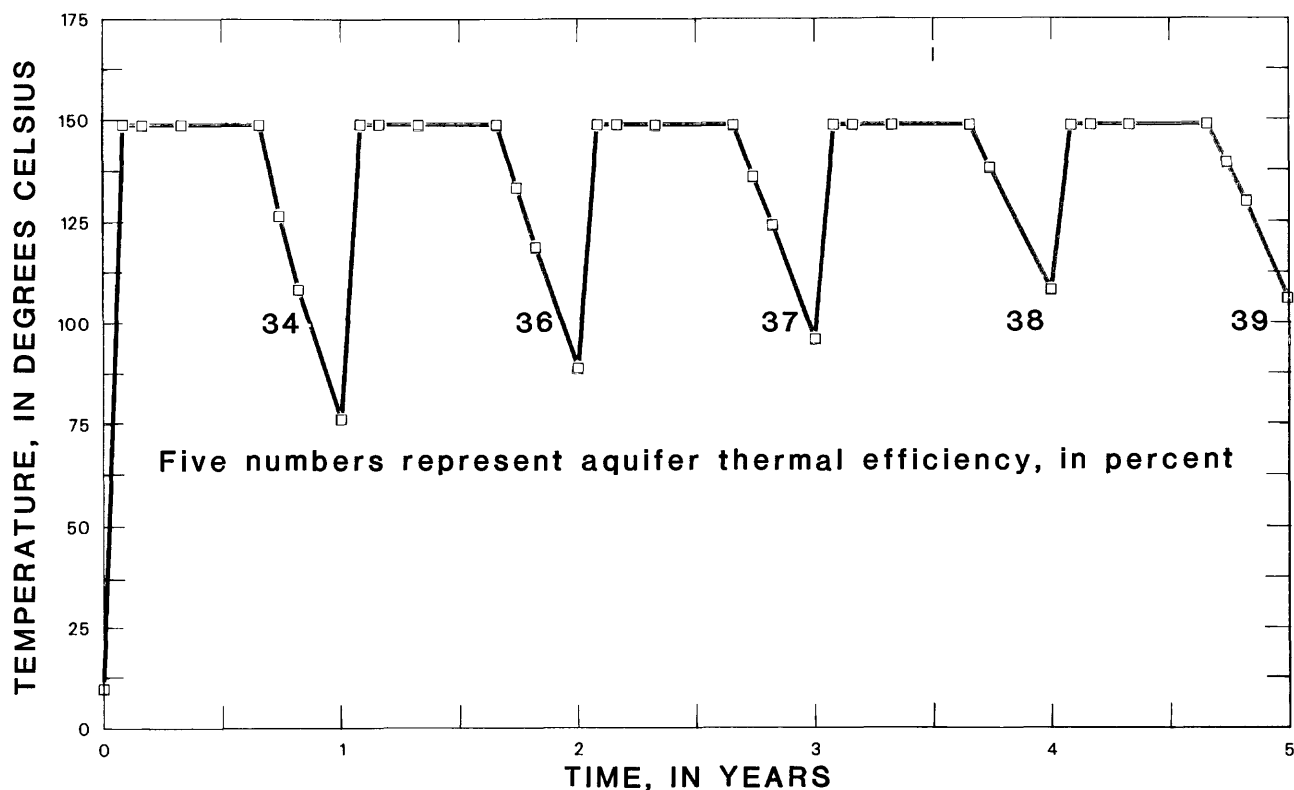


Figure 17. Model-computed well-bore temperatures and aquifer relative thermal efficiencies for five sequential 1-year cycles each consisting of 8 months of injection at 18.9 L/s of 150°C water and 4 months of withdrawal at 18.9 L/s.

tion at 18.9 L/s of 150°C water and 4 months of withdrawal at 18.9 L/s. The model conditions are similar to those previously described for five 24-day cycles. Relative thermal efficiencies of the aquifer range from 34 to 39 percent, and well-bore temperatures at the end of withdrawal range from approximately 80° to 105°C.

Figure 18 shows model-computed well-bore temperatures and relative thermal efficiencies of the aquifer for conditions similar to those shown in figure 17 except that the withdrawal rate is 37.7 L/s. The relative thermal efficiency of the aquifer ranges from 52 to 61 percent, and the well-bore temperature at the end of each cycle ranges from approximately 45° to 75°C.

Figure 19 shows model-computed well-bore temperatures and aquifer relative efficiencies calculated for five continuous 1-year cycles each consisting of 6 months of injection at 18.9 L/s of 150°C water and 6 months of withdrawal at 18.9 L/s. Relative thermal efficiency of the aquifer at the end of each cycle ranges from 51 to 59 percent, and the well-bore temperature at the end of each cycle ranges from approximately 45° to 70°C.

Figure 20 shows model-computed well-bore temperatures and relative thermal efficiencies of the

aquifer calculated for conditions similar to figure 19 except that the withdrawal rate is 37.8 L/s, or twice that used for the calculations in figure 19. Aquifer relative thermal efficiencies are the highest of any of the simulations and range from 73 to 84 percent. This simulation also produces the lowest well-bore temperatures at the end of each cycle ranging from approximately 25° to 35°C.

To summarize, figures 17 through 20 illustrate aquifer relative thermal efficiencies and well-bore temperatures based on 1-year cycles with hypothetical injection-withdrawal rates and periods. It is obvious, from a comparison of the graphs, that operational methods which increase aquifer thermal efficiency also lower well-bore temperatures at the completion of each cycle. Thus, for a working ATEs system, a required minimum well-bore temperature also may limit the aquifer thermal efficiency. The simulations shown in figures 16 through 20 also demonstrate one method for developing an optimization scheme for a working ATEs system by use of a calibrated groundwater-flow and thermal-energy-transport model.

Finally, a similarity between the relative thermal efficiencies of the aquifer in figures 16 and 19 should be noted. Each curve represents a different hypothetical cyclic scheme in terms of time and rate.

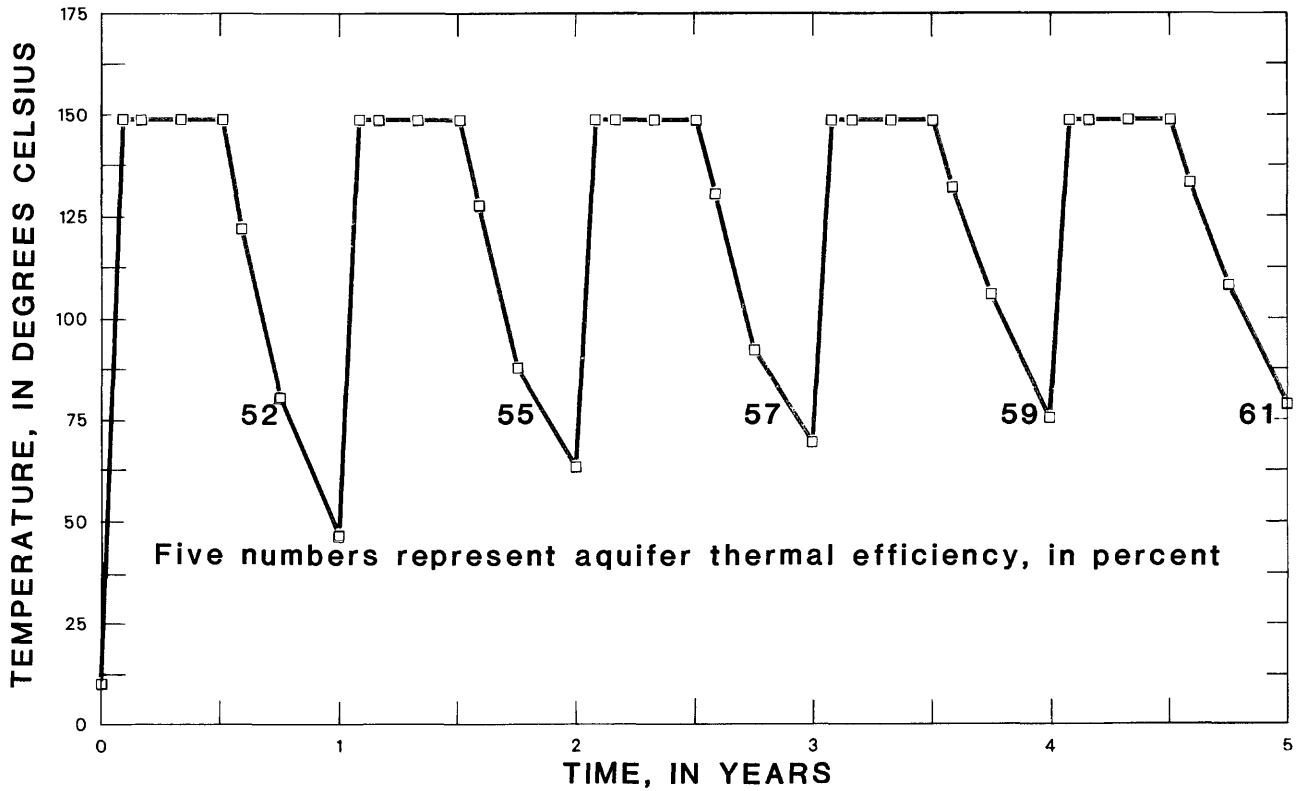


Figure 18. Well-bore temperatures and calculated aquifer relative efficiencies for five hypothetical 1-year cycles of 8 months of injection at 18.9 L/s of 150°C water and 4 months of withdrawal at 37.7 L/s.

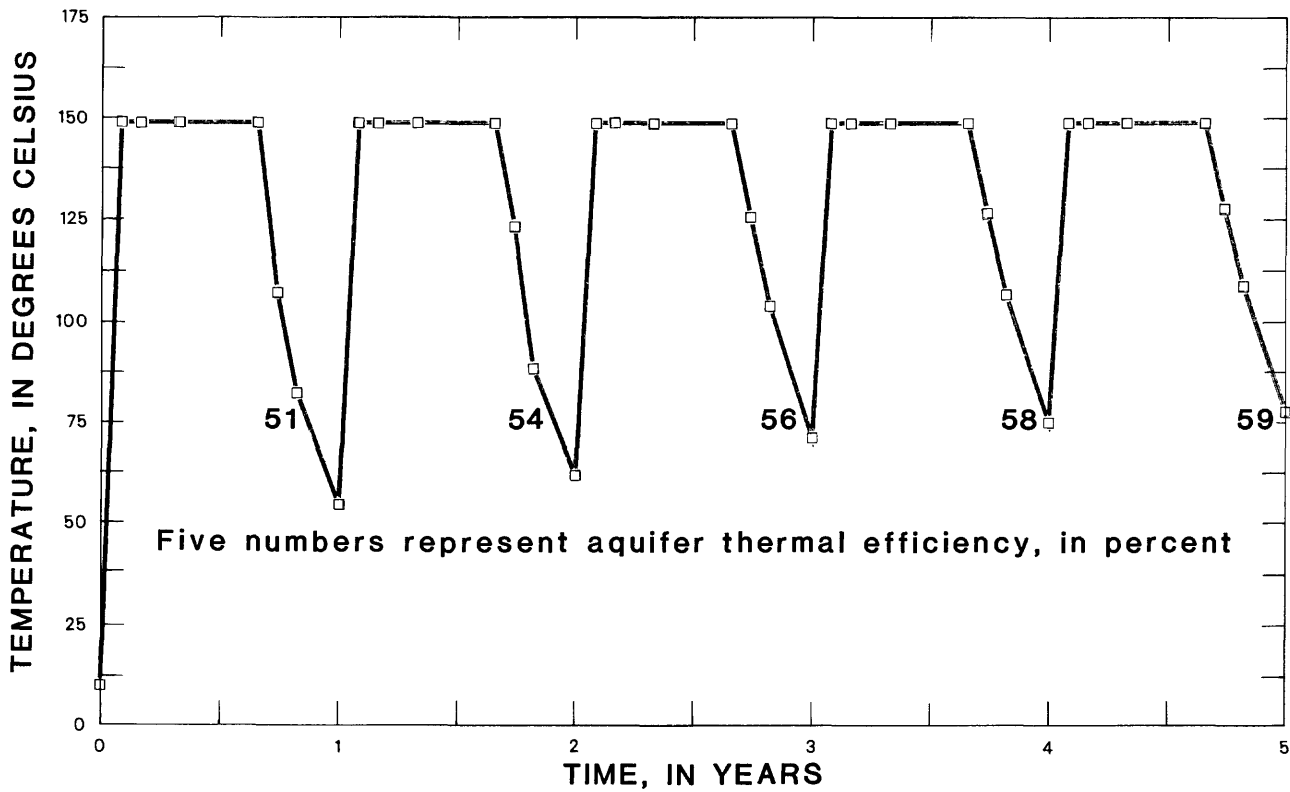


Figure 19. Well-bore temperatures and calculated aquifer relative efficiencies for five hypothetical 1-year cycles of 6 months of injection at 18.9 L/s of 150°C water and 6 months of recovery at 18.9 L/s.

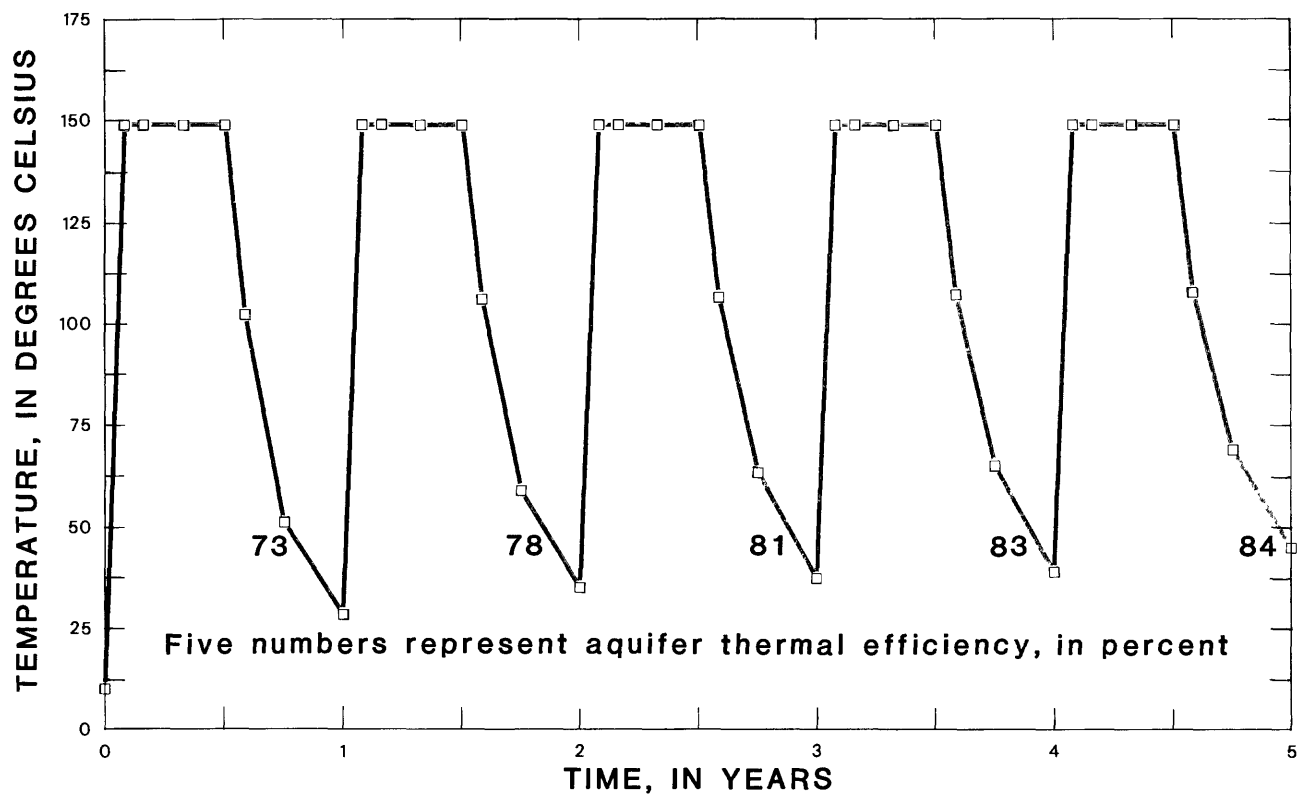


Figure 20. Well-bore temperatures and calculated aquifer relative efficiencies for five hypothetical 1-year cycles of 6 months of injection at 18.9 L/s of 150°C water and 6 months of withdrawal at 37.8 L/s.

The only common factor between them is the injection temperature and the total volume of water injected and withdrawn. Relative thermal efficiencies for the simulation depicted in figure 16, however, are calculated at a significantly reduced time scale (by a factor of approximately 15), which suggests that it may be possible to obtain adequate estimates of aquifer thermal efficiency and well-bore temperatures with reduced time-scale simulations.

SUMMARY

In May 1980, the University of Minnesota began an ATEs study on the St. Paul campus. The ATEs system uses a doublet-well design with an injection-withdrawal well spacing of approximately 250 m. Hot water (150°C) will be injected into the deep (180-240 m) Franconia-Ironton-Galesville aquifer, a consolidated sandstone. The aquifer is confined above by the St. Lawrence Formation, a dolomitic sandstone, and below by the Eau Claire Formation, a shale. Short-term testing will consist of 8 days of injection at 18.9 L/s of 150°C water, 8 days of storage, and 8 days of withdrawal of heated water at 18.9 L/s.

The U.S. Geological Survey is constructing a ground-water-flow and thermal-energy-transport

model to aid in evaluation of the ATEs concept. A preliminary radial-flow model for ground-water flow and thermal-energy transport was constructed with a code developed for the U.S. Geological Survey for calculating the effects of liquid waste disposal in deep saline aquifers. Vertically, the model consists of 16 layers ranging in thickness from approximately 5 to 10 m, which simulates the aquifer and the confining layers. The radial spacings range from 0.18 to 26.8 m. The smallest radial spacing represents the well bore, and the largest radial spacing is one-half of the distance between the doublet wells, or a radius of 125 m.

Sensitivity analysis was made on the preliminary radial-flow and thermal-energy-transport model for hydraulic conductivity, porosity, K_H/K_V , rock thermal conductivity, rock-heat capacity, and thermal dispersivity. Each simulation consisted of 8 days injection at 18.9 L/s of 150°C water, 8 days of storage, and 8 days of withdrawal at 18.9 L/s for one complete 24-day cycle. Individual model properties were varied for the assumed base values and plots of model-computed temperature versus time were constructed for a radial distance of 6.5 m from the well bore. Resulting curves then were compared with each other and with curves for other model properties to determine model sensitivity in terms of calculated temperature and aquifer thermal efficiency. Model

results indicate that hydraulic and thermal properties may be ranked in terms of increasing model sensitivity as follows: K_H/K_V , rock thermal conductivity, hydraulic conductivity, porosity, rock-heat capacity, and thermal dispersivity.

The preliminary radial-flow and thermal-energy-transport model also was used to study the potential effects of thermal convection, or buoyancy flow, due to density differences between the cooler natural-temperature ground water and the heated injection water. The preliminary model simulated 8 days of injection of 150°C water at 18.9 L/s, 8 days of storage, and 8 days of withdrawal at 18.9 L/s. Values of K_H and K_H/K_V were varied individually by an order of magnitude. Vertical profile plots of temperature were constructed at the end of injection, storage, and withdrawal at a radial distance of 6.5 m. Tilting of the thermal front caused by buoyancy flow was not apparent in the temperature profile plots at the end of injection, storage, or withdrawal for the assumed base values of hydraulic and thermal properties. Simulating horizontal K_H at 10 times the base value and K_V equal to K_H resulted in significant tilting of the thermal front at the end of storage and withdrawal, indicating the importance of accurate data collection and analyses for these two hydraulic properties.

The preliminary radial-flow and thermal-energy-transport model also was used to examine the effects on aquifer thermal efficiency of hypothetical test cycles consisting of various periods of injection and withdrawal of hot water and varying withdrawal rates. Simulations consisted of five injection-withdrawal cycles of 1 year each representing a total of 5 years of system operation. In all simulations, injection was 18.9 L/s of 150°C water. Aquifer thermal efficiency was calculated as total energy withdrawn divided by total energy injected. The least efficient cycle simulated consisted of 8 months of injection at 18.9 L/s and 4 months of withdrawal at 18.9 L/s. The aquifer efficiency computed at the end of the fifth cycle was 39 percent, and the final well-bore temperature was 130°C. The most efficient simulation consists of 6 months of injection at 18.9 L/s and 6 months of withdrawal at 37.8 L/s. The computed efficiency after five cycles was 84 percent, and the final well-bore temperature was 46°C.

REFERENCES CITED

- Birch, Francis, and Clark, Harry, 1940, The thermal conductivity of rocks and its dependence upon temperature and composition: *American Journal of Science*, v. 238, no. 9, p. 614–635.
- Clark, S. P., 1966, *Handbook of physical constants*: Geological Society of America Memoir 97, 587 p.
- Hellgeson, H. C., Delaney, J. M., Nesbitt, H. W., and Bird, D. K., 1978, Summary and critique of the thermodynamic properties of rock forming minerals: *American Journal of Science*, v. 278–A, 229 p.
- Hellstrom, Goran, Tsang, Chin-Fu, and Claesson, Johan, 1979, Heat storage in aquifers. Buoyancy flow and thermal stratification problems: Lund University, Sweden, 70 p.
- Intercomp Resources Development and Engineering, Inc., 1976, A model for calculating effects of liquid waste disposal in deep saline aquifers: U.S. Geological Survey Water-Resources Investigations Report 76–61, 128 p.
- Martin, W. L., and Dew, J. N., 1965, How to calculate air requirements for forward combustion: *Petroleum Engineer*, February 1965, 12 p.
- Miller, R. T., 1984, Analysis of areal anisotropy of the Ironton-Galesville aquifer, St. Paul, Minnesota: *Ground Water*, v. 22, no. 4, 8 p.
- Norvitch, R. F., Ross, T. G., and Brietkrietz, Alex, 1973, Water resources outlook for the Minneapolis-St. Paul Metropolitan Area, Minnesota: Metropolitan Council of the Twin Cities, 219 p.
- Papadopoulos, S. S., and Larson, S. P., 1978, Aquifer storage of heated water; Part II, Numerical simulation of field results: *Ground Water*, v. 16, no. 4, p. 242–248.
- Robie, R. A., Hemingway, B. S., and Fisher, J. R., 1978, Thermodynamic properties of minerals and related substances at 298.15°K and 1 Bar (105 pascals) pressure and at higher temperatures: U.S. Geological Survey Bulletin 1452, 465 p.
- Sauty, J. P., Gringarten, A. C., and Landel, P. A., 1979, The effects of thermal dispersion on injection of hot water in aquifers: *Proceedings of Second Invitational Well Testing Symposium*, Lawrence Berkeley Laboratory, Berkeley, California, p. 122–131.
- Sommerton, W. H., Mehta, M. M., and Dean, G. W., 1965, Thermal alteration of sandstones: *Journal of Petroleum Technology*, May, p. 589–593.
- Walton, Matt, 1981, The University of Minnesota aquifer thermal energy storage system, *in Proceedings of the Mechanical, Magnetic, and Underground Energy Storage 1981 Annual Contractors Review*, August 24–26, 1981, Washington, D.C., U.S. Department of Energy.

Low-Level Radioactive Ground-Water Contamination From a Cold-Scrap Recovery Operation, Wood River Junction, Rhode Island

By Barbara J. Ryan and Kenneth L. Kipp, Jr.

Abstract

In 1981, the U.S. Geological Survey began a 3-year study of ground-water contamination at a uranium-bearing cold-scrap recovery plant at Wood River Junction, Rhode Island. Liquid wastes from this industrial site were discharged to the environment through evaporation ponds from 1966 to 1980. Leakage from the polyethylene- and polyvinylchloride-lined ponds resulted in a plume of contaminated ground water that extends from the ponds northwestward to the Pawcatuck River through a highly permeable sand and gravel aquifer of glacial origin.

Electrical conductivity, determined by electromagnetic methods, was used to delineate the plume areally before observation wells were installed. These data, combined with water-quality data from more than 100 observation wells, indicate that the plume is approximately 2,300 feet long and 300 feet wide and is confined to the upper 80 feet of saturated thickness where sediments consist of medium to coarse sand and gravel. No contamination has been detected in fine sands and silts underlying the coarser materials. Piezometric head and water-quality data from wells screened at multiple depths on both sides of the river indicate that contaminants discharge to the river and to a swampy area at the west edge of the river. Dilution precludes detection of contaminants once they have entered the river, which has an average flow of 193 cubic feet per second.

Water-quality data collected from April 1981 to June 1983 indicate that strontium-90, technetium-99, boron, nitrate, and potassium exceed background concentrations by an order of magnitude in much of the plume. Concentrations of gross beta emitters range from 5 to 500 picoCuries per liter. No gamma emitters above detection levels have been found. Electrical conductivity of the water ranges from 150 to 4,500 micromhos per centimeter at 25 degrees Celsius. Water-quality sampling shows zones of concentrated contaminants at both ends of the plume, separated by a zone of less contaminated water. Laboratory tests for exchangeable cations indicate little capacity for uptake by the coarse sediments. In the swamp, reducing conditions may promote observable solute interaction with sediments or organic material.

INTRODUCTION

Liquid wastes containing radionuclides and other chemical solutes from an enriched uranium cold-scrap recovery plant have leaked from polyethylene- and polyvinylchloride (PVC)-lined ponds and trenches into a highly permeable sand and gravel aquifer in southern Rhode Island. The resultant plume of ground-water contamination extends about 2,300 ft from the ponds and trenches to the Pawcatuck River and the contiguous swamp into which ground-water discharge occurs. In 1981, the U.S. Geological Survey began a 3-year study of this ground-water contamination at a plant at Wood River Junction, Rhode Island (fig. 1). The objectives of the study are to (1) identify constituents in the plume, (2) determine solute interaction with aquifer materials, (3) model ground-water flow and solute transport in the study area, and (4) use the model to predict residence times in the aquifer and fate of contaminants in the plume.

Contaminated ground water at this site moves through a highly permeable glacial outwash aquifer that yields water readily to wells. The Rhode Island Water Resources Board has conducted test drilling around Wood River Junction and has considered developing ground water from the Meadow Brook Pond area for use both within and outside the basin. The possibility that supply wells developed in the area might be contaminated as a result of migration of contaminated water beneath the Pawcatuck River is of concern to the Water Resources Board.

By October 1982, most of the data collection network for the investigation was in place, and routine water-level measurements, water-quality sampling, and precipitation measurements were begun. This paper describes geohydrologic conditions at the site, the source of ground-water contamination, and presents preliminary findings based on data collected through June 1983. National Geodetic Vertical Datum of 1929 is referred to as sea level in this report.

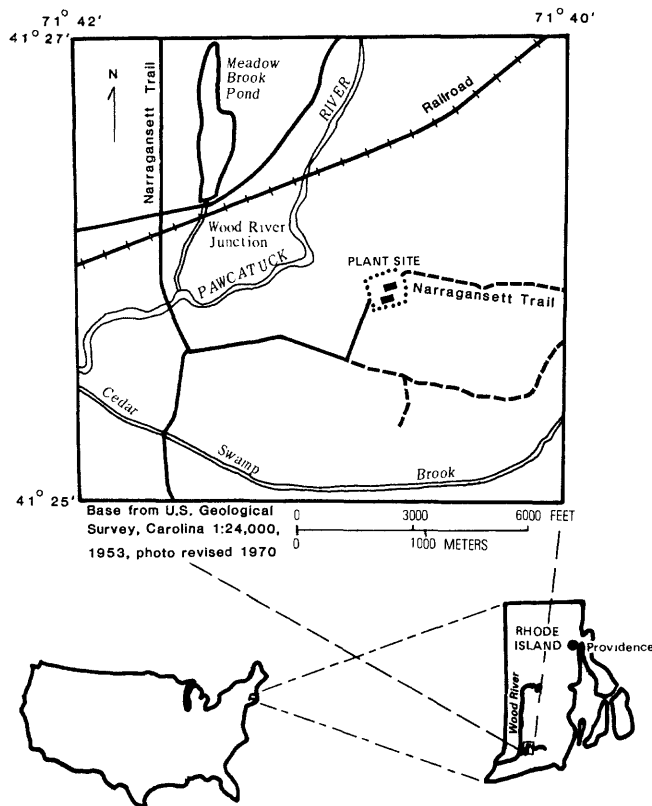


Figure 1. Location of study area.

PLANT HISTORY AND CONTAMINATION SOURCE

From 1964 to 1980, an enriched uranium cold-scrap recovery plant was operated (fig. 2) at Wood River Junction, Rhode Island. Acid digestion with hydrofluoric and nitric acids and organic separation with tributyl phosphate and kerosene were used in the process. Solid wastes from the process were shipped offsite, and liquid wastes were discharged to the Pawcatuck River through a drain pipe from 1964 to 1966 and to uncovered "evaporation" ponds and trenches from 1966 to 1980.

In southern Rhode Island, however, average annual precipitation is much greater than average annual evaporation; for example, from 1950 to 1970, precipitation at the National Weather Station at Kingston, Rhode Island, 9 mi northeast of the study area, averaged 46.06 in/yr while estimated annual free water surface evaporation for the same period was only 29 in/yr (National Oceanic and Atmospheric Administration, 1982). This and the fact that highly permeable sediments occur beneath the ponds

and trenches indicate that much of the liquid waste discharged to the ponds and trenches did not evaporate but rather percolated into unconsolidated deposits beneath the site.

The depth of the ponds and trenches ranged from 3 to 15 ft below land surface; the bottoms of the ponds were 9 to 13 ft and the bottoms of the trenches were 1 to 3 ft above high water table.

From 1964 to 1966, liquid wastes were discharged to the Pawcatuck River through a buried drain 1,500 ft in length. Beginning in 1966, liquid wastes were discharged into a pond approximately 5,000 ft² in area and 6 ft in depth (fig. 2). Pond capacity or overflow problems due to precipitation and disposal flow rates (estimated by plant officials to have averaged about 400 gal/d) led to periodic construction of additional ponds and trenches. In 1967, a second pond (8,400 ft² in area and 4 ft in depth) was used as a replacement, and, in 1972, a new pond was constructed in the same area as the original pond. A series of trenches were built to replace the first and second ponds in 1977 and were used until 1979. The liquid waste disposal ponds and trenches encompassed approximately 25,000 ft². These disposal sites are considered to be the source of the contaminated liquid percolation to the water table. In 1979, a covered tank with a double polyethylene liner was constructed 50 ft north of the original pond area (fig. 2) to hold the liquid waste during evaporation and concentration processing. To date, no evidence exists for ground-water contamination from the covered tank storage area.

Because data on chemical composition and physical properties of the liquid wastes are limited and concentrations of chemical and radiochemical constituents in waste discharges changed with time, defining the actual source loadings is not possible. In addition to hydrofluoric and nitric acids, tributyl phosphate, and kerosene, the following chemicals were used in the recovery process and were present in the liquid wastes in varying concentrations: aluminum nitrate, calcium hydroxide, mercury, sodium carbonate, sodium hydroxide, and potassium hydroxide. Although primarily nonirradiated fuel elements were processed from 1964 to 1980, slightly irradiated fuel elements from test reactors were processed from 1967 to 1980. This could account for the strontium-90 and technetium-99 that are in the contaminated water.

Processing at the plant, which ended in August 1980, currently is being decommissioned. Material from the bottom of the ponds and trenches and sediment from below the ponds and trenches were removed and combined with a cementlike mixture and shipped offsite for burial. Sediments in the unsatu-

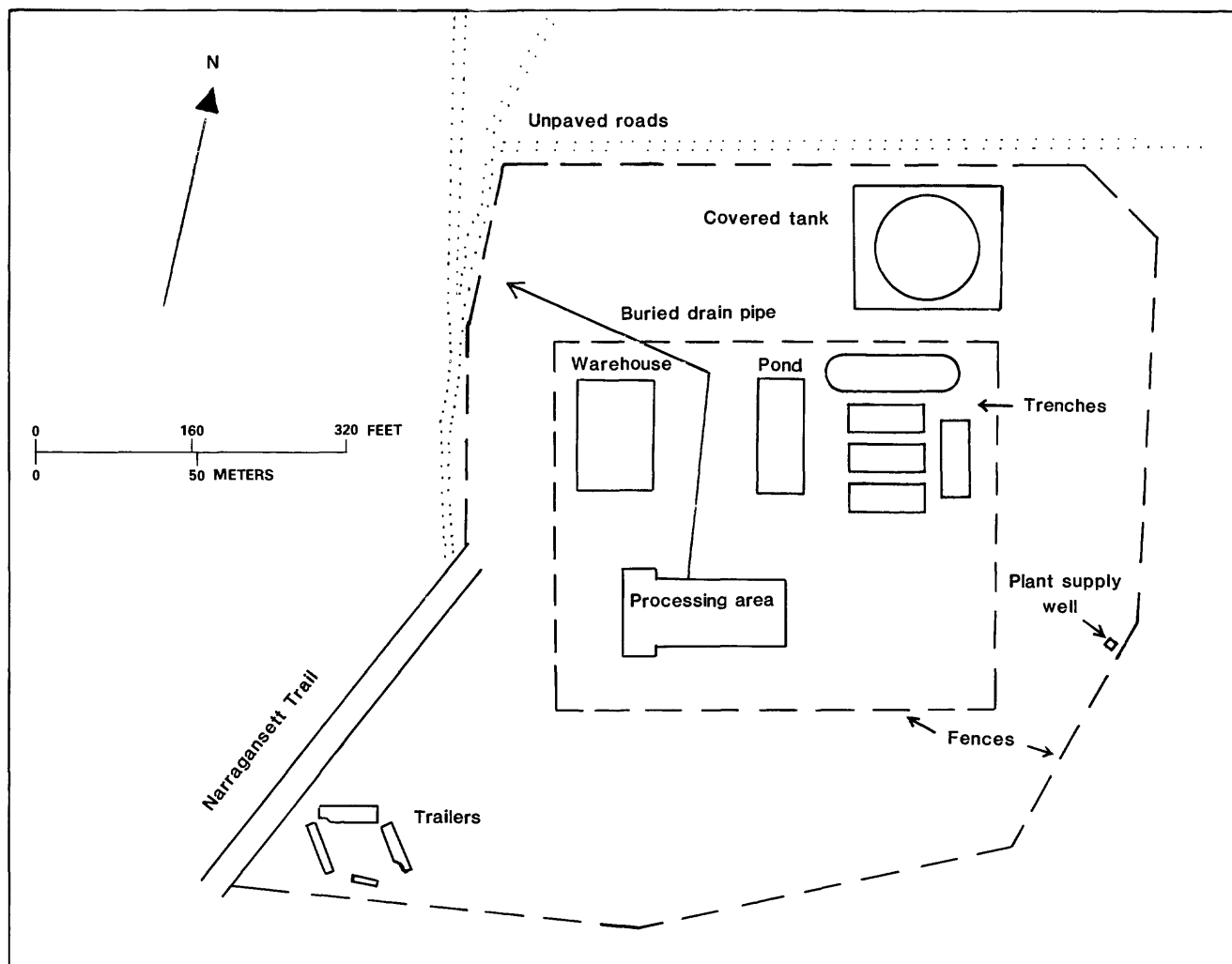


Figure 2. Location of processing area, evaporation pond, trenches, and covered tank in 1979.

rated zone between the pond and trench bottoms and the water table were not sampled.

PREVIOUS SITE INVESTIGATIONS

From 1974 to 1977, the Rhode Island Water Resources Board drilled approximately 20 test holes on the plant property to obtain lithologic and water-quality data for evaluating potential areas for ground-water development. Water-quality data obtained as part of the Water Resources Board investigation indicate ground water of high conductivity ($5,500 \mu\text{mho/cm}$ at 25°C), high nitrate (225 mg/L), and significant gross alpha (43 pC/L) and gross beta (489 pC/L) emitters 1,100 ft from the source area (Dickerman and Silva, 1980, p. 177–178). In 1977, the company installed 10 observation wells between

the plant and the river that ranged in depth from approximately 50 to 80 ft. Water-quality data obtained by the company from one of these wells indicate ground water of high conductivity ($14,500 \mu\text{mho/cm}$ at 25°C), high nitrate ($2,200 \text{ mg/L}$), and significant gross beta emitters ($1,518 \text{ pC/L}$) 200 ft from the source area (Dickerman and Silva, 1980, p. 177–178).

In 1977, resistivity surveys were conducted by David Huntley, University of Connecticut, and by Daniel Urish, University of Rhode Island. Results of these surveys indicated a plume of ground water with high conductivity between the plant site and the Pawcatuck River. Adjacent to the source area, depth below land surface of the highest conductance water was estimated to be 40 ft (David Huntley, written commun., 1981). Maximum known extent of contamination at the start of the present study (October

1982) was approximately 1,200 ft from the source area.

STUDY AREA DESCRIPTION

Geology

The study area is underlain by the Hope Valley Alaskite Gneiss, a metamorphic rock unit of Late Proterozoic age (570–900 million years old). The gneiss was an igneous rock unit that underwent one and possibly two episodes of metamorphism (Moore, 1959). The bedrock crops out east, northeast, west, and southwest of the study area, and unconsolidated glacial deposits of Pleistocene age (less than 1 million years old) have been deposited on top of the bedrock.

Glacial till deposits (poorly sorted clays, silts, sands, gravels, and boulders) form a relatively thin (less than 20 ft) mantle over the bedrock (LaSala and Hahn, 1960) and appear at land surface east of the plant site (fig. 3). Glacial outwash deposits (well-sorted silts, sands, and gravels) were deposited in the bedrock valley (fig. 4) and range in thickness from 0 to 300 ft in some parts of the valley.

In the bedrock valley, the outwash deposits consist of predominantly medium to coarse sands and gravels to a depth of about 80 ft below land surface and mostly fine sands and silts below a depth of 80 ft (fig. 4). A glacial terminal moraine (till with some stratified deposits) approximately 3 mi south of the study area may be responsible for the fine sands and silts at depth. Slow-moving glacial meltwater flowing into a lake behind the moraine apparently resulted in the deposition of the fine-grained sediments.

The fine sands and silts are cohesive in places; however, few clay-sized particles have been found to date. Clay-sized particles from two split spoon samples taken from the fine sand and silt unit were 2.94 and 3.07 percent. Clay-sized particles taken from seven split spoon samples from the coarse sand and gravel unit ranged from 0.12 to 7.60 percent, with an average value of 1.53 percent and a median value of 0.38 percent. In two locations (one approximately 100 ft south of Meadow Brook Pond and one between the plant site and river) where test holes have exceeded 150 ft in depth, a zone (5–15 ft) of coarse sands has been encountered below the fine silts and sands and above the bedrock surface. The mineralogy of the outwash deposits is predominately quartz and feldspars; dark minerals (biotite and hornblende) are generally more abundant in the finer sediments (F. T. Manheim, written commun., 1983).

Hydrology

The plant site, located within the lower Pawcatuck River basin, is approximately 2 mi east of the junction of the Pawcatuck and Wood Rivers. Unconsolidated deposits near the junction of these two rivers comprise the most extensive accumulation of sediments in the lower Wood aquifer (Gonthier and others, 1974, p. 7). The aquifer is approximately 8 mi in length and ranges from 2,000 to 8,000 ft in width with the majority of it extending north, northwest, and west of the plant site. Saturated thickness in the Ellis Flats area exceeds 290 ft. Swamp and till deposits form the southern and eastern limits of the aquifer, respectively.

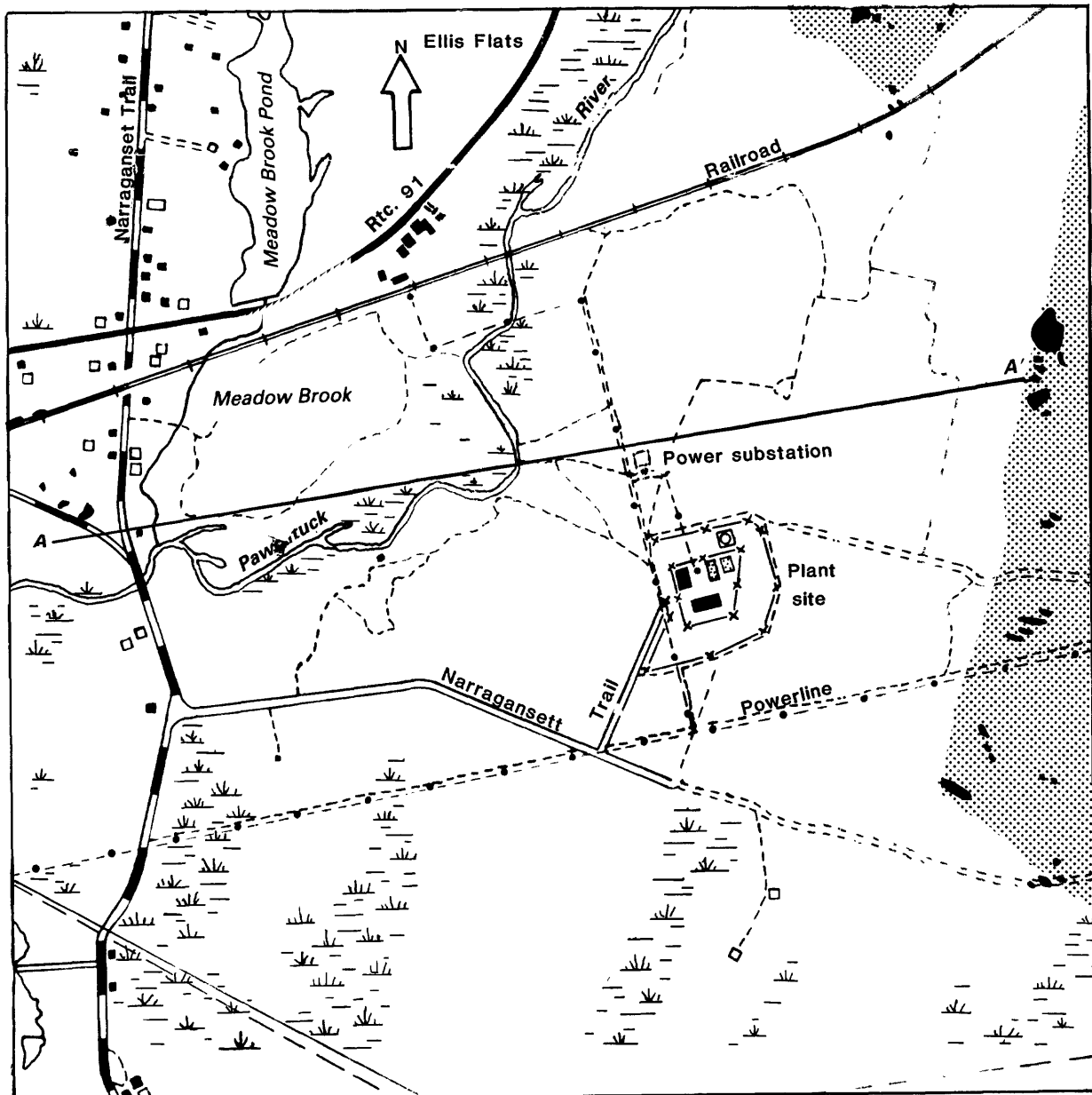
The aquifer is unconfined with a water table that slopes westward from the plant site at an average gradient of 28 ft/mi. The lower boundary of the aquifer is the bedrock surface (fig. 4). Generally, ground-water movement in the aquifer is from the lateral boundaries or till upland areas toward the Pawcatuck River (fig. 5). Ground water discharges to the Pawcatuck River, which is the major surface water drainage from the study area. Ground-water potentials (fig. 6) show upward vertical movement of water into the Pawcatuck River and contiguous swampy area west of the river.

Water enters the ground-water system through infiltration of precipitation (rainfall or snowmelt). Overland runoff and some ground-water flow from adjacent till-covered bedrock areas also enter the aquifer. Based on annual average runoff of 27.51 in from 1966 to 1980 upstream of the U.S. Geological Survey gage on the Pawcatuck River at Wood River Junction and a relation developed by Mazzaferro and others (1978, p. 45), long-term average annual recharge to the aquifer is estimated to be 26 in/yr. Assuming ground-water outflow is a conservative estimate of the amount of natural recharge, Mazzaferro and others (1978) related ground-water outflow to the percentage of stratified drift in a drainage basin. The relation developed by linear regression is described by the equation,

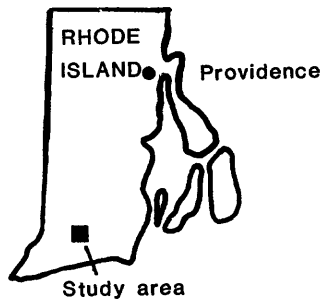
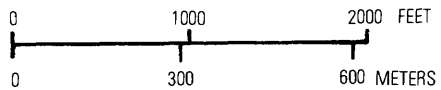
$$Y = 35 + 0.6X,$$

where Y equals ground-water outflow as a percent of total runoff and X equals percentage of total basin area underlain by stratified drift. For this case, $X = 100$.

Discharge of water from the aquifer occurs through ground-water runoff and evapotranspiration, primarily where the water table is near the land surface. Hydraulic conductivity of till is estimated to average about 1 ft/d as does the till in the nearby upper Pawcatuck River basin (Allen and others,



Base from U.S. Geological Survey, Carolina, 1:24,000, 1953, photorevised 1970



- Explanation**
- Swamp
 - Bedrock outcrop
 - Till
 - Outwash
 - Line of geologic section

Figure 3. Generalized surficial geologic map of the study area and location of cross-sectional line A-A'.

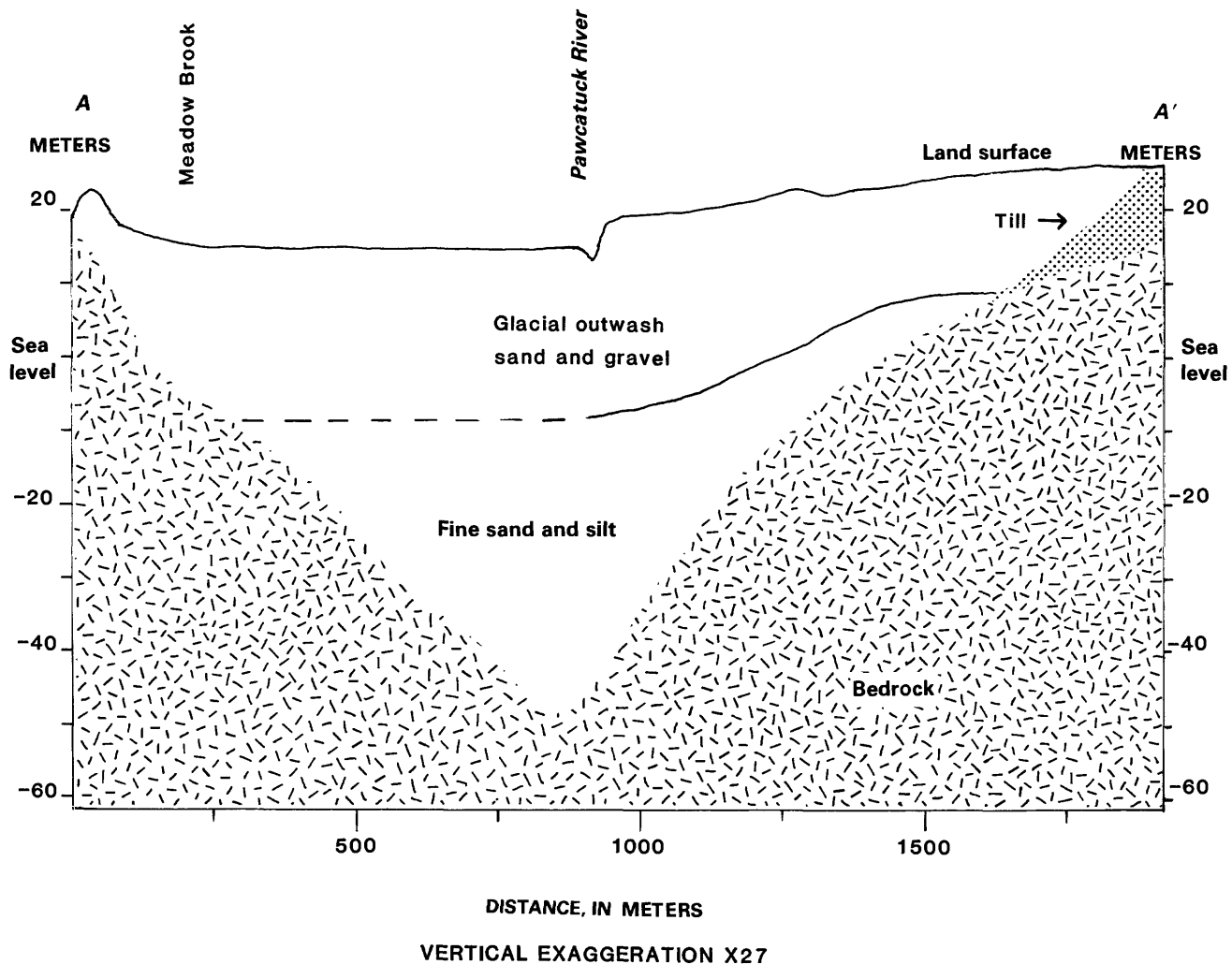


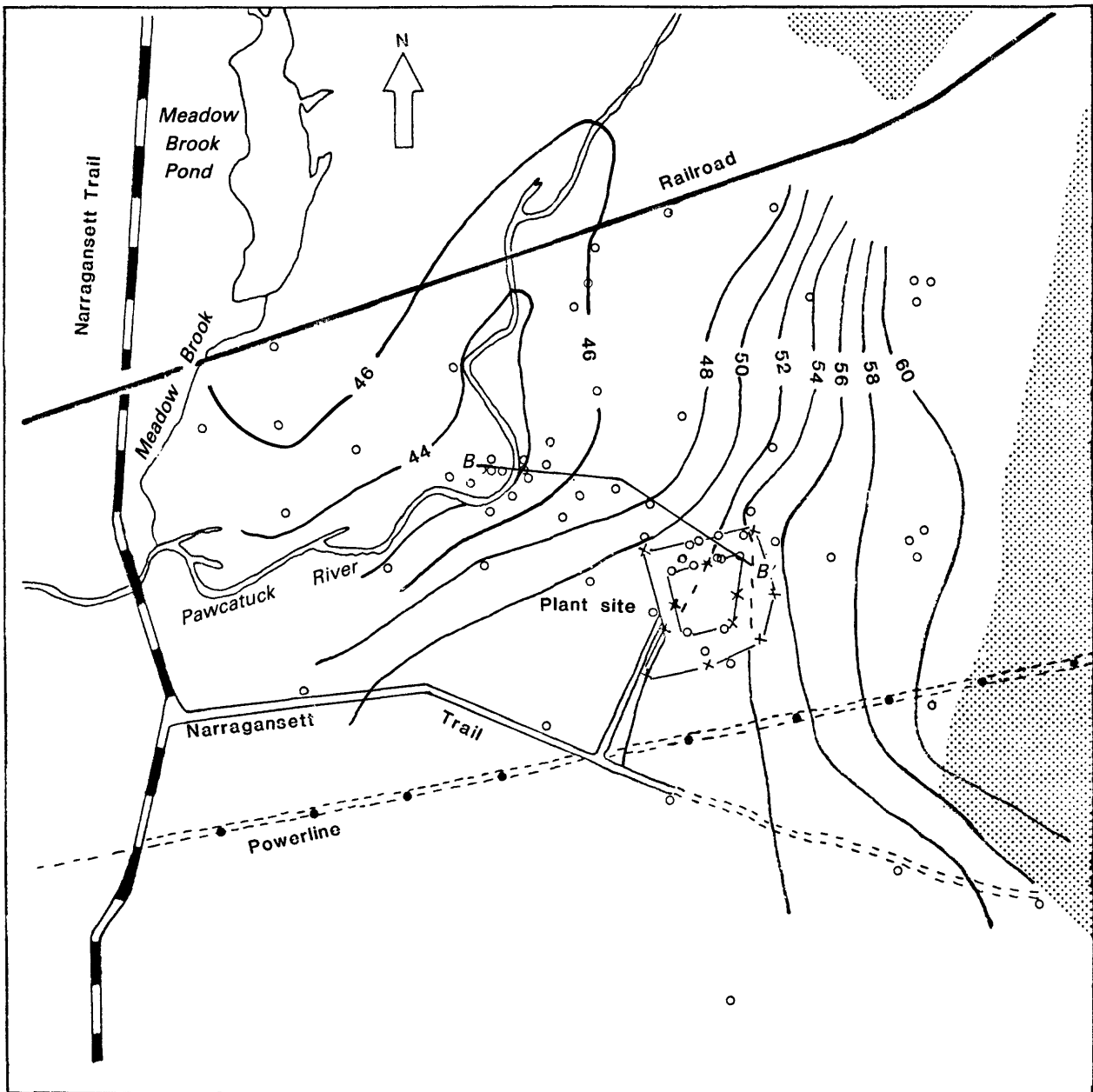
Figure 4. Generalized geologic section along line A-A'.

1966, p. 9), whereas hydraulic conductivity of outwash deposits at the plant, estimated from lithologic logs, is about 180 ft/d (Gonthier and others, 1974, plates 2, 4). Hydraulic conductivity determined from analyses of three aquifer tests made within a 1-mi radius of the site, including one on the plant supply well (fig. 2), ranged from 140 to 190 ft/d (D. C. Dickerman, oral commun., 1983). Hydraulic conductivity of the fine sands and silts at depth probably falls somewhere in between those of the tills and coarse outwash deposits. Fractures in the bedrock also yield water to wells but generally only enough for domestic supplies (5 gal/min or less) (Allen, 1953, p. 26). Ground-water flow, which was calculated from a water-table gradient of 28 ft/mi, an estimated aquifer porosity of 0.38 (obtained from averaging porosity values from six sediment samples), and hydraulic-conductivity estimates that ranged from 140 to 190 ft/d, ranged from 1.95 to 2.65 ft/d.

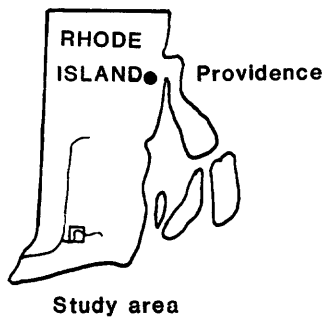
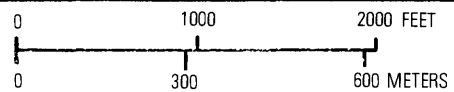
Uncontaminated ground and surface water in the study area generally meet U.S. Environmental Protection Agency (1976) drinking water standards. Specific conductance, an indication of dissolved minerals in the water, is generally less than 100 $\mu\text{mho/cm}$ at 25°C. Principal cations, sodium, calcium, potassium, and magnesium are present in concentrations of 14 mg/L or less; principal anions, sulfate, chloride, and nitrate are present in concentrations of 20 mg/L or less. Some naturally occurring radionuclides, such as potassium-40 (1 pC/L), radium-226 (3 pC/L), radium-228 (2 pC/L), and strontium-90 (3 pC/L), have been detected in ground and surface water in the study area.

EXPLORATION TECHNIQUES

Geophysical techniques and well drilling were used to define the hydrogeologic system and contam-



Base from U.S. Geological Survey, Carolina, 1:24,000, 1953, photorevised 1970



EXPLANATION







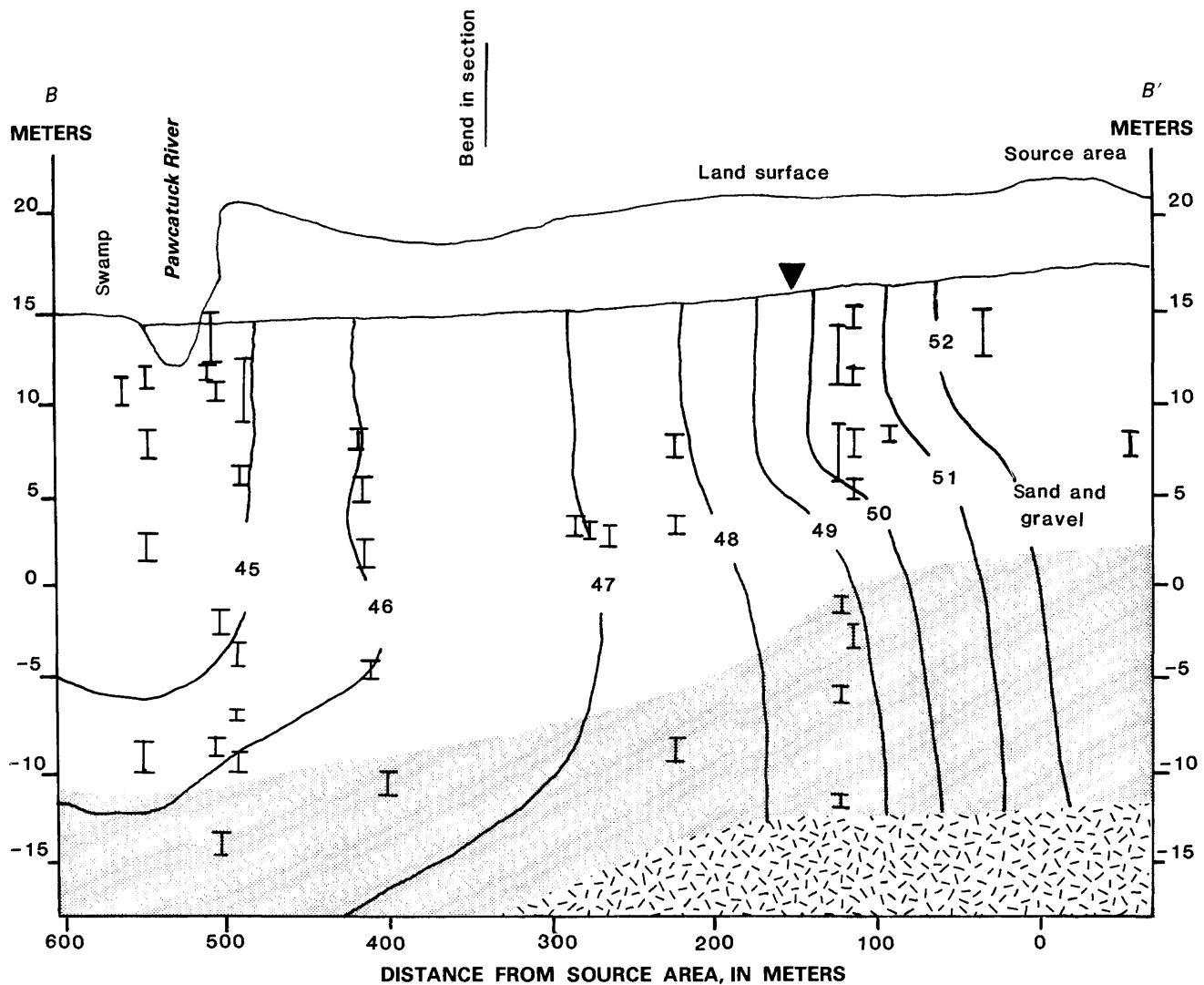
-  Till
-  Outwash
-  -46- Water-table contour shows altitude of water table, datum is sea level. Contour interval 2 feet.
-  B — B' Line of hydrogeologic section
-  o Observation well
-  X — X Fence


Figure 5. Average water-table altitude from July 1982 to June 1983; location of observation wells and cross-sectional line B-B'.




EXPLANATION

— 48-- Equipotential line. -- shows altitude at which water level would have stood in tightly cased well. Contour interval, 1 foot

I Screened interval in observation wells

 Bedrock

 Fine sand and silt

VERTICAL EXAGGERATION X10

Figure 6. Hydrogeologic section showing average ground-water potential from July 1982 to June 1983.

ination plume. Geophysical techniques included seismic refraction to determine depth to bedrock, geophysical well logging (gamma gamma, natural gamma, and neutron) to determine relative lithologic differences within a given well and from well to well, and electromagnetic (inductive) conductivity surveys

to locate areas within the aquifer containing water of high specific conductance.

More than 135 observation wells ranging in depth from 10 to 230 ft were installed during six drilling phases using hollow-stem auger, mud rotary, and drive-and-wash methods. Wells generally were

constructed of 1¼- to 1½-in diameter flexible polyethylene or rigid PVC plastic pipe. Two wells were constructed with 5-in diameter rigid PVC pipe for geophysical logging purposes, and two wells were constructed with 1¼-in diameter galvanized steel for continuous water-level recording. Screened intervals or well points ranged from 2 to 10 ft in length and were either No. 10 (0.010-in) or No. 12 (0.012-in) slot. The first drilling phases were used to install relatively shallow (less than 30-ft) observation wells to determine the water-table configuration. Later phases were devoted to the installation of wells ranging in depth from 10 to 100 ft to locate the contamination plume horizontally and vertically. Ten split spoon samples were taken for such sediment analyses as cation exchange capacities, mineralogic descriptions, porosity tests, and sieve analyses.

CONTAMINATION PLUME

The plume of contaminated ground water extends from the source area northwestward approximately 1,500 ft to the Pawcatuck River and southwestward approximately 800 ft in a downstream direction through the swampy area west of the river, a total distance of 2,300 ft (figs. 7, 8). Dilution precludes detection of contaminants once they have en-

tered the river which has an average discharge of 193 ft³/s. The plume is approximately 300 ft in width and is confined to the upper 80 ft of saturated thickness (fig. 9) where sediments consist of medium to coarse sand and gravel. The top of the contamination plume is depressed below the water table, and its depth increases as it moves away from the source area. The plume obtains a maximum depth (80 ft below land surface) between 1,400 and 1,500 ft from the source area. Beneath the discharge area (river and adjacent swamp), the plume rises to land surface.

Specific gravity of three samples of contaminated ground water collected in 1981 ranged from 1.000 to 1.001 (Daniel Urish, written commun., 1982). It is assumed, therefore, that freshwater recharge on top of the plume is probably responsible for increased depth of the plume away from the pond area. Seasonal variations in hydrologic conditions may affect dimensions of the plume; for example, high precipitation in the spring of 1983 depressed the contamination plume below the water table at the river-swamp interface (fig. 10).

Chemical and radiochemical constituents in the contaminated water include nitrate (5–600 mg/L), boron (20–400 µg/L), potassium (3–25 mg/L), strontium-90 (4–250 pC/L), and technetium-99 (75–1,350 pC/L). Due to the expense of the analytical proce-

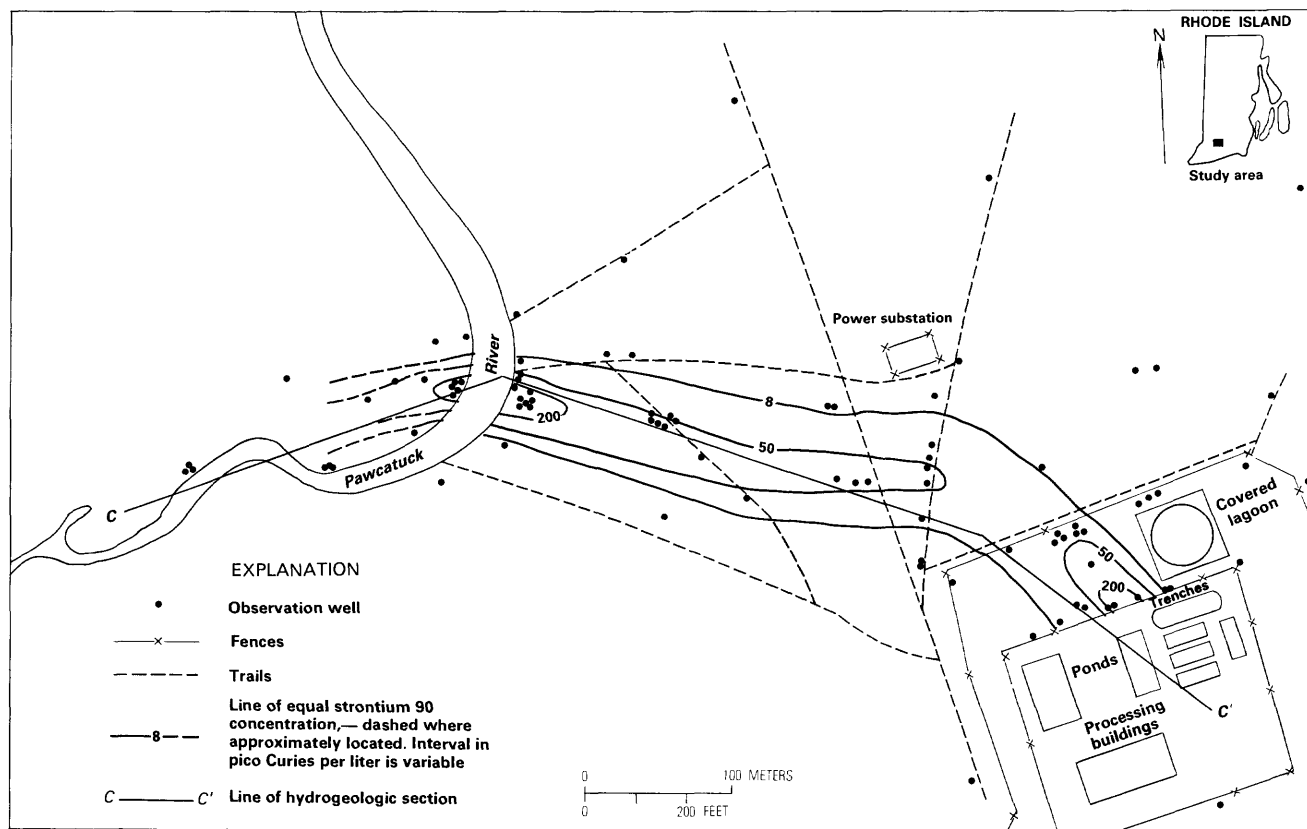


Figure 7. Strontium-90 concentration in ground water at the plant site, October 1982.

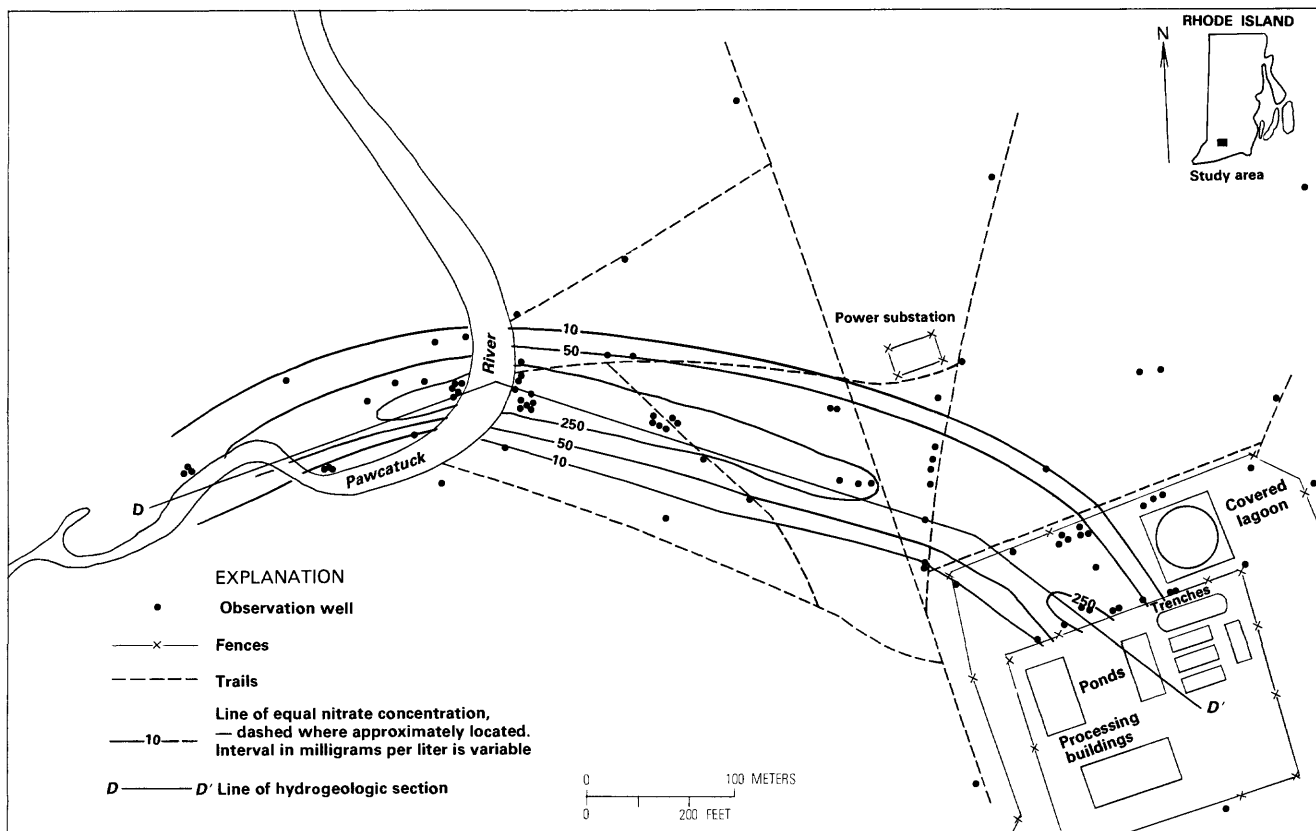


Figure 8. Nitrate concentration in ground water at the plant site, October 1982.

ture, only five water samples have been analyzed for technetium-99 (two by the U.S. Geological Survey and three by Oak Ridge Associated Universities). In these five samples, strontium-90 accounts for 10 to 30 percent of the gross beta activity; the remainder is attributed to technetium-99. The sums of strontium-90 and technetium-99 actually may exceed the gross beta activity level for a given sample; this is most likely due to the fact that the separation and counting efficiency for individual radionuclide measurements is greater than that of the gross beta counting apparatus. Concentrations of gross beta emitters range from 5 to 500 pC/L. No gamma emitters above detection levels have been found. Electrical conductivity of the water ranges from 150 to 4,500 $\mu\text{mho}/\text{cm}$ at 25°C. Dissolved solids have been measured up to 3,500 mg/L, and these concentrations interfere with the detection of alpha emitters. Concentrations of chemical constituents in contaminated water at the plant site, and background concentrations are summarized in table 1.

From 1982 to 1983, two zones of concentrated contaminants were present at both ends of the plume and were separated by a zone of less contaminated water. The zone near the Pawcatuck River resulted from infiltration of contaminants while the plant was

processing material (1964–80). The zone near the source area apparently resulted from flushing of additional contaminants from the unsaturated zone while the sediment below the ponds and trenches was being excavated for site-decommissioning.

Sediment- and water-quality analyses from sampling locations from the plant to the river indicate chemical and radiochemical constituents are not being sorbed by aquifer materials. Cation-exchange capacities from five split spoon samples ranged from 0.1 to 4.2 milliequivalent per 100 grams (meq/100 g), with a median value of 0.5 meq/100 g. Technetium-99 and strontium-90 have been detected in water from observation wells that are 1,500 and 2,000 ft, respectively, from the plant. In the swamp, however, reducing conditions may promote observable solute interaction with sediments or organic material once the plume rises to land surface. Additional sediment- and water-quality analyses are being conducted on materials from the swamp.

SUMMARY

Liquid wastes from an enriched uranium cold-scrap recovery plant have leaked into a highly permeable sand and gravel aquifer in southern Rhode Is-

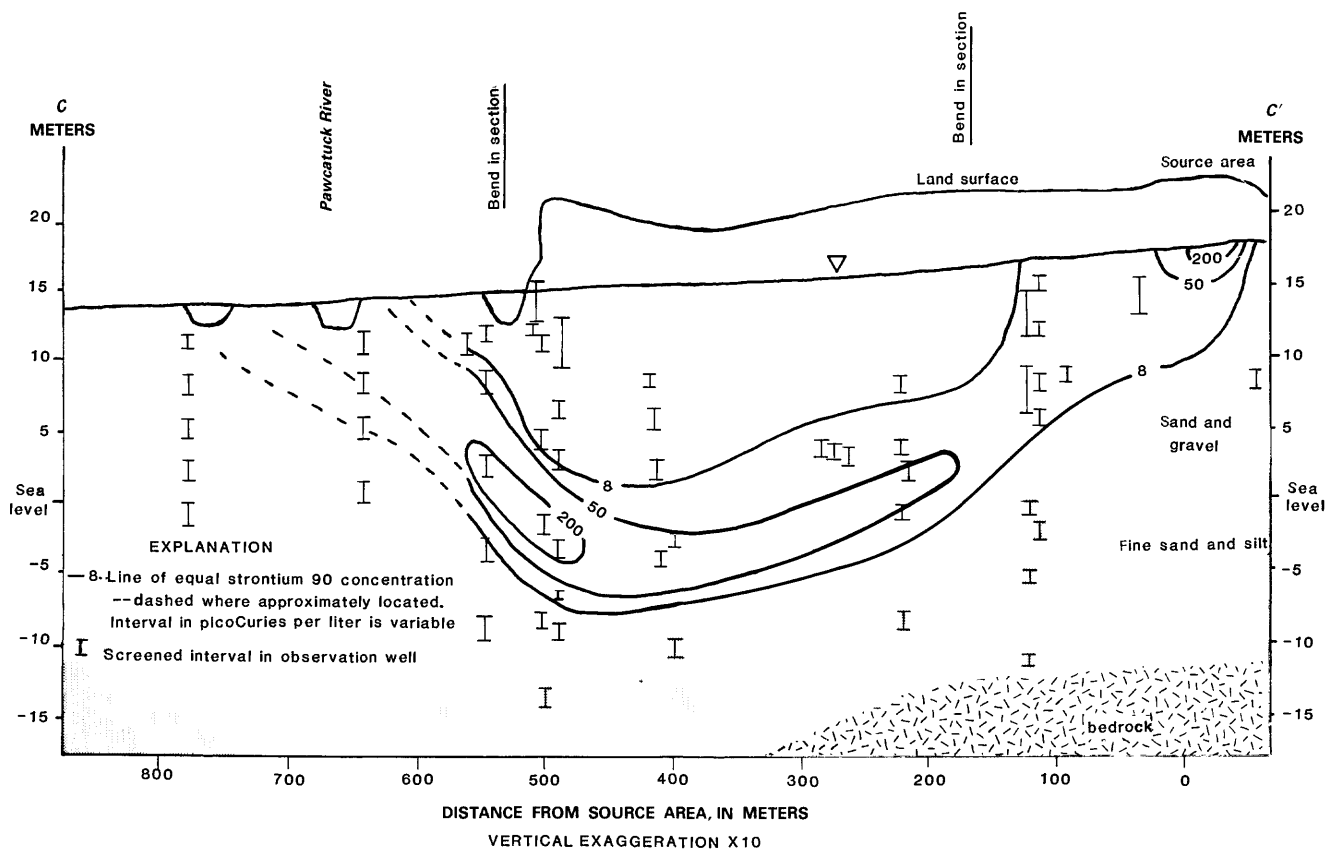


Figure 9. Strontium-90 concentration in ground water at the plant site, October 1982.

land. The resultant plume of contamination extends 2,300 ft from the source area (evaporation ponds and trenches) to the aquifer's discharge area (the Pawcatuck River and swampy area west of the river). Dilution, however, precludes detection of contaminants once they have entered the river. Chemical and radiochemical constituents in the plume include nitrate, boron, potassium, strontium-90, and technetium-99. Unconsolidated deposits comprising the aquifer contain few clay-sized particles, and contaminants do not appear to be interacting significantly with the sediments. In the swamp, reducing conditions may promote observable solute interaction with sediments or organic material.

SELECTED REFERENCES

- Allen, W. B., 1953, The ground-water resources of Rhode Island: Rhode Island Development Council Geological Bulletin No. 6, 170 p.
- Allen, W. B., Hahn, G. W., and Brackley, R. A., 1966, Availability of ground water, Upper Pawcatuck River

- basin, Rhode Island: U.S. Geological Survey Water-Supply Paper 1821, 66 p.
- Dickerman, D. C., and Silva, P. J., 1980, Geohydrologic data for the Lower Wood River ground-water reservoir, Rhode Island: Rhode Island Water Resources Board Water Information Series Report 4, 193 p.
- Duran, P. B., and Haeni, F. P., 1982, The use of electromagnetic conductivity techniques in the delineation of ground-water contamination plumes: Proceedings of the Symposium on the Impact of Waste Storage and Disposal on Ground-Water Resources, sponsored by the U.S. Geological Survey, and Cornell University, Ithaca, New York, June 28-July 1, 1982, 38 p.
- Gonthier, J. B., Johnston, H. E., and Malmberg, G. T., 1974, Availability of ground water in the Lower Pawcatuck River basin, Rhode Island: U.S. Geological Survey Water-Supply Paper 2033, 40 p.
- LaSala, A. M., Jr., and Hahn, G. W., 1960, Ground-water map of the Carolina quadrangle, Rhode Island: U.S. Geological Survey Ground-Water Map 9, scale 1:24,000.
- Mazzaferro, D. L., Handman, E. H., and Thomas, M. P., 1978, Water resources inventory of Connecticut, Part 8, Quinnipiac River basin: Connecticut Water Re-

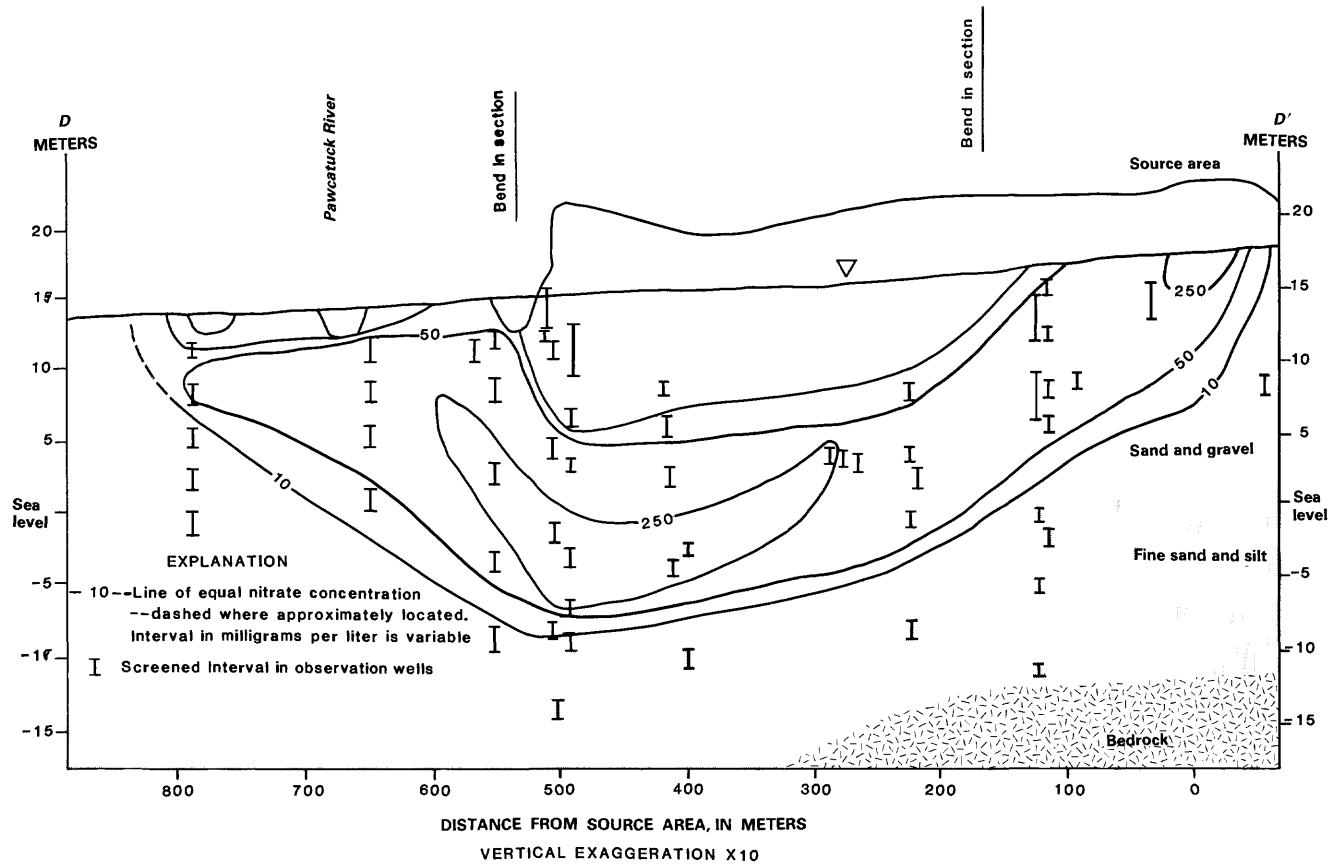


Figure 10. Nitrate concentration in ground water at the plant site, May 1983.

Table 1. Representative chemical analyses of water from observation wells near the middle of, the edge of, and outside the contaminant plume
[Results in milligrams per liter except as indicated]

Chemical constituent	Observation well in middle of plume, Feb. 17, 1982	Observation well on edge of plume, Feb. 3, 1982	Observation well outside of plume, Dec. 23, 1981
Alkalinity-CaCO ₃	7	3	9
Boron (µg/L)	230	50	<10
Cadmium (µg/L)	1	2	<1
Calcium	720	50	4.1
Chloride	180	9.2	5.0
Copper (µg/L)	4	2	5
Fluoride	<.1	<.1	<.1
Hardness	1,900	130	16
Iron (µg/L)	250	20	310
Lead (µg/L)	5	6	1
Magnesium	23	1.5	1.4
Manganese (µg/L)	600	67	1,600
Nickel (µg/L)	14	1	2
Nitrate (NO ₂ + NO ₃)	580	37	.18
pH (units)	5.6	5.7	5.6
Phosphorus (ortho as P)	<.01	<.01	<.01
Potassium	21	3.4	2.5
Silica	<.1	11	6.9
Sodium	25	7.8	4.4
Specific conductance (µmho/cm at 25°C)	4,260	376	77
Strontium-90 (pC/L)	222	6.7	2.9
Sulfate	50	14	14
Water temperature (°C)	12.0	11.5	10.5
Zinc (µg/L)	50	11	16

sources Bulletin No. 27, 88 p.

Moore, G. E., Jr., 1959, Bedrock geology of the Carolina and Quonchontaug quadrangles, Rhode Island: U.S. Geological Survey Quadrangle Map 117, scale 1:31,680.

National Oceanic and Atmospheric Administration, 1982, Evaporation atlas for the contiguous 48 United States: NOAA Technical Report NWS 33, 27 p.

U.S. Environmental Protection Agency, 1976, Quality criteria for water: U.S. Government Printing Office, Washington, D.C. 20402, Stock No. 055-001-01049-4, 256 p.

An Electromagnetic Method for Delineating Ground-Water Contamination, Wood River Junction, Rhode Island

By Paul M. Barlow and Barbara J. Ryan

Abstract

Surface electromagnetic (EM) surveys were conducted in August 1981 to delineate the areal and vertical extent of ground-water contamination at a site in Wood River Junction, Rhode Island. The surveys were conducted in conjunction with a 3-year study of low-level radioactive ground-water contamination from a cold-scrap recovery operation (Ryan and Kipp, 1983).

Surface electromagnetic induction techniques that measure terrane conductivity were used in August 1981 at a low-level radionuclide waste site in Wood River Junction, Rhode Island, to delineate areal and vertical extent of contamination in a sand and gravel aquifer of glacial origin. Data from the terrane-conductivity survey were consistent with values of specific conductance of ground water measured as part of a 3-year study of ground-water contamination at the site. Data from the terrane- and specific-conductance surveys indicate that a plume of contaminated ground water extends from wastewater lagoons and trenches at the plant site to the Pawcatuck River. Above background terrane conductivities are present over an area that is 370 meters in length, ranges in width from 100 to 200 meters, and ranges in depth from land surface to 25 meters below land surface.

Electromagnetic data were contoured in linear and in dimensionless logarithmic units. Electromagnetic data contoured in linear units indicated high-conductivity zones that suggested potential ground-water contamination. Linear contouring also depicted changes in conductivity with depth more clearly than did the logarithmic contouring.

Logarithmic contouring of electromagnetic data was successful in masking background noise, thereby delineating boundaries of the contamination plume more clearly. Selection of background apparent-conductivity values at the site for the logarithmic contouring schemes proved to be the greatest objection to the logarithmic method. Background values which were too high caused an unrealistic reduction in the boundaries of the contamination plume, whereas background apparent-conductivity values that were too low allowed interference from background noise to bias the hydrogeologic interpretation.

INTRODUCTION

Surface electromagnetic (EM) surveys were conducted in August 1981 to delineate the areal and vertical extent of ground-water contamination at a site in Wood River Junction, Rhode Island. The surveys were conducted in conjunction with a 3-year study of low-level radioactive ground-water contamination from a cold-scrap recovery operation (Ryan and Kipp, 1983).

Surface electromagnetic induction techniques that measure terrane conductivity have been found to be an effective tool in the preliminary assessment of ground-water pollution at many industrial and municipal contamination sites (Kelly, 1976, p. 7; Greenhouse and Slaine, 1983, p. 49; McNeill, 1980b, p. 11). Electromagnetic induction techniques are a relatively inexpensive and reliable method of mapping contamination plumes and may, in the early stages of a study of ground-water contamination, aid in the placement of water-quality observation wells (Greenhouse and Slaine, 1983, p. 49).

The ability of earth materials to transmit an electrical current is related directly to the electrical conductivity of the interstitial pore fluid and, to a lesser extent, the rock type. Electrical conductivity of the interstitial pore fluid (water) is determined primarily by ion concentrations in the solution. As the ion content of the pore fluid increases, the ability of the fluid to conduct an electrical charge and the conductivity of the earth material also increase.

The instrument used in the EM surveys consists of an alternating-current transmitter coil that produces a time varying magnetic field (primary field), which, in turn, induces small eddy currents in the earth (fig. 1). These currents produce a secondary magnetic field, which, together with the primary magnetic field, are intercepted by a receiver coil (McNeill, 1980b, p. 5; Evans, 1982, p. 105-108; Zohdy and others, 1974, p. 55). Because the magnitude of

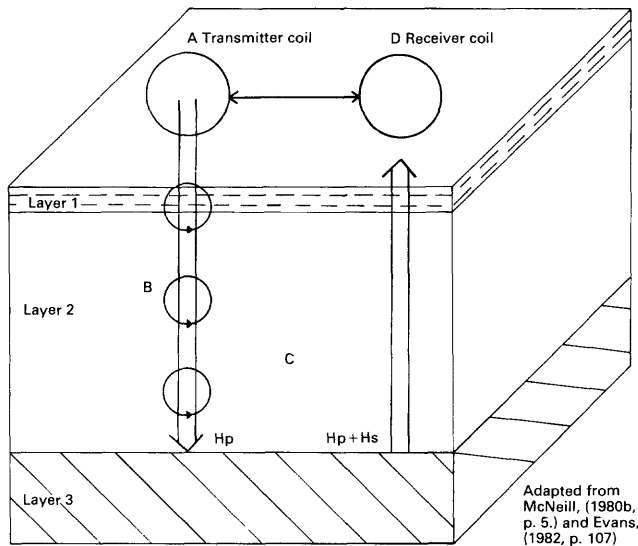


Figure 1. Schematic model showing theory of electromagnetic instrumentation and terrane-conductivity measurement. (A) Transmitter coil produces primary magnetic field (H_p); (B) Induced current loops produce a secondary magnetic field (H_s). Relationship to eddy currents not shown; (C) Current flow is achieved by the availability of charged particles in the sediments and pore fluids; and (D) Receiver coil senses primary and secondary magnetic fields. Conductivities are recorded.

the currents induced by the transmitter is a function of hydrogeologic conditions, the magnitude of the secondary EM field is linearly proportional to the terrane conductivity (relative ease with which an electrical current will flow through the rock type).

The apparent terrane conductivity measured by the receiver coil is a function of the thickness of the rock type layer, the electrical conductivity of the pore fluid, depth of the rock type layer from the surface, intercoil spacings, and operating frequencies of the instrument (Evans, 1982, p. 108; McNeill, 1980b, p. 5). The relative contributions to the apparent conductivity of each of these factors need not be determined to interpret electromagnetic data. Results of data collected from many traverses at a study site are adequate to indicate relative lateral changes in the terrane conductivity (Evans, 1982, p. 108).

Greenhouse and Slaine (1983, p. 47–59) suggested that the presentation of electromagnetic data should be standardized by converting measured apparent conductivity values to logarithmic ratios of measured values to background apparent-conductivity values. The dimensionless ratios then are contoured to outline the zone of contamination. Greenhouse and Slaine cited three advantages to logarithmic contouring of converted data over linear contouring of raw data: First, logarithmic contours of converted data do not cluster near the contaminant

source to the extent that linear contours of raw data might; second, a common format of instrument and survey results may be realized by the use of nondimensional contour units with a zero background value; and, finally, the method of contouring logarithmic values is objective except for the choice of a background apparent-conductivity value.

This report summarizes the use of EM surveys to delineate a ground-water contamination plume at a low-level radioactive waste site in Wood River Junction, Rhode Island (fig. 2). The objectives of this paper are to compare the results of EM surveys to specific conductance measurements of ground water to evaluate the ability of such a survey to delineate ground-water contamination and the advantages and disadvantages of linear and logarithmic contouring of electromagnetic data.

In this report, the results of horizontal- and vertical-dipole measurements are included. It has been noted (McNeill, 1980b, p. 6; Greenhouse and Slaine, 1983, p. 48) that data acquired from the vertical-dipole configuration are more commonly subject to cultural interferences than data acquired from horizontal-dipole configurations. Misalignment of coils in the vertical-dipole configuration and a pronounced departure from linearity of response at high

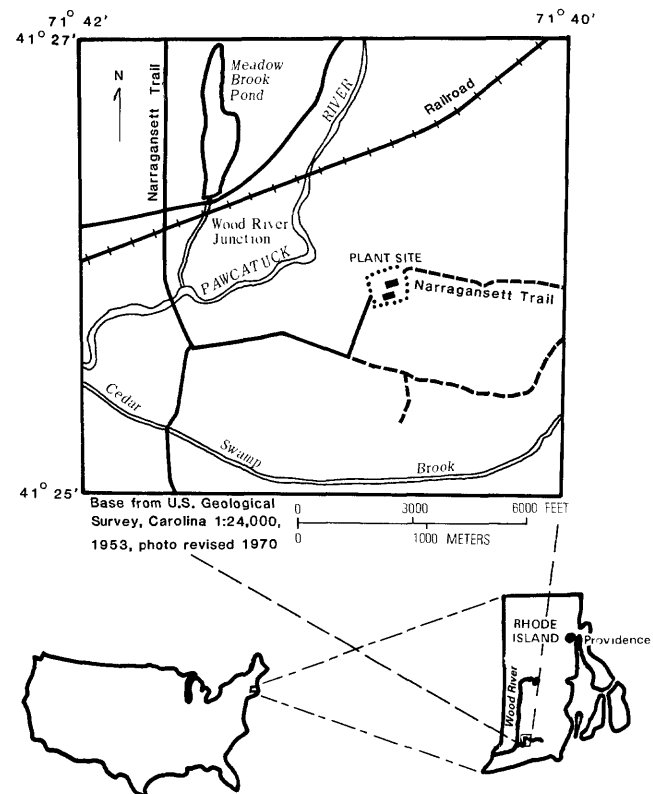


Figure 2. Location of study area.

values of terrane conductivity also may be causes for spurious readings in the vertical-dipole configuration.

SITE DESCRIPTION

From 1966 to 1980, liquid wastes containing radionuclides and other chemical solutes were discharged to lined lagoons at a cold-scrap uranium-recovery plant in Wood River Junction, Rhode Island (fig. 3). Leakage from the lagoons resulted in contamination of a highly permeable sand and gravel aquifer of glacial origin. Chemical constituents in the contaminated ground water included nitrate, potassium, strontium-90, and technetium-99. Concentrations of nitrate and calcium, both of which were present in plant effluents, ranged from 3 to 600 mg/L and from 10 to 700 mg/L, respectively. Nitrate and calcium ions were the predominant constituents of the high dissolved-solids concentrations (as much as 1,960 mg/L) in the contaminated ground water.

Specific conductance of contaminated ground water sampled from approximately 100 observation

wells ranged from 150 to 5,000 $\mu\text{S}/\text{cm}$ at 25°C; uncontaminated ground water at the site generally had a specific conductance of less than 100 $\mu\text{S}/\text{cm}$ at 25°C. Specific conductance data indicate that a plume of contaminated ground water extends from the plant area to the Pawcatuck River and adjacent swamp. The plume is 520 m long and 100 m wide (fig. 4) and is confined to the upper 25 m of saturated thickness, where sediments consist of medium to coarse sand and gravel (fig. 5). The top of the contamination plume is about 10 m below the water table between the plant and river, whereas contamination is encountered at the water table within the swamp area.

ELECTROMAGNETIC SURVEY

Method

The EM surveys were conducted in August 1981 (Duran, 1982) with a Geonics EM 34-3 inductive terrane-conductivity meter. Measurements were obtained in both horizontal- and vertical-dipole modes at 20-m intercoil separations, providing effec-

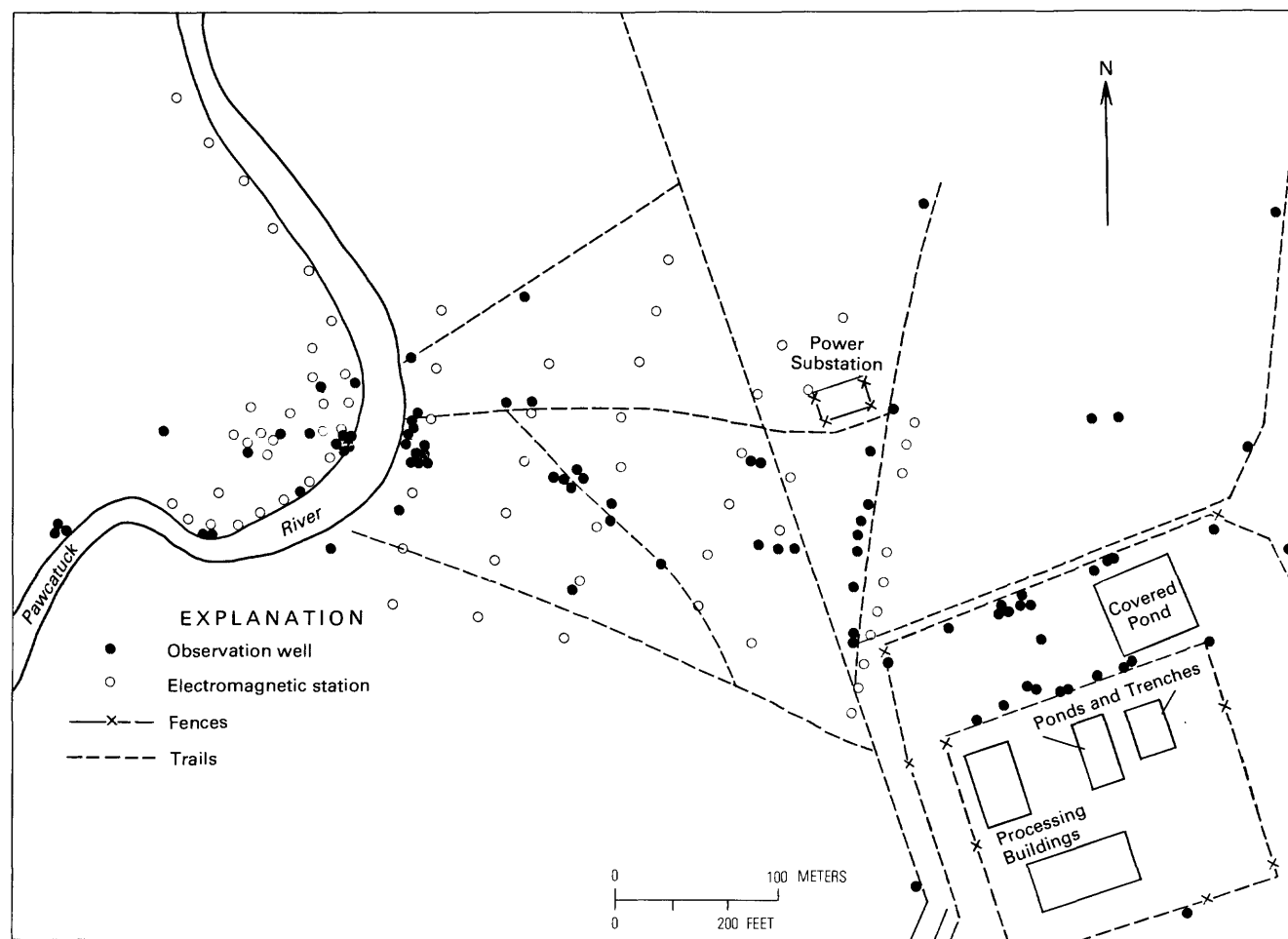


Figure 3. Location of observation wells and electromagnetic stations.

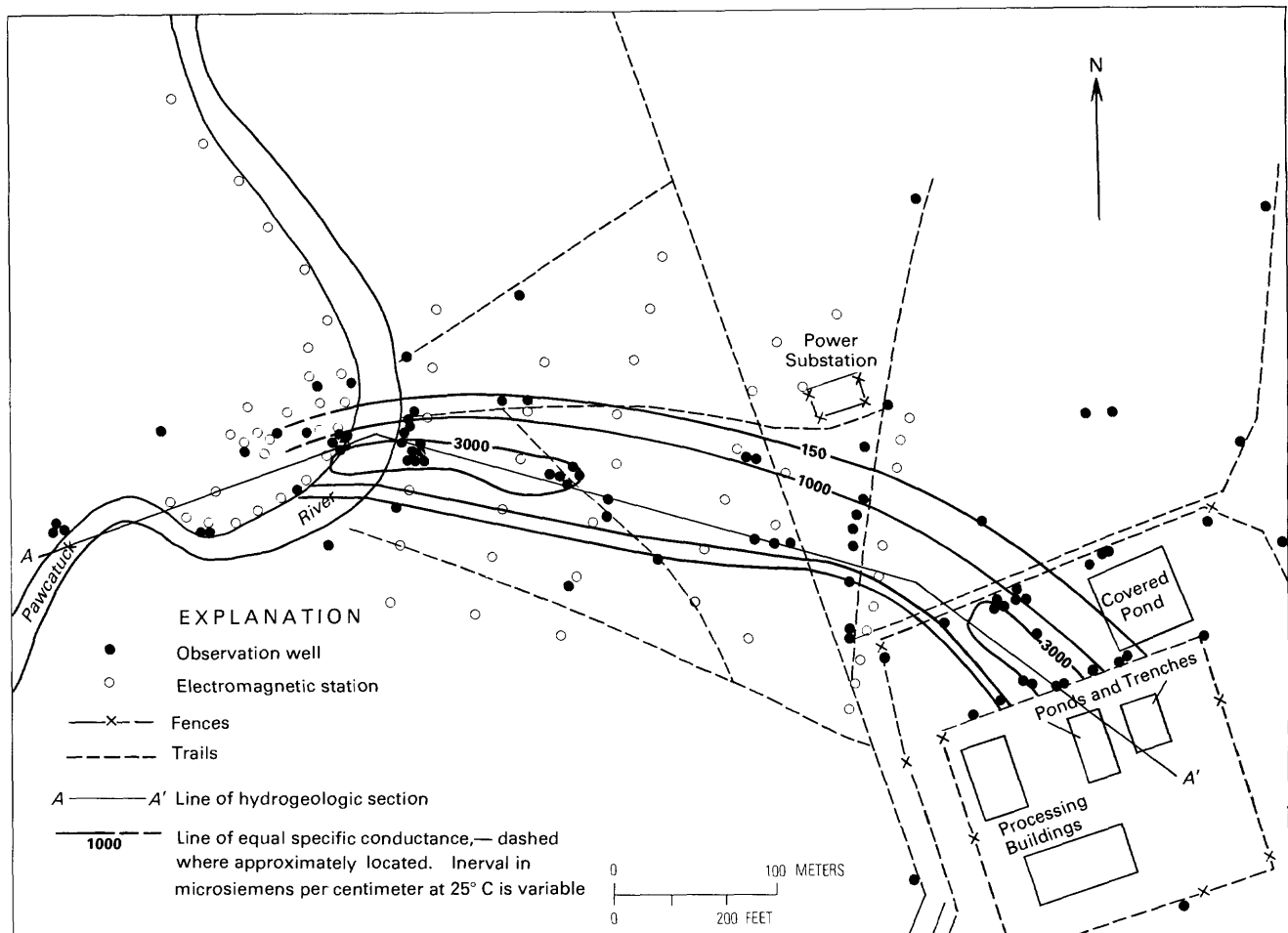


Figure 4. Specific conductance of ground water, Wood River Junction, Rhode Island, April 1982.

tive depths of exploration on the order of 15 and 30 m, respectively (fig. 6). A thorough explanation of the electrical conductivity of soils and rocks and of the theory and operation of the EM 34-3 instrument has been given by McNeill (1980a, b).

EM stations were located by pace and compass with the aid of aerial photographs. Data stations were located midway between the transmitter and receiver coils (Duran, 1982, p. 106). Six traverses (lines 3-8) were made approximately perpendicular to the direction of ground-water flow between the plant and the eastern bank of the Pawcatuck River (fig. 7; table 1). On the western side of the river, one traverse (line 2) was made parallel to the river; this traverse then formed the basis for several traverses perpendicular to the river (line 1). Station spacings were approximately 33 m, with the exception of those located near the plant and in the swamp west of the Pawcatuck River, which were 15 m apart.

Linear and Logarithmic Contouring

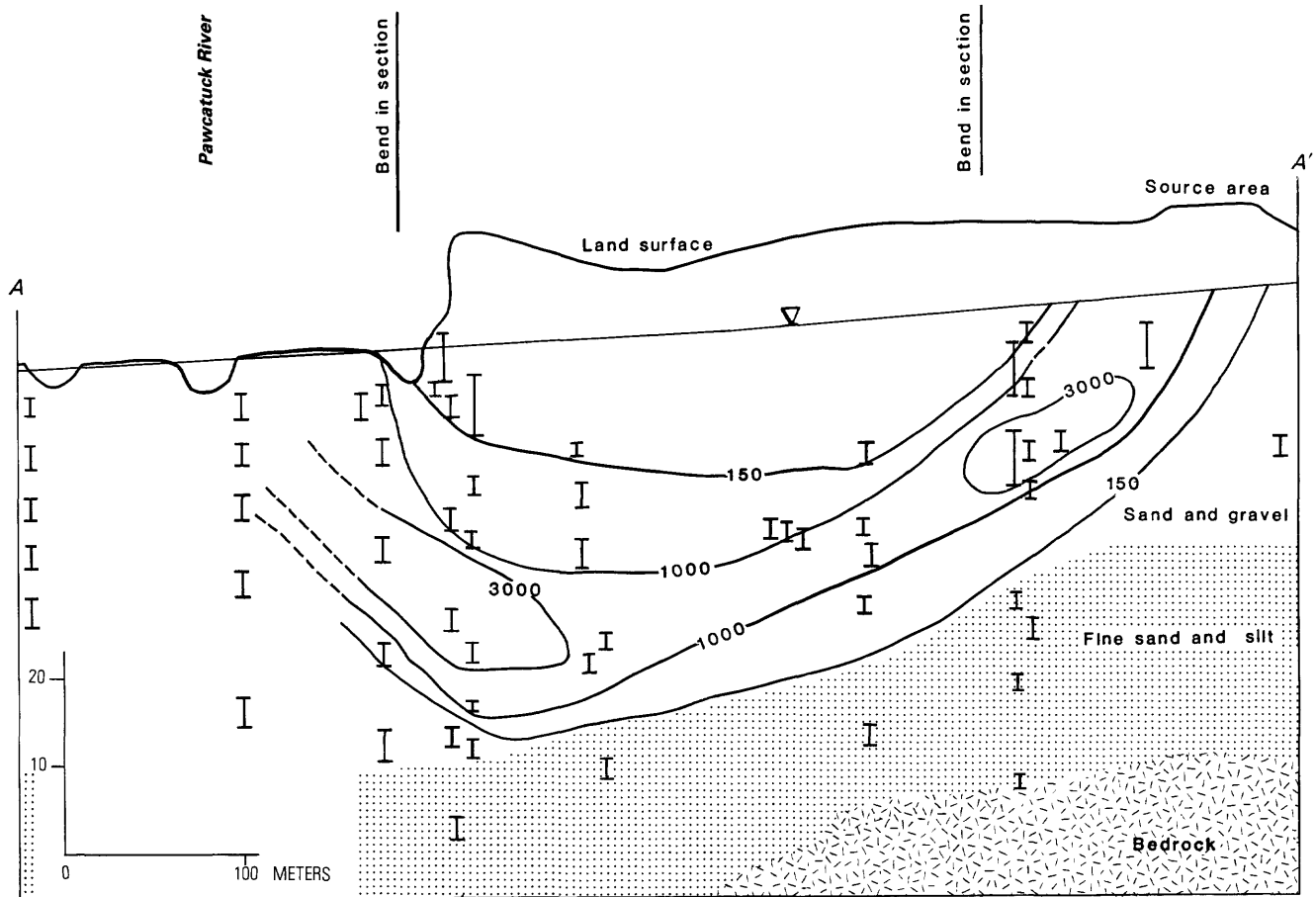
Contouring of the electromagnetic data was done by two methods using linear and logarithmic

units. The first method (linear contouring) consisted of contouring apparent-conductivity values from field measurements at 1.0 to 2.0 mS/m at 25°C contour intervals. Contouring of EM data in this manner did not necessitate the determination of a background apparent-conductivity level. Therefore, no attempt was made to determine the level of background noise [natural scatter of terrane-conductivity values caused by "topography, spatial or temporal variations in the depth to water table, observation accuracy, lateral changes of lithology, and cultural interference from power lines, metal fences, etc.", Greenhouse and Slaine (1983, p. 48)].

The second method of contouring follows the recommendation of Greenhouse and Slaine (1983, p. 49). They suggested the conversion of data to the following logarithmic format:

$$20 \log_{10} \frac{\sigma(x, y)}{\sigma(\text{background})}$$

where $\sigma(x, y)$ equals apparent conductivity readings at any location on a grid with x and y coordinates and $\sigma(\text{background})$ equals the background apparent-conductivity value.



EXPLANATION

- I Screened interval
- 150 — Line of equal specific conductance,
 -- dashed where approximately located.
 Interval in microsiemens per centimeter
 at 25 °C is variable.

Figure 5. Specific conductance of ground water, Wood River Junction, Rhode Island, April 1982, cross-sectional view.

The dimensionless ratios (decibel units) obtained from the logarithmic format for each station and the linear nondimensionless values then are contoured. The zero logarithmic contour [0 decibel (db)] then separates contaminated from noncontaminated areas. Contour intervals of 4 db, which were used in this study, correspond to incremental changes of a factor of approximately 1.6 above background apparent conductivity.

Results

Data from the EM surveys indicate a high-conductivity zone at the site in an area which extends from the plant to the Pawcatuck River and adjacent swamp (figs. 8–13). Above background conductivi-

ties are present over an area 370 m in length by 100 to 200 m in width; this is compatible with specific conductance results (fig. 14).

Although difficult to quantify, the vertical extent of the high-conductivity zone has been qualitatively identified with the aid of effective depths of penetration for the horizontal- and vertical-dipole configurations (fig. 6). Contours of linear vertical-dipole data show local high-conductivity zones near the power substation and near the plant, where fences and transmission lines are concentrated (fig. 11). These elevated conductivity values may be the result of electrical currents produced by the power substation and power lines that interfere with the electromagnetic instrumentation or high ground-water conductivity between 6 and 12 m below land surface [the

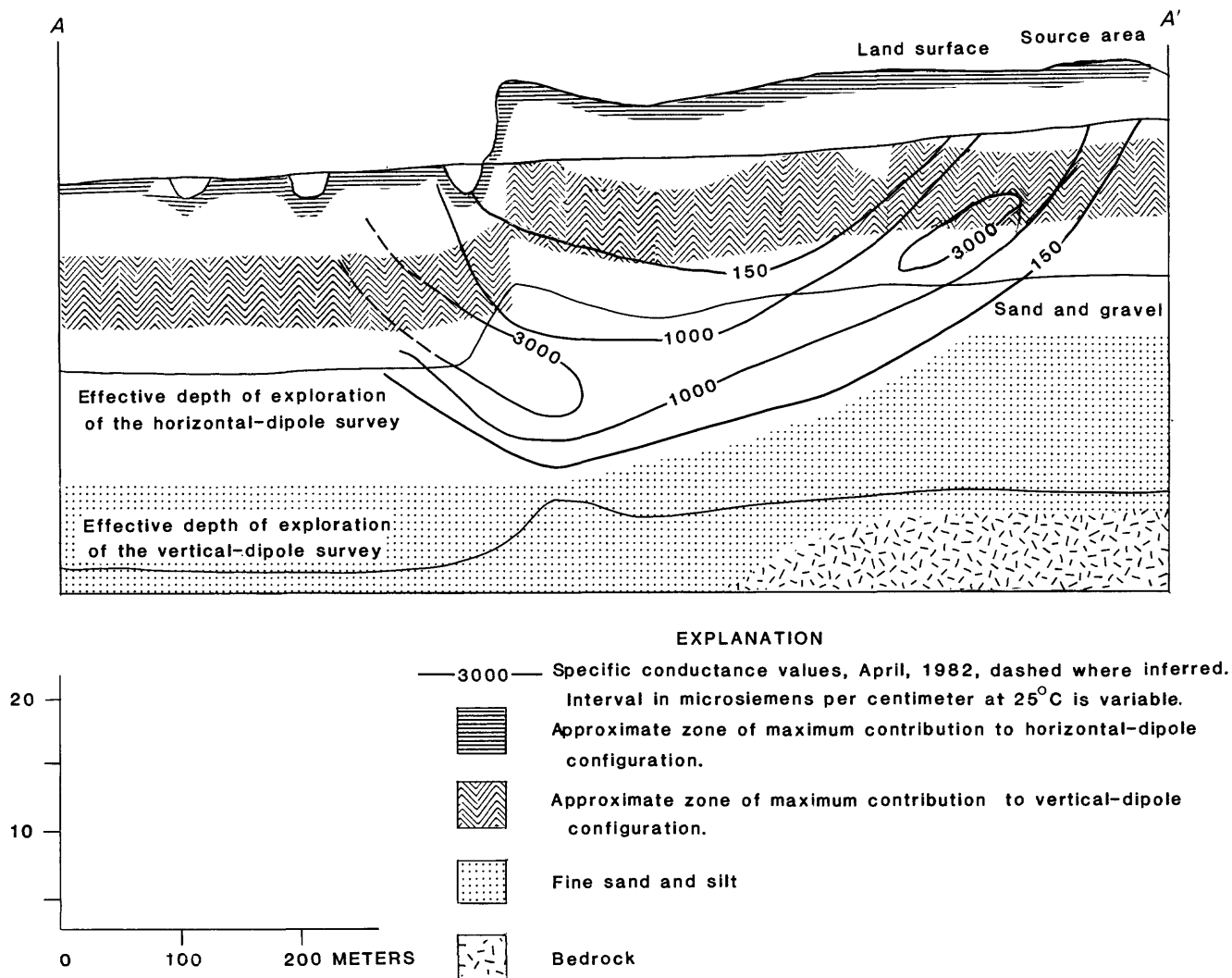


Figure 6. Section showing effective depths of penetration and plot comparing relative responses for horizontal and vertical dipoles.

interval of the aquifer that contributes most to the vertical-dipole configuration (fig. 6)].

Vertical-dipole values remain high (5 mS/m at 25°C) from the plant to within about 100 m of the Pawcatuck River and indicate that some groundwater contamination has occurred of 6 to 12 m below land surface. However, specific conductance values indicate that the most contaminated ground water is present 13 to 20 m below land surface near the river (fig. 5). Because the maximum contribution to the vertical-dipole configuration occurs in the depth interval between 0.3 and 0.6 percent of the intercoil spacing, the vertical-dipole configuration has not sensed fully this high-conductivity zone. A greater intercoil spacing (such as 40 m), however, may have sensed this zone. Vertical-dipole values increase from 4 to 6 mS/m at 25°C on the western side of the Pawcatuck River, which suggests that contamination

may occur within the 6- to 12-m interval in this swampy area.

On the contrary, however, horizontal-dipole measurements (fig. 8) remain low (2–3 mS/m at 25°C) to the east of the Pawcatuck River but increase to between 4 and 8 mS/m at 25°C to the west of the river in the swampy area. Because the greatest contribution to horizontal-dipole measurements is from near-surface electrical conditions (fig. 6), elevated conductivity measurements in the swamp may result from (1) the absence of a resistive, unsaturated layer in the area, (2) the variation in grain size from unconsolidated sand and gravel east of the river to silt and organic matter in the swamp, or (3) a rise in the electrical conductivity of the ground water. Although the absence of a resistive, unsaturated layer in the swampy area probably adds to the overall increase in

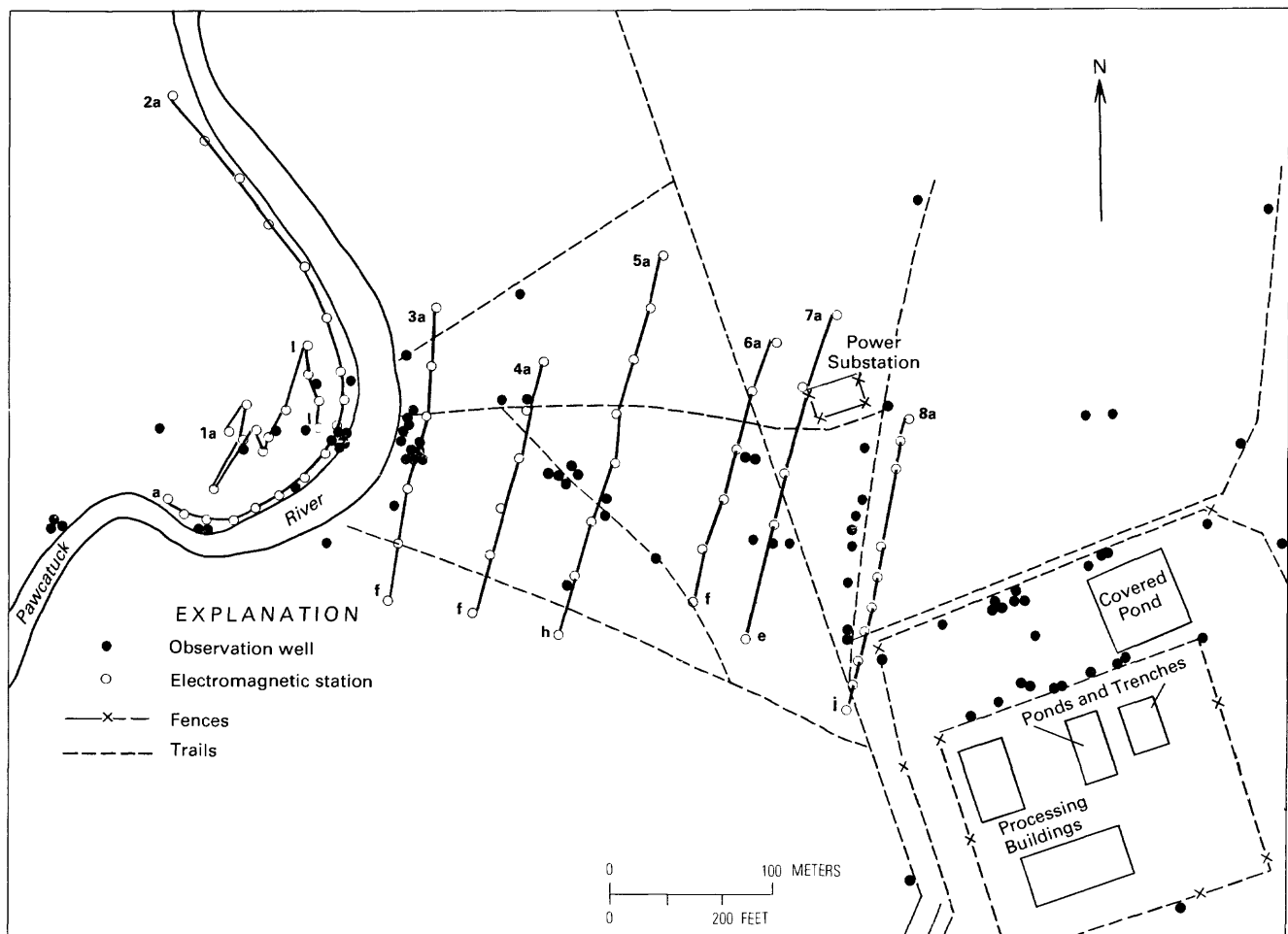


Figure 7. Numbering system of electromagnetic stations.

conductivity levels there, elevated levels of ground-water contamination are suspected. Horizontal- and vertical-dipole linear contouring of EM data show clustering of contour lines in this area (figs. 8, 11).

Logarithmic contouring schemes (figs. 9 and 10, 12 and 13) were obtained by first assigning background values to the logarithmic equation given by Greenhouse and Slaine (1983). Background values at the study site were obtained in the following ways: (1) By averaging the low apparent-conductivity values for those stations which are believed to reflect uncontaminated terrane conductivities and (2) by subjectively setting a background apparent-conductivity value below which contamination does not seem likely.

Background values are determined more easily if the lithology of the study site is known. In the present study, the presence of a conductive, saturated, swampy zone to the west of the Pawcatuck River, consisting of silt, clay, and organic material, resulted

in a higher range of background apparent-conductivity values than to the east of the river, which consists of unconsolidated sands and gravels. To bring the western and eastern areas of the site into a common range of decibel values, higher values were assigned to the western side of the river than to the eastern side.

Differences in the ranges of apparent-conductivity values for the horizontal- and vertical-dipole modes also necessitated the use of two background apparent-conductivity values (one for the horizontal and one for the vertical configuration) in each area of the site to the east and to the west of the river.

Table 2 summarizes background apparent-conductivity values used in this study.

Contours of logarithmic data reflect above background conductivities from the plant to the river in the vertical and horizontal modes. Contours of horizontal-dipole values converted to averaged background apparent-conductivity levels (fig. 6) show

Table 1. Electromagnetic data from horizontal and vertical dipoles at study area [Data in millisiemens per meter at 25°C.; ---, no measurement]

Electromagnetic station	Dipole		Electromagnetic station	Dipole	
	Horizontal	Vertical		Horizontal	Vertical
Line 1:			Line 4:		
A	3.9	5.1	A	1.9	2.1
B	3.9	3.5	B	3.2	4.8
C	4.4	5.5	C	2.9	3.7
D	3.3	---	D	3.1	3.3
E	4.2	4.3	E	1.7	2.6
F	6.3	4.3	F	---	2.6
G	4.9	6.4	Line 5:		
H	3.5	3.7	A	1.8	2.3
I	3.9	3.3	B	1.8	1.7
J	4.1	4.1	C	3.0	2.4
K	4.6	6.3	D	2.8	3.4
L	8.4	4.8	E	3.0	5.0
Line 2:			F	3.5	4.8
A	2.3	3.4	G	2.0	2.6
B	2.3	3.2	H	---	2.6
C	2.6	3.3	Line 6:		
D	2.4	3.0	A	1.9	2.6
E	2.4	2.5	B	1.9	3.4
F	2.9	3.0	C	2.2	3.2
G	4.6	6.0	D	2.9	5.4
H	6.6	4.9	E	3.2	5.0
I	9.0	6.0	F	1.9	2.6
J	8.5	5.7	Line 7:		
K	7.2	6.5	A	1.4	2.5
L	9.7	3.4	B	1.9	5.2
M	7.2	5.8	C	2.6	4.0
N	6.2	7.2	D	2.5	5.0
O	3.7	5.5	E	1.5	2.8
P	3.5	3.5	Line 8:		
Q	3.4	3.4	A	1.6	1.9
Line 3:			B	2.8	2.7
A	1.8	2.0	C	1.0	1.8
B	2.3	3.4	D	3.3	5.0
C	4.8	4.8	E	3.2	5.6
D	2.6	4.6	F	4.4	7.5
E	1.8	3.3	G	3.3	8.4
F	---	2.5	H	4.4	13.0
			I	3.2	6.2
			J	1.8	2.6

higher decibel levels (8 db) in the swamp than to the east of the river (as they did in the linear-contouring scheme). Because lithologic variations have been masked deliberately in the logarithmic ratios, higher decibel levels probably reflect increased ground-water contamination, which was suggested by the clustering of linear contours in the swamp. However, if contamination has occurred in the swamp, it has been masked slightly by the second scheme of contouring logarithmic ratios in which a subjectively assigned background apparent-conductivity value was used (fig. 10).

DISCUSSION

The principal advantage of plotting terrane conductivities in dimensionless logarithmic ratios is that it is possible to mask the contribution of background noise to the survey results; that is, local lithologic variations, differences in the apparent and terrane conductivities resulting from variations in depth to the water table due to topographic variations, cultural interferences, and inaccurate measurements. With the data converted, identification of contaminated zones is easier, inasmuch as any increase in the deci-

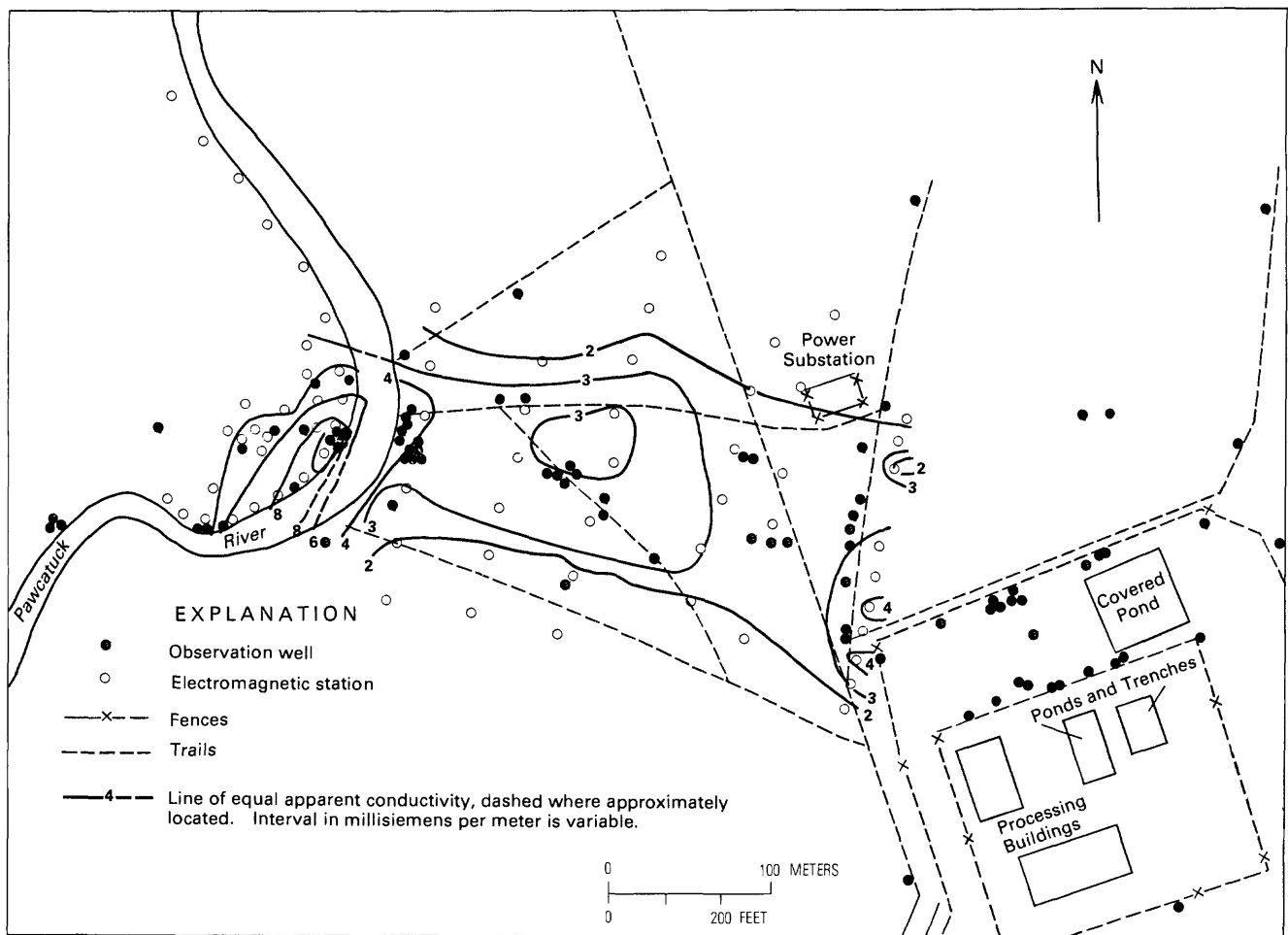


Figure 8. Linear contouring of horizontal-dipole electromagnetic data.

bel level indicates an increase in the apparent conductivity over and above what might be caused by background noise.

The selection of a background apparent-conductivity value for contours of logarithmic ratios, however, is quite subjective (Greenhouse and Slaine, 1983, p. 49) and presents the greatest drawback to this method of data presentation. Difficulties were found with both techniques for determining background values used in this study. If too low a background value is used, local lithologic variations may obscure the hydrogeologic interpretation (as with contouring of linear values). Conversely, too high a background value will not give sufficient definition of the boundaries of the plume, thereby masking areas of potential contamination. The authors propose that both methods of determining background apparent-conductivity values be used in the contouring of logarithmic ratios. Low background values will then aid in the delineation of the boundaries of the plume, whereas high background values will show most clearly the core of the contamination plume.

Linear apparent-conductivity values are spaced more closely near zones of elevated contamination and suggest that the plume is composed of a broad zone of relatively lower contamination (2–3 mS/m at 25°C in the horizontal-dipole configuration and 3–5 mS/m at 25°C in the vertical-dipole configuration) with zones of relatively higher contamination near the plant and in the swamp. Although linear contouring of apparent-conductivity values does not show a continuous zone of contamination as clearly as does the logarithmic contouring of apparent-conductivity ratios (due to local variations in lithology and cultural interference), linear contours emphasize high levels of contamination, thereby outlining areas of possible importance.

Contours of linear values also portray the differences in vertical and horizontal electromagnetic results more clearly than the logarithmic format. This is especially true west of the Pawcatuck River where linear contours show high levels of conductivity in the upper layers of the aquifer. Differences between horizontal- and vertical-dipole results are not seen as

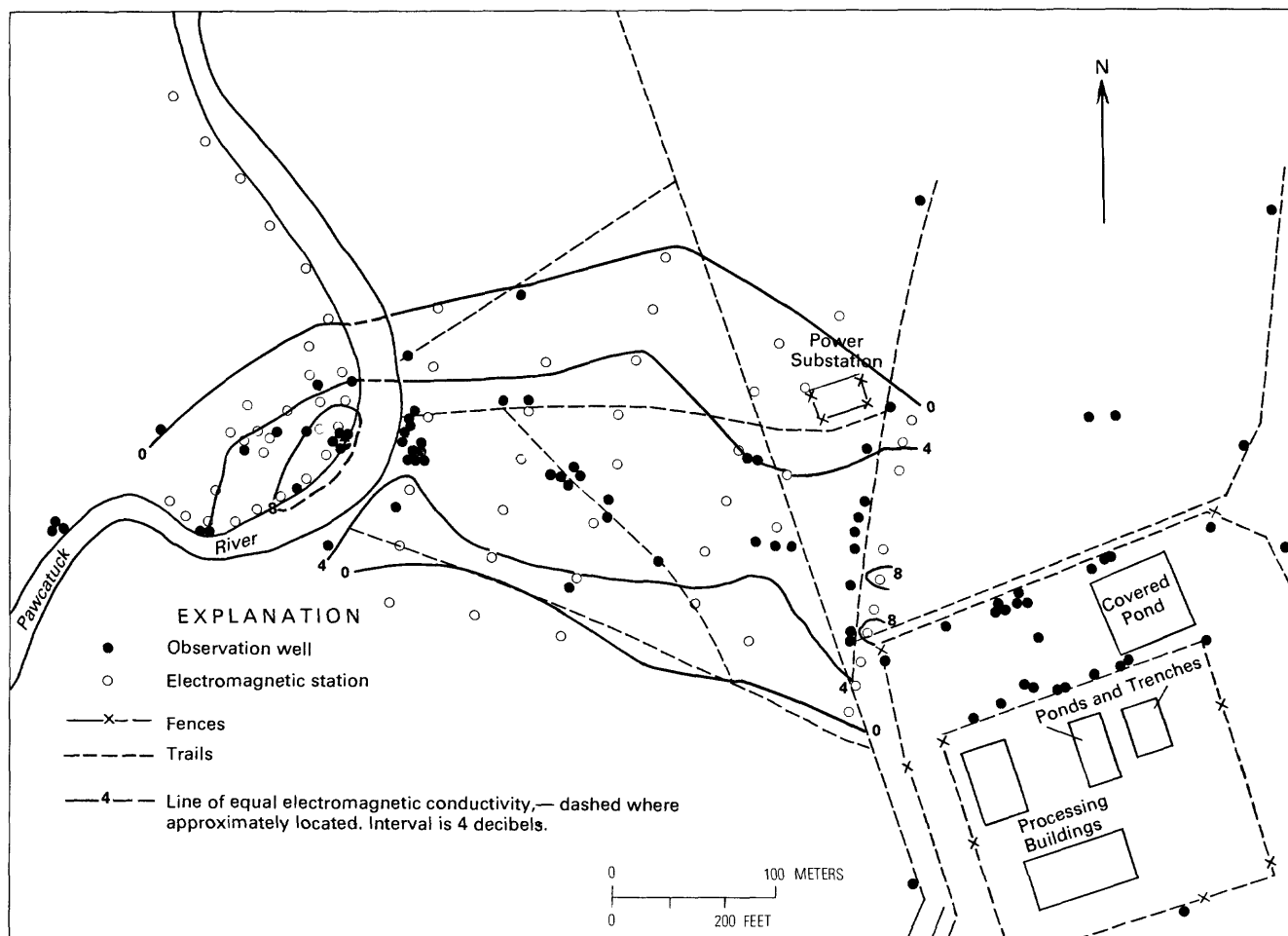


Figure 9. Logarithmic contouring of horizontal-dipole electromagnetic data using averaged background values.

clearly with contours of logarithmic ratios because different background apparent conductivities were used purposefully with horizontal and vertical configurations to put all values at the site into a similar range. As a result, contours of linear values are more helpful in determining the relative depth of contamination than are the contours of logarithmic ratios.

CONCLUSIONS

Results of EM surveys at a low-level radionuclide ground-water contamination site indicate that areas of high apparent conductivity coincide with areas of high specific conductance. Measurements in horizontal- and vertical-dipole configurations indicate chemical stratification that is confirmed by specific conductance samples from wells screened at various depths in the aquifer. Specific conductance results do show, however, that contamination has occurred at greater depth than has been sensed by the 20-m intercoil spacing of the vertical-dipole configuration. The vertical-dipole configura-

tion was helpful in qualitatively determining shallow versus deep levels of contamination.

Contouring of the EM data by linear and logarithmic methods shows that advantages and disadvantages are associated with each method. Advantages to the linear method of contouring include an emphasis on high-conductivity zones that are potential contamination source areas and better depiction of differences in the response of the horizontal- and vertical-dipole configuration with depth. However, interference from background noise and some uncertainty in delineating boundaries between contaminated and uncontaminated areas of the site create problems in the hydrogeologic interpretation of linearly plotted EM data.

The ability to mask the contribution of background noise to EM survey results, thereby outlining more accurately areas of contamination, is the principal advantage to logarithmic contouring. The selection of background apparent-conductivity values at the study site posed the greatest drawback to logarithmic

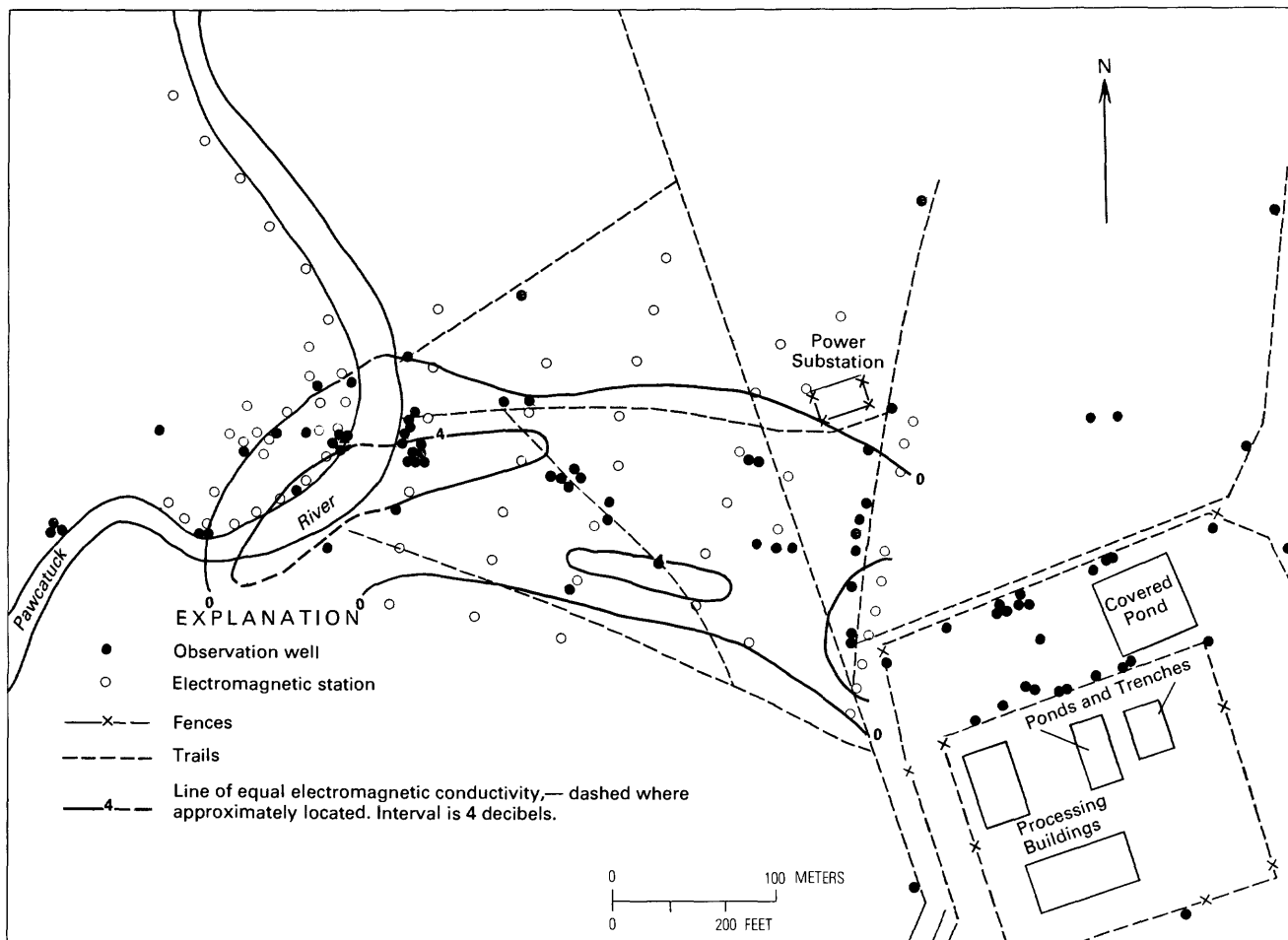


Figure 10. Logarithmic contouring of horizontal-dipole electromagnetic data using assigned background values.

mically contoured data. Background values that were too high caused an unreal reduction in the boundaries of the contamination plume, whereas low background apparent-conductivity values allowed interference from background noise to bias the hydrogeologic interpretation.

SELECTED REFERENCES

- Dickerman, D. C., and Silva, P. J., 1980, Geohydrologic data for the Lower Wood River ground-water reservoir, Rhode Island: Rhode Island Water Resources Board Water Information Series Report 4, 193 p.
- Duran, P. B., 1982, The use of electromagnetic conductivity techniques in the delineation of ground-water contamination plumes, *in* The impact of waste storage and disposal in ground-water resources: Proceedings of the Northeast Conference, Ithaca, N.Y., June 28–July 1, 1982, U.S. Geological Survey and Center for Environmental Research, Cornell University, p. 8.4.1–8.4.33.
- Evans, R. B., 1982, Currently available geophysical methods for use in hazardous waste site investigations: American Chemical Society Symposium Series, No. 204 Risk Assessment at Hazardous Waste Sites, F. A. Long and G. E. Schweitzer, eds., p. 93–115.
- Greenhouse, J. P., and Slaine, D. D., 1983, The use of reconnaissance electromagnetic methods to map contaminant migration: *Ground Water Monitoring Review*, v. 3, no. 2, p. 47–59.
- Kelly, W. E., 1976, Geoelectric sounding for delineating ground-water contamination: *Ground Water*, v. 14, no. 1, p. 6–10.
- McNeill, J. D., 1980a, Electrical conductivity of soils and rocks: Geonics Limited Technical Note TN-5, Mississauga, Ontario, 22 p.
- 1980b, Electromagnetic terrane conductivity measurements at low induction numbers: Geonics Limited Technical Note TN-6, Mississauga, Ontario, 15 p.
- Ryan, B. J., and Kipp, K. L., 1983, Ground-water contamination plume from low-level radioactive wastes, Wood River Junction, Rhode Island (abs): *Transactions of the American Geophysical Union*, v. 64, no. 18, p. 224.

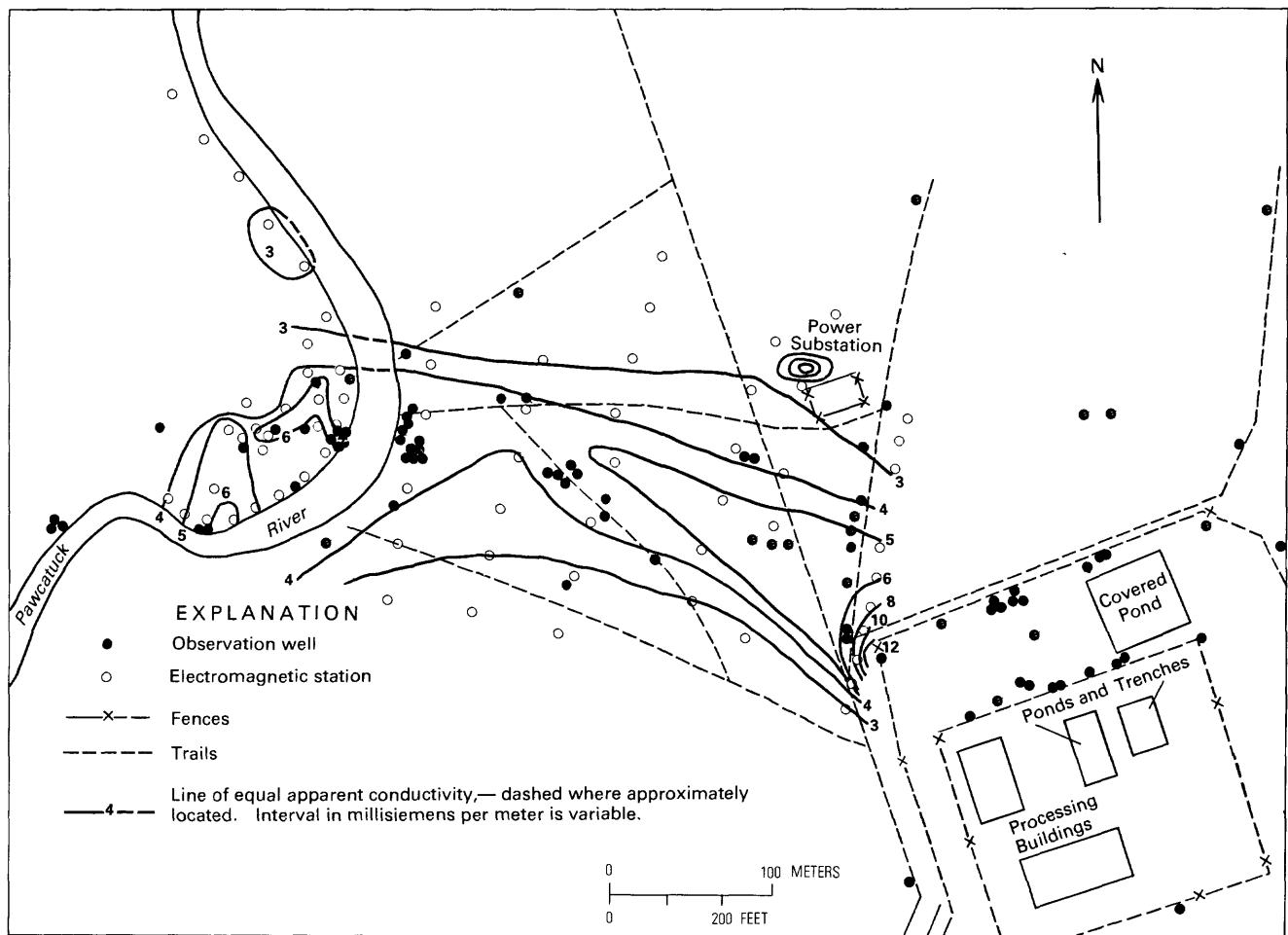


Figure 11. Linear contouring of vertical-dipole electromagnetic data.

Slaine, D. D., 1983, Predicting the response of mapping subsurface contamination with inductive conductivity techniques, *in* 1983 Technical Education Session: Ground Water Technology Division, National Water Well Association, 34 p.

Zohdy, A. A. R., Eaton, G. P., and Mabey, D. R., 1974, Application of surface geophysics to ground-water investigations: Techniques of Water-Resources Investigations of the U.S. Geological Survey, Book 2, Chapter D1, 116 p.

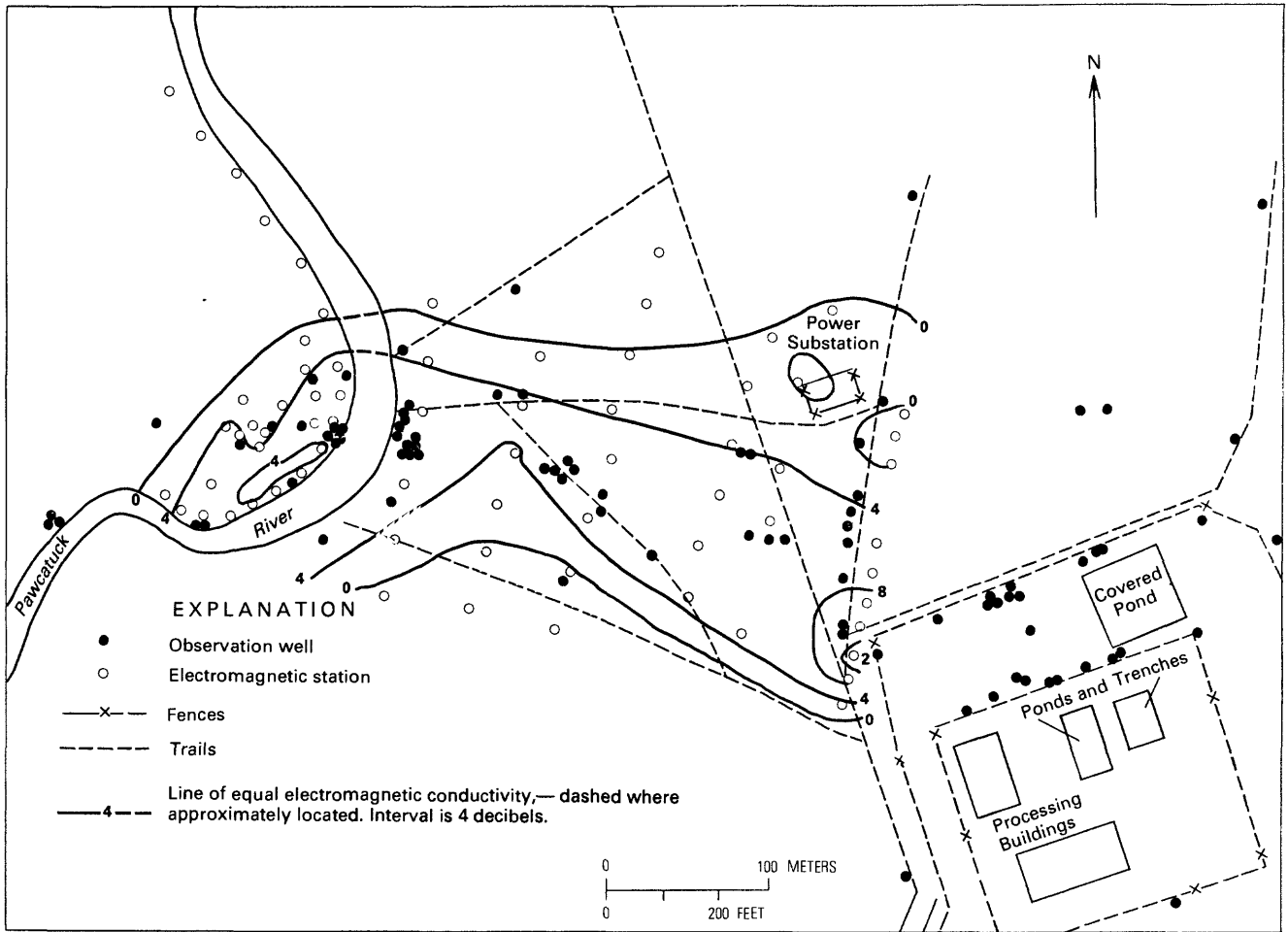


Figure 12. Logarithmic contouring of vertical-dipole electromagnetic data using averaged background values.

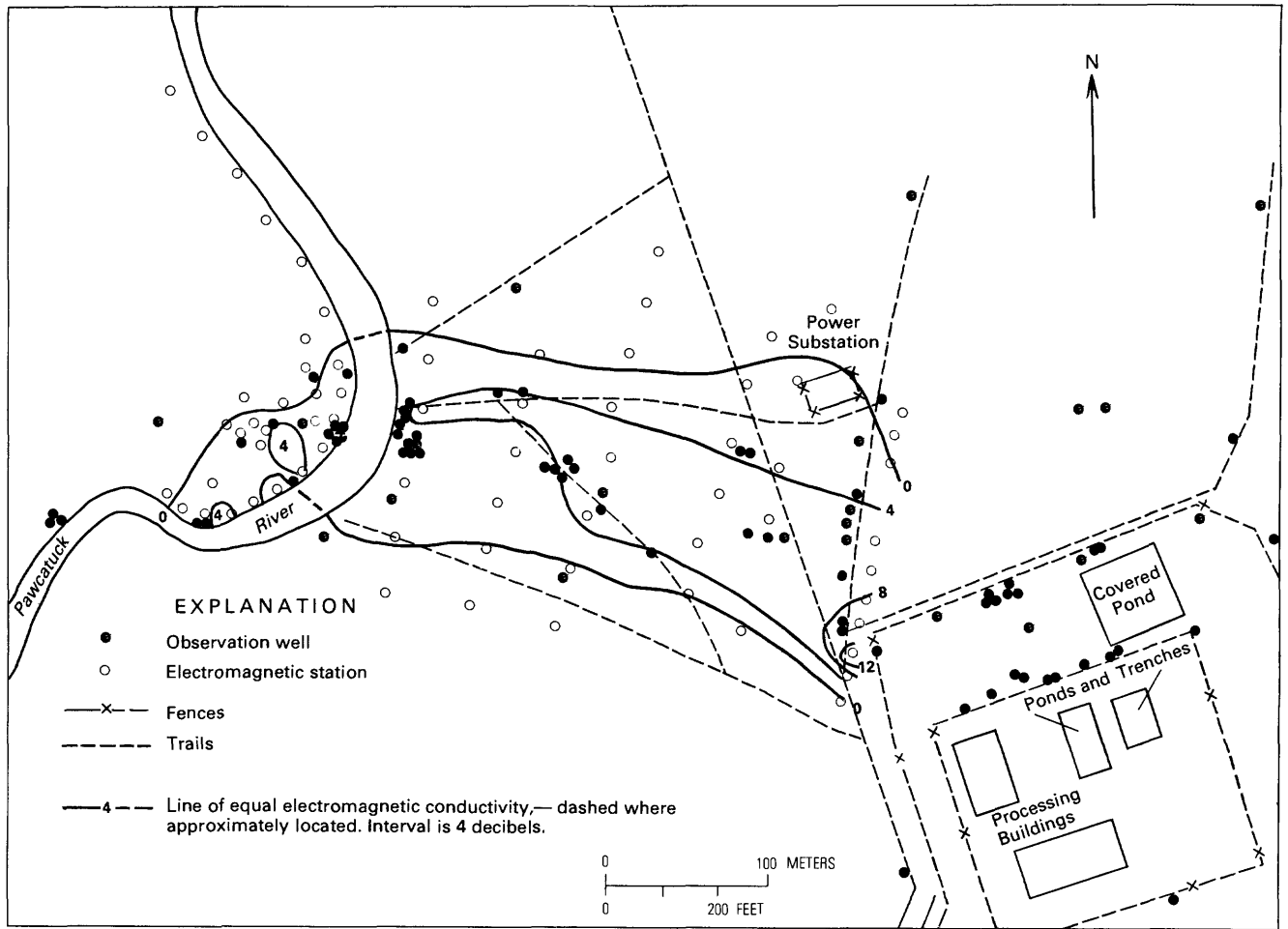


Figure 13. Logarithmic contouring of vertical-dipole electromagnetic data using assigned background values.

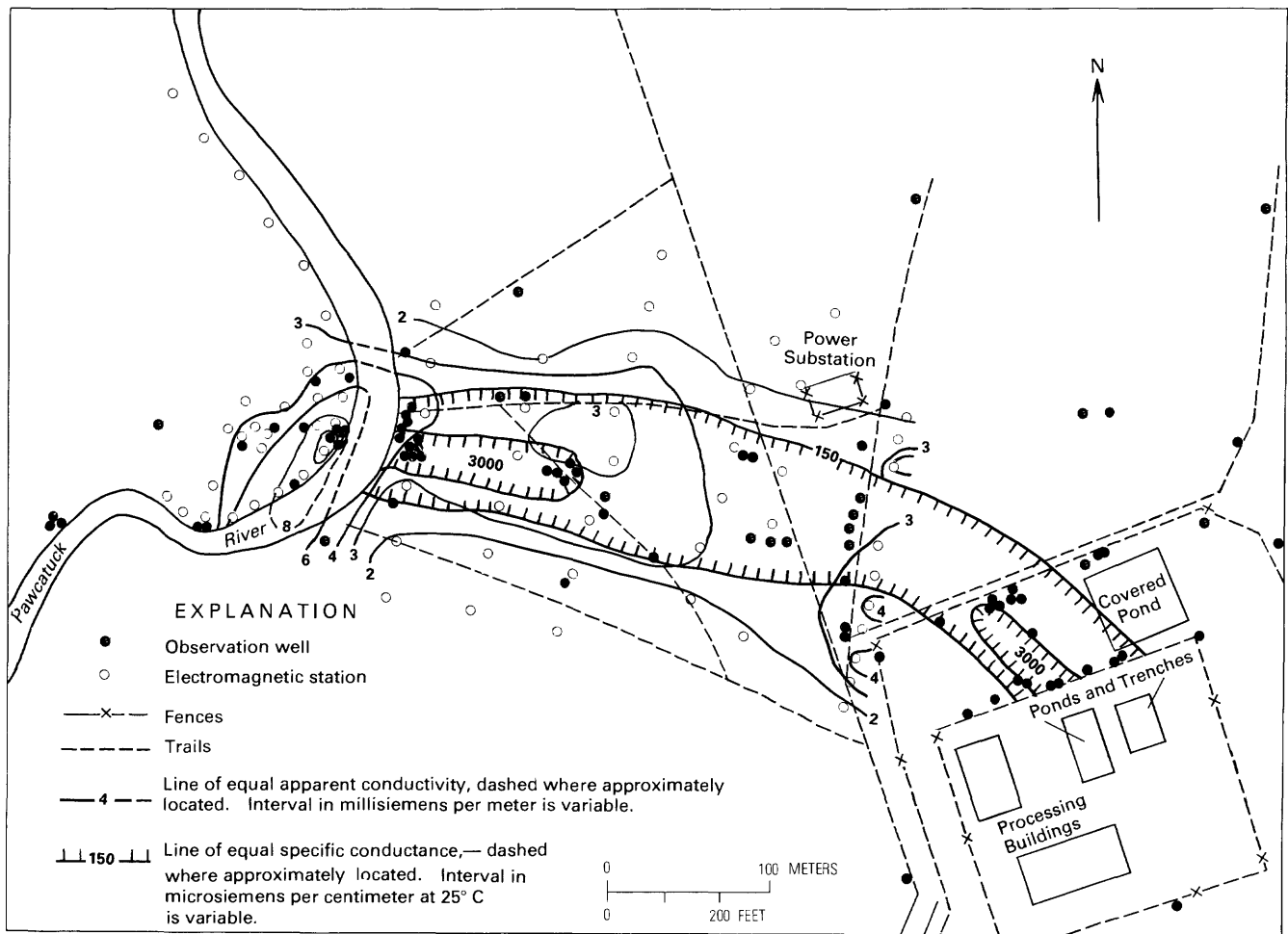


Figure 14. Comparison of specific conductance in ground water to linear horizontal-dipole electromagnetic data; April 1982.

Table 2. Background apparent-conductivity values used to normalize the electromagnetic data
 [All values in millisiemens per meter at 25°C]

Values	Dipole orientation			
	Vertical		Horizontal	
	East	West	East	West
Averaged	2.4	3.3	1.7	3.3
Assigned	3.0	4.0	2.0	4.0

Three-Dimensional Simulation of Free-Surface Aquifers by Finite-Element Method

By Timothy J. Durbin *and* Charles Berenbrock

Abstract

An iterative finite-element algorithm has been developed for the simulation of three-dimensional free-surface aquifers. The Galerkin finite-element method is applied to tetrahedral or triangular elements for volume or surface integrations. Integrations in time are by a fully implicit finite-difference representation. The algorithm solves the equation of ground-water flow subject to the free-surface boundary condition as described by a linearized partial-differential equation. To account for geometric changes in the flow domain resulting from movement of the free surface, the finite-element grid is deformed during transient-state simulation. The algorithm allows for local rotation of the hydraulic-conductivity tensor.

INTRODUCTION

The simulation of the hydraulic response of three-dimensional free-surface aquifers can be accomplished by one of several approaches. The most commonly applied approach is to represent a ground-water system as a quasi-three-dimensional system of two-dimensional aquifers, which are connected hydraulically by leakage through interaquifer aquitards. To solve this problem, Bredehoeft and Pinder (1970) used the finite-difference method, and Durbin (1978) used the finite-element method. A finite-difference algorithm for simulating quasi-three-dimensional ground-water flow was described by Trescott (1975) and Trescott and Larson (1977). In each of these methods, the free surface is represented by applying the Dupuit assumptions to the upper layer of a model. For the upper layer, the transmissivity is a function of computer head, and the storage coefficient is set to a value representing the specific yield of the free surface.

In fully three-dimensional representations of a ground-water system, the effect of the free surface is approximated sometimes by keeping the geometry of the flow domain fixed while assigning a specific-yield value to the upper parts of the model grid. By this approach, the large storage effect at the free surface is represented, but the nonlinear effects of changed sat-

urated thickness are not included. Another approach involving fixed geometry is to represent the free-surface problem as a saturated-unsaturated-flow problem. Freeze (1971) used this approach within a finite-difference approximation, and Frind and Verge (1978) used it within a finite-element approximation.

The effects of geometry changes can be included by utilizing a deforming model grid. Leake (1977) used this approach by eliminating or adding blocks to a finite-difference grid as the computed heads for the aquifer change with time. Leake demonstrated his algorithm for the two-dimensional x-z case, but the results can be extended to three dimensions. By this approach, the effects of storage changes at the free surface and deformation of the flow domain are included. A more rigorous approach has been taken by Neuman and Witherspoon (1971). Starting with the governing equation of ground-water flow and a linearized partial-differential equation that describes the free-surface boundary condition, they developed a finite-element algorithm for the two-dimensional case that employs a deforming grid and can be applied to several field problems.

The work described below extends that of Neuman and Witherspoon (1971) to the three-dimensional case using the Galerkin finite-element method. The resulting algorithm then is applied to a large-scale field problem. The algorithm satisfies a linearized form of the partial-differential equation for the free-surface boundary condition and includes the effects of elastic storage. The model grid, which is constructed from tetrahedral elements, expands or contracts to represent changes with time in the position of the free surface.

MATHEMATICAL FORMULATION

Governing Equations

A diagrammatic section of a three-dimensional flow domain Ω of ground-water flow is shown in figure 1. That domain is defined by the free surface F and the remaining boundary surfaces A_1 and A_2 . The

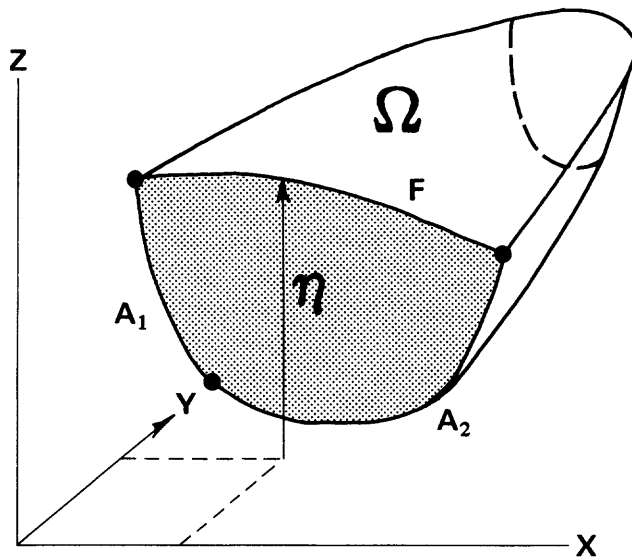


Figure 1. Diagrammatic section of three-dimensional flow domain.

union of F , A_1 , and A_2 defines the overall boundary surface η of the flow domain Ω . The position of the free surface is defined by η , which is its height above the datum used to reference hydraulic head within the flow domain. On the boundary surface A_1 , head is prescribed, and, on the surface A_2 , flux is prescribed. The position of the free surface, prescribed head, and prescribed flux are each functions of location and time.

The initial- and boundary-value problem associated with this three-dimensional flow domain can be described by the following set of equations, written in repeating index notation (Neuman and Witherspoon, 1971):

$$\frac{\partial}{\partial x_i} \left(K_{ij} \frac{\partial h}{\partial x_j} \right) - S_s \frac{\partial h}{\partial t} - w = 0, \quad (1)$$

$$h(x_i, 0) = h_o(x_i), \quad (2)$$

$$\eta(x_1, x_2, 0) = \eta_o(x_1, x_2), \quad (3)$$

$$h(x_i, t) = h_B(x_i, t) \text{ on } A_1, \quad (4)$$

$$K_{ij} \frac{\partial h}{\partial x_j} n_i = -q(x_i, t) \text{ on } A_2, \quad (5)$$

$$\eta(x_1, x_2, t) = h(x_1, x_2, t) \text{ on } F, \quad (6)$$

$$K_{ij} \frac{\partial h}{\partial x_j} n_i = S_y \frac{\partial h}{\partial t} n_3 \text{ on } F, \quad (7)$$

where h is hydraulic head, L;
 h_B is hydraulic head on the prescribed-head boundary, L;

K_{ij}	is the hydraulic conductivity tensor, LT^{-1} ;
n_i	is the outward normal vector, L_0 ;
w	is the discharge per unit volume, T^{-1} ;
S_s	is specific storage, L^{-1} ;
S_y	is specific yield, L_0 ;
q	is flux normal to the prescribed flux boundary, Lt^{-1} ;
t	is time, T;
x_i	is coordinate x, y, and z, L; and is elevation of the free surface above datum from which is measured, L.
h	

Numerical Solution

Finite-Element Approximation

The Galerkin finite-element method can be used to solve the initial- and boundary-value problem. The fundamental idea of the method is to replace the exact continuous solution of the original partial-differential equation by an approximate piecewise-continuous solution. The piecewise-continuous function is specified by values that are specified at a finite number of discrete points called nodes. Functional values between these points are calculated by using the piecewise-continuous interpolating functions defining over a finite number of subdomains called elements. The interpolating functions will provide an exact representation as the element size approaches zero in the limit. For a finite number of nodes, the approximation will not exactly satisfy equation 1, and a residual will result. The Galerkin method forces this residual to zero, in an average sense, through selection of coefficients for the interpolating functions.

To apply the Galerkin method, the linear operator L is defined as

$$L(h) \equiv \frac{\partial}{\partial x} \left(K_{xx} \frac{\partial h}{\partial x} \right) + \frac{\partial}{\partial y} \left(K_{yy} \frac{\partial h}{\partial y} \right) + \frac{\partial}{\partial z} \left(K_{zz} \frac{\partial h}{\partial z} \right) - S_s \frac{\partial h}{\partial t} - w = 0, \quad (8)$$

where equation 1 has been simplified by the assumption that the coordinate system is aligned with the principal components of the hydraulic-conductivity tensor; this assumption is unrelated to the application of the Galerkin method. Later the results will be modified to allow local rotation of the hydraulic-conductivity tensor from the global-coordinate system.

To solve $L(h) = 0$, interpolating function of the form

$$h(x, y, z, t) \approx \hat{h}(x, y, z, t) = \sum_{i=1}^n H_i(t) \phi_i(x, y, z) \quad (9)$$

is used where \hat{h} is a series approximation to h , and Φ_i are linearly independent interpolating functions defined over the flow domain Ω . H_i are undetermined coefficients, and n is the number of nodal points.

The series approximation to equation 8 will provide an exact representation as n approaches infinity (Forray, 1968, p. 191). For a finite series, however, the approximation will not exactly satisfy equation 8, and a residual R will result. The residual is defined by

$$R(x, y, z, t) = L \left[\sum_{i=1}^n H_i(t) \phi_i(x, y, z) \right]. \quad (10)$$

If the trial solution were the exact solution, the residual would vanish. For the approximate solution, however, the residual is forced to zero in an average sense through the selection of the undetermined coefficients H_i .

The undetermined coefficients are calculated by setting the weighted integrals of the residual to zero. In the Galerkin method (Galerkin, 1915), the interpolating functions are used as weighting functions. That is, the inner product of the residual with each O_i linearly interpolating function is set to zero, or

$$\int_{\Omega} L \left[\sum_{j=1}^n H_j(t) \phi_j(x, y, z) \right] \phi_i(x, y, z) d\Omega = 0 \quad \text{for } i = 1, 2, \dots, n. \quad (11)$$

From equation 11, n linear equations are obtained, which can be solved for the n values of H_i .

To solve the system of equations, equation 11 can be simplified. First, equation 11 is expanded to obtain a system of n equations by

$$\begin{aligned} & \int_{\Omega} \left[\frac{\partial}{\partial x} \left(K_{xx} \frac{\partial}{\partial x} \sum_{j=1}^n H_j \phi_j \right) \right. \\ & + \frac{\partial}{\partial y} \left(K_{yy} \frac{\partial}{\partial y} \sum_{j=1}^n H_j \phi_j \right) \\ & + \frac{\partial}{\partial z} \left(K_{zz} \frac{\partial}{\partial z} \sum_{j=1}^n H_j \phi_j \right) \\ & \left. - S_s \frac{\partial h}{\partial t} - W \right] \phi_i d\Omega = 0 \end{aligned}$$

for $i = 1, 2, \dots, n$.

(12) is obtained.

Second, equation 12 can be integrated by parts. By assuming hydraulic conductivity to be constant over each element and recalling that H_i is a function of time only, integration by parts yields (Pinder and Frind, 1972)

$$\begin{aligned} & \int_{\Omega} \sum_{j=1}^n \left(K_{xx} \frac{\partial \phi_i}{\partial x} \frac{\partial \phi_j}{\partial x} + K_{yy} \frac{\partial \phi_i}{\partial y} \frac{\partial \phi_j}{\partial y} \right. \\ & + \int_{\Omega} S_s \phi_i \frac{\partial h}{\partial t} d\Omega + \int_{\Omega} W \phi_i d\Omega \\ & \left. + K_{zz} \frac{\partial \phi_i}{\partial z} \frac{\partial \phi_j}{\partial z} \right) H_j d\Omega \\ & - \int_{\Gamma} \left(K_{xx} \frac{\partial h}{\partial x} n_x + K_{yy} \frac{\partial h}{\partial y} n_y + K_{zz} \frac{\partial h}{\partial z} n_z \right) \\ & \phi_i d\Gamma = 0 \quad \text{for } i = 1, 2, \dots, n, \quad (13) \end{aligned}$$

where the boundary integral represents the flux across the boundary of the flow domain. Third, by substituting equations 5 and 7 into the last term of equation 13 and replacing the partial derivatives by the general definition of the total derivative (which is described in the following section), the result

$$\begin{aligned} & \int_{\Omega} \sum_{j=1}^n \left(K_{xx} \frac{\partial \phi_i}{\partial x} \frac{\partial \phi_j}{\partial x} + K_{yy} \frac{\partial \phi_i}{\partial y} \frac{\partial \phi_j}{\partial y} \right. \\ & \left. + K_{zz} \frac{\partial \phi_i}{\partial z} \frac{\partial \phi_j}{\partial z} \right) H_j d\Omega \\ & + \int_{\Omega} S_s \phi_i \phi_j \frac{dH_j}{dt} d\Omega \\ & + \int_{\Omega} W \phi_i d\Omega - \int_{A_2} q \phi_i d\Gamma \\ & - \int_{F} S_y \phi_i \phi_j \frac{dH_j}{dt} n_z d\Gamma = 0 \\ & \text{for } i = 1, 2, \dots, n \quad (14) \end{aligned}$$

The n equations of equation 14 can be written in matrix form as

$$[A]\{H\} + [B]\left\{\frac{dH}{dt}\right\} + \{F\} = 0, \quad (15)$$

where the typical elements of $[A]$, $[B]$, and $\{F\}$ are

$$A_{ij} = \int_{\Omega} \left(K_{xx} \frac{\partial \phi_i}{\partial x} \frac{\partial \phi_j}{\partial x} + K_{yy} \frac{\partial \phi_i}{\partial y} \frac{\partial \phi_j}{\partial y} + K_{zz} \frac{\partial \phi_i}{\partial z} \frac{\partial \phi_j}{\partial z} \right) d\Omega, \quad (16)$$

$$B_{ij} = \int_{\Omega} S_s \phi_i \phi_j d\Omega + \int_F S_y \phi_i \phi_j d\Gamma, \quad (17)$$

and

$$F_i = \int_{\Omega} W \phi_i d\Omega - \int_{A_2} q \phi_i d\Gamma. \quad (18)$$

Free-Surface Boundary

The last term of equation 14, or the matrix $[B]$ of equation 15, needs more explanation. As pointed out by Neuman and Witherspoon (1971), the partial derivatives of head with respect to time that appear in equation 13 represent the change in head at a fixed point in space. However, because the free-surface position changes with time, the nodal points in the finite-element grid that represent the free surface also change position with time. Accordingly, the partial derivatives appearing in equation 13 must be evaluated using the total derivative of head (Neuman and Witherspoon, 1971), or

$$\frac{\partial h}{\partial t} = \frac{dh}{dt} - \frac{\partial h}{\partial x} \frac{dx}{dt} - \frac{\partial h}{\partial y} \frac{dy}{dt} - \frac{\partial h}{\partial z} \frac{dz}{dt}. \quad (19)$$

If the nodal points in the grid are allowed to change position only in the z direction, then derivatives of the nodal position in the x and y directions equal zero, and equation 19 reduces to

$$\frac{\partial h}{\partial t} = \frac{dh}{dt} - \frac{\partial h}{\partial z} \frac{dz}{dt}. \quad (20)$$

Before considering equation 20 further, the hydraulic head is replaced by its interpolating function (eq 9). This substitution yields

$$\frac{\partial h}{\partial t} = \sum_{j=1}^n \frac{dH_j}{dt} \phi_j - \sum_{j=1}^n H_j \frac{\partial \phi_j}{\partial z} \frac{dz_j}{dt}, \quad (21)$$

where z_j is the z coordinate of the j^{th} node.

Then, separate considerations are made in evaluating equation 21 in the interior of the flow domain and on the free surface. In general, in the interior of the flow domain, the nodal points are not allowed to move and

$$\frac{dz_j}{dt} = 0. \quad (22)$$

Therefore,

$$\frac{\partial h}{\partial t} = \sum_{j=1}^n \frac{dH_j}{dt} \phi_j \quad (23)$$

within the flow domain. On the free-surface boundary, head is a function only of x , y , and t (Neuman and Witherspoon, 1971). Therefore,

$$\frac{\partial h}{\partial z} = 0, \quad (24)$$

and, from equation 20,

$$\frac{\partial h}{\partial t} = \frac{dh}{dt}, \quad (25)$$

or, from equation 21,

$$\frac{\partial h}{\partial t} = \sum_{j=1}^n \frac{dH_j}{dt} \phi_j, \quad (26)$$

on the free surface. Consequently, both on the free surface and in the interior of the flow domain, the partial derivatives $\partial h / \partial t$ can be replaced in equation 13 by equations 23 or 26 as appropriate.

Interpolating Function

To generate the set of algebraic equations represented by equation 15, integrations of the interpolating functions of the form

$$\int \frac{\partial \phi_i}{\partial x} \frac{\partial \phi_j}{\partial x} d\Omega,$$

$$\int \phi_i \phi_j d\Omega,$$

$$\int \phi_i d\Omega,$$

$$\int \phi_i \phi_j d\Gamma,$$

and

$$\int \phi_i d\Gamma$$

must be carried out.

To facilitate these integrations, the interpolating functions are defined piecewise in each element,

the union of which produces the global-interpolating functions within the flow domain. The elemental-interpolating functions used in this work are linear and are defined over tetrahedral elements within the flow domain and over triangular elements on the boundary surfaces.

Tetrahedral elements.—Within a tetrahedral element the approximate solution (eq 9) can be expressed as

$$h \approx \sum_{i=1}^4 H_i \phi_i^e, \quad (27)$$

where Φ_i^e represent the elemental interpolating functions that are defined only within the element e . The interpolating functions for the node i are given by the relation (Zienkiewicz, 1977, p. 137)

$$\phi_i^e = \frac{1}{6V} (a_i + b_i x + c_i y + d_i z), \quad (28)$$

where

$$a_i = \begin{vmatrix} x_j & y_j & z_j \\ x_m & y_m & z_m \\ x_p & y_p & z_p \end{vmatrix}, \quad (29)$$

$$b_i = - \begin{vmatrix} 1 & y_j & z_j \\ 1 & y_m & z_m \\ 1 & y_p & z_p \end{vmatrix}, \quad (30)$$

$$c_i = - \begin{vmatrix} x_j & 1 & z_j \\ x_m & 1 & z_m \\ x_p & 1 & z_p \end{vmatrix}, \quad (31)$$

$$d_i = - \begin{vmatrix} x_j & y_j & 1 \\ x_m & y_m & 1 \\ x_p & y_p & 1 \end{vmatrix}, \quad (32)$$

$$6V = \begin{vmatrix} 1 & x_i & y_i & z_i \\ 1 & x_j & y_j & z_j \\ 1 & x_m & y_m & z_m \\ 1 & x_p & y_p & z_p \end{vmatrix}, \quad (33)$$

p, i, j, m are the nodal numbers for a tetrahedral element, V is its volume, and $x, y,$ and $z,$ are coordinates of the node i . The ordering of nodal numbers must follow a right-hand rule. By this rule, the first three nodes are numbered in a counterclockwise manner when viewed from the last one.

From equations 28 through 33, integrations involving derivatives of the trial functions are given by the following relations:

$$A_{ij}^e = \int_e K_{xx} \frac{\partial \phi_i^e}{\partial x} \frac{\partial \phi_j^e}{\partial x} d\Omega = \frac{K_{xx}}{36V} b_i b_j, \quad (34)$$

$$A_{ij}^e = \int_e K_{yy} \frac{\partial \phi_i^e}{\partial y} \frac{\partial \phi_j^e}{\partial y} d\Omega = \frac{K_{yy}}{36V} c_i c_j, \quad (35)$$

and

$$A_{ij}^e = \int_e K_{zz} \frac{\partial \phi_i^e}{\partial z} \frac{\partial \phi_j^e}{\partial z} d\Omega = \frac{K_{zz}}{36V} d_i d_j, \quad (36)$$

where $K_{xx}, K_{yy},$ and K_{zz} are assumed constant over an element and A_{ij}^e is the elemental contribution to matrix $[A]$ for $i = 1, 2, 3, 4$ and $j = 1, 2, 3, 4$ locally.

Integrations involving only the interpolating function and not their derivatives are given by the relations (Zienkiewicz, 1977, p. 174)

$$B_{ij}^e = \int_e S_s \phi_i^e \phi_j^e d\Omega = \frac{S_s V}{20} \quad \text{for } i \neq j \quad (37)$$

and

$$B_{ij}^e = \int_e S_s \phi_i^e \phi_j^e d\Omega = \frac{S_s V}{10} \quad \text{for } i = j, \quad (38)$$

where S_s is assumed constant over an element and B_{ij}^e is the elemental contribution to matrix $[B]$ for $i = 1, 2, 3, 4$ and $j = 1, 2, 3, 4$ locally.

Hydraulic-conductivity tensor.—Equation 1 was simplified above by the assumption that the coordinate system is aligned with the principal components of the hydraulic-conductivity tensor, and the results obtained to this point are based on that assumption. However, local rotation of the hydraulic-conductivity tensor is reintroduced easily. This is accomplished simply by performing the integrations of equations 34 through 36 in a local coordinate system that is aligned with the principal components of the local hydraulic-conductivity tensor. By the approach, the global coordinates for the nodes of an element are translated into the local coordinate system.

The coordinate transformation are obtained from the relations

$$x' = x \cos \alpha_{xx} + y \cos \alpha_{yx} + z \cos \alpha_{zx}, \quad (39)$$

$$y' = x \cos \alpha_{xy} + y \cos \alpha_{yy} + z \cos \alpha_{zy}, \quad (40)$$

$$z' = x \cos \alpha_{xz} + y \cos \alpha_{yz} + z \cos \alpha_{zz}, \quad (41)$$

where x' , y' , and z' are local coordinates and $\cos \alpha_{ij}$ is the direction cosine between the i^{th} direction of the global system and the j^{th} direction of the local system. If $\cos \alpha_{ii}$ is specified for the x' , y' , and z' coordinate axes, then the remaining direction cosines are determinate, and equations 39 through 41 can be solved. The relations for obtaining the remaining direction cosines are

$$\begin{aligned} \cos^2 \alpha_{yx} &= \cos^2 \alpha_{xy} \\ &= -\cos^2 \alpha_{xx} + \cos^2 \alpha_{zz}, \end{aligned} \quad (42)$$

$$\cos^2 \alpha_{zx} = \cos^2 \alpha_{xz} = 1 - \cos^2 \alpha_{zz}, \quad (43)$$

and

$$\begin{aligned} \cos^2 \alpha_{yz} &= \cos^2 \alpha_{zy} = 1 + \cos^2 \alpha_{xx} \\ &\quad - \cos^2 \alpha_{yy} - \cos^2 \alpha_{zz}. \end{aligned} \quad (44)$$

Triangular elements.—On the free surface, it is necessary to perform integrations of the interpolating functions of the form

$$\int_e \phi_i^e \phi_j^e d\Gamma,$$

where the functions are now defined on the surface. Whereas the flow domain is defined by an assemblage of tetrahedral elements, the free surface (and other boundary surfaces) can be defined by selected faces of those tetrahedral elements that form the free surface. In other words, the free surface is defined by an assemblage of triangular elements representing the faces of those tetrahedral elements. Furthermore, if the free surface is assumed to be approximately a horizontal surface, then the integrations can be carried out in the x - y plane according to the description below.

Within a triangular element, the approximate solution (eq 9) can be expressed as

$$h \approx \sum_{i=1}^3 H_i \phi_i^e, \quad (45)$$

where Φ_i^e represent the elemental interpolating functions that are defined only within the element e . The

interpolating function for the node i is given by the relation (Zienkiewicz, 1977, p. 166)

$$\phi_i^e = \frac{1}{2A} (a_i + b_i x + c_i y), \quad (46)$$

where

$$a_i = \begin{vmatrix} x_j & y_j \\ x_m & y_m \end{vmatrix}, \quad (47)$$

$$b_i = - \begin{vmatrix} 1 & y_j \\ 1 & y_m \end{vmatrix}, \quad (48)$$

$$c_i = - \begin{vmatrix} x_j & 1 \\ x_m & 1 \end{vmatrix}, \quad (49)$$

$$2A = \begin{vmatrix} 1 & x_i & y_i \\ 1 & x_j & y_j \\ 1 & x_m & y_m \end{vmatrix}, \quad (50)$$

i , j , and n are the nodal numbers for a triangular element, A is its area, and x_i and y_i are coordinates of the node i . The ordering of nodal numbers must follow a right-hand rule. By this rule, the nodes are numbered in a counterclockwise direction.

From equations 37 through 41, integrations of the trial functions are given by the relations (Zienkiewicz, 1977, p. 168)

$$B_{ij}^e = \int_e S_y \phi_i^e \phi_j^e d\Gamma = \frac{S_y}{12} A \quad \text{for } i \neq j \quad (51)$$

and

$$B_{ij}^e = \int_e S_y \phi_i^e \phi_j^e d\Gamma = \frac{S_y}{6} A \quad \text{for } i = j, \quad (52)$$

where S_y is assumed constant over an element and B_{ij}^e is the elemental contribution to matrix $[B]$ for $i = 1, 2, 3$ and $j = 1, 2, 3$ locally.

Source-Sink Terms

The source-sink term that occurs in equations 1 and 15 includes point and areally distributed sources and sinks. Additionally, the strength of some of these

may be dependent on the hydraulic head in the aquifer, and others may be independent. In general, recharge and pumpage represent head-independent point sources and sinks. Recharge by deep percolation of precipitation represents a head-independent areally distributed source. Ground-water discharge by phreatophytes represents a head-dependent sink. Constant-head boundary surfaces also are treated as head-dependent sources or sinks. Constant-flux boundary surfaces are treated as head-independent sources or sinks.

Accordingly, the source-sink term of equation 15 can be expanded to include these flux terms separately as follows:

$$F_i = \int_{\Omega} \phi_i \sum_{k=1}^m Q_k \delta(x - x_k, y - y_k, z - z_k) d\Omega + \int_F \phi_i P d\Gamma + \int_F \phi_i E d\Gamma, \quad (53)$$

where Q_k is the point volumetric recharge or pumpage from the aquifer, x_k, y_k, z_k are the coordinates of the location of the point source or sink, δ is the Dirac delta function, m is the number of point sources and sinks, P is volumetric precipitation recharge per unit area, and E is the volumetric evapotranspiration discharge per unit area.

Point sources and sinks.—Because of the properties of the Dirac delta function (Korn and Korn, 1961, p. 876), the integral in equation 48,

$\int \phi_i \sum_{k=1}^m Q_k \delta(x - x_k, y - y_k, z - z_k) d\Omega$, is equal to Q_k , if x_k, y_k , and z_k are the coordinates of a node. Therefore, the vector $\{F\}$ that appears in equation 15 is assembled by simply adding Q_k to F_i , where Q_k is located at the node i .

Distributed sources and sinks.—Distributed sources and sinks are handled somewhat differently. The function $P \equiv P(x, y, t)$ can be approximated by using trial functions to interpolate nodal values on a triangular element on the free surface. The function P is replaced by the series

$$P(x, y, t) \approx \sum_{j=1}^n P_j \phi_j, \quad (54)$$

where P_j is the value of $P(x, y, t)$ at the node j . The integral in equation 48,

$$\int_F \phi_i P d\Gamma,$$

is then replaced by the integral

$$F_i^e = \sum_{j=1}^n P_j \int_F \phi_i \phi_j d\Gamma \quad (55)$$

which can be evaluated by relations similar to equations 51 and 52, where F_i^e is the elemental contribution to the vector $\{F\}$ for $i = 1, 2, 3$ locally.

The evapotranspiration discharge $E \equiv E(x, y, t)$ is a function of depth below the land surface to the free surface and is given by the relations

$$E(x, y, t) = E_o \quad \text{for } d < 0, \quad (56)$$

$$E(x, y, t) = E_o - E_o \frac{d}{d_{\max}} \quad \text{for } 0 \leq d \leq d_{\max}, \quad (57)$$

and

$$E(x, y, t) = 0 \quad \text{for } d > d_{\max}, \quad (58)$$

where E is the volumetric discharge per unit area, E_o is the discharge with the free surface at land surface, d is the depth below the land surface to the free surface, and d_{\max} is the depth at which evapotranspiration discharge ceases.

The nodal evapotranspiration flux E_i can be given by the relations

$$E_i = A_E \int \left[E_o \delta(x - x_i, y - y_i, z - z_i) \phi_i d\Gamma \right] \quad \text{for } h > h_L, \quad (59)$$

$$E_i = A_E \int \left[E_o \left(1 - \frac{h_L}{d_{\max}} \right) + E_o \frac{h}{d_{\max}} \right] \phi_i d\Gamma \quad \text{for } h_L - d_{\max} \leq h \leq h_L, \quad (60)$$

and

$$E_i = 0 \quad \text{for } h < h_L - d_{\max}, \quad (61)$$

where A_E is the area of phreatophytes contributing discharge to node i and h_L is the altitude for the land surface.

Equations 59 through 61 are integrated over an element by considering the properties of the Dirac delta function. From those properties, the integral is given by

$$E_i = A_E E_o \quad \text{for } h > h_L, \quad (62)$$

$$E_i = A_E E_o \left(1 - \frac{h_L}{d_{\max}} \right) - A_E E_o \frac{h}{d_{\max}} \quad \text{for } h_L - d_{\max} \leq h \leq h_L, \quad (63)$$

and

$$E_i = 0 \quad \text{for } h < h_L - d_{\max} \quad (64)$$

because x_i , y_i , and z_i are coordinates of a node. Therefore, evapotranspiration is incorporated into equation 15 by adding the quantity

$$A_E E_o \left(1 - \frac{h_L}{d_{\max}} \right)$$

to F_i and by adding the quantity

$$A_E \frac{E_o}{d_{\max}}$$

to A_{ii} when $h_L - d_{\max} < h < h_L$. Similarly, the quantity $A_E E_o$ is added to F_i when $h > h_L$.

Prescribed-flux and prescribed-head boundaries.—Constant-head boundary surfaces are treated as head-dependent sources or sinks in a manner similar to that used for evapotranspiration. The nodal constant-head flux is a function of the displacement of hydraulic head from the specified boundary head, and is given by the relation

$$Q_i = \int C \left(h_{B_i} - h_i \right) \delta(x - x_i, y - y_i, z - z_i) \phi_i d\Gamma, \quad (65)$$

where Q_i is the volumetric discharge at node i on the boundary surface, h_{B_i} is the specified boundary hydraulic head at node i , h_i is hydraulic head at node i , and C is a coefficient.

If C is sufficiently large, the computed head for the boundary will be close to h_B when equation 65 is satisfied.

Equation 65 is integrated over an element by considering again the properties of the Dirac delta

function. From those properties, the integral is given by

$$Q_i = C \left(h_{B_i} - h_i \right) \quad (66)$$

because x_i , y_i , and z_i are coordinates of a node. Therefore, constant-head nodes are entered into equation 15 by adding the quantity Ch_{B_i} to F_i and the quantity C to A_{ii} .

On a prescribed-flux boundary surface, it is necessary to perform integrations of the interpolating functions of the form

$$q\phi_i d\Gamma,$$

where q is the flux rate normal to the boundary surface. Following from the derivation of Pinder and Gray (1977, p. 124), this integral is given for a triangular element in the prescribed-flux surface by the relation

$$F_i^e = \int_e q\phi_i^e d\Gamma = \bar{q} \frac{A}{3}, \quad (67)$$

where q is the average flux rate normal to the surface of the element, A is the area of the element, and F_i^e is the elemental contribution to the vector $\{F\}$ for $i = 1, 2, 3$ locally.

Integration in Time

Although the matrices $[A]$ and $[B]$ and the vector $\{F\}$ can now be evaluated, the ordinary differential equation,

$$[A]\{H\} + [B]\left\{\frac{dH}{dt}\right\} + \{F\} = 0, \quad (15)$$

must still be solved. To do this, the time derivative is approximated using the first-order correct, implicit, finite-difference scheme

$$[A]\{H_{t+\Delta t}\} + \frac{1}{\Delta t}[B]\{H_{t+\Delta t} - H_t\} + \{F\} = 0, \quad (68)$$

which can be rearranged to obtain

$$\left([A] + \frac{1}{\Delta t}[B] \right) \{H_{t+\Delta t}\} = \frac{1}{\Delta t}[B]\{H_t\} - \{F\}, \quad (69)$$

where Δt is the time step. By the implicit approximation of the time derivative, the matrices $[A]$ and $[B]$ and the vector $\{F\}$ are evaluated at the new time step $t + \Delta t$.

Iterative Solution

Each value of the coefficients of the matrices $[A]$ and $[B]$ and the vector $\{F\}$ is dependent in part on hydraulic head, and equation 69 represents a system of nonlinear algebraic equations. The most important source of nonlinearity is that the position of the free surface changes with time, and the configuration of the finite-element grid correspondingly changes with time. In general, the z coordinate of nodes in the free surface are moved upward or downward with the free surface. However, if a node in the free surface is moved downward sufficiently close to another node in the interior of the flow domain, then that interior node also is moved downward to maintain some specified minimum vertical spacing between nodes in the finite-element grid.

Nonlinearity also is introduced by the evapotranspiration term. Although the function E (eqs 62–64) is piecewise linear, it represents a nonlinear term in equation 69.

Fortunately, the nonlinearity introduced by the deforming grid and evapotranspiration term is not severe, and solution of equation 69 can be obtained by a simple iterative procedure. By this procedure, at the k^{th} iteration, equation 69 takes the following form:

$$\begin{aligned} \left([A]^{k-1} + \frac{1}{\Delta t} [B]^{k-1} \right) \{H_t + \Delta t\}^k \\ = \frac{1}{\Delta t} [B]^{k-1} \{H_t\} - \{F\}^{k-1}. \quad (70) \end{aligned}$$

At each iteration, the matrices $[A]$ and $[B]$ and vector $\{F\}$ are updated, and a solution is obtained for new values of $[H_{t+\Delta t}]$ by the square-root method (Pinder and Gray, 1977). The process is repeated until the difference between $\{H_{t+\Delta t}\}^{k-1}$ and $\{H_{t+\Delta t}\}^k$ at any particular node is less than some specified value. In most applications, convergence is obtained in two to five iterations.

APPLICATION TO BORREGO VALLEY

Geohydrologic Setting

The algorithm for the three-dimensional simulation of free-surface aquifers was applied to the Borrego Valley ground-water basin (fig. 2), which is located in a desert area of southern California. Borrego Valley is bounded on the north, west, and south by desert mountains that rise as much as 7,000 ft above the valley floor. On the east, the valley is open to Imperial Valley. The valley floor has a surface area of about 110 mi².

The Borrego Valley ground-water basin (fig. 3) is underlain by consolidated rocks and three alluvial

aquifers (Moyle, 1982). The consolidated rocks are composed of granite, schist, and gneiss, all of pre-Tertiary age, which are virtually impermeable. Ground water occurs in alluvial deposits of Pliocene to Holocene age, which comprise the three alluvial aquifers. A lower aquifer (fig. 4) includes moderately consolidated alluvial deposit of siltstone, sandstone, and conglomerate. This aquifer is as much as 1,800 ft thick, and the average hydraulic conductivity is about 1 ft/d. A middle aquifer is composed of unconsolidated to moderately consolidated deposits of sand, gravel, and boulders. This aquifer is as much as 700 ft thick, and the average hydraulic conductivity is about 6 ft/d. An upper aquifer is composed of unconsolidated deposits of gravel, sand, silt, and clay. These deposits are as much as 1,000 ft thick, and the average hydraulic conductivity is about 60 ft/d.

The ground-water basin is bounded by consolidated rock or by faults that act as barriers to ground-water flow. On the north, west, and south sides of the basin, consolidated rocks form no-flow boundaries. On the east side, a fault forms what is assumed to be a no-flow boundary. Water-level contours show that ground water flows parallel to the fault, and abnormally high gradients cross the fault (Moyle, 1982). Two explanations for the barrier effect are fault gouge in the zone of rupture, which causes reduced permeability, and the juxtaposition of sediments of different permeability on opposite sides of the fault. In Borrego Valley, evidence supports both mechanisms (Moyle, 1982).

Ground-water recharge to the Borrego Valley ground-water basin is by streamflow and precipitation infiltration. Runoff is generated by precipitation, which ranges from 3 to 30 in/yr in the mountain areas adjacent to the basin. The resulting streamflow discharges from the mountain canyons onto alluvial fans that, in part, form the ground-water basin. On these fans, infiltration occurs as streamflow moves toward the center of the basin. Part of the streamflow infiltration percolates downward to become ground-water recharge, and the rest is consumed by evapotranspiration from the shallow soil profile. Most streamflow either percolates or is consumed, and very little streamflow leaves the basin as surface-water discharge. The average annual recharge by streamflow infiltration is 5,100 acre-ft/yr. In the model, that recharge is represented as time-invariant point sources at nodal points located on the stream channels.

Recharge also occurs from the deep percolation of precipitation on the valley floor. The range of annual precipitation on the valley floor is from 3 to 6 in, but is more variable from year to year; for exam-

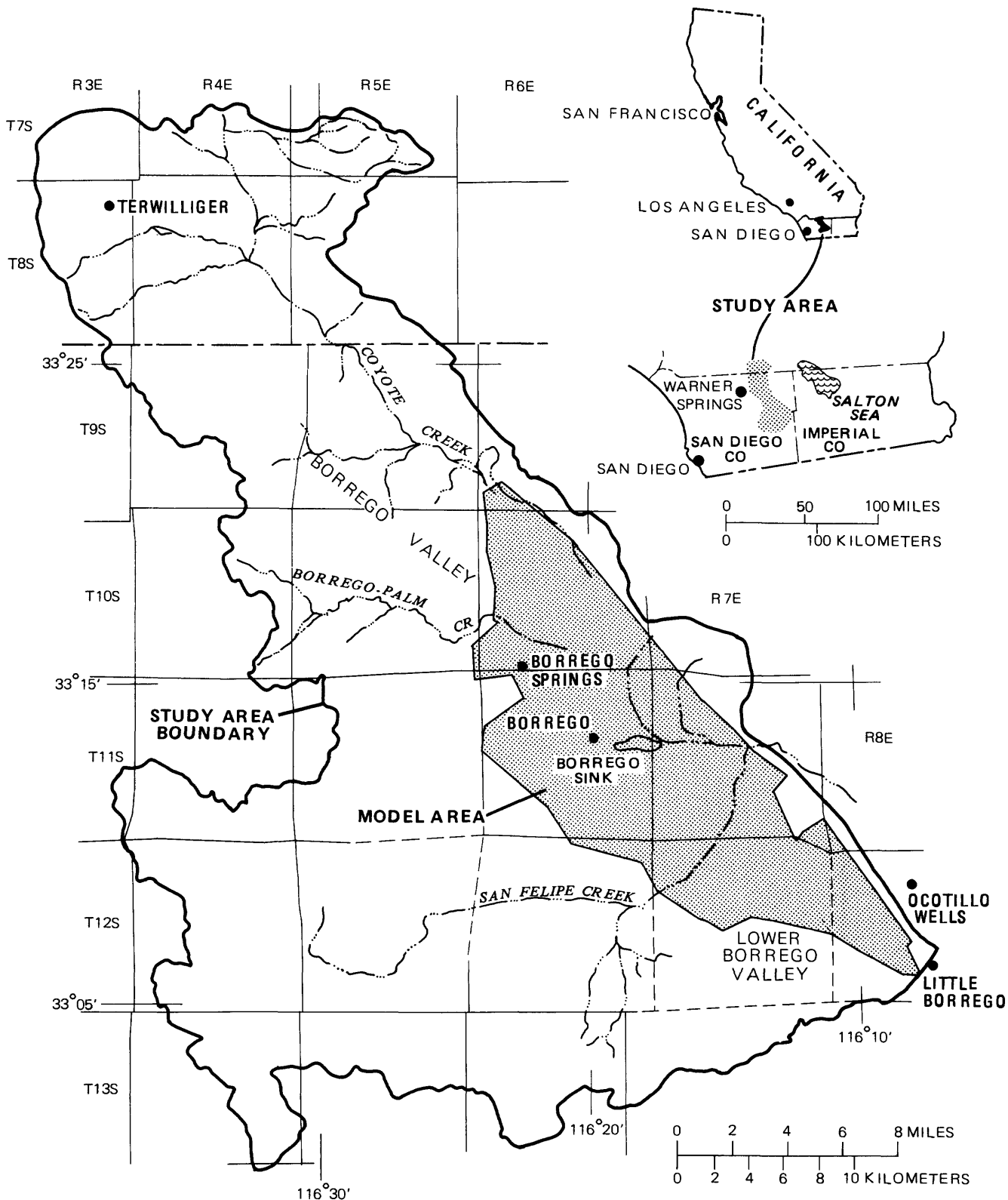


Figure 2. Location of study and model area.

ple, from 1954 through 1980, annual precipitation at a gage in the valley floor ranged from 1 to 14 in. In the drier years, ground-water recharge probably does not occur by the infiltration of precipitation. Howev-

er, in the wet years, recharge probably does occur. Results of a water-budget analysis for the Borrego Valley ground-water basin indicated that the average annual recharge to the basin from precipitation is

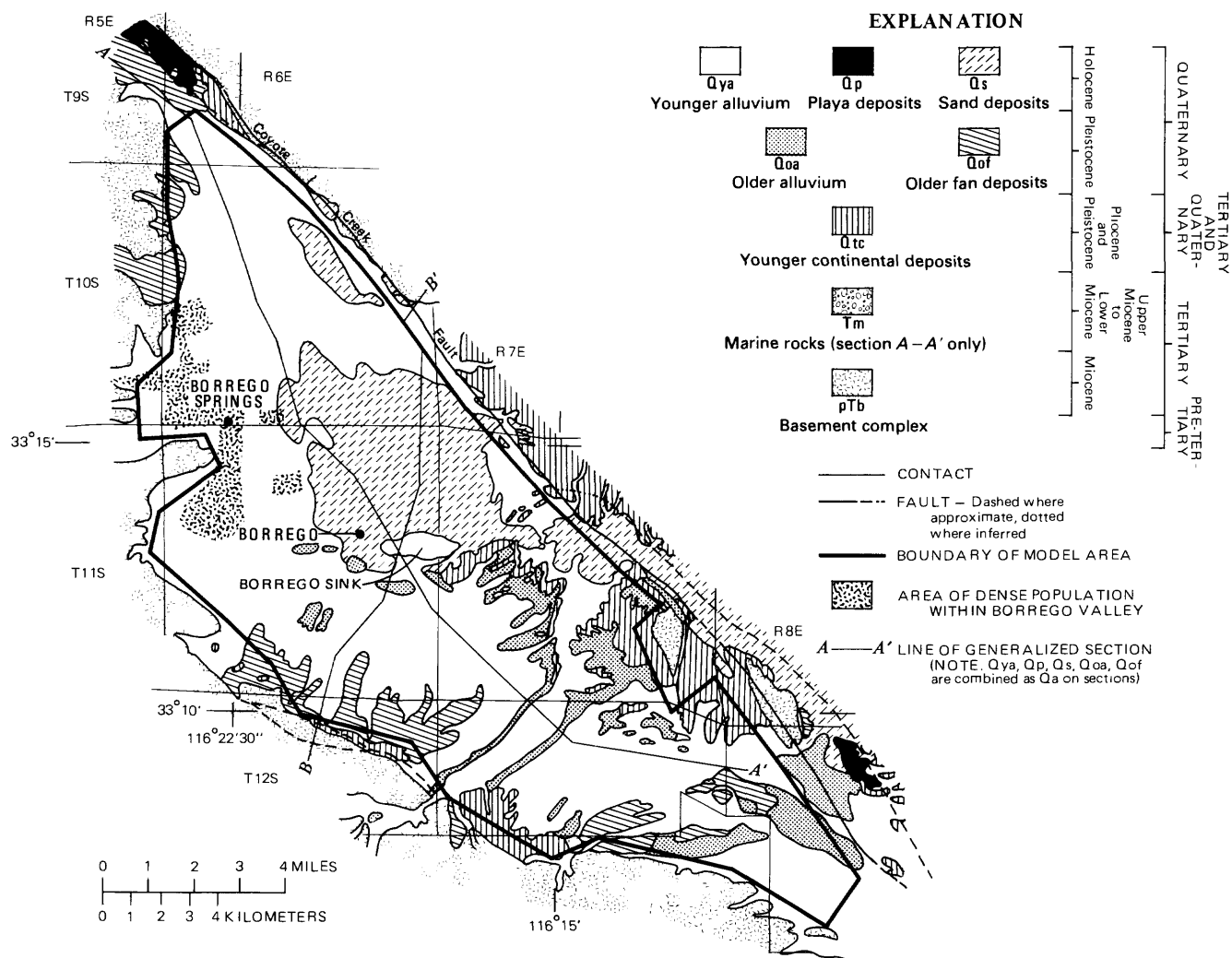


Figure 3. Geologic features of Borrego Valley, California, and location of sections A-A' and B-B'.

3,300 acre-ft/yr. In the model, that recharge is represented as a time-invariant distributed source over the upper surface of the basin.

Ground-water discharge from the Borrego Valley ground-water basin is by evapotranspiration of phreatophytes, pumping, and underflow. Mesquite and tamarisk cover about 4,500 acres in the central part of the ground-water basin, and model simulations indicate that these phreatophytes consume about 1,200 acre-ft/yr of ground water. This use of ground water is represented in the model by a linear relation with depth below the land surface to the water table. With the water table at the land surface, the simulated unit-area rate of consumption is 4 ft/yr. If the water table is at or below 10 feet from the land surface, then the rate is zero. Consequently, evapotranspiration is represented in the model as a head-dependent, areally distributed sink.

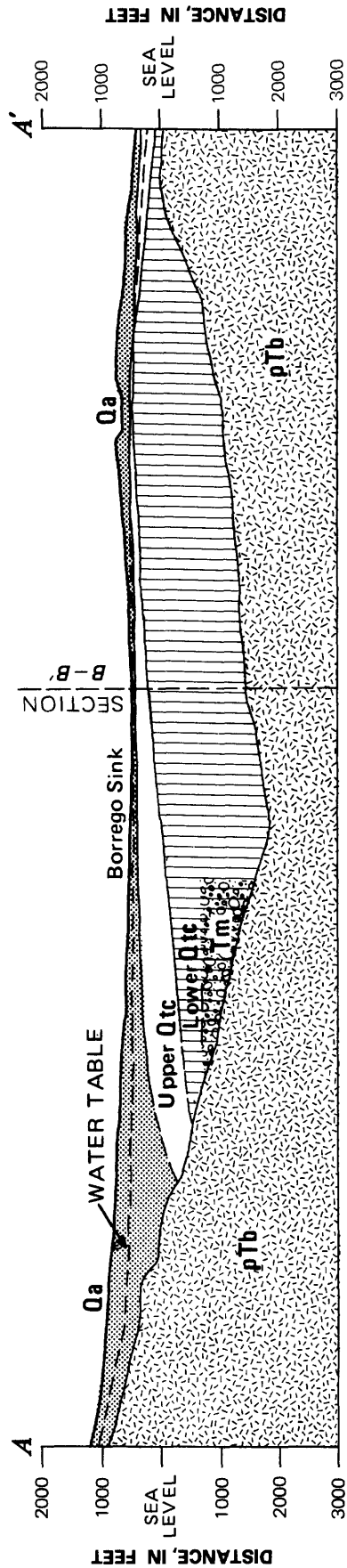
Net pumping from the ground-water basin (fig. 5), which is the difference between extractions and

consumptive use, ranged from 5,000 to 22,000 acre-ft/yr from 1945 to 1980. Most of this water, which is used for agricultural and domestic purposes, is pumped from wells that are shallow relative to the thickness of the ground-water basin. Consequently, net pumping is represented in the model as point sinks assigned to nodes on the upper surface of the ground-water basin.





Ground water also discharges from the basin as underflow into adjacent ground-water basins; for example, as indicated by model simulations and a water-budget analysis, about 2,100 acre-ft/yr of ground water discharges across the southern boundary of the lower Borrego Valley near the community of Ocotillo Wells. This discharge is represented in the model as a constant-head boundary.

Finite-Element Grid

The geology of the Borrego Valley ground-water basin is represented by a three-dimensional finite-



EXPLANATION

-  Upper aquifer
-  Middle aquifer
-  Lower aquifer
-  Basement complex

(See figure 3 for explanation of geologic units)

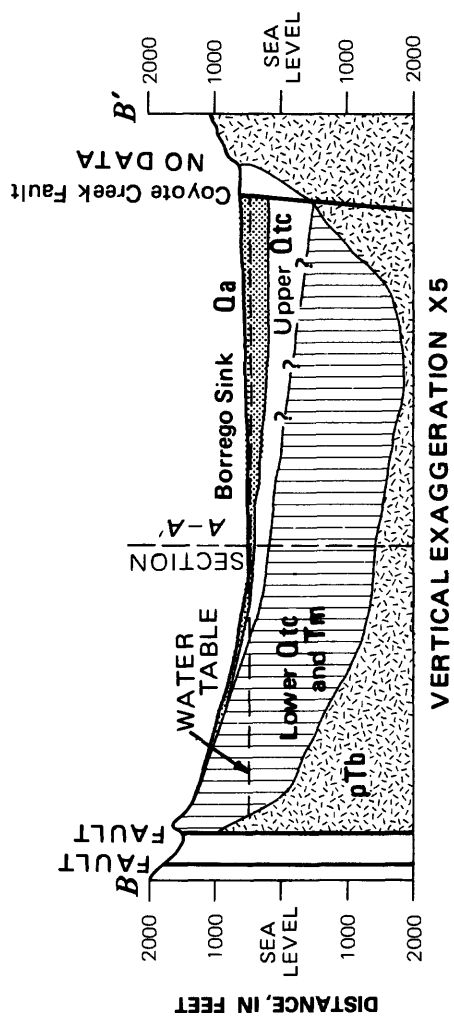
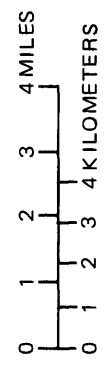


Figure 4. Geologic sections A-A' and B-B'.

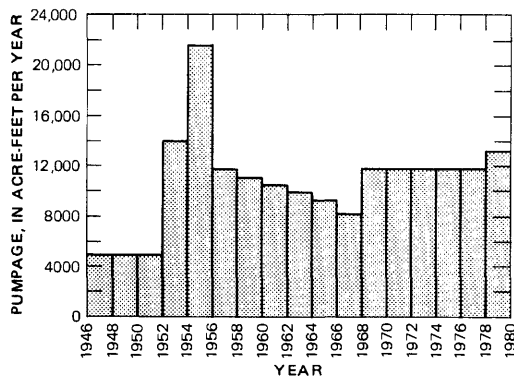


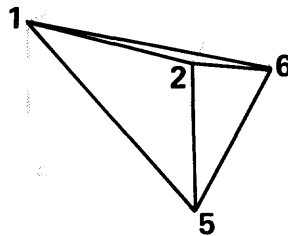
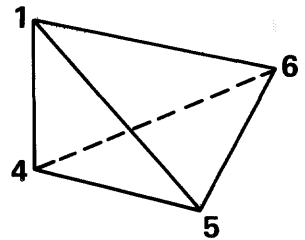
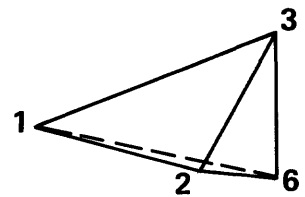
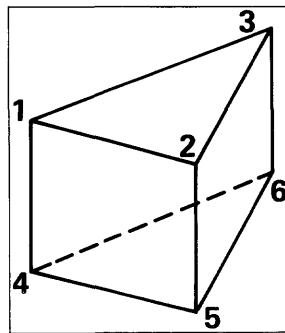
Figure 5. Ground-water pumpage.

element grid. The grid consists of a solid configuration of tetrahedrons. Because tetrahedrons are difficult solids with which to work, the actual grid is assembled from prismatic solids with a triangular cross section. The computer algorithm then automatically fits three tetrahedrons into each prismatic element as shown in figure 6. To allow flexibility in the construction of three-dimensional grids, the algorithm also accepts prismatic elements that contain edges of zero height as shown in figure 7. A prismatic element with one zero-height edge contains two tetrahedrons, and an element with two zero-height edges contains one. These special elements can be used to represent geologic features that taper to zero thickness or to include a fine grid in zones of particular interest. Without these special elements, a zone of fine gridding can only be terminated by carrying it to the edge of the grid.

The regular and special prismatic elements were used to construct a finite-element grid for the Borrego Valley ground-water basin (fig. 8). The grid is assembled for the most part from the three-high stacks of prismatic elements. The upper, middle, and lower prisms in each stack represent, respectively, the upper, middle, and lower alluvial aquifers. In places, these aquifers taper to zero thickness, which also is represented in the finite-element grid. These and other geologic features of the ground-water basin are represented in a grid that includes 336 nodes and 405 prismatic and 1,132 tetrahedral elements. The dimension in the x-y plane of elements ranges from 2,500 to 18,000 ft, and the dimension in the z direction ranges from 50 to 1,500 ft.

The model includes three types of boundary conditions. The top surface of the finite-element grid is a free-surface boundary surface. Most of the remaining boundary surface is a prescribed-flux boundary with zero flux, which is a no-flow boundary representing the contact between the alluvial deposits of the ground-water basin and the nonwater-bearing consolidated rocks underlying the alluvial deposits

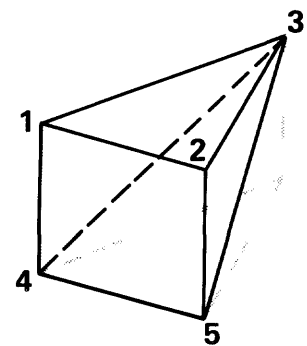
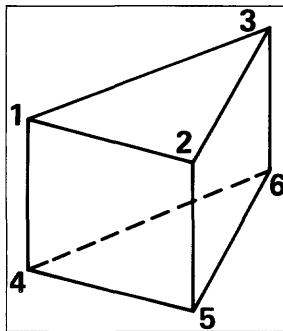
PRISMATIC ELEMENT



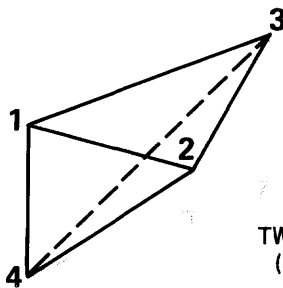
TETRAHEDRONS

Figure 6. Subdivision of prismatic element into tetrahedrons.

PRISMATIC ELEMENT



ONE ZERO-HEIGHT SIDE
(Indicated by 1,2,3,4,5,0)



TWO ZERO-HEIGHT SIDES
(Indicated by 1,2,3,4,0,0)

Figure 7. Prismatic element with one or two zero-height edges.

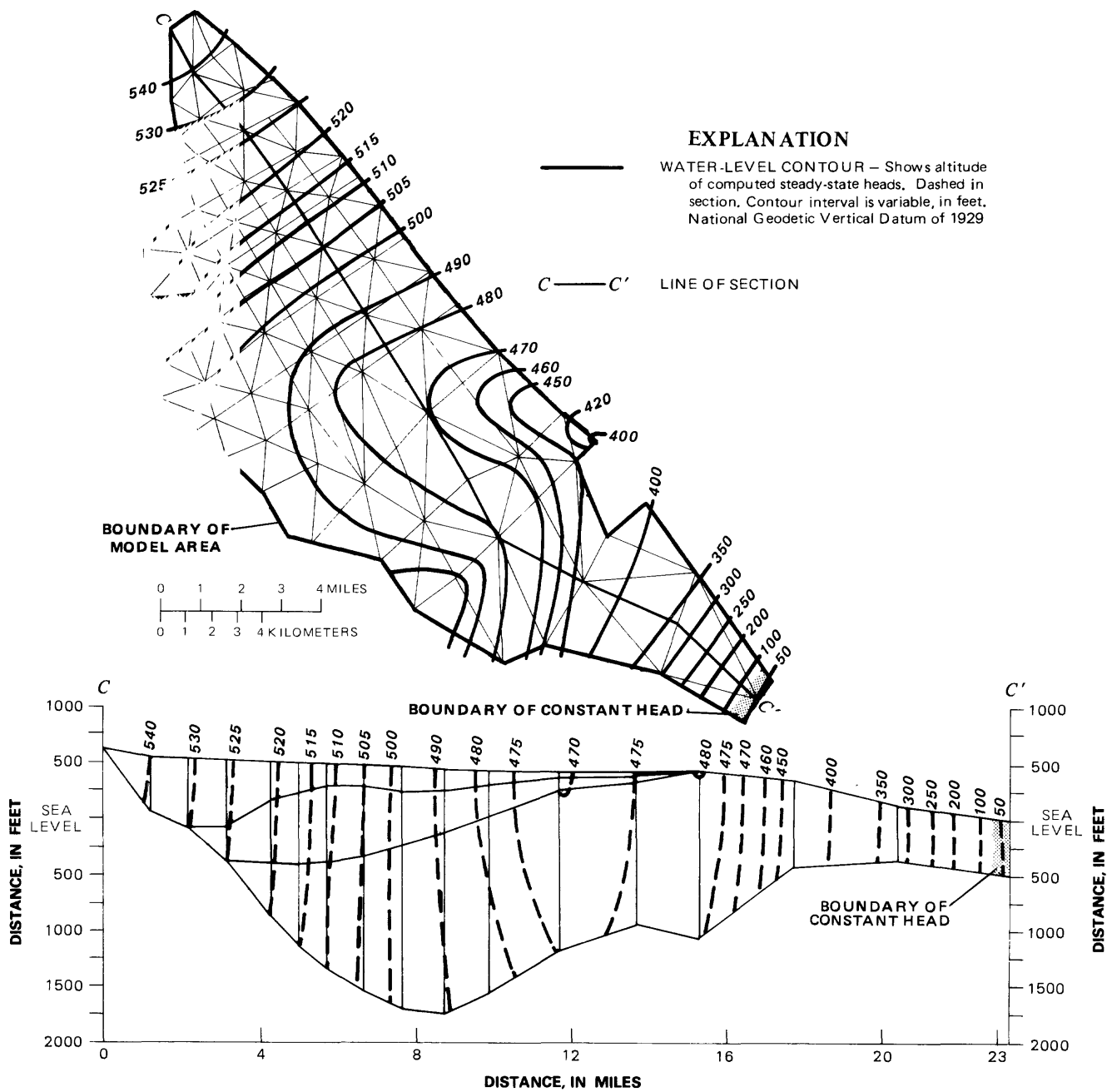


Figure 8. Finite-element grid, computed steady-state heads for 1945, and section C-C'.

and the adjacent mountains or the nonwater-transmitting faults. However, one small part of the boundary surface of the finite-element grid is a constant-head boundary (fig. 8), which represents the interaction of the Borrego Valley ground-water basin with an adjacent ground-water basin.

The hydraulic characteristics of the ground-water basin are represented by assigning values of aquifer parameters to each prismatic element, while, in turn, these values are assigned to the tetrahedral elements that comprise the prismatic element. The

quantities assigned values are the hydraulic conductivity for the three principal components of the conductivity tensor, the local orientation of the principal components to the global-coordinate system, storage coefficient, and specific yield (for elements in the free surface). Particular values used to represent the Borrego Valley ground-water basin are shown in table 1.

Simulation Results

The model was used to simulate steady- and transient-state hydraulic heads. Computed steady-

Table 1. Aquifer parameter-values used in the model

Parameter	Units	Aquifer		
		Upper	Middle	Lower
K_{xx}	Feet per day	58.0	5.8	1.4
K_{yy}	do	58.0	5.8	1.4
K_{zz}	do	1.6	.16	.016
α_{xx}	Degree	0	0	0
α_{yy}	do	0	0	0
α_{zz}	do	0	0	0
S_s	Per foot	10^{-6}	10^{-6}	10^{-6}
S_y	Dimensionless	.12	.12	.12

state heads are shown in figure 8. For that distribution of heads, ground-water discharge for the Borrego Valley basin is 40 acre-ft/yr across the constant-head boundary and 6,300 acre-ft/yr from water use by phreatophytes. Computed heads at the end of the 34-year transient-state simulation are shown in figure 9. Figure 10 shows that during this period, simulated evapotranspiration discharge declined to 1,300 acre-ft/yr as heads declined. Discharge across the constant-head boundary changed very little.

Simulation of heads for the Borrego Valley ground-water basin indicates that the algorithm is efficient. The transient-state simulation required about 9 minutes of processor time on a Prime 750. The simulation utilized 17 2-year time steps. At each time step, about two iterations were required to adjust the grid coordinates and head-dependent evapotranspiration discharge. Closure of the mass balance for the ground-water basin was less than 1 percent.

CONCLUSIONS

Three-dimensional free-surface aquifers can be simulated by the finite-element method utilizing a deforming grid. The formulation starts with the equation of ground-water flow in three dimensions and a linearized form of the partial-differential equation that describes the free-surface boundary condition. The governing equation is solved for the initial and boundary conditions by the Galerkin finite-element approach. In implementing this approach, volume integrations within the flow domain are carried out by linear interpolating functions on tetrahedral elements. Surface integrations on the boundary surfaces are carried out by linear interpolating functions on triangular elements. Time derivatives resulting from the Galerkin finite-element approach must be evaluated by their total derivatives. However, by placing some restrictions on the movement on nodes within

the deforming grid, the total derivatives are reduced to simple expressions. The end result is an efficient algorithm that more or less rigorously represents the initial system of governing and boundary equations.

Of the several approaches available for the three-dimensional simulation of free-surface aquifers, the finite-element approach presented here offers some advantages over others. For aquifer systems lacking definable interaquifer aquitards, the approach better represents such systems as a three-dimensional continuum than does the quasi-three-dimensional approach. The finite-element approach represents the nonlinear effects of a changing flow-domain geometry, which is lacking in other fully three-dimensional representations that keep the flow-domain geometry fixed. The approach is more efficient than those defining the free-surface problem as one of saturated-unsaturated ground-water flow. The finite-element approach is more rigorous than finite-difference approaches that utilize a deforming grid but nevertheless do not explicitly solve the initial- and boundary-value problem for the free-surface boundary condition.

REFERENCES CITED

- Bredehoeft, J. D., and Pinder, G. F., 1970, Digital analysis of the areal flow in multi-aquifer ground-water systems; A quasi three-dimensional model: *Water Resources Research*, v. 6, no. 3, p. 883-888.
- Durbin, T. J., 1978, Calibration of a mathematical model of the Antelope Valley ground-water basin, California: U.S. Geological Survey Water-Supply Paper 2046, 51 p.
- Forsay, M. J., 1968, *Variational calculus in science and engineering*: New York, McGraw-Hill, 193 p.
- Freeze, R. A., 1971, Three-dimensional transient, saturated-unsaturated flow in a ground-water basin: *Water Resources Research*, v. 7, no. 2, p. 347-366.

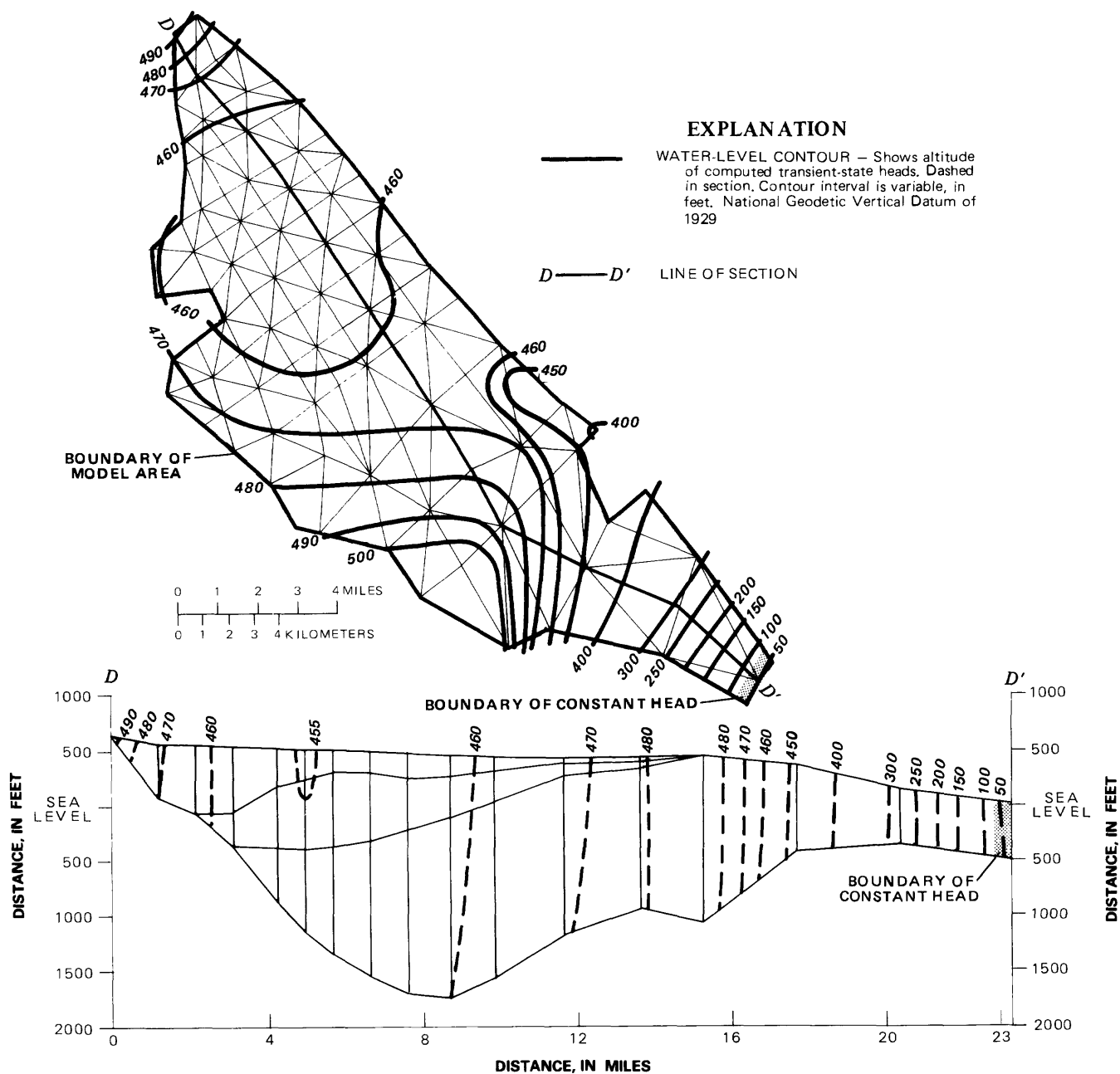


Figure 9. Finite-element grid, computed transient-state heads for 1980, and section $D-D'$.

- Frind, E. O., and Verge, M. J., 1978, Three-dimensional modeling of ground-water flow systems: *Water Resources Research*, v. 14, no. 5, p. 844-856.
- Galerkin, B. G., 1915, Rods and plates: *Vestn. Inzh. Tech. (USSR) Rept. 19*, p. 897-908. Translation PB 63-18924, National Technical Information Service, U.S. Department of Commerce, Springfield, VA 22161.
- Korn, G. A., and Korn, T. M., 1961, *Mathematical handbook for scientists and engineers*: New York, McGraw-Hill, 1130 p.
- Leake, S. A., 1977, Simulation of flow from an aquifer to a partially penetrating trench: *U.S. Geological Survey Journal of Research*, v. 5, no. 5, p. 535-540.
- Moyle, W. R., Jr., 1982, Water resources of Borrego Valley and vicinity, California—Phase 1, Definition of geologic and hydrologic characteristics of basin: U.S. Geological Survey Open-File Report 82-855, 39 p.
- Neuman, S. P., and Witherspoon, P. A., 1971, Analysis of nonsteady flow with a free surface using the finite-element method: *Water Resources Research*, v. 7, no. 3, p. 611-623.
- Pinder, G. F., and Frind, E. O., 1972, Application of Galerkin's procedure to aquifer analysis: *Water Resources Research*, v. 9, no. 1, p. 108-120.
- Pinder, G. F., and Gray, W. G., 1977, *Finite-element simulation in surface and subsurface hydrology*: New York,

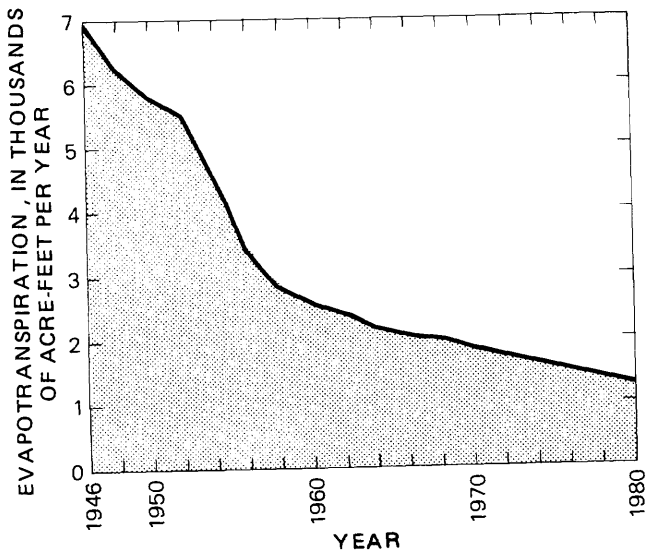


Figure 10. Simulated ground-water use by phreatophytes.

Academic Press, 295 p.

Trescott, P. C., 1975, Documentation of finite-difference model for simulation of three-dimensional ground-water flow: U.S. Geological Survey Open-File Report 75-438, 32 p.

Trescott, P. C., and Larson, S. P., 1977, Solution to three-dimensional ground-water flow equations using the strongly implicit procedure: *Journal of Hydrology*, v. 35, p. 49-60.

Zienkiewicz, O. C., 1977, *The finite-element method* (3d ed.): New York, McGraw-Hill, 787 p.

Measurement of Reaeration by the Modified Tracer Technique in the Wabash River Near Lafayette and Terre Haute, Indiana

By Charles G. Crawford

Abstract

The modified tracer technique was used to measure reaeration in the Wabash River at streamflows ranging from 65 to 210 cubic meters per second near Lafayette and Terre Haute, Indiana, as part of a series of multidisciplinary studies on the Wabash River in cooperation with the Indiana State Board of Health. Chemically pure grade ethylene was used as the tracer gas, and rhodamine-WT dye was used as the dispersion-dilution tracer. Ethylene was bubbled into the water at rates of 362.5 to 580 grams per minute through a series of 20 to 32 porous flat-plate diffusers.

Injection efficiencies for the ethylene were estimated to range from 16 percent when the diffusers were submerged in 0.8 meter of water to 64 percent when the diffusers were submerged in 3.4 meters of water. The injection efficiency was highly correlated with the depth of the overlying water. Rates of recovery of the rhodamine-WT dye ranged from 83 to 98 percent and were lowest at the highest streamflows.

Reaeration coefficients measured in a 29.7-kilometer-long reach near Lafayette, Indiana, at streamflows of 65 and 97 cubic meters per second were 1.2 and 0.8 per day at 20 degrees Celsius. Reaeration coefficients measured in a 21.8-kilometer-long reach near Terre Haute, Indiana, at streamflows of 95 and 210 cubic meters per second were 1.4 and 1.1 per day at 20 degrees Celsius.

None of the equations commonly found in the literature predicted reaeration coefficients similar to those measured for the Lafayette and Terre Haute reaches of the Wabash River. The average prediction error for 10 commonly used reaeration equations ranged from 22 to 154 percent. Prediction error was much smaller in the Terre Haute reach than in that of Lafayette. The overall average of the absolute prediction error for all 10 equations was 22 percent for the Terre Haute reach and 128 percent for the Lafayette reach. Confidence limits of results obtained from the modified gas-tracer technique were smaller than those obtained from the equations in the literature.

INTRODUCTION

Overview

Reaeration is the process of the absorption of oxygen from the atmosphere by surface water. This mechanism is the primary means by which oxygen is replenished in streams. Consequently, the amount of biodegradable waste that can be assimilated by a stream without detrimental effects on aquatic life in the stream is dependent upon reaeration. The reaeration, or oxygen-gas-transfer, coefficient is a measure of the rate at which the oxygen is absorbed or transferred from the atmosphere to the stream.

Because of the importance of the reaeration coefficient in assessing waste assimilation capacity, several methods for its estimation have been reported in the literature. These methods are discussed in detail by Bennett and Rathbun (1972). Churchill, Elmore, and Buckingham (1962) used a dissolved-oxygen (DO)-balance method to measure reaeration in several rivers in Tennessee. They measured the rate of oxygen absorption in deoxygenated water released from thermally stratified reservoirs. Owens, Edwards, and Gibbs (1964) used a similar technique on small English streams. They measured the rate of oxygen absorption in waters deaerated with sodium sulfite and a cobalt catalyst. Both of these methods require that all other factors influencing the oxygen balance be known or negligible. Because of the difficulty in measuring the other factors accurately, the two techniques are subject to considerable error.

Slug-Injection Gas-Tracer Method

Tsivoglou (1967) developed a gas-tracer method for directly measuring gas transfer in streams to eliminate the need for the oxygen-balance infor-

mation. In this method, a fluorescent tracer is used for determining time of flow and longitudinal dispersion, tritium as an indicator of total dispersion, and krypton-85 as a gaseous tracer. The tracers are added instantaneously to the stream, and samples are collected at several points downstream to measure the rate of loss of the gas tracer. Because the tracers are added so quickly at the same points, no mixing zone is needed, and the first sampling point is typically only a short distance downstream from the injection point. The gas desorption coefficient is assumed to be related to the reaeration coefficient by a laboratory-determined proportionality constant.

Of the various methods, the gas-tracer method of Tsivoglou (1967) is superior because it does not require estimating any other factor affecting the oxygen balance. This method, however, requires the handling and the injecting of radioactive tracers into streams. Application of the method is limited because use of radioactive tracers in the natural environment is subject to public-health restrictions. Additionally, measurements with the method are limited to streamflows of 10 to 20 m³/s because of the difficulty in handling the quantity of radioactive material required.

Modified Gas-Tracer Method

Rathbun, Schultz, and Stephens (1975) modified Tsivoglou's method to use nonradioactive hydrocarbons (ethylene or propane) as the gaseous tracers. The modified gas-tracer technique uses a short, continuous injection rather than an instantaneous injection. The continuous injection is used because of the low solubilities of ethylene and propane in water. An instantaneous injection of these gases would require large quantities of tracers not handled easily for most streams. Because the gas and conservative tracers cannot be injected at exactly the same points, the first sampling cross section for this method typically is located farther downstream than for the slug-injection gas-tracer method to permit mixing of the tracers across the stream width.

The use of hydrocarbon tracers circumvents the restrictions placed on the slug-injection gas-tracer method of measuring reaeration by radioactive tracers. However, the low solubility of hydrocarbon gases in water and the difficulties involved in adding the tracer gases to streams have prevented this method from being widely applied, except at streamflows of less than about 30 m³/s.

The techniques used to apply the modified tracer technique developed by Rathbun, Schultz, and Stephens (1975) at streamflows ranging from 65 to 210 m³/s and the results of the measurements are

described in this paper. The measured reaeration coefficients are compared with alternative methods of estimating reaeration.

Acknowledgements

The study was done in cooperation with the Indiana State Board of Health as part of a series of multidisciplinary studies on the Wabash River to evaluate the waste-assimilation capacity of the river. The author thanks Stephen H. Boswell of the Indiana State Board of Health for assistance in planning and collecting the data and John D. Vaupotic of the U.S. Geological Survey for determining the concentrations of ethylene.

STUDY AREA

The Wabash River in western Indiana is the largest free-flowing tributary to the Ohio River. The river is economically important for agricultural, municipal, and industrial uses; the predominant land use in the basin is agriculture, although the basin contains several urban areas and several chemical and other manufacturing plants, many of which use water from the Wabash River and discharge wastewater directly to the river.

The locations of the study area and measured reaches are shown in figure 1. Reaeration was measured in one reach near Terre Haute, Indiana, and one reach near Lafayette, Indiana. The reach near Lafayette was 29.7 km long and extended from Lafayette to Attica. The reach near Terre Haute was 21.8 km long and extended from Terre Haute to Darwin. Average hydraulic characteristics of the reaches during the measurements are presented in table 1. Measurements were done at approximately 3.5 and 5.2 times the annual 10-year, 7-day low flow (7Q₁₀) for the reach near Lafayette and 3.1 and 6.9 times the annual 7Q₁₀ for the reach near Terre Haute.

METHODS OF STUDY

Modified Tracer Technique

This technique involves (1) injecting two tracers into the river concurrently, (2) sampling the tracers at two or more locations downstream of the injection location, and (3) determining the concentrations of ethylene and rhodamine-WT dye in the samples. The procedure used for the Wabash River is discussed in the following paragraphs. Additional information about the method is given in Rathbun, Shultz, and Stephens (1975) and Rathbun and Grant (1978).

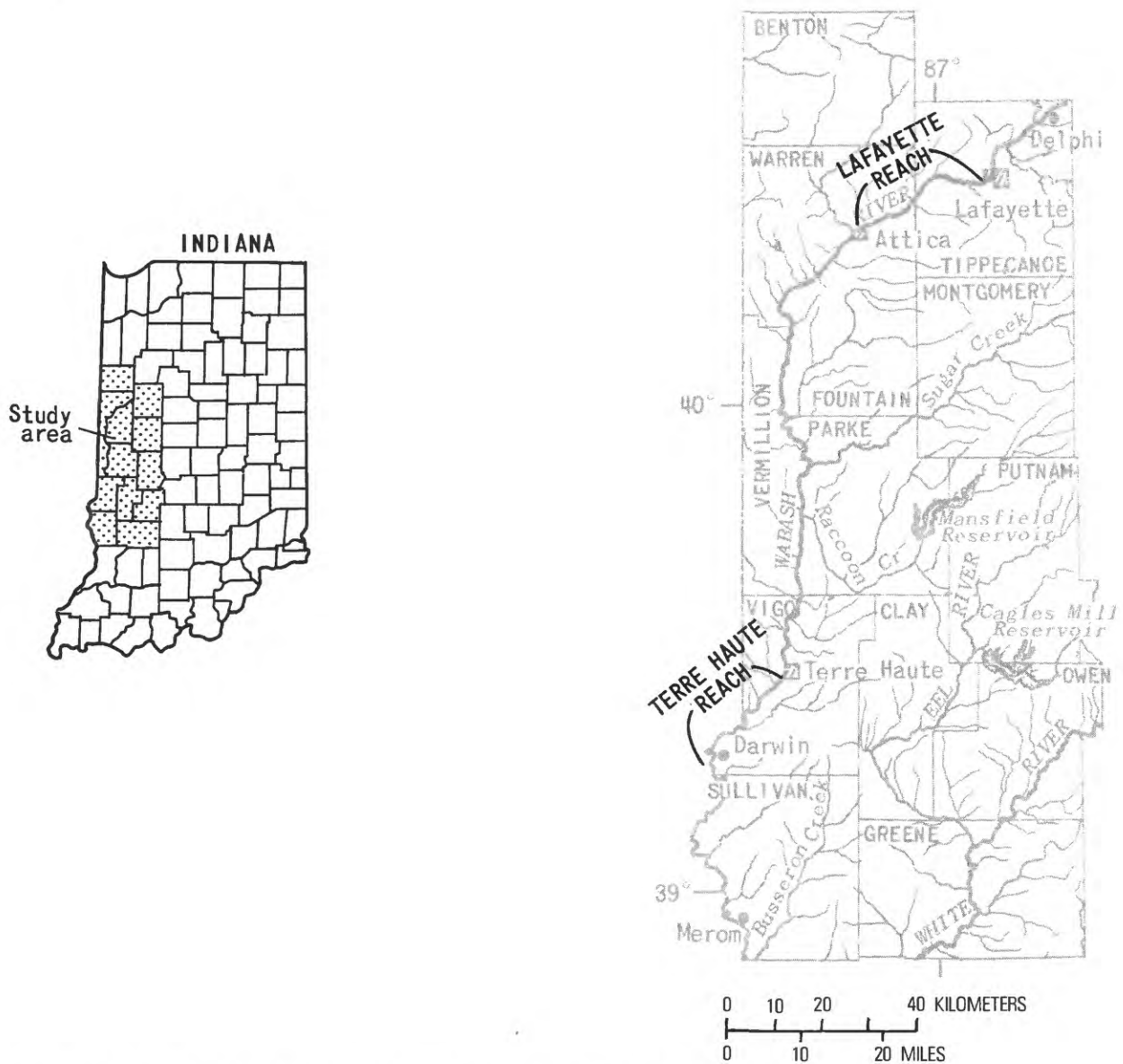


Figure 1. Locations of study area and measured reaches on the Wabash River.

Table 1. Average hydraulic characteristics of reaches of the Wabash River near Lafayette and Terre Haute during the reaeration measurements

Reach	Date	Average streamflow (m ³ /s)	Percentage of time			Slope (m/m)
			average streamflow is equaled or exceeded	Average depth (m)	Average velocity (m/s)	
Near Lafayette (29.7 km)	--- 11/18-19/81	97	53	1.3	0.58	0.000133
	7/26-27/82	65	70	1.0	.49	.000133
Near Terre Haute (21.8 km)	--- 10/21-22/81	210	43	2.3	.64	.000114
	8/25-26/82	95	71	1.6	.43	.000114

Chemically pure grade (99.5-percent pure) ethylene was bubbled into the river through a series of Zimpro passive diffusers. The pore size of these po-

rous flat-plate diffusers is 1.5 to 2.0 μm . Each diffuser (1.05 x 75 x 9 mm) consisted of 12 plates epoxied in a fiberglass channel. Diffusers were assembled into

racks of four, and the individual diffusers were connected in parallel by plastic tubing (Tygon). Ethylene was released into the diffusers from high-pressure cylinders through two-stage regulating valves (Linde model UP-E). Plastic tubing was used to connect the gas cylinders to the diffusers. The gas flow rate was measured by a flowmeter (Linde model 150K) connected to the outlet of the regulating valve. One gas cylinder, one regulating valve, and one flowmeter were used for each rack of four diffusers. A diagram of the injection apparatus is shown in figure 2.

An injection point 1 to 2 hours time of travel upstream from each reach was selected because it was desirable to have the tracers mixing in the flow at both downstream sampling sites. The diffusers were placed parallel to the flow on the bottom of the river at the deepest part of the channel near the center of flow. The racks were placed 5 to 15 m apart. Eight diffuser racks were used for the high-flow measure-

ment in the reach near Terre Haute, and five racks were used for all other reaches. Ethylene was injected at 72.5 to 98 g/min from each gas cylinder. The ethylene cylinders were placed on the river bank near the location of the diffusers. Except at the point where the tubing entered the water over the diffuser, the tubing was suspended out of the water from a steel wire stretched across the river.

A 20-percent solution of rhodamine-WT dye was injected through plastic tubing into the river by one or two pumps, which were manufactured by FMI Corp. and were operated by 12-volt batteries. Two to four tubes from the pumps were fastened to each of the diffuser racks so that the distribution of the dye and the ethylene would be similar and mixing downstream for both tracers would be virtually the same.

The ethylene and the rhodamine-WT dye were injected for 2 hours during each measurement. Injection rates were estimated by procedures described by

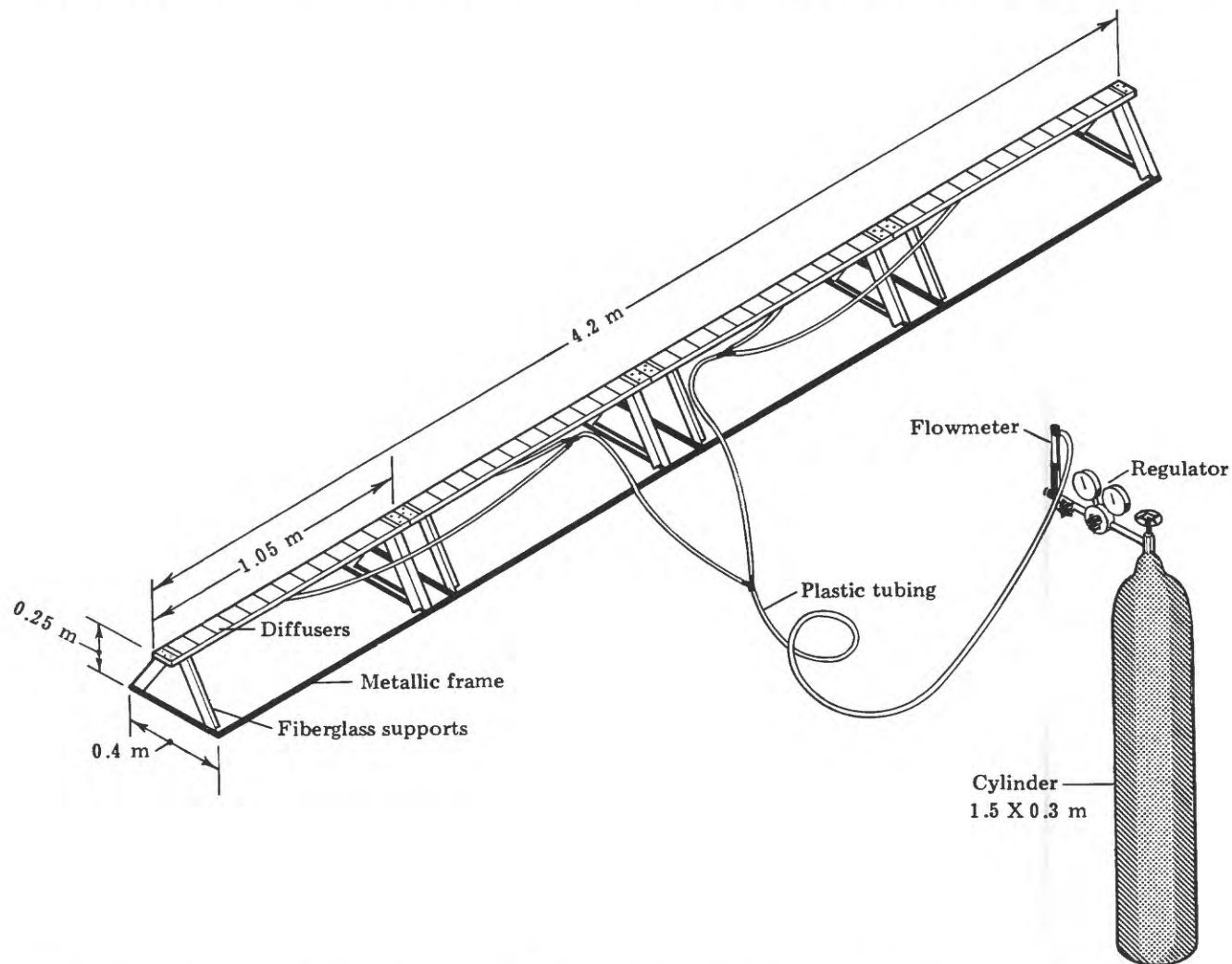


Figure 2. Injection apparatus used for the modified gas-tracer technique. Equipment shown is for one rack of four diffusers.

Rathbun (1979). The procedure for ethylene was modified to account for the pressure drop of the Zimpro diffusers (R. E. Rathbun, written commun., 1981). A diagram of the equipment setup at the injection site is given in figure 3.

Water samples for determining concentrations of ethylene and rhodamine-WT were collected at three to five points in each cross section at the upstream and downstream ends of each reach so that tracer concentrations and the degree of mixing could be estimated.

Samples for determining concentrations of ethylene were collected at approximately middepth of the sampling point in a DO sampler (Hach model 1962) equipped with septum vial sampling bottles of 40-mL capacity. Samples were preserved for laboratory analysis by adding 1 mL of formalin to each sample bottle. Ethylene concentrations were determined by the procedure described by Shultz and others (1976).

Samples for determining concentrations of dye were collected in 32-mL bottles for analysis in the laboratory. Dye concentrations were determined by a fluorometric method described by Wilson (1968).

The ethylene gas transfer coefficients were computed by the peak concentration method (Rathbun and Grant, 1978):

$$K_E = \frac{1}{T_D - T_U} \ln \frac{\frac{E_U}{D_U}}{\frac{E_D}{D_D \times DCF}}, \quad (1)$$

- where
- K_E is the ethylene gas transfer coefficient at the ambient stream temperature, in minute^{-1} ,
 - T_U the time between the start of the dye injection and the peak dye concentration at upstream cross section, in minutes,
 - T_D the time between the start of the dye injection and the peak dye concentration at downstream cross section, in minutes,
 - \ln the natural logarithm,
 - E_U peak ethylene concentration at upstream cross section, in micrograms per liter,
 - D_U peak dye concentration at upstream cross section, in micrograms per liter,
 - E_D peak ethylene concentration at downstream cross section, in micrograms per liter,
 - D_D peak dye concentration at downstream cross section, in micrograms per liter, and
 - DCF the dye-loss correction factor.

The dye-loss correction factor, DCF , which is based on the concept of conservation of mass, ensures that the dye mass, QA , is constant throughout the reach, where Q is the water discharge, and A is the area under the time-concentration dye curve. The factor is derived as follows:

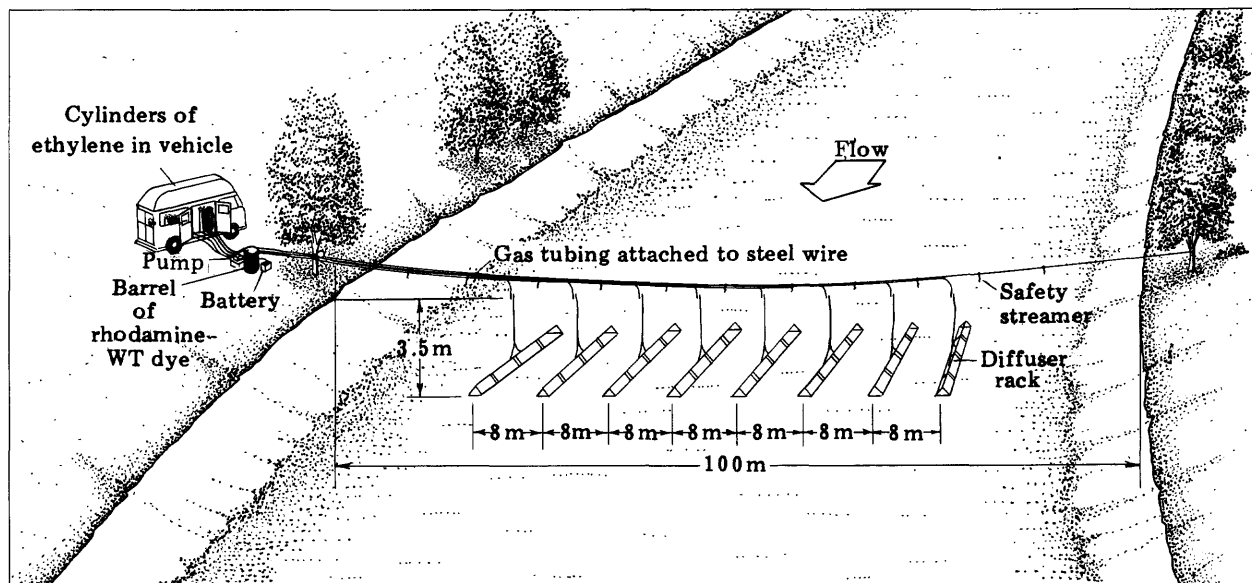


Figure 3. General arrangement of equipment used at the sites where ethylene and rhodamine-WT tracers were injected.

$$Q_U A_U = Q_D A_D \times DCF \quad (2)$$

or

$$DCF = \frac{Q_U A_U}{Q_D A_D}, \quad (3)$$

where *U* and *D* are subscripts referring to the upstream and downstream cross sections.

The area under the time-dye-concentration curve is determined by plotting the observed dye concentrations against time and integrating the area under the curve. The resulting units are minutes-microgram per liter. The areas were integrated by a Wang 2262-3 digitizer and a Wang 2200 T minicomputer.

The reaeration coefficient can be calculated from the ethylene gas-transfer coefficient by multiplying the latter by an experimentally determined coefficient ratio for oxygen and ethylene. This coefficient ratio is the ratio of the rate at which oxygen absorbs into a body of water and the rate at which ethylene desorbs from the same body.

$$C = \frac{K_a}{K_E} \quad (4)$$

where *K_a* is the oxygen gas-transfer coefficient,
K_E is the ethylene gas-transfer coefficient, and
C equals 1.15.

All reaeration and ethylene-gas-transfer coefficients presented in this paper are given to the base *e* (natural logarithm base, *e* = 2.7183).

Hydraulic Measurements

Streamflow was measured by the current-meter method (Rantz and others, 1982) at each end of the two reaches studied. Average stream width was determined by averaging widths measured at approximately 300-m intervals along each reach. The width at each point was measured with an optical range finder. Average stream velocity was determined by tracing the speed of the rhodamine-WT dye through the reach. Average depth of the reach was determined by dividing the average streamflow by the product of average velocity and average stream width.

RESULTS AND DISCUSSION

A summary of the data collected is presented in table 2. No major problems were experienced in using the modified gas-tracer technique at the large streamflows present during the study. The ethylene-injection apparatus was capable of diffusing sufficient quantities of gas for successful use of the method. Peak concentrations of ethylene at the sampling locations ranged from 13.8 to 28.8 µg/L at the

upstream cross section and 3.2 to 15.9 µg/L at the downstream cross section. These concentrations are well above the detection limit on most gas chromatographs and are measured easily.

Several minor problems, however, were experienced during the measurements. First, the tracers were not mixed laterally at the upstream sampling cross section of the reach near Lafayette. Percentage mixing (as defined in Yotsukura and Cobb, 1972) was approximately 56 percent for the November 1981 measurement and 73 percent for the July 1982 measurement. Lack of complete lateral mixing has the potential for being a common problem when using the modified tracer technique on large rivers. In the reach near Lafayette, tradeoffs had to be made between placing the diffusers in locations of sufficient depth with good mixing characteristics and allowing access to boat traffic on the river. Discharge weighted (average) concentrations were calculated by the procedure described by Yotsukura and Cobb (1972) to adjust for the poor mixing. Dividing the injection point into sections of equal flow and placing one diffuser rack in each section would improve mixing and help to solve this problem.

A second problem experienced was considerable scatter in the concentrations of the tracers at the upstream sampling cross sections. This problem was observed with the rhodamine-WT dye and ethylene but was most pronounced with the dye. Because of the scatter in concentrations observed in the reaches near Lafayette and Terre Haute, discernment of the peak tracer concentrations was difficult. The cause of the scatter is unknown. A previous investigator (Rathbun, 1979) reported problems with gas-regulating valves freezing at high flow rates (greater than 40 g/min). During the injections into the Wabash River, the regulating valves became thickly coated with frost. However, the flowmeters indicated that a constant flow of gas was entering the plastic tubing, and the high flow rate was not difficult to maintain. Likewise, except for a brief failure of one dye pump during the October 1981 measurement in the reach near Terre Haute, the flow rate of the dye did not fluctuate. Because of the width of the river, large lengths of plastic tubing (as much as 150-200 m) were needed to transport the tracers from the bank to the diffusers in the river. Because plastic tubing was used to inject the gas and the dye, the scatter at the upstream cross section could be related to the use of this tubing, possibly due to fluctuations in the pressure gradients across the length of the tubing. Another possibility is uneven longitudinal mixing due to unsteady flow in the river.

The mean tracer concentrations at the upstream cross section were estimated by taking the mean of all

Table 2. Summary of data collected during measurements of reaeration on the Wabash River
[All analyses and measurements by U. S. Geological Survey]

Reach	Date	Peak ethylene concentration (µg/L)		Peak dye concentration (µg/L)		Time of travel between upstream and downstream dye peaks ⁴ (min)	Streamflow (m ³ /s)		Area of time-dye concentration curve (min-µg/L) ¹	
		At upstream		At downstream			At upstream		At downstream	
		cross section ²	cross section ³	cross section ²	cross section ³		cross section ⁵	cross section ⁶	cross section ⁵	cross section ⁶
Near Lafayette	11/18-19/81	13.8 ± 1.4	5.4 ± 0.1	47.9 ± 2.8	25.6 ± 0.5	850 ± 30 (14.2h)	98.3 ± 4.9	95.2 ± 4.8	5,640 ± 282	5,550 ± 111
	7/26-27/82	18.4 ± 2.4	3.2 ± 0.2	47.3 ± 2.9	18.4 ± 0.3	985 ± 15 (16.4h)	64.9 ± 3.3	65.7 ± 3.3	5,830 ± 340	5,550 ± 112
Near Terre Haute	10/21-22/81	28.8 ± 1.9	15.9 ± 0.3	43.7 ± 2.2	27.8 ± 0.6	555 ± 30 (9.3h)	206 ± 10.3	213 ± 10.6	6,040 ± 300	4,820 ± 240
	8/25-26/82	25.2 ± 2.3	6.3 ± 0.1	33.5 ± 1.0	14.9 ± 0.3	820 ± 20 (13.7h)	91.5 ± 4.6	98.6 ± 4.9	4,350 ± 109	3,410 ± 71

¹Min-µg/L is the measurement unit obtained by determining the area under a time-concentration curve when time is measured in minutes and concentration in µg/L.

²Confidence intervals were calculated at the 95-percent level from replicate measurements and the confidence interval for a mean value formula (Walpole and Meyers, 1978, p. 189).

³The peak value was estimated by fitting a surface-response function to the observed data and solving for the maximum value. Confidence intervals were estimated by calculating the 95-percent confidence limits for the mean value of the surface-response function at the time of the peak.

⁴Confidence intervals were assumed to be plus or minus the sum of the sampling frequencies of the upstream and downstream cross section; h, hour.

⁵Confidence intervals were figured subjectively on the basis of the number of verticals measured, the uniformity of the cross section, and the steadiness of the flow in the cross section. (See Rantz and others, 1982, p. 179-183.)

⁶Confidence intervals were estimated by calculating the areas of the time-dye concentration curve with the minimum and maximum errors of the dye measurements.

data collected on the "plateau" of the time concentration curve. The plateau is the flat, equilibrium level of concentration of a tracer reached after a period of constant injection. The tracer curves at the upstream cross section approximate a square wave owing to the 2-hour injection time and the short time of travel between the injection point and the sampling location. Error due to the scatter can be minimized by taking a large number of samples during passage of the tracers. An example of the scatter and the method used to estimate the peak tracer concentrations is shown in figure 4.

The dye-loss correction factors for the measurements in the reach near Lafayette were 1.02 and 1.04. This means that 96 to 98 percent of the rhodamine-WT dye measured at the upstream cross section also was measured at the downstream cross section. The recovery percentages for the measurements in the reach near Terre Haute were not as high. Dye-loss correction factors for this reach were 1.21 and 1.18 (83–85 percent recovery). The reason for the loss of dye between the two sampling cross sections in the reach near Terre Haute is not known.

To estimate quantities of ethylene gas needed in a specific application of the modified gas-tracer technique, it is necessary to know the efficiency of the gas-injection apparatus, which cannot be measured directly. However, the efficiency can be estimated on the basis of the ratio of the measured and

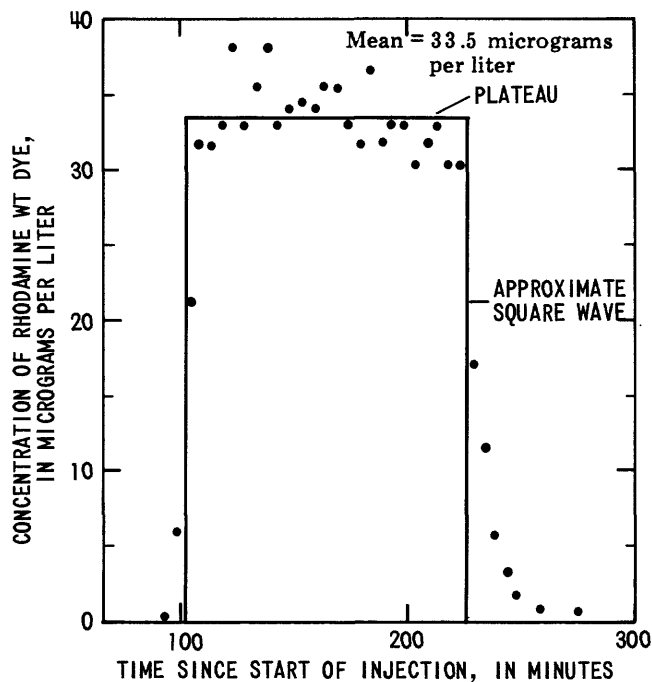


Figure 4. Example of scatter observed in the time tracer concentration curves at the upstream cross section. Data are from the measurement in the reach near Terre Haute, August 25 to 26, 1982.

maximum theoretical concentration of ethylene in the plateau for the upstream cross sections. The maximum theoretical concentration of ethylene in the plateau was determined by assuming that 100 percent of the gas was absorbed into the water at the injection site and that longitudinal dispersion was zero. This concentration was calculated by dividing the rate of gas injection by the streamflow and adjusting for loss of gas to the atmosphere between the injection point and the upstream cross section. Rate of gas loss was assumed to be the same as that measured between the sampling cross sections; for example, the maximum theoretical concentration of ethylene in the plateau for the November 1981 measurement in the reach near Lafayette was $(362.5\text{g/min}) (10^6 \mu\text{g/g}) / (5.89206 \times 10^6 \text{minutes}^{-1}) (e^{(-3.901 \times 10^{-4} \text{minutes}^{-1})(60\text{min})})$ or $60.1 \mu\text{g/L}$.

Estimates of gas-injection efficiencies are shown in table 3. Correlation $r = 0.99$ between the estimates and the depth of the water overlying the diffusers is good and may be expressed as

$$E = 18.6 D + 1.3, \quad (5)$$

where E is the estimate of gas-injection efficiency, in percent, and D is the depth of the water overlying the gas diffusers, in meters.

The efficiency of the Zimpro flat-plate diffusers in the configuration used for this study (fig. 2) was higher than that of the Norton tube diffusers used by previous investigators (Bauer and others, 1979; Rathbun and Grant, 1978). Rathbun (1979) estimated the efficiency of the Norton diffusers to be from 7.5 to 30 percent.

Calculation of Reaeration Coefficients

Reaeration (oxygen gas-transfer) coefficients for the Wabash River are presented in table 4. The ethylene-gas-transfer coefficients were converted to the oxygen gas-transfer coefficients by multiplying them by the coefficient ratio for oxygen and ethylene. This ratio, 1.15 ± 0.0226 (2 percent) at the 95 percent confidence limit, was determined experimentally by Rathbun and others (1978). For comparison between measurements at different stream temperatures, the oxygen gas-transfer coefficients were adjusted to a common temperature (20°C). Temperature was adjusted by the following equation (Elmore and West, 1961):

$$Ka_{20} = Ka_T (1.0241)^{20-T}, \quad (6)$$

where Ka_{20} is the oxygen gas-transfer coefficient at 20°C , in day^{-1} ,

Table 3. Estimates of efficiencies of ethylene-injection for reaeration measurements in the Wabash River

Reach	Date of measurement	Rate of ethylene injection (g/min)	Maximum theoretical concentration of ethylene in the plateau (µg/L)	Concentration of ethylene in the plateau calculated from field data (µg/L)	Temperature of water (°C)	Depth of gas diffusers below water surface (m)	Estimate of efficiency of ethylene injection ¹ (percent)
Near Lafayette - - - - -	11/18-19/81	362.5	60.1	13.8	9.0	1.2	0.23
	7/26-27/82	490.0	118.7	18.4	28.0	.8	.16
Near Terre Haute - - - - -	10/20-21/81	580.0	44.9	28.8	14.0	3.4	.64
	8/25-26/82	362.5	59.9	25.2	23.5	2.1	.42

¹ Ratio of measured and maximum theoretical concentration in the plateau.

Ka_T the oxygen gas-transfer coefficient at T°C, in day⁻¹,
 T is the stream temperature, in degrees Celsius, and
 1.0241 is the conversion factor.

Elmore and West (1961) did not publish a confidence limit for the conversion factor (1.0241). However, by using their published data, the author calculated a value of 1.0241 ± 0.0010 at the 95-percent confidence limit.

Also included in table 4 is a subjective confidence limit determined from errors in the concentrations of ethylene and rhodamine-WT, time of travel, streamflow, and the time-dye concentration curves. This confidence limit is based on the largest change in the computed ethylene-gas-transfer coefficient, where all variables differ by the maximum amount in such a way that all errors are additive. The confidence limits reported here, in essence, represent the entire possible range that the reaeration coefficient could fall between.

The reader should be aware that reaeration measurements on large rivers are quite sensitive to measurement errors in the tracers because reaeration

rates are low (Nobuhiru Yotsukura, written commun., 1982). This condition can be illustrated by considering the general form of the exponential decay equation used to estimate K_E in the modified tracer technique:

$$C_T = C_0 \exp(-kT), \quad (7)$$

where C_T is the concentration at time T,
 C_0 is the concentration at time zero,
 k is the decay coefficient, and
 T is the time.

(Eq 1 can be derived from this general form by substituting E_U/D_U for C_0 and $E_D/(D_D \times DCF)$ for C_T and solving for k .) Differentiating C with respect to k yields

$$\frac{dC}{dk} = -CT. \quad (8)$$

If the right hand side of equation 8 is rearranged and multiplied by k/k then the following relation can be developed:

Table 4. Experimentally determined reaeration coefficients for reaches of the Wabash River near Lafayette and near Terre Haute

Reach	Date of measurement	Oxygen-gas-transfer coefficient (day ⁻¹ at 20°C)		
		Best estimate	Upper confidence limit ¹	Lower confidence limit ¹
Near Lafayette - - - - -	11/18-19/81	0.8	1.5	0.3
	7/26-27/82	1.2	1.9	.7
Near Terre Haute - - - - -	10/20-21/81	1.1	2.6	<.1
	8/25-26/82	1.4	2.0	.8

¹Includes errors in the coefficient ratio for oxygen and ethylene and the temperature-conversion factor, as well as in measurements listed in table 2.

$$\frac{dC}{C} = kT \frac{dk}{k} \quad (9)$$

The measurement error of concentration, dC/C , is shown to be related to the estimate of error of the decay coefficient, dk/k , by the nondimensional number, kT (assuming that eq 7 is the correct model). Where kT is less than 1, concentration measurement errors result in larger errors in the estimate of k . The nondimensional $K_E (T_D - T_U)$ is shown to be 0.33 to 0.39 for the high-flow measurements and 0.80 to 0.82 for the low-flow measurements in an analysis of the Wabash River data. Thus, cumulative measurement errors in E_U , E_D , D_U , D_D , and DCF result in estimates of errors in K_E that are 1.25 to 3 times the cumulative measurement errors. This is the principal reason that the confidence limits for the estimated reaeration coefficients are so much larger than the individual measurement errors.

Comparison of Measured Reaeration Coefficients and Predictive Equations

The reaeration coefficients measured for the two reaches of the Wabash River were compared to various conceptual, empirical, and semiempirical predictive equations in the literature. Reaeration and the various predictive equations are discussed in Bennett and Rathbun (1972) and in Rathbun (1977). The conceptual equation used in the comparison was developed by O'Connor and Dobbins (1958). Its form is

$$K = 3.73U^{0.5}/H^{1.5}, \quad (10)$$

where U is the average reach velocity, in meters per second,
 H is the average reach depth, in meters; and
 K is reaeration coefficient, in day^{-1} at 20°C .

The empirical equations used were

$$K = 5.01 U^{0.969}/H^{1.673} \quad (\text{Churchill and others, 1962}), \quad (11)$$

$$K = 6.92 U^{0.67}/H^{1.85} \quad (\text{Owens and others, 1964}), \quad (12)$$

$$K = 5.13U/H^{1.33} \quad (\text{Langbein and Durum, 1967}), \quad (13)$$

$$K = 4.75 U/H^{1.5} \quad (\text{Isaacs and Gaudy, 1968}), \quad (14)$$

and

$$K = 5.58 U^{0.607}/H^{1.689} \quad (\text{Bennett and Rathbun, 1972}). \quad (15)$$

The semiempirical equations used were

$$K = 0.00217 U^{2.695}/H^{3.085} S^{0.823} \quad (\text{Churchill and others, 1962}), \quad (16)$$

$$K = 185.4 (US)^{0.5}/H \quad (\text{Cadwallader and McDonnell, 1969}), \quad (17)$$

$$K = 32.8 U^{0.413} S^{0.273}/H^{1.408} \quad (\text{Bennett and Rathbun, 1972}), \quad (18)$$

and

$$K = 1260 S U \quad (\text{Tsivoglou and Wallace, 1972}), \quad (19)$$

where S is the slope of the energy gradient, in meter per meter.

A comparison of the measured and predicted reaeration coefficients for the reaches of the Wabash River near Terre Haute and near Lafayette is presented in table 5. Predictions of reaeration obtained by the equations used in this comparison were much better in the reach near Terre Haute than in that near Lafayette. Although these equations tended to underestimate reaeration in the Terre Haute reach, predicted reaeration was within the possible range for the measured values. Of the 10 predictive equations, 9 (eqs 10–18) greatly overestimate reaeration measured in the reach near Lafayette. All but two of the equations (17, 19) predicted values of reaeration outside the confidence limits; the two exceptions are the semiempirical equations proposed by Cadwallader and McDonnell (1969) and Tsivoglou and Wallace (1972).

The lack of close agreement of the Wabash River data and that obtained by the predictive equations is not surprising. Most of the equations were developed by linear-regression analysis. The most commonly used of these contain only the terms velocity and depth. A reaeration coefficient obtained for a stated width and depth from one of the equations represents an estimate of the average reaeration coefficient that would be expected if reaeration were measured for a large number of streams with similar widths and depths. In a statistical sense, the coefficient is the mean expected for the sampling distribution and does not necessarily represent the mean reaeration expected for the stated hydrologic conditions in a specific stream. Confidence limits for the mean value expected and the range in discrete values expected are quite large if considerable error in measurement or scatter in the data used to develop the regression equation is present.

The large confidence limits can be illustrated by examining one of the common predictive reaeration equations. Bennett and Rathbun (1972) used data reported by O'Connor and Dobbins (1958), Churchill, Elmore, and Buckingham (1962), Owens, Edwards, and Gibbs (1964), and Tsivoglou (1967) to develop a predictive equation. Because this equation

Table 5. Measured reaeration coefficients and those determined by conceptual, empirical, and semi-empirical predictive equations for the reaches of the Wabash River near Lafayette and near Terre Haute [Reaeration coefficients (day^{-1} at 20°C , base e)]

Reach	Date	Measured	Conceptual equations		Empirical equations			
			O'Connor and Dobbins (1958)	Churchill, Elmore, and Buckingham (1962)	Owens, Edwards, and Gibbs (1964)	Langbein and Durum (1967)	Isaacs and Gaudy (1969)	Bennett and Rathbun (1972)
Near Lafayette	11/18-19/81	0.8	1.8	1.8	2.2	2.0	1.8	2.4
	7/26-27/82	1.2	2.5	3.6	3.1	2.4	2.2	3.4
Near Terre Haute	10/21-22/81	1.1	.9	.8	.9	1.1	.9	1.1
	8/25-26/82	1.4	1.2	1.0	1.2	1.1	1.0	1.4
Average absolute prediction error (percent)			66	95	91	68	64	96

Reach	Date	Measured	Semi-empirical equations				Average absolute prediction error for all equations (percent)
			Churchill, Elmore, and Buckingham (1962)	Cadwallader and McDonnell (1969)	Bennett and Rathbun (1972)	Tsivoglou and Wallace (1972)	
Near Lafayette	11/18-19/81	0.8	3.1	1.2	1.5	1.0	135
	7/26-27/82	1.2	4.4	1.4	2.0	.9	121
Near Terre Haute	10/21-22/81	1.1	.9	.7	.7	1.0	18
	8/25-26/82	1.4	.8	.8	1.0	1.0	25
Average absolute prediction error (percent)			154	37	55	22	

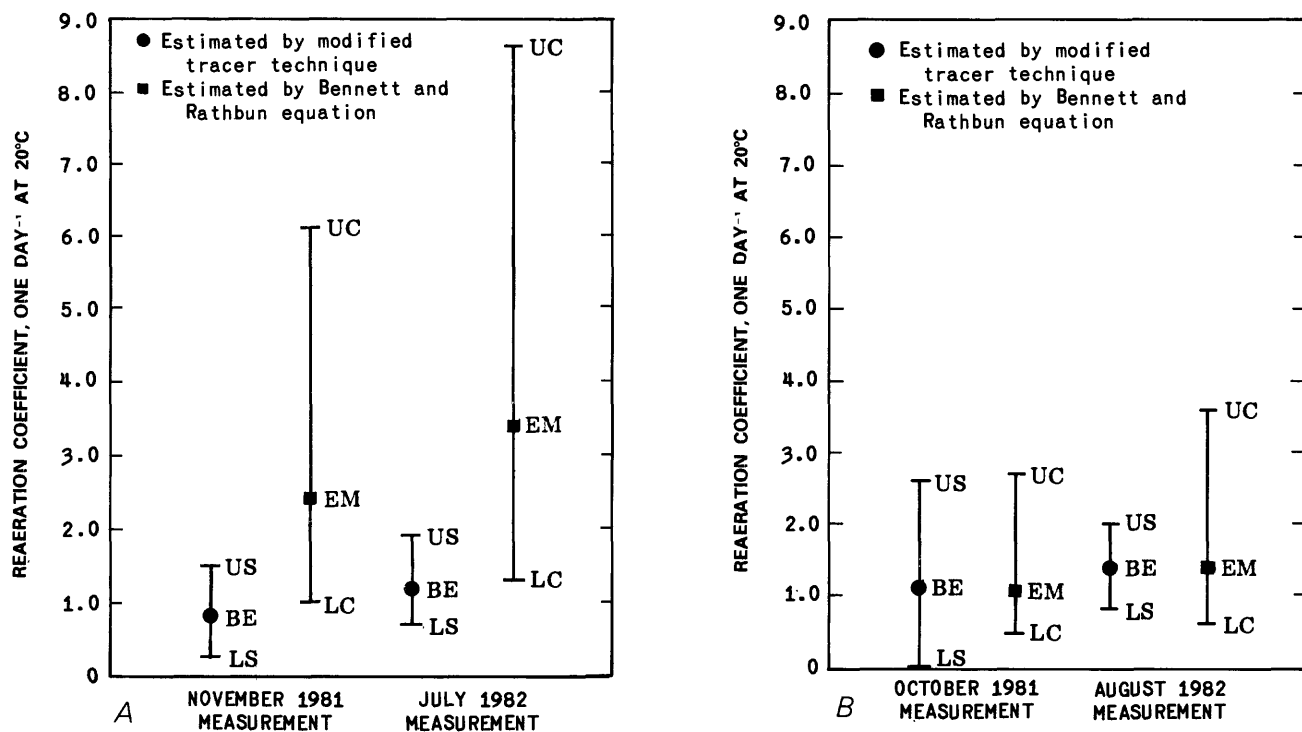
was based on the combined data of these investigators, it encompasses a much wider range of hydrologic conditions than any of the equations proposed by the individual investigators. A comparison of reaeration coefficients and their confidence limits estimated for reaches of the Wabash River near Lafayette and Terre Haute by the modified tracer technique and the Bennett and Rathbun equation are given in figures 5A and 5B. Confidence limits for the range in discrete values expected are shown for the Bennett and Rathbun equation. The confidence limits for reaeration predicted by the Bennett and Rathbun equation are large and overlap the confidence limits estimated for the measured values. The reader is referred to Walpole and Meyers (1978, p. 329-331) for a discussion of the confidence limits for linear-regression equations.

Even with the error inherent in the modified gas-tracer technique when used for large streamflows, confidence limits around estimates of reaeration are much smaller than corresponding estimates from predictive equations.

SUMMARY

The modified gas-tracer technique was used to measure reaeration coefficients in the Wabash River near Lafayette and Terre Haute, Indiana, at streamflows ranging from 65 to $210\text{m}^3/\text{s}$. The measurements were done in cooperation with the Indiana State Board of Health as part of a series of studies to determine the waste assimilative capacity of the middle Wabash River basin.

Chemically pure grade ethylene was used as the tracer gas, and rhodamine-WT dye was used as the dispersion-dilution tracer. Ethylene was bubbled into the water at rates of 362.5 to 580 g/min through a series of 20 to 32 porous flat-plate diffusers. Each diffuser was 1.05 m long and 75 mm wide, and its average pore size was from 1.5 to 2.0 μm . The gas was released into the diffusers from high-pressure cylinders through two-stage regulating valves. The rhodamine-WT dye was injected into the river by pumps operated by 12-volt batteries at rates ranging from 500 to 2,200 mL/min.



EXPLANATION

- BE Best estimate of the reaeration coefficient
- US Upper subjective confidence limit
- LS Lower subjective confidence limit
- EM Mean reaeration coefficient expected
- UC Upper 95 percent confidence limit
- LC Lower 95 percent confidence limit

Figure 5. Reaeration coefficients and their confidence limits estimated by the modified tracer technique and the Bennett and Rathbun equation for reaches of the Wabash River. A, Near Lafayette. B, Near Terre Haute.

The ethylene-injection apparatus used was capable of diffusing sufficient quantities of gas for successful use of the method at the large streamflows in the Wabash River during the study. Peak concentrations of ethylene at the sampling location ranged from 13.8 to 28.8 $\mu\text{g/L}$ at the upstream cross section and 3.2 to 15.9 $\mu\text{g/L}$ at the downstream cross section. These concentrations are well above the detection limit of most gas chromatographs and are measured easily.

Injection efficiencies for the ethylene were estimated to range from 16 percent, when the diffusers were submerged in only 0.8 m of water, to 64 percent, when the diffusers were submerged in 3.4 m of water. The efficiency was highly correlated with the depth of the overlying water.

Several minor problems were experienced in applying the modified gas-tracer technique to the Wabash River. First, lack of lateral mixing was observed during the two measurements at the upstream

sampling cross section of the reach near Lafayette. Second, considerable scatter was observed in the data collected at the upstream sampling cross section of both reaches near Lafayette and Terre Haute.

A high rate of dye loss was observed during both measurements in the reach near Terre Haute. Only 83 to 85 percent of the dye measured at the upstream cross section was measured at the downstream cross section. In contrast, the loss was not observed in the reach near Lafayette where 96 to 98 percent of the dye measured at the upstream cross section was measured at the downstream cross section.

Reaeration coefficients measured at a 29.7-km-long reach near Lafayette were 1.2 and 0.8 per day at 20°C at streamflows of 65 and 97 m^3/s . Reaeration coefficients measured at a 21.8-km-long reach near Terre Haute were 1.4 and 1.1 per day at 20°C at streamflows of 95 and 210 m^3/s . None of the common equations found in the literature predicted

reaeration coefficients similar to those measured for both reaches of the Wabash River near Lafayette and Terre Haute.

The modified gas-tracer technique is a feasible method for measuring reaeration coefficients at streamflows up to 200 m³/s. Confidence limits around measured reaeration coefficients were substantially smaller than coefficients predicted from commonly used equations in the literature.

REFERENCES CITED

- Bauer, D. P., Rathbun, R. E., and Lowham, H. W., 1979, Traveltime, unit concentration, longitudinal-dispersion, and reaeration characteristics of the upstream reaches of the Yampa and Little Snake River, Colorado and Wyoming: U.S. Geological Survey Water-Resources Investigations 78-122, 66 p.
- Bennett, J. P., and Rathbun, R. E., 1972, Reaeration in open channel flow: U.S. Geological Survey Professional Paper 737, 75 p.
- Cadwallader, T. E., and McDonnell, A. J., 1969, A multivariate analysis of reaeration data: *Water Research*, v. 3, p. 731-742.
- Churchill, M. A., Elmore, H. L., and Buckingham, R. A., 1962, The prediction of stream reaeration rates: American Society of Civil Engineers Proceedings, *Journal of the Sanitary Engineering Division*, v. 88, no. SA-4, p. 1-46.
- Elmore, W. L., and West, W. F., 1961, Effect of water temperature on stream reaeration: American Society of Civil Engineers Proceedings, *Journal of the Sanitary Engineering Division*, v. 87, no. SA-6, p. 59-71.
- Issacs, W. P., and Gaudy, A. F., 1968, Atmospheric oxygenation in a simulated stream: American Society of Civil Engineers Proceedings, *Journal of the Sanitary Engineering Division*, v. 94, no. SA-2, p. 319-344.
- Langbein, W. B., and Durum, W. N., 1967, The aeration capacity of streams: U.S. Geological Survey Circular 542, 6 p.
- O'Connor, D. J., and Dobbins, W. E., 1958, Mechanism of reaeration in natural streams: American Society of Civil Engineers Transactions, v. 123, p. 641-684.
- Owens, M., Edwards, R. W., and Gibbs, J. W., 1964, Some reaeration studies in streams: *International Journal of Air and Water Pollution*, v. 8, no. 819, p. 469-486.
- Rantz, S. E., and others, 1982, Measurement and computation of streamflow—Measurement of stage and discharge: U.S. Geological Survey Water-Supply Paper 2175, v. 1, 284 p.
- Rathbun, R. E., 1977, Reaeration coefficients of streams—State of the art: American Society of Civil Engineers Proceedings, *Journal of Hydraulics Division*, v. 103, no. HY-4, p. 409-424.
- 1979, Estimating the gas and dye quantities for modified tracer technique measurements of stream reaeration coefficients: U.S. Geological Survey Water-Resources Investigations 79-27, 42 p.
- Rathbun, R. E., and Grant, R. S., 1978, Comparison of the radioactive and modified techniques for measurement of stream reaeration coefficients: U.S. Geological Survey Water-Resources Investigations 78-68, 57 p.
- Rathbun, R. E., Shultz, D. J., and Stephens, D. W., 1975, Preliminary experiments with a modified tracer technique for measuring stream reaeration coefficients: U.S. Geological Survey Open-File Report 75-256, 36 p.
- Rathbun, R. E., Stephens, D. W., Shultz, D. J., and Tai, D. Y., 1978, Laboratory studies of gas tracers for reaeration: American Society of Civil Engineers Proceedings, *Journal of the Environmental Engineering Division*, v. 104, no. EE-1, p. 215-229.
- Shultz, D. J., Pankow, J. F., Tai, D. Y., Stephens, D. W., and Rathbun, R. E., 1976, Determination, storage, and preservation of low molecular weight hydrocarbon gases in aqueous solution: U.S. Geological Survey *Journal of Research*, v. 4, no. 2, p. 247-251.
- Tsivoglou, E. C., 1967, Tracer measurement of stream reaeration: Federal Water Pollution Control Administration Report, 86 p.
- Tsivoglou, E. C., and Wallace, J. R., 1972, Characterization of stream reaeration capacity: U.S. Environmental Protection Agency Report no. EPA-R3-72-012, 317 p.
- Walpole, R. E., and Meyers, R. N., 1978, Probability and statistics for engineers and scientists (2d ed.): New York, MacMillan and Co., 580 p.
- Wilson, J. F., 1968, Fluorometric procedures for dye tracing: U.S. Geological Survey Techniques of Water-Resources Investigations, Book 3, Chapter A12, 31 p.
- Yotsukura, Nobuhiro, and Cobb, E. E., 1972, Transverse diffusion of solutes in natural streams: U.S. Geological Survey Professional Paper 582-C, 19 p.

Performance of Sodium as a Transport Tracer— Experimental and Simulation Analysis

By Kenneth E. Bencala

Abstract

As part of a field solute-transport experiment, sodium was injected along with chloride and strontium into a mountain pool-and-riffle stream. Based on comparisons with the chloride and strontium transport, sodium was determined to be a potentially useful, although somewhat nonconservative, tracer. Three simulations of the sodium concentrations were obtained by using different assumptions as to the degree to which sodium was nonconservative. The simulation of sodium as conservative was typically a good reproduction of the timing of the sodium arrival, peak, and tail. The simulations of sodium as nonconservative provided somewhat closer approximations of the measured concentration values. The conservative simulation was based on stream parameters determined from the chloride transport. The reactive simulation was based on additional stream-sediment parameters determined from the strontium transport and on the chemical properties of sodium.

INTRODUCTION

Simulations of solute transport require that several physical parameters be specified; exactly which parameters are to be specified is a function of the model used. One method of determining such parameters is by calibration against a conservative solute in the stream. This is a particularly useful method if the predominant interest in the modeling exercise is in the simulation of a nonconservative solute. When the conservative transport submodel has been calibrated, then reactive submodels may be used to study chemical interactions in the system (Valocchi and others, 1981; Chapman, 1982; Bencala, 1983; Jackman and others, 1984). Under certain conditions, a tracer, which is not ideally conservative, may be treated usefully as conservative. This has been demonstrated by Chapman (1982).

Chapman (1982) obtained reliable simulations by treating sodium as a conservative tracer in the study of speciation of nonconservative chemical reactants in rivers. It generally is understood that the alkali metals are sorbed into clay minerals via ion

exchange (Rose and others, 1979). Chapman recognized the possibility of sodium exchange and noted that the simulation result "suggests that a slight attenuation might be occurring." Transport data obtained in South Carolina streams by Sharp (1974) suggested similar behavior. Because of the treatment of sodium as a conservative solute, the nature of its nonconservative properties should be investigated, and methods for simulating such properties should be suggested. The evaluation of chemical tracers for transport studies is becoming increasingly important as tracers are used in connection with evaluations of reactive systems in addition to traditional dilution, time of travel, or dispersion studies. As an example, Bencala and others (1983) have demonstrated limitations of rhodamine-WT dye in a study of transport and sorption in a mountain stream.

In this paper, experimental data and simulation analyses from the injection of solutes into a natural channel will be presented. The details of the field experiment and the simulation development have been described in previous reports, and, therefore, only brief outlines of this background information will be discussed here. The chloride data and the conservative solute-transport model were presented in Bencala and Walters (1983). The reactive submodel used for nonconservative solutes was published in Bencala and others (1983). The strontium data and the application of the coupled transport and reactive submodels were discussed in Bencala (1983).

Acknowledgments

The majority of the chemical data used in this paper first appeared in Zand and others (1976). Tabular summaries of these and other data were made available by G. W. Zellweger and R. J. Avanzino. The data from Uvas Creek were obtained under the direction of V. C. Kennedy in cooperation with S. M. Zand. The complete compilation of information on this experiment is available in the data report of Avanzino and others (1984). Assistance with the

field sampling was provided by J. W. Ball, D. W. Brown, J. M. Burchard, C. D. Cavit, R. V. James, E. A. Jenne, C. D. Ripple, J. Rubin, K. V. Slack, G. L. Smith, L. J. Tilley, and A. K. Worster. The author also benefitted from discussions with R. A. Walters (U.S. Geological Survey) and A. P. Jackman (University of California, Davis) regarding the results of their research on solute transport in Uvas Creek (Jackman and others, 1984).

Experimental Analysis

Zand and others (1976) described the steady injection of conservative and reactive tracers into Uvas Creek, Santa Clara County, California. Uvas Creek is a small mountain pool-and-riffle stream. The experiment occurred in late summer 1972 during a period of low flow ($0.0125 \text{ m}^3/\text{s}$). The pH of the stream was approximately 8. Chloride, strontium, and sodium tracers were injected at a steady rate for 3 hours. Solute concentrations were monitored at five stations in a 619 m reach. The locations of the sampling stations are shown in figure 1.

The comparative reactive properties of sodium and strontium relative to chloride are shown by the normalized tracer concentrations in figure 2. The concentrations of each component (fig. 2) have been normalized to their respective injection-level concentrations after accounting for background concentrations. (Normalized concentration is computed as observed minus background divided by injection level minus background. Injection-level concentration is

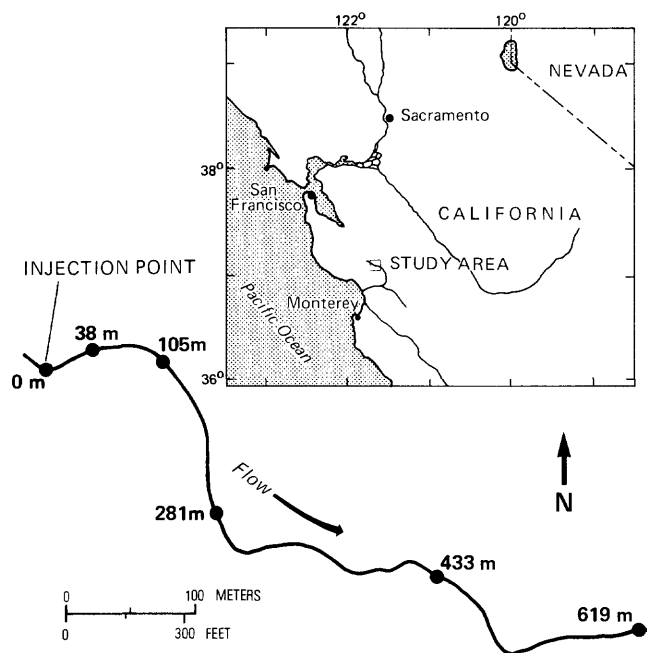


Figure 1. Location of Uvas Creek and monitoring stations. (From Bencala and Walters, 1983.)

the concentration measured in the stream several meters below a mixing reach at the point of injection.) The normalized concentrations show at the 619-m monitoring station that the chloride peak reached 50 percent of its relative injection concentration and that the sodium peak reached only 40 percent. At the other stations closer to the injection point, the sodium peak was not as strong as the chloride peak but always within 5 percent of it. Sorption is a significant process influencing strontium transport as is clearly shown by its normalized concentration at every location, relative to either the chloride or the sodium.

The processes of dilution, dispersion, and transient storage of solute all influence the attenuation of the chloride concentration. An interpretation of the role of these processes in determining solute transport in Uvas Creek may be found in Bencala and Walters (1983). Sorption onto the streambed sands and gravels further attenuates the strontium concentration (Bencala, 1983). Although the details of these processes are of interest, the points to be made with regard to the tracer properties of sodium can be made by considering the observed data and the known chemical properties of chloride and strontium. In Uvas Creek, chloride is assumed to be conservative (Kennedy and others, 1984), and strontium strongly sorbs onto streambed sediment.

The comparisons of chloride and strontium transport in this experiment are as follows: First, chloride was attenuated by dilution down to 50 percent. Additional sodium attenuation was only in the range of 5 to 10 percent, and the arrival of the leading edge, peak, and tail were well represented in the sodium data. Second, strontium was attenuated by a combination of physical and chemical processes down to a minimum level (at 619 m) of 10 percent. The difference between the sodium and strontium attenuations is appreciable at the 281-, 433-, and 619-m stations. Thus, sodium was approximately conservative, and its relative sorption was sufficiently low that it could be a useful tracer in transport studies involving sorption.

The concentration data from the stream serve as indirect evidence for the sorption of sodium onto the streambed sediment. Also, a limited amount of direct sediment desorption data illustrating the magnitude of the sodium sorption are available. The results presented in figure 3 show the relative sorption of sodium and strontium onto a range of sand- and gravel-sized sediment for two monitoring locations at 105 and 281 m. The details of sample collection and cation determination are given in Avanzino and others (1984); brief discussions are also in Bencala (1983), Bencala and others (1983), and Kennedy and others (1984). The initial sorbed cations before

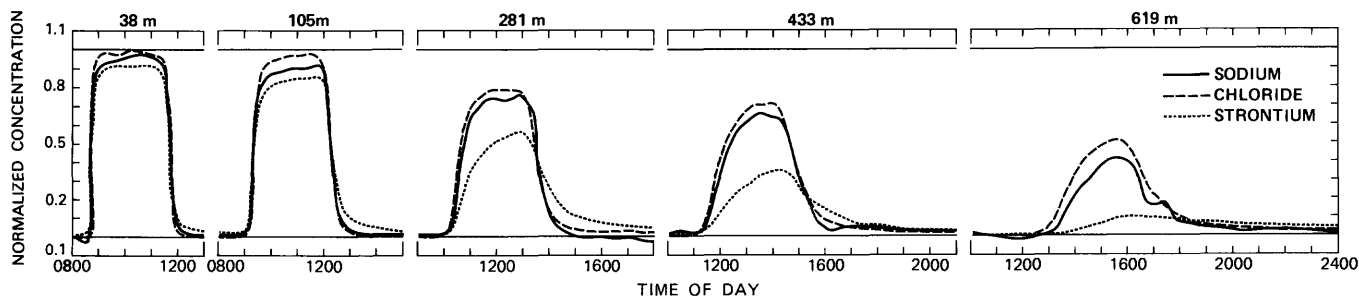


Figure 2. Observed tracer concentrations for steady injection at Uvas Creek. Injection started at 0830 and ended at 1130. Data are presented from this period until 2330 when rain began to fall. The data shown are for chloride, strontium, and sodium. The concentrations have been normalized to their respective injection-level concentrations after accounting for background concentrations.

the experiment and the amount of sorbed cations at a time later in the experiment are shown in figure 3 as bars and circles, respectively. A relative scale is used

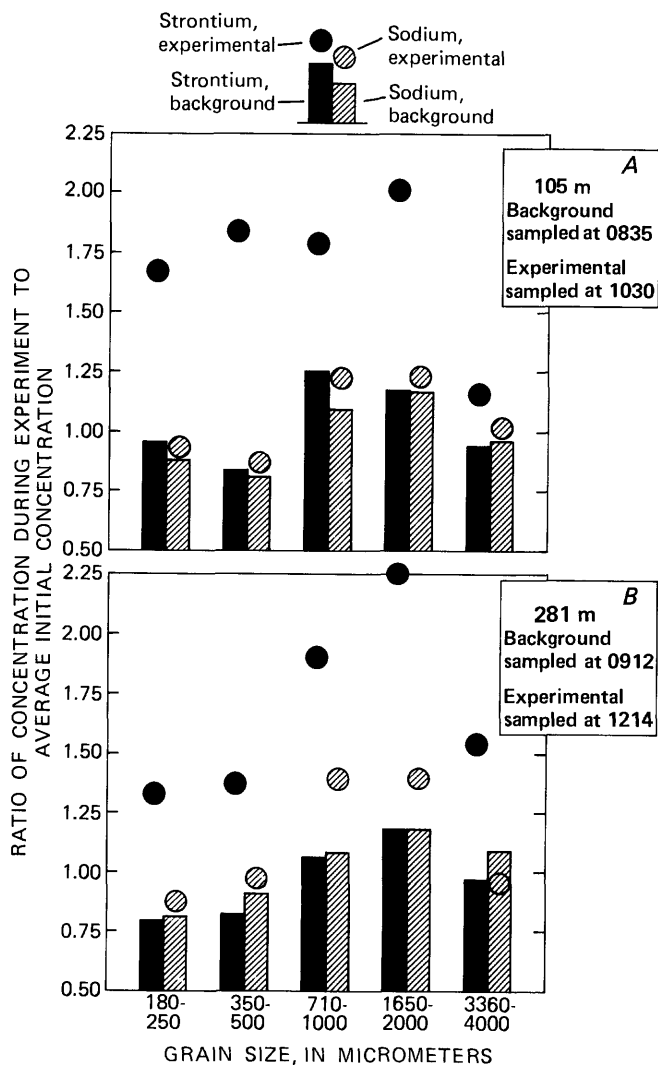


Figure 3. Sorption of sodium (Na) and strontium (Sr) onto streambed sands and gravels. A, Samples from station at 105 m. B, Samples from station at 281 m.

to allow comparisons of the five sizes of fractions and of sodium with strontium. On this scale, the strontium concentrations are increased by about a factor of two. The sorbed sodium concentrations are increased typically by a factor of less than 10 percent. Sorption of sodium clearly occurred to a lesser degree than sorption of strontium.

Sodium levels are attenuated by a combination of physical and chemical processes. Physical processes were of greater importance than chemical processes. For the purpose of this paper, the nature of the physical attenuation is not particularly relevant. However, if dilution by ground-water inflow was the dominant factor in the attenuation and if the solute concentrations in this inflow were considerably different from those at the head of the study reach, then the misinterpretation of the nature of the physical processes could lead to a further misinterpretation of the tracer properties of sodium. The nature of the physical attenuation is relevant to the simulation analysis presented later in this paper. With regard to the experimental analysis, the following two issues are of concern: The amount of ground-water inflow in the Uvas Creek study reach, and the spatial variability of background solute concentrations.

The relative roles of dilution and transient storage in the 3-hour injection at Uvas Creek were discussed by Bencala and Walters (1983). The interpretation presented in that report was that inflow over the study reach increased the flow by 12 percent. The remainder of the 50-percent chloride attenuation was accounted for by transient storage in the streambed gravels. This interpretation was consistent with the chloride concentration data from the leading edge, the peak, and, most importantly, the tail of the solute pulse. After a more intensive experiment in 1973, Kennedy and others, (1984) determined that, during a higher flow period (but still in the low-flow regime), "the discharge increase within the study reach due to ground-water inflow must

have been significantly less than 15 percent and probably was less than 10 percent.” Further, they conclude, “Care must be taken to assume that downstream dilution of tracer is not attributed to groundwater inflows when the dilution is the result of long-delayed underflow in the stream gravels.”

It is important to note the spatial consistency of the background concentrations of chloride, sodium, and strontium before the arrival of the injected pulse. Figure 4 shows normalized concentration data for the period up to the first arrival of the solute pulse at each of the five monitoring stations. The normalized scale has been defined above. A value of zero represents typical background. A value of 1 represents the injection-level concentration. On this normalized scale, the background chloride concentrations are within 0.01 unit of 0.0, and, with only a few exceptions, the sodium and strontium concentrations are within 0.02 unit of 0.0. No obvious patterns of spatial variability are evident in the background concentrations of any of the three tracers used in this experiment. Thus, the ground-water inflow, whatever its

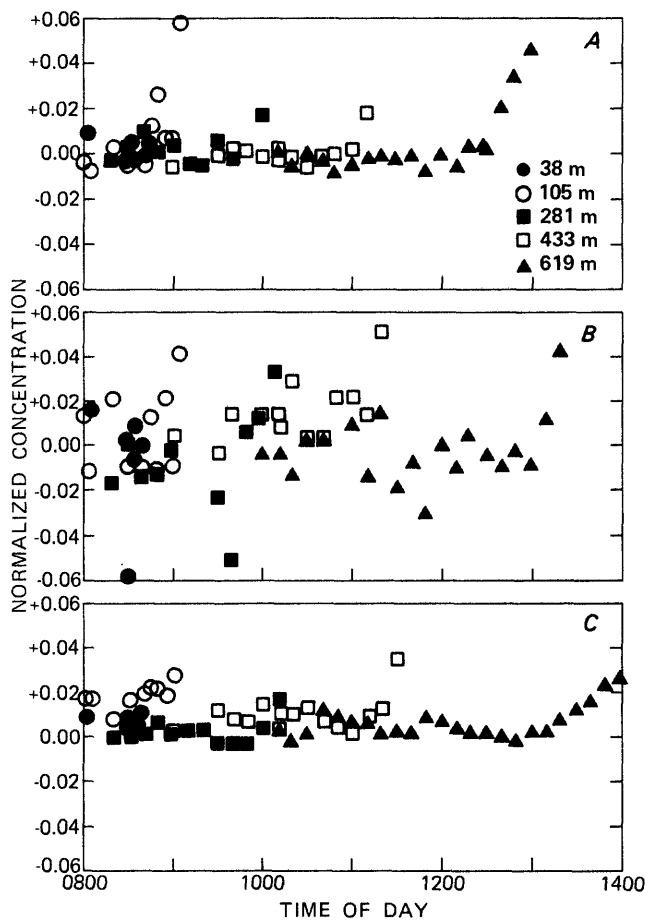


Figure 4. Observed background tracer concentrations for periods before arrival of tracer pulse. A, Chloride. B, Sodium. C, Strontium.

volumetric magnitude may have been, did not significantly alter the in-stream background concentrations of chloride, sodium, and strontium.

SIMULATION ANALYSIS

It is most convenient to think of the transport model as the composition of physical transport and reactive submodels. The simulation of a conservative tracer such as chloride requires the use of only the physical transport submodel. The simulation of a reactive tracer such as strontium requires the coupling of the reactive submodel to the physical transport submodel. The purpose of this section is to show the magnitude of the errors that result from considering sodium to be conservative and to suggest a reactive submodel for treating the (slight) reactive nature of the sodium.

The physical transport submodel is based on the standard one-dimensional convection-dispersion analysis. The “dead-zone” concept is included as a pseudotwo-dimensional, quasi-empirical mechanism for treating the observed transient storage of conservative solutes. With the dead-zone model, the hydrologic system is separated into the following two interacting compartments: The channel containing the flowing stream and the storage zones which mix with the stream channel water but have no longitudinal velocity. Bencala and Walters (1983) have shown that nonreactive solute transport in Uvas Creek can be simulated by the presence of expansive zones of water, which are either not moving or moving very slowly when compared to the bulk of the stream water. Solute mixing in and out of these storage zones results in the empirically observed transient storage of solute mass along the length of the stream. Other studies, in Uvas Creek (Kennedy and others, 1984), and in other streams (Sharp, 1974; Bencala and others, 1983) have suggested the importance of the role of the streambed gravel in this transient storage process. The transient storage mechanism is pseudotwo-dimensional because the inclusion of storage zones adds a transverse dimension. However, the full two-dimensional flow field is not considered. The mechanism is quasi-empirical because it describes uniform mixing in the storage zones, but spatial gradients will exist.

For each physical compartment, a reactive submodel is present. In the stream channel, solute sorption and desorption is treated by the first-order mass-transfer mechanism. Solute that enters storage has the potential for virtually continual contact with immobile bed materials. As a result, all reactive solute which enters a storage zone is assumed to be rapidly and permanently lost to the bed materials. The reac-

tive submodels, for the channel and for the storage zones, were discussed in detail in Bencala (1983). The basic description of the first-order mass-transfer model is that, as the chemical pulse passes a point along the stream channel, the solid-solution system is no longer in chemical equilibrium and, henceforth, mass (strontium, for example) transfers from the surrounding solution (the stream) to the solid (the streambed). The submodel for the storage zones is strictly an empirical sink term.

Figure 5 shows the simulation of sodium transport treated as a conservative solute. All parameter values are identical to those used in the "best-fit" chloride simulation (Bencala and Walters, 1983) with the exception of sodium-background concentration (12.3 mg/L), and sodium-injection concentration (16.4 mg/L). The simulation of the conservative tracer chloride has been adjusted only for the readily measured values of the sodium-background and injection-level concentrations. The chloride simulations were "curve-fit" to the observed chloride concentrations to estimate several "free parameters" of the system. No new free parameters have been introduced in the simulation of the sodium.

The simulation of sodium transport treated as a reactive solute following first-order mass transfer kinetics is also shown in figure 5. All parameter values are identical to those used in the best-fit strontium simulation (Bencala, 1983) with the exception of the two concentrations mentioned above and the measured value of the distribution coefficient.

In another sand and gravel stream bed, Little Lost Man Creek (Humboldt County, California), the distribution coefficient of rhodamine-WT dye was determined to be approximately 5 mL/g (Bencala and others, 1983). Typical distribution coefficients with streambed gravels in the White Oak Creek watershed, Tennessee, were determined by Cerling and Spalding (1982) for strontium, cobalt, and cesium to be 50.3,

564, and 8,460 mL/g, respectively. The distribution coefficient is a convenient indication of the amount of solute sorbed onto solids. It is defined as the ratio of the concentration on the solids to the concentration in the surrounding solution. The distribution coefficient for strontium sorbed onto sand and gravel in Uvas Creek is on the order of 10 to 100 mL/g (Bencala and others, 1983). The sodium-distribution coefficient (1.93 mL/g) is one or two orders of magnitude lower than the value for strontium.

The strontium simulations were curve-fit to the observed strontium concentrations to estimate several free parameters of the system in addition to those first estimated with the chloride simulations. All the physical system parameters estimated with the chloride simulations retained those values in the strontium and sodium simulations. Again, no new free parameters have been introduced in the simulation of the sodium.

Figure 6 shows sodium treated as a reactive solute with one free parameter relative to the chloride and strontium simulations. The free parameter chosen is the "accessible sediment density," or the mass of sediment available for sorption exposed to a cubic meter of solution. Of all the parameters in the simulations, this is least known. Accessible sediment density would be difficult to measure in the field. Figure 6 shows the sensitivity of the simulation results to a fivefold increase in this parameter relative to the reactive simulation results as shown in figure 5.

DISCUSSION

Comparisons with the chloride data show that strontium and sodium were attenuated in the stream, with only a small percentage of sodium attenuation in most of the stream. The sodium injection has been simulated as a conservative and a nonconserva-

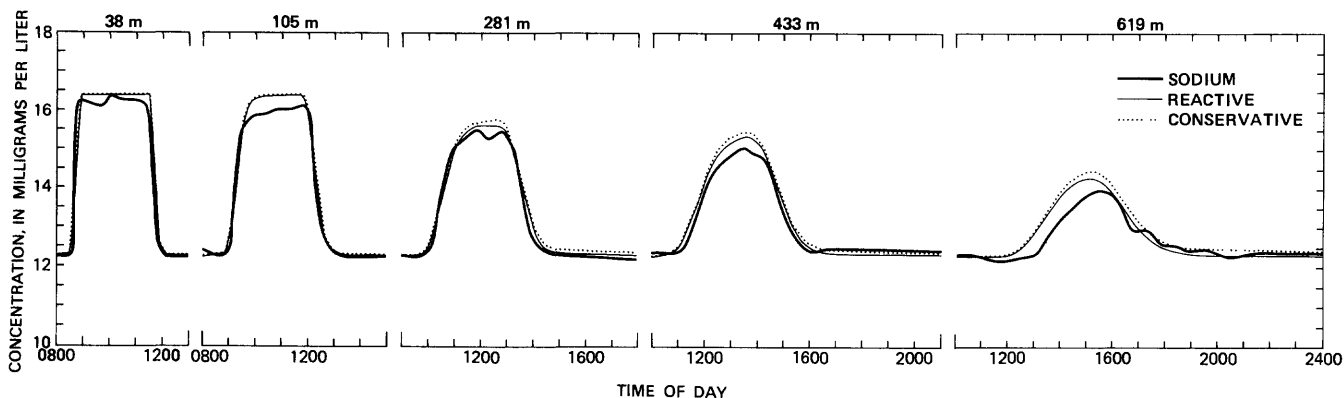


Figure 5. Observed sodium concentrations and simulations. Conservative simulation accounts for convection, dispersion, dilution, and transient storage. Reactive simulation includes sorption onto the streambed sands and gravels.

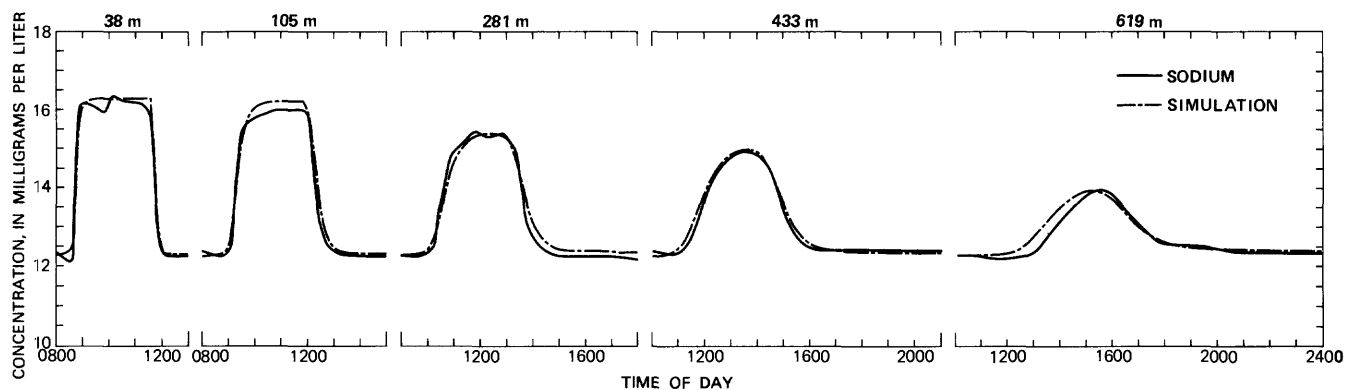


Figure 6. Observed sodium concentrations and simulations. To illustrate parameter sensitivity, concentrations are compared for simulations using the values of accessible sediment density as a free parameter. The values of accessible sediment density are five times the values used in the reactive simulation in figure 2.

tive solute. The differences between the simulations are not great; however, the nonconservative simulation does provide a better approximation to the data.

The relative concentration data from the field experiment show that a sodium attenuation of 5 to 10 percent (relative to chloride) was transported down the stream reach. The conservative simulation, however, shows that sodium would be an adequate conservative tracer for many purposes. For sodium transport in Uvas Creek, the proper interpretation of physical transport mechanisms is more important than consideration of chemical losses.

The kinetic first-order mass-transfer model for sorption of sodium provides a reasonable simulation of the data. With no additional free parameters, relative to the strontium simulation, the fit is "fair" and the improvement over the conservative model is only marginal. The sensitivity of the simulation to the accessible sediment density was quite weak. This parameter had to be increased fivefold to induce even a small change in simulation results. The reactive submodel is promising for use in modeling of sodium transport when the parameters will be calibrated based on the results of field experiment (Chapman, 1982). However, the lack of parameter sensitivity would indicate that sodium would be a weak choice as a tracer to define sorption properties and that it would probably be better used to define physical transport properties. Of course, just because one *can* improve the fit to the data, that in itself does not mean that one *should*. The "cost" of improving the fit is in the coupling of an additional submodel along with its associated parameters. The potential "benefit" of a closer fit will depend on the nature of the application. Finally, the field data must be of sufficient accuracy to warrant additional structure in the model.

One simulation improvement would be to alter the empirical sink term for the loss of all reactive

solute which enters a storage zone; however, we have no chemical data from the storage zones to indicate a more physically realistic submodel. The sensitivity of the overall strontium transport simulation to this submodel was discussed in Bencala (1983). In the strontium study, this term was not as important as the sorption to the streambed sediment. Similar sensitivity studies also have been completed for sodium.

The opposite extreme to assuming complete reaction in the storage zone is to assume no reaction in the storage zone. A 3-hour simulation experiment, which is not presented here, was performed with the assumption of no reaction in the storage zone. The differences in stream concentrations between this simulation and either of the simulations shown in figure 5 are only marginal.

In most "typical" tracer studies, sodium would not be a "better" or more cost-effective tracer than rhodamine-WT dye or chloride. However, situations exist in which sodium would be useful. In stream systems having a wide pH range, injection of sodium chloride and observation of the behavior of the cation sodium as well as the anion chloride may be beneficial. In an experiment designed to study chemical reactions, Chapman (1982) used sodium hydroxide to increase the pH of a stream, and, thus, sodium became the tracer. Calkins and Dunne (1970) described the use of sodium as a tracer for real-time field applications. They note that sodium can be measured with a sodium-ion probe and portable pH meter. This is inexpensive, light-weight equipment, well-suited for use in small mountain streams located in rough terrain. Finally, in complex hydrologic and chemical environments, multiple tracer injections may be used by injecting two tracers either in different locations or for different lengths of time. Because chloride and sodium appear to be two of the most useful tracers, it could be useful to "split" these tracers. Instead of using sodium chloride as one of the

injection salts, sodium bromide could be used as one tracer and lithium chloride as a second.

REFERENCES CITED

- Avanzino, R. J., Zellweger, G. W., Kennedy, V. C., Zand, S. M., and Bencala, K. E., 1984, Results of a solute transport experiment at Uvas Creek, September 1972: U.S. Geological Survey Open-File Report 84-236, 86 p.
- Bencala, K. E., 1983, Simulation of solute transport in a mountain pool-and-riffle stream—A kinetic mass transfer model for sorption: *Water Resources Research*, v. 19, no. 3, p. 732-738.
- Bencala, K. E., and Walters, R. A., 1983, Simulation of solute transport in a mountain pool-and-riffle stream—A transient storage model: *Water Resources Research*, v. 19, no. 3, p. 718-724.
- Bencala, K. E., Jackman, A. P., Zellweger, G. W., Avanzino, R. J., and Kennedy, V. C., 1983, Kinetic analysis of strontium and potassium sorption onto sands and gravels in a natural channel: *Water Resources Research*, v. 19, no. 3, p. 725-731.
- Bencala, K. E., Rathbun, R. E., Jackman, A. P., Kennedy, V. C., Zellweger, G. W., and Avanzino, R. J., 1983, Rhodamine-WT dye losses in a mountain stream environment: *Water Resources Bulletin*, v. 19, no. 6, p. 943-950.
- Calkins, Darryl, and Dunne, Thomas, 1970, A salt tracing method for measuring channel velocities in small mountain streams: *Journal of Hydrology*, v. 11, p. 379-392.
- Cerling, T. E., and Spalding, B. P., 1982, Distribution and relationship of radionuclides to streambed gravels in a small watershed: *Environmental Geology*, v. 4, p. 99-116.
- Chapman, B. M., 1982, Numerical simulation of the transport and speciation of nonconservative chemical reactants in rivers: *Water Resources Research*, v. 18, no. 1, p. 155-167.
- Jackman, A. P., Walters, R. A., and Kennedy, V. C., 1984, Transport and concentration controls for Cl, Sr, K, and Pb in Uvas Creek, a small cobble-bed stream in Santa Clara County, California, Part 2, Mathematical modeling: *Journal of Hydrology*, v. 75 (In press).
- Kennedy, V. C., Jackman, A. P., Zand, S. M., Zellweger, G. W., and Avanzino, R. J., 1984, Transport and concentration controls for Cl, Sr, K, and Pb in Uvas Creek, a small cobble-bed stream in Santa Clara County, California, Part 1, Conceptual model: *Journal of Hydrology*, v. 75 (In press).
- Rose, A. W., Hawkes, H. E., and Webb, J. S., 1979, *Geochemistry in mineral exploration* (2d ed.): New York, Academic Press, 657 p.
- Sharp, W. E., 1974, The dilution capacity of small streams in South Carolina: *Water Resources Research Institute, Clemson University, Clemson, South Carolina, Report No. 48*, 70 p.
- Valocchi, A. J., Street, R. L., and Roberts, P. V., 1981, Transport of ion-exchanging solutes in groundwater: Chromatographic theory and field simulation: *Water Resources Research*, v. 17, no. 5, p. 1517-1527.
- Zand, S. M., Kennedy, V. C., Zellweger, G. W., and Avanzino, R. J., 1976, Solute transport and modeling of water quality in a small stream: *Journal of Research of the U.S. Geological Survey*, v. 4, no. 2, p. 233-240.

Uptake and Regeneration of Nitrate by Epilithic Communities in a Nearly Pristine Lotic Environment

By Frank J. Triska, Vance C. Kennedy, and Ronald J. Avanzino

Abstract

Nitrate flux by epilithon was determined by change in a nitrate concentration using chloride as a conservative tracer. The experiment was conducted in a acrylic plastic flow-through channel set in Little Lost Man Creek, Humboldt County, California. Nylon shading (92 percent) was used to produce an epilithic community similar to that of near-surface intragravel habitats. The channel was augmented with nitrate (7.0 micromoles per liter) and phosphate (0.8 micromole per liter) to eliminate potential nutrient limitation. Uptake by the channel's epilithic community totaled 0.385 gram of nitrogen during the first 15 days. Regeneration amounted to 0.396 gram of nitrogen. Of that total, 0.298 gram was regenerated between days 15 and 20. Nitrate regeneration was highest at night and lowest during daylight hours. Maximum nitrate formation was 0.6 micromole per liter at a flow rate of 9.5 liters per minute. Community respiration exceeded net community primary production throughout the experiment. Dissolved organic nitrogen and particulate detritus were potential sources of reduced nitrogen. The observed nitrate regeneration indicates that intragravel communities may contribute nitrate as water is transported downstream, even in pristine streams, with low ammonium concentration.

INTRODUCTION

Nitrification commonly has been reported in fluvial and estuarine environments with high ammonium concentration. Sources of ammonium concentration to these waters include agricultural runoff, sewage outfalls, and geothermal ammonium input (Courchaine, 1968; Billen, 1975; Johnson and others, 1976; Ruane and Krenkel, 1978; Cole and Harmon, 1981; Wofsy and others, 1981; Cooper, 1983; S.W. Hager, written commun., 1983). In the Cascade Mountains of western Oregon and Washington, however, dissolved inorganic nitrogen (DIN) concentrations in headwater streams are extremely low compared to other regions of the United States (Minshall and others, 1983), and ammonium concentrations

can be virtually undetectable. In a continuum of first-through fifth-order tributaries of Lookout Creek, Oregon, Naiman and Sedell (1979) reported nitrate concentrations of 0.02 to 0.04 $\mu\text{mol/L}$ in the first-order stream, 0.24 to 5.43 $\mu\text{mol/L}$ in the third-order stream, and 0.39 to 3.07 $\mu\text{mol/L}$ in the fifth-order stream, spring through autumn (May, July, and October samples). Ammonium concentrations were generally higher in the first order (0.07–1.9 mmol/L) than in higher order streams indicating some potential for nitrification particularly between the first and third order. Unfortunately, data from a continuum of stream orders are scarce, and the above observations consisted of only single samples at each site seasonally.

Because data on nitrate flux during transport are so scarce from pristine mountain environments, a diel background study was conducted at four sites along a 265-m reach of a pristine third-order pool-and-riffle stream in Humboldt County, California (fig. 1). Diurnal nitrate concentrations were measured in mid-August 1979, a period of low summer flow. A significant increase in nitrate concentration was observed upstream to downstream and within short distances between stations (fig. 2). Almost all observed increase in nitrate concentration occurred between stations 1 and 3 (122-m reach), less than one-half the total length of the reach. Further downstream, between stations 3 and 4 (143-m reach), nitrate uptake was observed during daylight, and slight nitrate generation was observed after dark. The major habitat difference between stations was the presence of dense canopy between stations 1 and 3, which effectively darkened the stream. Because primary production can be inhibited severely by shading (Gregory, 1980; Triska and others, 1983) and nitrifying bacteria can be inhibited by light (Olson, 1981; Ward and others, 1982), we decided to test the hypothesis that nitrate regeneration by the interstitial epilithic community was a potential source of observed nitrate in the heavily shaded reach.

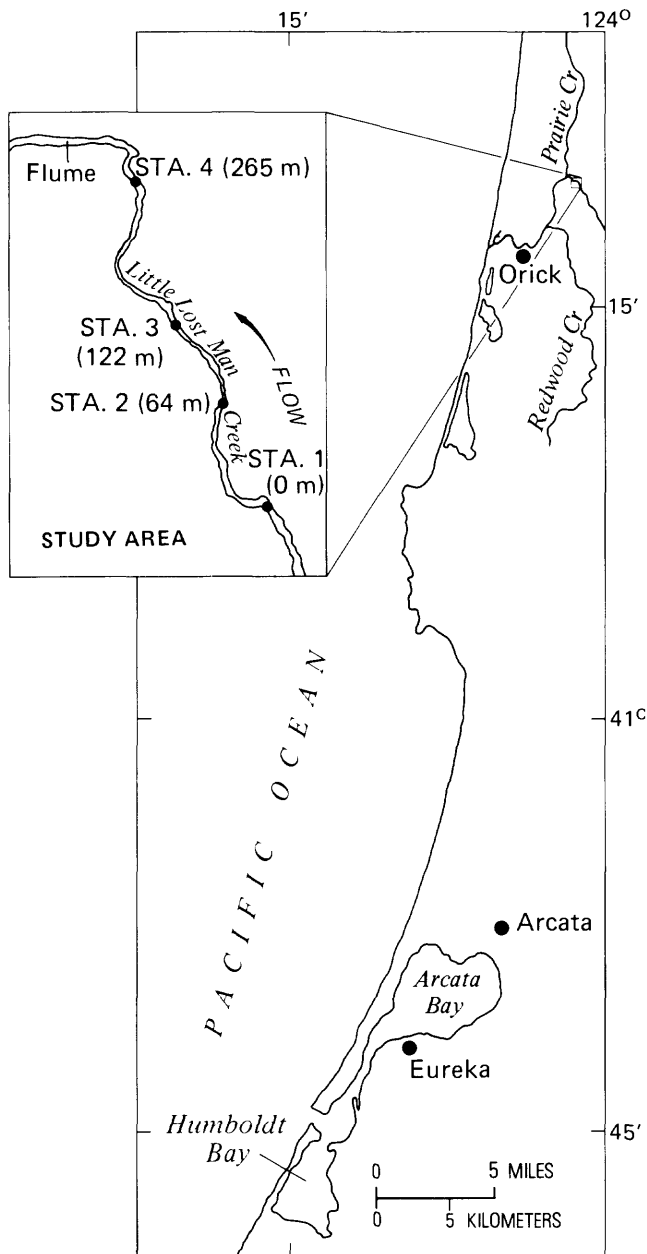


Figure 1. Location of experimental site in northern California. Stations sampled for diel background water chemistry and approximate location of the experimental acrylic plastic flume are indicated on the inset.

STUDY SITE

The study was conducted at Little Lost Man Creek, California (fig. 1), a small watershed stream in Redwood National Park, approximately 5 km from the Pacific Ocean. The watershed is 9.4 km², and mean altitude is 387 m. Channel gradient is 66 m/km. Approximately 92 percent of the vegetation is old-growth coastal redwood forest (*Sequoia sempervirens*), including associated Douglas-fir

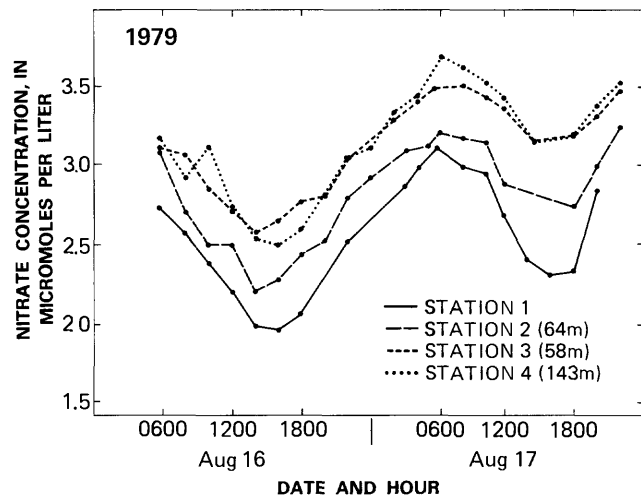


Figure 2. Diel change in background NO₃-N concentration at four stations within a 265-m reach of Little Lost Man Creek under low-flow conditions, August 16–17, 1979.

(*Pseudotsuga menziesii*) and western hemlock (*Tsuga heterophylla*). The lower portion of the basin was logged between 1962 and 1965, and natural revegetation has resulted in a dense stand of alder (*Alnus rubra*) as the major riparian component. Despite the nitrogen-fixing ability of the riparian vegetation, DIN and orthophosphate are low in the stream (table 1). The atomic ratio of nitrogen to phosphate (DIN:ortho-P) is low (approximately 7.8) indicating potential nitrogen limitation (Redfield, 1963; Rhee, 1978). Stream reaches vary from being almost completely open to solar radiation to dense shade. A more complete site description is presented in Iwatsubo and Averett (1981).

MATERIALS AND METHODS

The diel background nitrate chemistry was gathered in a 265-m reach of stream near the base of the watershed. Station 1 was the head of the reach and stations 2 to 4 were at meter 64, 122, and 265, respectively. Water samples were collected every 2 hours and then filtered and chemically analyzed as described below. The nitrate regeneration hypothesis was tested using an acrylic plastic channel set in an unshaded pool approximately 60 m downstream of the reach used for background nitrate concentration. Similar channels have been used in laboratory and field studies on streams of western North America to estimate nutrient uptake by periphyton (Stockner and Shortreed, 1978; Triska and others, 1983); primary production (McIntire and others, 1964; McIn-

Table 1. Channel properties and average background water chemistry for the experimental acrylic plastic flume set in Little Lost Man Creek, California
[DON-dissolved organic nitrogen; DOC-dissolved organic carbon]

Channel properties	Background water chemistry
Length ----- 9.75 m	DON 4.47 ± 0.75 (S.D.) $\mu\text{mol/L}$
Width ----- 15.0 cm	NO ₃ 2.94 ± 0.52 (S.D.) $\mu\text{mol/L}$
Depth ----- 10.0 cm	NO ₂ <0.2 $\mu\text{mol/L}$
Volume ----- 148.7 L	NH ₄ <0.3 $\mu\text{mol/L}$
Flow ----- 9.5 L/min	PO ₄ $0.40 \pm .03$ (S.D.) $\mu\text{mol/L}$
Surface area ----- 12.5 m ²	DOC 88.5 ± 23.3 (S.D.) $\mu\text{mol/L}$
(including slides)	
Water surface ----- 1.48 m ²	
Water traveltime approx. 15 minutes	

Background Irradiance

Mean from four dates in which primary production was determined:
363 ($\mu\text{E/m}^2$)/s

tire and Phinney, 1965; Stockner and Shortreed, 1978; Triska and others, 1983); grazing pressure (Gregory and others, 1980; Sumner and McIntire, 1982); and effect of light on periphyton production (McIntire and others, 1964; McIntire and Phinney, 1965; Triska and others, 1983). So far as known, this was the first use of such channels under heavily shaded (92 percent) conditions to estimate nitrate regeneration.

The channel was closed on the sides and bottom and had an exit pipe at the lower end. All water was supplied at the upstream end of the channel through a header box with an adjustable "V-notch" weir at approximately 9.5 L/min (single-pass flowthrough). Complete control of channel input and output prevented potential nitrogen contamination from outside the system (ground-water seepage from the alder riparian zone). Chloride was added along with a nutrient solution in a header box to provide an amendment of 7.0 $\mu\text{mol NO}_3/\text{L}$ and 0.8 $\mu\text{mol PO}_4/\text{L}$. Background ammonium concentration ($<0.3 \pm 0.2$ $\mu\text{mol/L}$) was unchanged. Dilution of the added chloride after mixing was used as a measure of the water flow through the channel. The change in the ratio of Cl to NO₃ while passing through the channel served as a measure of the gain or loss of NO₃. The header box also served as a settling basin for particulates and filtered all particles larger than 300 μm . Physical and hydrologic properties of the channel and background nutrient concentrations are reported in table 1.

Surface area for attachment of biota was supplied by 240 acrylic slides (10 x 20 x 0.03 cm), which were sandblasted to simulate benthic gravel surfaces. The slides were spaced uniformly throughout the

channel. The epilithic community was established by placing slides in a wide variety of stream habitats for 5 days along the same reach used for diel nitrate measurements approximately 10 days earlier. Slides then were placed in the channel, which was screened with 92 percent nylon greenhouse shading. The purpose of the shading was to produce a dark-adapted community characteristic of the sides and bottom surface gravels or the surface community of densely shaded reaches. After 3 days of shading, the experiment began when the water was first amended with nitrate and phosphate. The final DIN and orthophosphate concentrations (~ 10 and 1.0 $\mu\text{mol/L}$, respectively) approximated runoff during small storms. The experiment started at 1000 hours on August 24, and nutrient addition ended at 1300 hours on September 12, 1979. This period encompassed development of the epilithic community from the stage of active biomass (ash-free dry mass) accumulation through sloughing of mature epilithon.

Flume input and export water typically was sampled five times each day between August 28 and September 13 for NO₃ + NO₂, PO₄, Cl, and ammonium concentrations. Samples were collected before sunrise (approximately 0600) and at 1000, 1400, 1800, and 2200 hours. Previous studies on Little Lost Man Creek indicated this sampling scheme was sufficient to observe maximum diel fluctuations of NO₃ and PO₄.

Both background and flume samples were collected and analyzed identically for inorganic constituents. All samples except those for chloride, were filtered immediately through 0.45- μm Millipore filters into 250-ml HCl-washed bottles and stored fro-

zen (-20°C) until analysis. Sample bottles for chloride were rinsed thoroughly with distilled water. Chloride samples were filtered as above but not frozen. Analyses were made on a Technicon AutoAnalyzer II with a precision for dissolved reactive phosphorous of $\pm 0.03 \mu\text{mol/L}$ below $3.0 \mu\text{mol/L}$ (Technicon Industrial Method No. 155-71W) and for NO_3 of $\pm 0.07 \mu\text{mol/L}$ below and ± 1 percent above $7.0 \mu\text{mol/L}$ (Technicon Industrial Method No. 158-71W). Precision for Cl was ± 1 percent at $143 \mu\text{mol/L}$ and above (Technicon Industrial Method No. 99-70 W/B; O'Brien, 1962). Ammonium concentrations were $<0.3 \mu\text{mol/L}$ for all samples (Technicon Industrial Method No. 154-71W).

Dissolved organic nitrogen (DON) input was estimated in 16 samples, and output was estimated in 7 samples. Sample water was passed through a $0.45\text{-}\mu\text{m}$ silver filter into HCl-washed, oven-heated (500°C) glass bottles, and refrigerated until analysis. Samples were digested for 4 hours in quartz tubes under ultraviolet radiation with hydrogen peroxide to oxidize DON to nitrate. After digestion, the sample was analyzed for nitrate and nitrite as above and corrected for DIN concentration. Precision of the total DON procedure was approximately $\pm 0.7 \mu\text{mol/L}$.

Estimates of community primary production and respiration were made in the channel on four dates by 24-hour upstream-downstream oxygen determination. Oxygen concentration was determined by using YSI Model 57 temperature-compensated oxygen meters with YSI Series 5700 oxygen probes. Membranes were changed, and probes were calibrated before each run. Oxygen concentrations were measured at hourly intervals, and production was calculated by the method of Owens (1974). We assumed 1 mol of carbon fixed for each mol of oxygen produced.

Biomass was sampled five times by collecting 18 slides (approximately 6 percent of the channel area) on each date. Slides were scraped immediately, and the epilithon was frozen until analysis. Scraped slides were returned to the channel, and no location was sampled more than once. Ash-free dry mass was determined by combusting a subsample at 500°C for 4 hours. More complete details on biomass sampling are provided in Triska and others (1983).

Carbon and nitrogen content of biomass was estimated by 24-hour collections on six dates— August 23, 24, and 28; September 9, 11, and 18, 1979. Estimates were made by passing all export water through a 2.0-m long, $20\text{-}\mu\text{m}$ mesh plankton net. Samples were processed as for biomass. Detrital production was assessed at the conclusion of the experiment by collecting all unattached particulates in the same net.

RESULTS

During the first 2 weeks of nutrient addition, nitrate uptake dominated nitrogen flux in the developing epilithic community (fig. 4D). Within the diel cycle, net nitrate uptake was greatest at 1400 hours (fig. 3). Dark samples consistently indicated nitrate regeneration; however, before September 1, measured regeneration was often so small as to be within the error of our analytical precision. Nitrate concentration in the discharge was higher than input in 40 samples during the experiment, and, in 23, samples, the difference exceeded potential analytical error (data not shown). The dominance of uptake during the early growth phase particularly during mid-afternoon is illustrated by data from August 24 (fig. 3). The highest instantaneous rate of NO_3 uptake $529 (\mu\text{mol/hr})/\text{m}^2$ of water surface occurred 2 days later between 1400 and 1700 hours on August 26. For each square meter of water surface, 8 m^2 of surface was colonized. The highest daily rate of nitrate uptake occurred between 0500 hours on August 26 and 0500 hours on August 27 and was $4.3 (\text{mmol}/\text{m}^2)/\text{d}$. By August 28, nitrate uptake was observed only during daylight hours with some regeneration after dark. Between September 1 and 3 and after September 7, nitrate output exceeded input of the full day. Maximum instantaneous nitrate regeneration rate was $320 (\mu\text{mol/hr})/\text{m}^2$ of water surface between 1000 and 1400 hours on September 11. Maximum daily regeneration was $3.8 \text{ mmol}/\text{m}^2$ between 0600 hours on September 11 and 0600 hours on September 12. The injection ended on September 12 at 1300 hours.

The regeneration of nitrate was associated with biomass accumulation (fig. 4A) and a decrease in the carbon-nitrogen ratio of the epilithic community (fig. 4B). Biomass in the channel ranged from 2.43 ± 0.5 (S.D.) g at the start of the experiment to a maximum of 7.45 ± 2.42 (S.D.) g on September 11 (fig. 4A). Low epilithon production is attributed to the darkened condition of the channel. Lack of uniformity in biomass distribution and handling difficulties for small amounts of epilithon resulted in the large standard deviation. During the uptake phase (August 23-September 6), the carbon-nitrogen ratio of the epilithon decreased from 9.72 ± 0.11 (S.D.) to 6.92 ± 0.6 (S.D.) but increased with maximum nitrate regeneration (fig. 4B).

Although biomass accumulated, respiration dominated daily net community production (upstream-downstream oxygen) on all four sample dates (fig. 4C). Oxygen consumption was greatest on September 6. From 1800 hours on September 6 until the end of the experiment, nitrate regeneration was observed in all samples. The dominance of respiration in the face of increasing biomass suggests the pres-

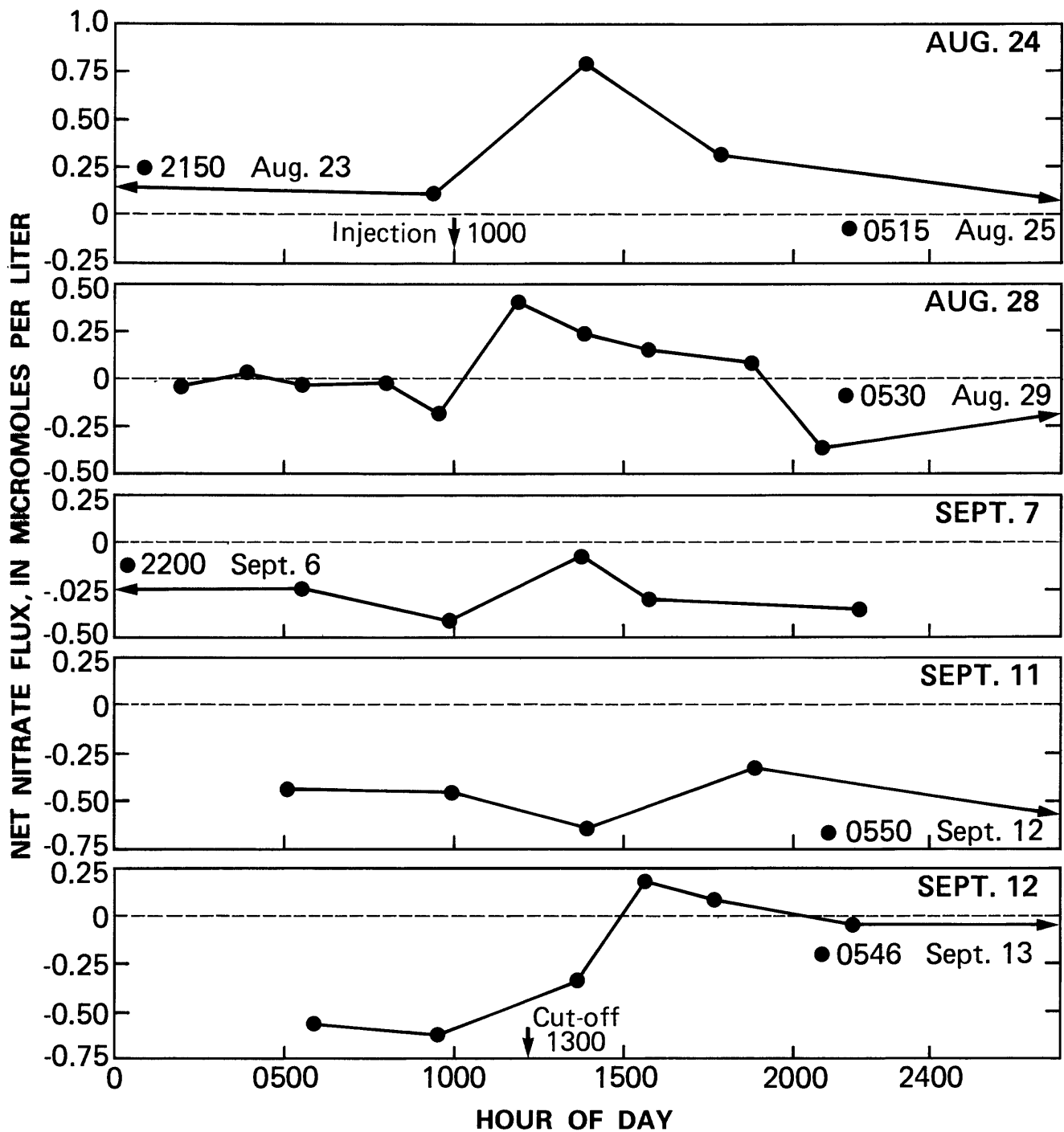


Figure 3. Diel net-nitrate flux (input concentration minus output concentration) by a dark-adapted epilithic community in a flowthrough channel. Data are presented for five sampling dates when biologic parameters were estimated simultaneously. Positive values indicate uptake; negative values indicate regeneration. Nutrient addition began at 1000 hours on August 24, and ended at 1300 hours on September 12, 1979. Flux estimates off the time axis are denoted by arrows.

ence of a large heterotrophic community. This component utilized dissolved organic carbon, organic microparticulates (which passed our filter screen), or sloughed epilithon in conjunction with some simultaneous oxidation of reduced nitrogen. Despite the dominance of oxygen consumption, the system re-

mained aerobic due to the continual throughput of fresh water.

DISCUSSION

In northern California, western Oregon, and Washington, stream gravels generally are well oxy-

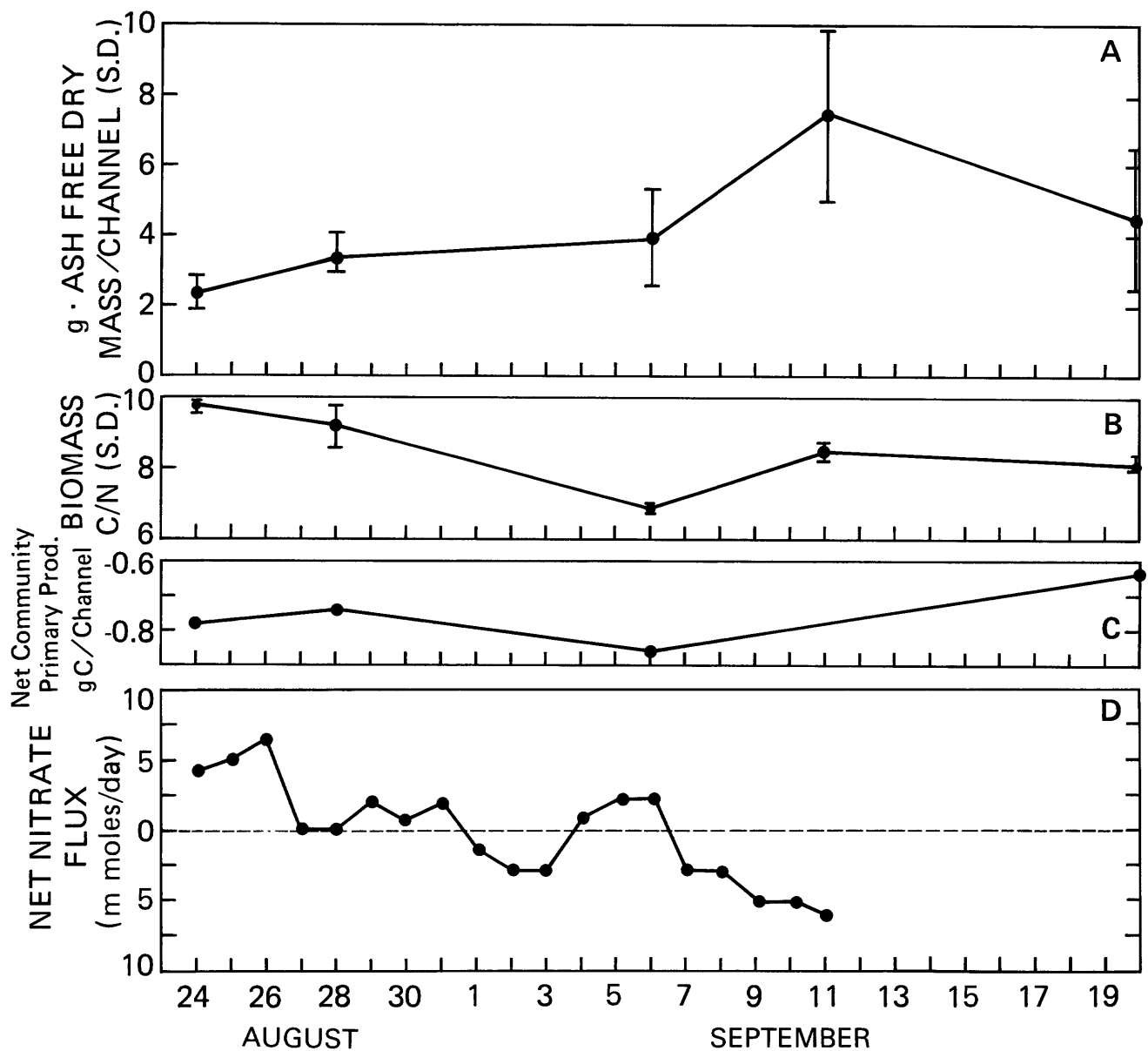


Figure 4. Selected biological and chemical parameters associated with the development of a dark-adapted epilithic community. *A*, Total community biomass (ash-free dry mass). Error bars are one standard deviation (S.D.). *B*, Carbon-nitrogen ratio (C/N) of epilithic biomass. *C*, Daily net community primary production by the epilithic community in grams of carbon (gC) per day. *D*, Net daily nitrate flux in millimoles per day (mmol/d) at a flow rate of 9.5 L/min. Data points above the dashed line indicate uptake, and points below the line indicate regeneration.

generated by water passing through the porous bed. In Little Lost Man Creek, interstitial waters are well saturated with oxygen at all seasons (Woods, 1975). Within the darkness of these surface gravels live a myriad of invertebrates, and fine particulate organics can accumulate in large quantities especially during low flow (Naiman and Sedell, 1979; Triska and others, 1982; Minshall and others, 1983). If any nutrient is biologically limiting, it is nitrogen. As noted previously, DIN concentration is often low in first-order streams and may increase in a downstream direction. In reaches with an open canopy (between stations 3 and 4 in our initial measurements), nitrate

regeneration would have been difficult to measure in situ because, under nitrogen-limited conditions, algae can take up nitrogen both day and night (Conway and Whitley, 1979; Triska and others, 1983; D.H. Peterson, written commun., 1984; Sebetich, 1984). However, in reaches with dense canopy (between sites 1 and 3), nitrate regeneration is more readily measured because algal uptake is minimal due to shading which simultaneously prevents light inhibition of nitrifying bacteria (Olson, 1981; Ward and others, 1982).

The maximum rate of nitrate regeneration was 0.6 $\mu\text{mol/L}$ for a single sample and 0.4 $\mu\text{mol/L}$ for a

full day (five samples) at a flow rate of 9.5 L/min. In a nitrogen-dilute marine environment Harrison (1978) reported rates of ammonium regeneration of 0.56 to 1.5 ($\mu\text{mol/L/d}$) in CEPEX columns using ^{15}N bottle experiments. He also reported lower rates of 0.02 to 0.17 ($\mu\text{mol/L/d}$) from the Southern California Bight, also using ^{15}N methods. Nitrogen regeneration in bottle experiments using DIN concentration increase has been reported by Cole and Harmon (1981) and S.W. Hager (written commun., 1983) for San Francisco Bay (maximum 0.6 ($\mu\text{mol/L/d}$)). In the more polluted Potomac River estuary, a maximum rate of 9.9 ($\mu\text{mol/L/d}$) has been reported by the same authors.

The source of ammonia for nitrate regeneration is uncertain. Background ammonium concentration was less than $0.3 \pm 0.2 \mu\text{mol/L}$ throughout the experiment. Ammonium generally is considered to be the preferred nitrogen source for phytoplankton (McCarthy and others, 1977), and, even under severe nutrient limitation, intermittent exposure can be sufficient to meet the daily nutrient ration (McCarthy and Goldman, 1979). Assuming epilithic communities are similar, ammonium regenerated from DON or particulate nitrogen would be recycled rapidly during the day primarily by the algal component of the epilithon and at night by nitrifying bacteria. Up to one-half of DON was removed when the community was rapidly accumulating biomass, and DON was generated when nitrate regeneration was observed. However, the number of samples (seven) was too small to draw any definite conclusions about the role of DON during community growth and senescence. The most likely source of ammonia was mineralization of sloughed epilithon deposited in the detrital pool. Nitrogen concentration in detritus was only 0.65 percent compared to 2.05 percent in attached biomass at the end of the experiment.

Triplicate analysis of dried, ground, epilithon sampled September 11 (day 19) indicated nitrate was less than 2 percent of the total internal nitrogen pool. Complete loss of internal nitrate would account for less than 3 percent of the nitrate regeneration observed on September 11. Absence of nitrate in cells of senescent algae has been reported by Conover (1975) in cultures of *Thalassiosira fulvialtilis* after 18 days. Thus, nitrate loss from the internal epilithic pools was probably insignificant.

Cumulative net nitrate uptake and regeneration nearly balanced over the term of the experiment (table 2). Total net nitrate uptake was 0.385 gN, all of which was removed between August 21 and September 6. Cumulative net regeneration was 0.396 gN, of which almost 0.298 g was produced between September 6 and 11. While the net DIN uptake and regener-

Table 2. Cumulative uptake and regeneration of nitrate, standing mass, and particulate organic nitrogen in the epilithic community, as of the time and date indicated

Date at 0600 hours	Net cumulative nitrate uptake (gN)	Particulate nitrogen (gN)	Net cumulative nitrate regeneration (gN)
August 25	— — 0.087	Attached ¹ 0.036 Transport ² 0.014	0 0
August 29	— — 0.247	Attached ¹ 0.062 Transport ² 0.028	0
September 7	— — 0.385	Attached ¹ 0.099 Transport ² 0.084	0.098
September 12	— — 0.385	Attached ³ 0.165 Transport ² 0.126 Detritus ⁴ 0.084	0.396

¹Instantaneous estimate of nitrogen associated with epilithic biomass.

²Cumulative loss as particulate organic nitrogen, based on sloughed tissue collected in export nets.

³Not sampled on September 12, based on September 11 data.

⁴Particulate organic nitrogen associated with detritus at end of experiment.

ation of nitrate were approximately equal, nitrogen in the particulate organic pool totaled 0.375 gN. Therefore, mass balance indicates significant utilization of dissolved organic nitrogen and (or) ammonium during development of the epilithon.

The experiment ended while rates of nitrate regeneration were still increasing; therefore, the maximum rate in our artificial channel is unknown. Because our results show only net nitrate regeneration for the channel, gross nitrate regeneration may be higher. Furthermore, water surface (1.5 m²) and surface area available for colonization (12.5 m²) in our channel were small relative to the surface area of stream gravels. These data cannot be extrapolated directly to in situ conditions because net regeneration was highly variable between stations under natural conditions, depending on light conditions and the growth stage of other nitrate sources to our initial field measurements (nitrification in the riparian zone). The results, however, did demonstrate the potential of the epilithic intergravel community to regenerate nitrate in small headwater streams even when the ammonium concentration is nearly undetectable.

REFERENCES CITED

- Billen, G., 1975, Nitrification in the Scheldt Estuary (Belgium and the Netherlands): Estuarine and Coastal Marine Science, v. 3, p. 79–89.
- Cole, B. E., and Harmon, D. D., 1981, Phytoplankton productivity, respiration, and nutrient uptake and regeneration in the Potomac River, August 1977–August 1978: U.S. Geological Survey Open-File Report 81–700, 51 p.

- Conover, S. A. M., 1975, Partitioning of nitrogen and carbon in cultures of the marine diatom *Thalassiosira fulvialtilis* supplied with nitrate, ammonium or urea: *Marine Biology*, v. 32, p. 231–246.
- Conway, H. L., and Whitlege, T. E., 1979, Distribution, fluxes, and biological utilization of inorganic nitrogen during a spring bloom in the New York Bight: *Journal of Marine Research*, v. 37, p. 657–668.
- Cooper, A. B., 1983, Effect of storm events on benthic nitrifying activity: *Applied and Environmental Microbiology*, v. 46, p. 957–960.
- Courchaine, R. J., 1968, Significance of nitrification in stream analysis: Effects on oxygen balance: *Journal of the Water Pollution Control Federation*, v. 40, p. 835–847.
- Gregory, S. V., 1980, Effects of light, nutrients and grazing on periphyton communities in streams: Ph.D. dissertation, Oregon State University Corvallis, Oregon, 151 p.
- Harrison, W. G., 1978, Experimental measurements of nitrogen remineralization in coastal waters: *Limnology and Oceanography*, v. 23, p. 684–694.
- Iwatsubo, R. T., and Averett, R. C., 1981, Aquatic biology of the Redwood Creek and Mill Creek drainage basins, Redwood National Park, Humboldt and Del Norte Counties, California: U.S. Geological Survey Open-File Report 81–143, 115 p.
- Johnson, A. H., Bouldin, D. R., Goyette, E. A., and Hedges, A. M., 1976, Nitrate dynamics in Fall Creek, New York: *Journal of Environmental Quality*, v. 5, p. 386–391.
- McCarthy, J. J., Taylor, W. R., and Taft, J. L., 1977, Nitrogenous nutrition of the plankton in the Chesapeake Bay; Part 1, Nutrient availability and phytoplankton preferences: *Limnology and Oceanography*, v. 22, p. 996–1011.
- McCarthy, J. J., and Goldman, J. C., 1979, Nitrogenous nutrition of marine phytoplankton in nutrient depleted waters: *Science*, v. 203, p. 670–672.
- McIntire, C. D., Garrison, Phinney, H. K., and Warren, C. E., 1964, Primary production in laboratory streams: *Limnology and Oceanography*, v. 9, p. 92–102.
- McIntire, C. D., and Phinney, H. K., 1965, Laboratory studies of periphyton production and community metabolism in lotic environments: *Ecological Monographs*, v. 35, p. 237–258.
- Minshall, G. W., Peterson, R. C., Cummins, K. W., Bott, T. L., Sedell, J. R., Cushing, C. E., and Vannote, R. L., 1983, Interbiome comparison of stream ecosystem dynamics: *Ecological Monographs*, v. 53, p. 1–25.
- Naiman, R. J., and Sedell, J. R., 1979, Characterization of particulate organic matter transported by some Cascade Mountain streams: *Journal of the Fisheries Research Board of Canada*, v. 36, p. 17–31.
- O'Brien, J. E., 1962, Automatic analysis of chlorides in sewage: *Wastes Engineering*, v. 33, p. 670–672.
- Olson, R. J., 1981, Differential photoinhibition of marine nitrifying bacteria: A possible mechanism for the formation of the primary nitrate maximum: *Journal of Marine Research*, v. 39, p. 227–238.
- Owens, M., 1974, Measurements of primary production on non-isolated natural communities in running waters, in Vollenwieder, R.A., ed., *A manual on methods for measuring primary production in aquatic environments* (2 ed.): Blackwell Scientific Publications, Oxford, 22 p.
- Redfield, A. C., Ketchum, B. H., and Richards, F. A., 1963, The influence of organisms on the composition of seawater, in Hill, M. N., ed., *The sea*, v. 2: Wiley-Interscience, New York, p. 26–77.
- Rhee, G-Yull, 1978, Effects of N/P ratios and nitrate limitation on algal growth, cell composition, and nitrate uptake: *Limnology and Oceanography*, v. 23, p. 10–25.
- Ruane, R. J., and Krenkel, P. A., 1978, Nitrification and other factors affecting nitrogen in the Holston River: *Journal of the Water Pollution Control Federation*, v. 50, p. 2016–2028.
- Sebetich, M. J., Kennedy, V. C., Zand, S. M., Avanzino, R. J., and Zellweger, G. W., 1984, Dynamics of added nitrate and phosphate compared in a northern California woodland stream: *Water Resources Bulletin*, v. 20, no. 1, p. 93–101.
- Stockner, J. G., and Shortreed, K. R. S., 1978, Enhancement of autotrophic production by nutrient addition in a coastal rainforest stream on Vancouver Island: *Journal of the Fisheries Research Board of Canada*, v. 35, p. 28–34.
- Sumner, W. T., and McIntire, C. D., 1982, Grazer-periphyton interactions in laboratory streams: *Archiv fur Hydrobiologie*, v. 93, p. 135–157.
- Triska, F. J., Sedell, J. R., and Gregory, S. V., 1982, The coniferous forest stream, in Edmonds, R. L., ed., *Analysis of coniferous ecosystems in the Western United States*: Dowden, Hutchinson and Ross, Stroudsburg, Pennsylvania, p. 292–332.
- Triska, F. J., Kennedy, V. C., Avanzino, R. J., and Reilly, B. N., 1983, Effect of simulated canopy cover on regulation of nitrate uptake and primary production by natural periphyton assemblages, in Fontaine, T. D., III, and Bartell, S. M., eds., *Dynamics of lotic ecosystems: Savannah River Ecology Laboratory Seventh Ecological Symposium*, August 19–22, 1980, p. 129–159.
- Ward, B. B., Olson, R. L., and Perry, M. J., 1982, Microbial nitrification rates in the primary nitrite maximum: *Deep-Sea Research*, v. 29, p. 247–255.
- Wofsy, S. C., McElroy, M. B., and Elkins, J. W., 1981, Transformation of nitrogen in a polluted estuary: Nonlinearities in the demand for oxygen at low flow: *Science*, v. 213, p. 754–757.
- Woods, P. F., 1975, Intergravel and surface water conditions in three tributaries of Redwood Creek: M.S. thesis, Humboldt State University, Arcata, California, 68 p.

Streambed Oxygen Demand Versus Benthic Oxygen Demand

By John E. Terry and Edward E. Morris

Abstract

To effectively model dissolved-oxygen dynamics in a stream, all sources and sinks must be simulated adequately. In many streams, the demand for oxygen from streambed deposits is a very significant sink. Many investigators attempt to quantify this demand by analyzing "point samples" by *in vitro* or *in situ* methods. In terms of areal application with respect to model simulations, these measurements are deficient because of

1. Spatial variations due to patch deposition and distance from contributing sources;
2. Inclusion of periphytic algal respiration; and
3. Unsamplable substrates.

Studies conducted by the U.S. Geological Survey in cooperation with the Arkansas Department of Pollution Control and Ecology on stream water quality in Arkansas indicate that an indirect technique for the quantification of dissolved-oxygen demands from streambed deposits is more practical and results in more representative values than do the analyses of point samples. The application of these techniques requires that all sources and sinks for instream dissolved oxygen, except the demands from streambed deposits, be measured or determined. The demand for dissolved oxygen from streambed deposits then is quantified indirectly as the only unknown in the oxygen-balance equation. Projected changes in this demand are simulated as a function of projected changes in instream organic deposition rates.

INTRODUCTION

During the last two decades, degradation of the quality of water in many of our lakes, estuaries, rivers, and streams has received a great deal of national attention. This degradation has been due to man's activities and is the result of point-source waste discharges and nonpoint-source contaminant washoff into these water bodies. Detrimental point sources are typically municipal wastewater-treatment plants and industries that discharge untreated or poorly treated wastes directly into a water body. Nonpoint sources are agricultural areas, residential areas, and surface disposal sites from which contaminants can

be "washed off" into a water body during rainfall-runoff events. Because of the national concern for good water quality, various Federal, State, and local agencies have undertaken the task of restoring and (or) maintaining good water quality in lakes, estuaries, rivers, and streams. Water quality in lakes and estuaries is no less important than that of rivers and streams; however, this paper deals almost exclusively with the latter.

The most practical way to simulate the water quality of a stream system is with a mathematical model in which the most important processes of the system are represented numerically. This representation includes a description of system parameters, process reaction kinetics, and the coupling of related processes. It is imperative to know

1. The rates at which system processes change in form or magnitude;
2. The extent and nature of the coupling of these processes; and
3. How these changing processes affect the magnitude of those parameters by which the quality of the system is judged. Except for those systems that are very simple and uncomplicated, the only efficient way to manage such a model is with a digital computer. The digital model has become, therefore, a very important tool in the environmental science field.

According to existing water-quality standards, the key criterion for determining the "quality" of a stream system is the instream concentration of dissolved oxygen (DO). Various physical and biochemical components simultaneously impact the DO profile in a stream, resulting in diel and spatial variations in DO concentration. Some of the components help replenish the DO (sources), whereas, others are consumers. Determining the assimilative capacity of a stream entails defining how large the oxygen-demanding processes (sinks) can be before DO concentrations fall below standard.

Demands for oxygen exerted from streambed deposits can be very significant instream oxygen sinks especially in shallow streams where bottom de-

posits are rich in organic material. If the oxygen demands from bottom deposits are not included in simulations of a stream's DO regime, other source or sink terms may be exaggerated grossly to effect a "fit" between simulated and observed DO profiles. In many attempts at analytically or digitally simulating instream DO concentrations, nutrient decay-rate coefficients and reaeration-rate coefficients have been given unrealistic values because oxygen demands from bottom deposits were not included in the simulation.

As the state-of-the-art in DO modeling advanced, oxygen demands from the streambed were termed "sediment oxygen demands" and values were determined by analyzing point samples of bed material by either in vitro or in situ methods. Hereafter in this paper, the demand measured by either of these techniques will be designated "streambed oxygen demand" (SOD) which the authors feel is a more accurate denotation. However, several distinct fallacies are associated with both of these measurement techniques; these will be discussed later.

Streambed Oxygen Demand

Streambed oxygen demand is a measure of the quantity of oxygen removed from overlying waters by processes occurring through a unit area of streambed in unit time. The demand from the streambed for oxygen is primarily due to the decay of such natural organic detritus such as leaves and of settleable organics contributed by man from point and nonpoint sources.

As used in this paper, SOD does not include the respiration of periphyton nor does it include the respiration of benthic invertebrates and bacteria attached to noncollectable substrates. These noncollectable substrates include submerged trees, aquatic macrophytes, bedrock outcrops, large gravel, and boulders.

Benthic Oxygen Demand

As used in this paper, the term "benthic oxygen demand" (benthic demand) has a broader meaning than SOD. It includes all of the demand that is measurable as SOD plus the bacterial and invertebrate oxygen demands from noncollectable substrates. In addition, it is more representative in that it accounts for spatial variations and patch deposition within a stream reach.

DIRECT MEASUREMENT OF STREAMBED OXYGEN DEMAND

Measurement Technique

Sampling Procedure

An in vitro technique has been used to measure SOD in our studies. Representative bed-material samples are collected by use of grab samplers or a shovel. Approximately 9 kg of the top 50 to 75 mm of bed material is collected in a large pan. The surface of the material is covered with plastic wrap. Then the sample is chilled and transported to the laboratory for analysis, which is begun within 24 hours of collection.

Laboratory Analysis and Rate Calculation

A respirometer, adapted from Noland and Johnson (1979), is used in the determination of SOD in the laboratory test. The respirometer (fig. 1) consists of a 0.305-m-diameter cylinder constructed from clear acrylic pipe with acrylic end plates, a DO probe and container, a continuous recorder, a peristaltic pump, and polyethylene tubing.

The bed-material sample is placed on the bottom of the respirometer to a depth of 25.4 mm. The surface area of the sample is 0.069 m². The inlet port is 30 mm above the sample surface, and the exit port is 90 mm below the lid of the respirometer. After a sample has been placed in the respirometer and the DO probe has been calibrated, the respirometer is filled with 8.53 L of aerated, demineralized water, the peristaltic pump is started, and the lid is placed on the respirometer forming an airtight container. The system is operated at room temperature ($21^{\circ} \pm 1^{\circ}\text{C}$) for 4 to 8 hours.

The first step in calculating the oxygen demand of the sample is to examine the DO versus time plot obtained from the continuous recorder. Initial DO (O_i) and final DO (O_f) (fig. 2) are determined from that portion of the plot where oxygen consumption versus time is constant (fig. 2). DO concentrations of less than 2 mg/L are not used in rate determinations because of changing rates of oxygen demand by aquatic organisms during low DO periods. As a control, the analysis also is done without streambed material using demineralized water, and the appropriate blank correction is made in the final calculation as follows:

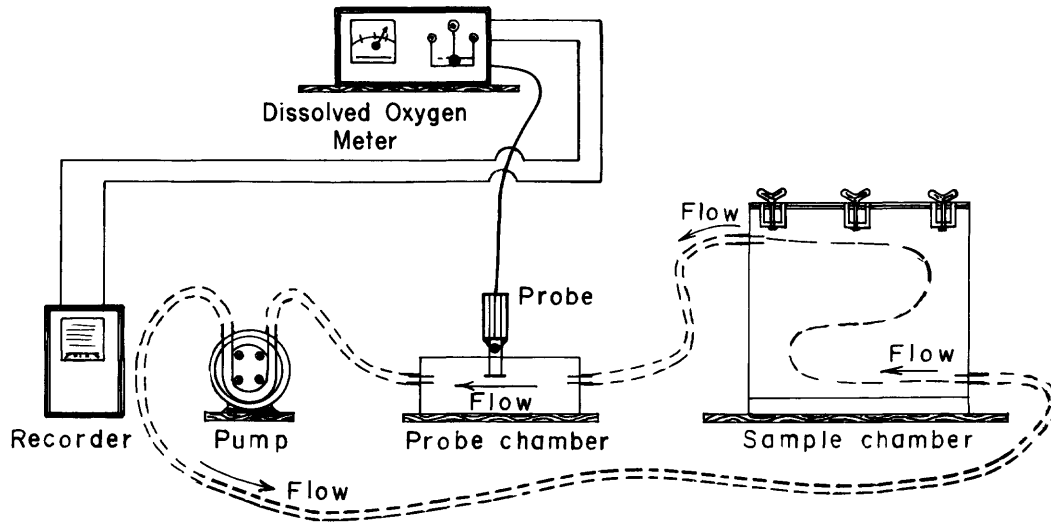


Figure 1. Respirometer, from Noland and Johnson (1979), used for measuring streambed oxygen demand (Terry and others, 1984).

$$SOD = \frac{[(O_i - O_f) - (B_i - B_f)]V}{SA} \bigg/ \Delta t, \quad (1)$$

where *SOD* equals streambed oxygen demand in grams per square meter per day, *O_i* equals initial DO in milligrams per liter, *O_f* equals DO final in milligrams per liter, *B_i* equals blank initial DO in milligrams per liter, *B_f* equals blank final DO in milligrams per liter, *V* equals volume confined water in cubic meters, *SA* equals sample surface area in square meters, and Δt equals *t_i* - *t_f*, change in time in days.

Streambed oxygen demand values differ considerably between streams. Butts and Evans (1978) found that for several streams in the State of Illinois, values ranged from 0.27 (g/m²)/d for a clean stream to 9.3 (g/m²)/d for a very polluted stream.

Application Fallacy

Conceptualization

If either in vitro or in situ techniques are used to measure SOD, the results may be deficient in the following three respects:

1. Spatial variations usually are significant due to patch deposition patterns and distance from contributing sources and, if averaging techniques are used, the number of point samples that would have to be analyzed in order to obtain a representative SOD value for a given stream reach must be determined, if possible;
2. Values unintentionally may reflect the respiration of periphytic algae; and
3. Oxygen demands from bacteria and organisms that reside upon such unsamplable substrates as submerged trees, aquatic macrophytes, bedrock outcrops, large gravels, and boulders may be significant, and the oxygen demands exerted from these substrates cannot be accounted for by direct in situ or in vitro measurement techniques.

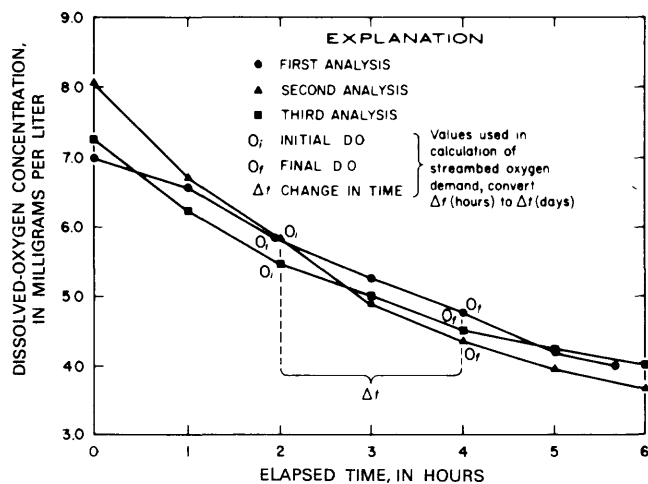


Figure 2. Dissolved oxygen curves resulting from three respirometer analyses of a Muddy Fork bed-material sample collected on September 4, 1981 (Terry and others, 1984).

Digital Model Simulations

The U.S. Geological Survey, in cooperation with the Arkansas Department of Pollution Control and Ecology, has conducted streamwater-quality assessments on several river basins in Arkansas. A major part of these efforts involves the application of steady-state modeling techniques to simulate observed and projected DO profiles to assist the State in waste-load allocation. Recent studies have been done for the Illinois River basin located in northwest Arkansas. The applied model requires that each stream reach be segmented into discrete subreaches in which all DO sources and sinks must be defined.

We have found that the demand for DO exerted from the streambed and from all submerged surfaces lying on or adjacent to the streambed is a very significant, if not the most significant, oxygen sink. We also have found that measured values of SOD do not adequately simulate this sink. We, therefore, have developed a procedure for indirectly quantifying benthic demand.

MODEL-DERIVED BENTHIC OXYGEN DEMAND

To indirectly quantify benthic demand, it is necessary to measure directly or determine the magnitude of all other source and sink terms that impact upon the DO regime in a stream. Consequently, the reaction kinetics of all ongoing processes must be simulated adequately.

Dissolved-Oxygen Modeling Approach

As discussed above, the only practical way to simulate the water quality of a complex stream system is with a digital model. The steps that are followed in simulating instream DO profiles and, consequently, the steps that are necessary in order to indirectly quantify benthic demand are as follows:

1. Collection of an adequate biochemical data set under steady flow and loading conditions;
2. Measurement of time of travel using dye-injection techniques to define stream velocities for the flows of interest;
3. Determination of instream-reaeration coefficients for the flows of interest using hydrocarbon-gas-injection techniques;
4. Determination of average stream geometry by using measured time of travel as fitting tools;

5. Development or choosing of a reaeration-coefficient-prediction equation based upon the results of the gas injection experiment and average stream geometry;
6. Computation of values for daily average net photosynthetic DO production based upon observed diel DO and temperature data and using a modified Odum analysis technique;
7. Calibration of all DO-related constituent profiles such as those for carbonaceous biochemical oxygen demand (CBOD), organic nitrogen, ammonia, nitrite, and nitrate. In so doing, the validity of reaction coefficients that define the rate at which oxygen is utilized as these constituents decay and change form can be confirmed;
8. Complete calibration of the daily average DO profile. Any difference between the observed and simulated DO profiles can now be attributed to an incorrect quantification of benthic demand, and these values are adjusted accordingly. When the computed DO profile adequately simulates the observed, we feel that we have quantified accurately average benthic demand for each stream subreach designated in the model. At this point, we believe that our model is calibrated for adequate simulation of the daily average DO profile; and
9. If necessary, simulation of the observed diel minimum DO profile by adjusting the daily average net photosynthetic DO production values to synthesize the cumulative effects of nighttime aquatic plant respiration upon the DO profile.

Definition and Quantification of Measurable Impacting Components

Within each modeled subreach, we independently define and quantify the following components which directly impact the DO regime:

1. Reaeration;
2. Respiration and oxygen production of periphyton and phytoplankton algae;
3. Decay of carbonaceous material in the water column;
4. The forward reaction and decay of the nitrogen forms—organic nitrogen, ammonia, nitrite, and nitrate;
5. Initial DO concentration;
6. Point and nonpoint sources of DO;
7. Temperature; and
8. Time of travel.

Then, as mentioned earlier, during the model calibration and verification procedure, we indirectly quantify benthic demand for each modeled subreach. As

might be expected, the benthic demands are usually higher than measured values of SOD. It is important to describe in some detail how values for each of these components are measured to substantiate the reliability of indirectly determined values of benthic demand.

Instream-Reaeration Coefficient

Reaeration is the single most important source of dependable oxygenation in a stream. This process goes on at a rate that is proportional to the existing DO deficit. The deficit is defined as the difference between the existing DO concentration in a stream and the possible saturation concentration at the existing water temperature.

The following equation is often used to express the rate of absorption of oxygen per unit time (rate of reaeration);

$$dc/dt = k_2(c_s - c), \quad (2)$$

where dc/dt equals reaeration rate in milligrams per liter, k_2 equals reaeration coefficient in per day, c_s equals DO saturation concentration at a given temperature in milligrams per liter, and c equals existing DO concentration in milligrams per liter. These units are used for convenience in this paper; other consistent units may be used. The most difficult variable to define in this equation is k_2 . However, to adequately simulate DO dynamics in a stream, it is essential to define.

The reaeration coefficient expresses the effect of stream hydraulic properties on the rate of reaeration. Available data indicate that a functional relation between k_2 and mean velocity, mean depth, and (or) channel slope exists. This relation has been defined differently by various investigators, and a number of predictive equations are available.

An oxygen balance is often attained in streamwater-quality simulations by using one of the available predictive equations to estimate k_2 . Some simulations also are attempted in which the reaeration coefficient is treated as the only unknown in the oxygen-balance equation, and values of k_2 are adjusted until computed DO concentrations match those that have been observed reasonably well. Problems associated with each of these techniques for defining k_2 , especially the latter, can be significant. A more viable method for defining k_2 is a field measurement of the coefficient for the particular stream and flow conditions being studied.

Measurement Technique.—The measurement technique that we have used involves the injection of a low molecular-weight hydrocarbon gas (ethylene

and (or) propane) and rhodamine-WT dye into the stream as “tracers”. This particular technique was first described by Rathbun and others (1975).

The hydrocarbon-gas-tracer technique is based on the observation that the rate coefficient for the tracer gas desorbing from water and that the rate coefficient for oxygen being absorbed by the same water are related by a proportionality constant such that

$$k_2 = k_T \theta, \quad (3)$$

where k_2 equals a reaeration coefficient in per day, k_T equals a desorption coefficient for the hydrocarbon gas in per day, and θ equals an experimentally determined proportionality constant. Values of θ for ethylene and propane were determined from a series of mixing-tank experiments in which k_2 and k_T were measured simultaneously (Rathbun and others, 1978); these values are 1.15 and 1.39 for ethylene and propane, respectively.

The rhodamine-WT dye is used as a dispersion-dilution tracer. However, it is recognized that the dye is not completely conservative, and provisions are built into the computation procedure to correct for dye losses.

The gas and dye concentration-versus-time curves obtained at the beginning and the end of a stream reach are used to define the gas-desorption-rate coefficient for that reach.

Details of the field procedures for measuring reaeration coefficient have been described in several sources (Rathbun and others, 1975; Shultz and others, 1976; Rathbun, 1977; Rathbun and others, 1978).

Data Interpretation.—The basic equation for determining the gas-desorption coefficient using the peak gas-concentration method is

$$k_T = [1/(t_d - t_u)] \ln [(C_T/C_D)_u / (C_T/C_D)_d], \quad (4)$$

where k_T equals desorption coefficient for the hydrocarbon gas in per day, t equals time of arrival of peak gas concentration, C_T equals peak concentration of gas in micrograms per liter, C_D equals peak concentration of dispersion-dilution tracer in micrograms per liter, and subscripts d and u indicate downstream and upstream, respectively.

An assumption is made in equation 4 that the dispersion-dilution tracer is conservative. Under many stream conditions, rhodamine-WT dye is not completely conservative. In such cases the following procedure can be used to account for possible dye losses:

$$Q_2 A_2 = Q_3 A_3 J_3 = Q_4 A_4 J_4, \quad (5)$$

where Q equals discharge in cubic meters per second, A equals area under the dye concentration-ver-

sus-time curve, J equals correction factor used to maintain equality, and the subscripts 2, 3, and 4 indicate sampling sites in a downstream direction. Complete mixing is required for this correction to be valid. Equation 4 then takes the following form between hypothetical sampling sites 3 and 4:

$$k_T = [1/(t_{d_4} - t_{u_3})] \ln [(C_{T_3}/C_{D_3}J_3)/(C_{T_4}/C_{D_4}J_4)]. \quad (6)$$

After application of equations 4 and 6, k_2 can be determined by substituting the resulting k_T value and the appropriate value of θ into equation 3. These values of k_2 are representative of the flow conditions and water temperature during the gas- and dye-injection and sampling period.

Details on the derivation and application of equations 3 through 6 are given by Rathbun and others (1975) and Rathbun and Grant (1978). The interested reader should refer to these publications for further explanation.

Net Photosynthetic Dissolved-Oxygen Production

Net photosynthetic DO production, defined as the difference between gross photosynthesis and algal respiration, is an integral component in the community metabolism of most streams. Hereafter in this paper, net photosynthetic DO production will be referred to as "net DO production." In our studies, net DO production has been determined from an analysis of a diel series of DO and temperature measurements and chlorophyll α measurements made at selected sampling sites. An approach developed by Odum (1956) is used to solve the oxygen-balance equation for each set of diel data collected. This analysis yields net daytime productivity, total nighttime respiration, and total 24-hour community metabolism.

The Odum methodology has been coded into a digital program and documented by Stephens and Jennings (1976). The program solves the oxygen bal-

ance equation at a single station or as the difference between upstream and downstream stations. In our studies, the single-station analysis has been used. Problem solution is for the following oxygen-balance equation:

$$X = P - R + D + \Phi, \quad (7)$$

where X equals rate of change of dissolved oxygen per unit area, P equals rate of photosynthetic production per unit area, R equals gross rate of community respiration per unit area, D equals rate of gain or loss of oxygen through diffusion (reaeration), and Φ equals rate of accrual of oxygenated water. In addition to the diel DO and temperature data, values for some additional parameters must be supplied to the program to solve the preceding equation. For these analyses, the additional parameters necessary are as follows:

1. Oxygen diffusion coefficient

$$DIFC = k_2(9.07)/(BP/760), \quad (8)$$

where $DIFC$ = diffusion coefficient in grams per cubic meters per hour,

k_2 = reaeration coefficient in per hour,

9.07 = DO saturation in milligrams per liter at 20°C, and

BP = barometric pressure in millimeters of mercury.

2. Barometric pressure in millimeters of mercury,
3. Stream depth in meters, and
4. Time of sunrise and sunset.

A sample of printed results from the program is shown in figure 3.

As an example, applying the results of the Odum analysis (fig. 3) and measured chlorophyll α concentrations of 1.04 $\mu\text{g/L}$ for phytoplankton and 8.31 $\mu\text{g/L}$ for periphyton, the following procedure is used to derive values for net photosynthetic DO production at each station where diel DO and temperature data are collected:

Equalities:

OXYGEN METABOLISM				
STATION NUMBER 01: SR2I:ST05:08/25-08/26:PC-CLR				
NET DAYTIME PROD.	1.939 GM O2/M3/DAY	0.605 GM C /M3/DAY	1.299 GM O2/M2/DAY	0.405 GM C /M2/DAY
NIGHT RESPIRATION	-4.931 GM O2/M3/DAY	-1.538 GM C /M3/DAY	-3.304 GM O2/M2/DAY	-1.031 GM C /M2/DAY
*PRODUCTION DURING TIME PERIOD 0630 TO 1945 HRS				
	P/R RATIO	0.3931		
24 HOUR COMMUNITY METABOLISM=	-2.005 GM O2/M2/DAY			
(DIFFERENCE BETWEEN NET DAILY PRODUCTION AND NIGHT RESPIRATION)				

Figure 3. Sample printout of results of Odum single-station method for determining community metabolism at site 5, Illinois River, Arkansas (Terry and others, 1984).

1. Net daytime oxygen production = gross photosynthesis + (daytime benthic demand + daytime BOD + daytime respiration of periphyton + daytime respiration of phytoplankton).
2. Nighttime respiration = nighttime benthic demand + nighttime BOD + nighttime respiration of periphyton + nighttime respiration of phytoplankton.
3. 24-hour community metabolism = net daytime oxygen production + nighttime respiration.
4. Algal respiration = -0.025 (chlorophyll α concentration), (Shindala, 1972).

Assumptions:

1. Daytime benthic demand and BOD = nighttime benthic demand and BOD.
2. Daytime algal respiration = nighttime algal respiration.
3. Periphyton respiration = phytoplankton respiration; in the absence of good periphyton data.

Computations:

- Phytoplankton chlorophyll $\alpha = 1.04 \mu\text{g/L}$:
 therefore, by equality 4, phytoplankton respiration = $-0.025 (1.04 \mu\text{g/L}) = -0.026 \text{ (g/m}^3\text{)/d}$ of oxygen.
- Periphyton chlorophyll $\alpha = 8.31 \mu\text{g/L}$: therefore, by equality 4, periphyton respiration = $-0.025 (8.31 \mu\text{g/L}) = 0.208 \text{ (g/m}^3\text{)/d}$ of oxygen.
- By equality 2, nighttime benthic demand + nighttime BOD = nighttime respiration – nighttime respiration of periphyton – nighttime respiration of phytoplankton = $-4.931 - (-0.026/2) - (-0.208/2) = -4.814 \text{ (g/m}^3\text{)/d}$.

Define:

Net DO production = gross photosynthesis + daytime respiration of periphyton + daytime respiration of phytoplankton + nighttime respiration of per-

iphyton + nighttime respiration of phytoplankton.

By equality 1, net DO production = net daytime production – (daytime benthic demand + daytime BOD) + nighttime respiration of periphyton + nighttime respiration of phytoplankton.

Therefore, using assumptions 1 and 2, net DO production = $1.939 - (-4.814) + (-.208/2) + (-.026/2) = 6.64 \text{ (g/m}^3\text{)/d}$, and = 6.64 (mg/L)/d .

Carbonaceous Biochemical Oxygen Demand

Carbonaceous biochemical oxygen demand is a single stage reaction defining the quantity of oxygen used by organisms in the water column as they consume organic material. Demands can be defined for any period of time but are typically defined for periods of 5 days or until complete assimilation of CBOD occurs. The maximum quantity of DO required for the complete assimilation of carbonaceous material in a given parcel of water is defined as the ultimate CBOD, or CBODU.

Each water sample is analyzed for CBOD according to the methods described by R. J. Pickering (written commun., 1980) and Stamer and others (1983). To inhibit nitrification, 2-chloro-6 (trichloromethyl) pyridine is introduced into each sample. The observed decline in DO concentration in each sample then is assumed to be only due to the respiration of those organisms that consume carbonaceous material. The DO concentration in each sample is recorded initially and on day 1 of the test; thereafter, the concentration is recorded every other day for a period of 20 days.

The single-stage decay of carbonaceous material can be defined by the first-order kinetics model expressed in the following equation:

$$L_t = L_0 e^{-kt}, \quad (9)$$

where t equals time in days, e equals base of natural logarithms, L_t equals concentration of carbonaceous biochemical oxygen demand in milligrams per liter remaining after t days, L_0 equals initial concentration of CBOD at time zero (CBODU) in milligrams per liter, and k equals first-order CBOD decay coefficient, base e in per day. We determine L_0 and k by defining a best-fit curve for the time-series DO data recorded during the laboratory CBODU test. This fitting is accomplished by using a computer program described by Jennings and Bauer (1976).

The fitting methods available in the program are the Thomas method, the least-squares method, and the nonlinear least-squares method. Estimates of L_o and k produced by the fitting procedure with the smallest computed root mean-square error are considered most accurate. Each reaction coefficient, k , determined in this manner represents the deoxygenation-rate coefficient, k_1 , because deposition is not accounted for in the “bottle-time” test.

Values for the removal rate coefficient, k_r , are determined by fitting the computed-average CBODU profile, based upon all sources defined, to the observed average profile (fig. 4). Values for the instream deoxygenation coefficient, k_d , are determined from k_1 values and a stream characteristic correction factor defined by Bosko (1966). Values of k_1 are averaged by subreach, and the following equation applied:

$$k_d = k_1 + n(V/D), \quad (10)$$

where k_d equals instream deoxygenation-rate coefficient in per day, k_1 equals mean bottle-time deoxygenation-rate coefficient in per day, V equals mean stream velocity in meters per second, D equals mean stream depth in meters, and n equals coefficient of bed activity. The dimensionless coefficient n is determined by channel slope in feet per mile. Values of n are obtained as a step function of slope and are given by Tierney and Young (1974) and Zison and others (1978). The term $n(V/D)$ in equation 10 reflects the importance of organisms in the streambed that utilize CBOD. The k_d values are not adjusted during

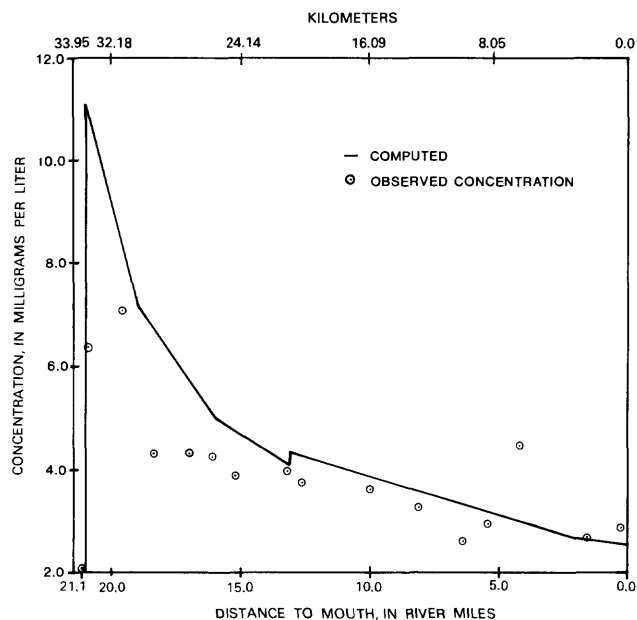


Figure 4. Observed and calculated carbonaceous biochemical oxygen demand profiles, Osage Creek, Arkansas (Terry and others, 1984).

calibration verification unless observed CBOD data indicated that, in a particular subreach, k_r is less than the computed k_d . In such a case, k_d is set equal to the smaller k_r .

Nitrification

The nitrogen-cycle transformation is a biologically coupled sequentially mediated reaction involving the decay of organic-N to ammonia-N through $\text{NO}_2\text{-N}$ to $\text{NO}_3\text{-N}$. The forward reaction of each nitrogen form to the next nitrogen form and the associated concentration coupling is determined by the forward-reaction coefficient. These forward reactions—the transformation of one nitrogen form to another—generally are the most significant. However, other reactions are possible; these include the deposition of organic-N, plant utilization of ammonia-N, reduction of $\text{NO}_3\text{-N}$ to ammonia-N, and the escape as gas of un-ionized ammonia-N and molecular nitrogen. The rates at which these reactions occur are included in the decay rate coefficients.

We use the following rationale for the definition of all of the nitrogen-decay-rate and forward-reaction-rate coefficients. Values for the decay-rate coefficient for organic-N are defined by the observed change in organic-N concentration with distance. Based upon past experience and comparable literature values, the organic-N forward reaction rate coefficient has been set to 0.05 per day. The decay-rate coefficient and forward-reaction-rate coefficient are set equal for ammonia-N and also for $\text{NO}_2\text{-N}$. Profiles for nitrogen forms are fit sequentially from organic-N through $\text{NO}_3\text{-N}$. The values of the reaction coefficient pairs for ammonia-N and $\text{NO}_2\text{-N}$ and for the $\text{NO}_3\text{-N}$ decay rate coefficient are functions of the observed loss in that constituent in a downstream direction and the source contributions from the preceding reaction. The equality of the reaction coefficient pairs for ammonia-N and for $\text{NO}_2\text{-N}$ and the organic-N forward reaction coefficient of 0.05 per day at 20°C are maintained unless the calibration-verification process indicates that a deviation for a particular subreach is necessary. Examples of “fitted” nitrogen form profiles are shown in figures 5 through 8.

The decay rates describe the total rate of removal of the nitrogen forms from the water, whereas, the forward-reaction coefficients describe the rate at which one form of nitrogen decays sequentially forward to the next form. Therefore, each decay rate should always be greater than, or equal to, its associated forward-reaction coefficient. The rate at which nitrate is utilized is described by the $\text{NO}_3\text{-N}$ decay rate, which includes reduction of $\text{NO}_3\text{-N}$ to ammonia-N and, primarily, plant utilization of $\text{NO}_3\text{-N}$.

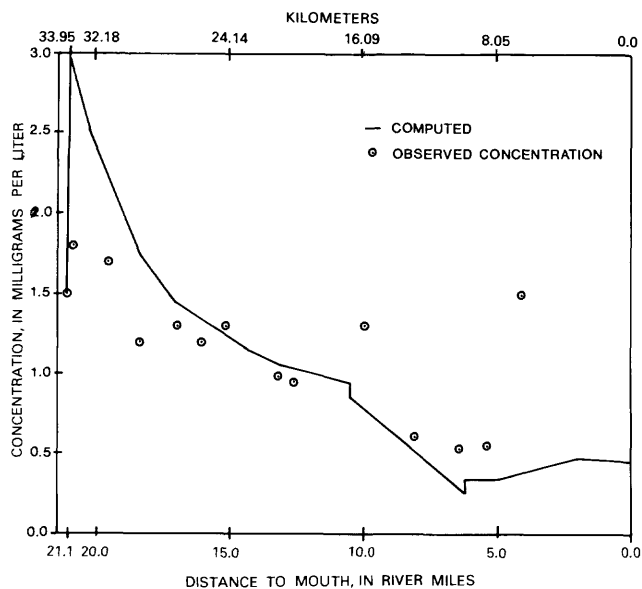


Figure 5. Observed and computed organic nitrogen concentration profiles, Osage Creek, Arkansas (Terry and others, 1984).

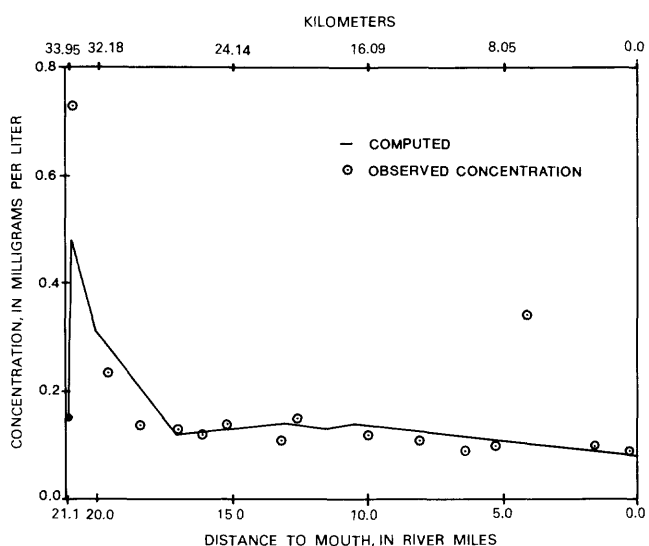


Figure 6. Observed and computed ammonia-N concentration profiles, Osage Creek, Arkansas (Terry and others, 1984).

COMPARISON OF MEASURED VALUES AND DERIVED BENTHIC DEMAND VALUES

Studies have been conducted on several streams in Arkansas (Terry and others, 1983, 1984) in which SOD and derived benthic demands have been determined independently. Table 1 contains measured values of SOD and derived benthic demands for streams included in these studies. SOD values are generally quite different than values

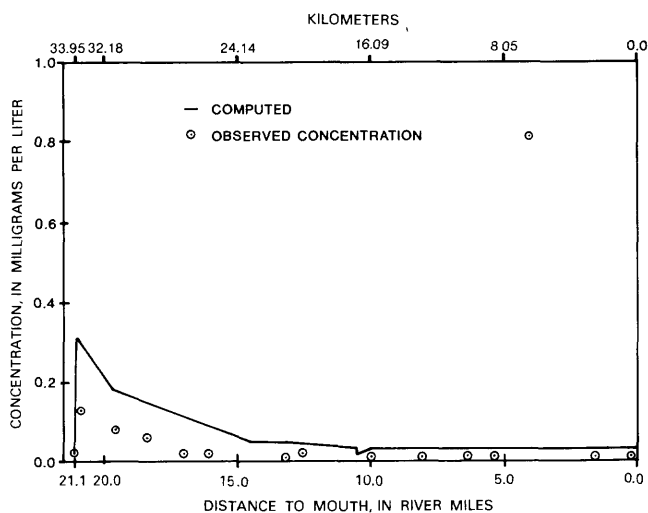


Figure 7. Observed and computed nitrite-N concentration profiles, Osage Creek, Arkansas (Terry and others, 1984).

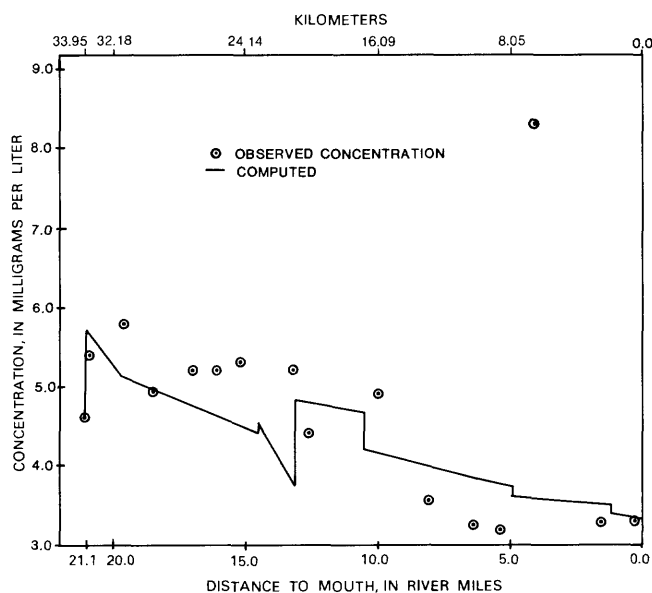


Figure 8. Observed and computed nitrate-N concentration profiles, Osage Creek, Arkansas (Terry and others, 1984).

of derived benthic demand. If measured SOD's had been used in modeling these streams, significant adjustments would have had to be made in other components that impact the DO regime; for example, figure 9 shows a computed DO profile for Osage Creek after the model calibration process is complete except for the indirect quantification of benthic demand; measured SOD values have been input instead. The computed profile does not simulate adequately observed DO data. When determined as described earlier in this paper, we believe that the values of the other impacting components are much more representative than values of SOD. Therefore,

Table 1. Values of derived benthic oxygen demand and measured streambed oxygen demand for Osage Creek, Illinois River, White River, Spring Creek, and Muddy Fork, Arkansas [SOD-streambed oxygen demand]

Subreach		Model derived benthic oxygen demand [(g/m ²)/d at 20°C]	Measured SOD		
Begin mile	End mile		Mile location of collection site	Date of collection	SOD [(g/m ²)/d at 20°C]
Osage Creek					
21.1	21.0	0.5	21.1	8-27-81	0.65
21.0	19.6	14.0	19.6	8-27-81	.94
17.1	14.5	4.0	15.2	8-29-81	.72
2.0	1.2	5.0	1.6	9-02-81	.74
Illinois River					
144.5	142.2	4.0	143.0	8-31-81	1.82
138.2	138.0	6.0	138.1	8-03-79	.30
135.6	132.8	2.4	136.4	8-31-81	1.70
129.6	123.7	2.5	124.6	9-02-81	.74
123.5	121.4	4.0	121.5	9-02-81	.42
112.0	109.0	4.0	111.3	8-28-81	.08
White River					
684.0	682.9	0.7	684.0	9-24-80	2.1
				10-07-80	4.5
			683.5	9-24-80	2.5
				10-07-80	4.3
682.9	682.3	7.8	682.8	9-24-80	3.7
				10-07-80	3.1
682.3	680.9	7.8	681.8	9-24-80	6.0
				10-07-80	6.0
680.9	679.4	8.5	680.0	9-24-80	3.5
679.4	677.8	11.0	678.8	9-24-80	2.4
				10-07-80	2.8
677.4	677.2	8.2	677.4	9-24-80	1.8
				10-07-80	2.5
677.1	673.8	2.8	677.1	9-24-80	1.9
				10-07-80	3.1
			675.8	9-24-80	1.2
				10-07-80	1.6
Spring Creek					
6.2	6.1	1.0	6.2	8-30-81	0.66
5.9	5.5	4.0	5.5	8-31-81	.81
4.9	4.2	6.0	4.3	8-29-81	.82

Table 1. Values of derived benthic oxygen demand and measured streambed oxygen demand for Osage Creek, Illinois River, White River, Spring Creek, and Muddy Fork, Arkansas—Continued

Subreach		Model derived benthic oxygen demand [(g/m ²)/d at 20°C]	Measured SOD		
Begin mile	End mile		Mile location of collection site	Date of collection	SOD [(g/m ²)/d at 20°C]
Spring Creek—continued					
2.3	1.4	14.0	1.6	8-29-81	.83
1.4	.0	18.0	.5	8-28-81	1.58
Muddy Fork					
8.6	8.3	3.0	8.6	9-04-81	3.20
8.3	8.2	4.0	8.2	8-04-79	.70
				9-04-81	1.85
1.4	.0	2.8	1.1	9-03-81	1.35

we believe that the indirect quantification of benthic demand results in a much more representative simulation of instream DO dynamics. The “goodness of fit” between observed and model derived DO profiles after indirect quantification of benthic demand for Osage Creek is shown in figure 10.

Simulating Changes in Benthic Demands

Most DO modeling is done for the purpose of point-source waste-load allocation. The general procedure is to calibrate and verify a steady state streamwater-quality model by using independent sets of observed data. Simulations then are made for projected changes in point-source waste loading and the

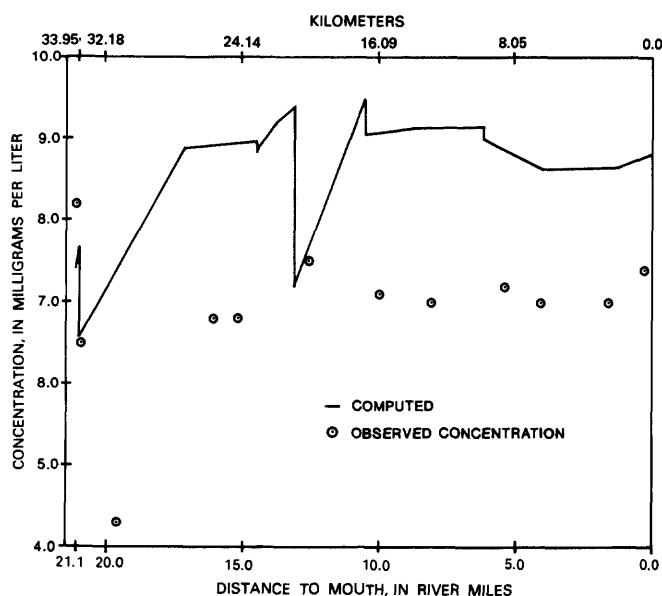


Figure 9. Observed and computed average dissolved-oxygen profiles using measured streambed oxygen demand values, Osage Creek, Arkansas.

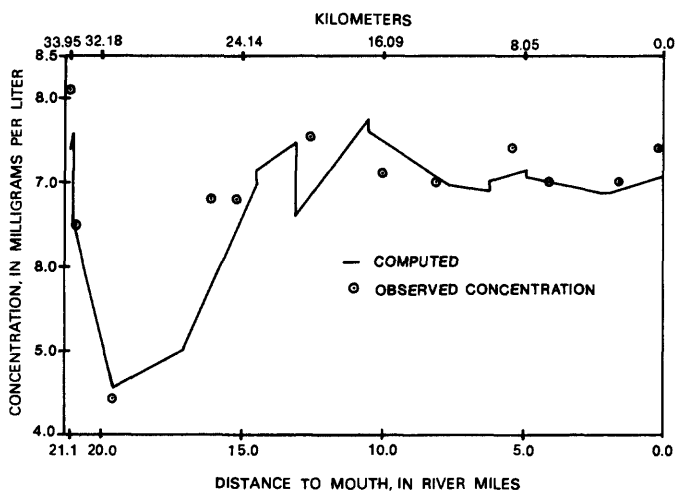


Figure 10. Observed and computed average dissolved-oxygen profiles after indirect quantification of benthic oxygen demand, Osage Creek, Arkansas (Terry and others, 1984).

resulting effects upon the DO profile are observed. It is assumed that a stream can assimilate a given BOD wasteload if DO concentrations remain above certain standards.

Instream benthic demands are dependent upon naturally recurring organic detritus and settleable organics contributed by man. The demand from natural detritus is usually small and represents background conditions; unusually high benthic demands are often the result of man's activities. If these man-made waste loads are reduced, then, ultimately, instream benthic demands should be reduced.

Application Technique

For the purpose of waste-load allocation, the calibrated and verified model is used to simulate the effects of projected changes in waste loading on the DO profile. If an existing waste discharger contributes significantly to benthic demands, then it may be assumed that, if this discharger upgrades his wastewater treatment process, instream benthic demands subsequently will be reduced.

Rationale

Our rationale for making these benthic reductions in the model for simulated projections is related to the instream decay and deposition of carbonaceous material. In most cases, carbonaceous waste material discharged into a stream is the most significant manmade contribution to instream benthic demands. The deposition of particulate carbonaceous matter is reflected by the observed differences between CBOD removal rate coefficients (k_r) and deoxygenation rate coefficients (k_d) as previously described in the CBOD determination section. If waste dischargers to a stream upgrade treatment levels to secondary or better, then all instream carbonaceous removal will probably be due to decay, and k_r will equal k_d . This rationale can be further extended to estimate accompanying changes in benthic demands as follows:

$$B_{new} = (k_{r_{new}}/k_{r_{exist}}) B_{exist}, \quad (11)$$

where B equals benthic demand in grams per square meters per day, k_r equals CBOD removal rate coefficient in per day, and the subscripts *new* and *exist* equal values used in projections and calibration verification, respectively.

In this manner, representative values of benthic demand, resulting from changed point-source loading, can be computed and used in realistic simulations of DO profiles.

SUMMARY

The application of indirect techniques for the quantification of benthic demand requires that all other sources and sinks of dissolved oxygen in a modeled reach be adequately defined and quantified. If realistic values for benthic demand are not obtained—if measured values of SOD from the analyses of point samples are used instead—the other impacting sources and sinks probably cannot be defined or quantified properly.

It is no less important that a viable procedure be used to simulate projected changes in benthic demand resulting from changed instream nutrient loading. The technique offered in this paper probably is not accurate, totally, but is a numerically sound representation based upon observed organic deposition rates that are associated with various wastewater-treatment levels.

REFERENCES CITED

- Bosko, K., 1966, Discussion to paper I-1 in *Advances in water pollution research*: Munich International Association on Water Pollution Research, Pergamon Press, v. III.
- Butts, T. A., and Evans, R. L., 1978, Sediment oxygen demand studies of selected northeastern Illinois streams: Urbana, Illinois, State Water Survey Circular 129, 177 p.
- Jennings, M. E., and Bauer, D. P., 1976, Determination of biochemical-oxygen demand parameters: U.S. Geological Survey Computer Program Documentation, 55 p.
- Nolan, P. M., and Johnson, A. F., 1979, A method for measuring sediment-oxygen demand using a bench model benthic respirometer: Lexington, Massachusetts, U.S. Environmental Protection Agency, 5 p.
- Odum, H. T., 1956, Primary production in flowing waters: *Limnology and Oceanography*, v. 1, no. 2, p. 102-117.
- Rathbun, R. E., 1977, Reaeration coefficients of streams—State-of-the-art: American Society of Civil Engineers, *Journal of the Hydraulics Division*, v. 103, no. HY-4, p. 409-424.
- Rathbun, R. E., and Grant, R. S., 1978, Comparison of the radioactive and modified techniques for measurement of stream reaeration coefficients: U.S. Geological Survey Water-Resources Investigations 78-68, 57 p.
- Rathbun, R. E., Shultz, D. J., and Stephens, D. W., 1975, Preliminary experiments with a modified tracer technique for measuring stream reaeration coefficients: U.S. Geological Survey Open-File Report 75-256, 35 p.
- Rathbun, R. E., Stephens, D. W., Shultz, D. J., and Tai, D. Y., 1978, Laboratory studies of gas tracers for reaeration: American Society of Civil Engineers Proceedings, *Journal of Environmental Engineering Division*, v. 104, no. EE2, p. 215-229.

- Shindala, Adnan, 1972, Mathematical modeling for water quality management in streams and estuaries: Mississippi State University, Department of Civil Engineering, 62 p.
- Shultz, D. J., Pankow, J. F., Tai, D. Y., Stephens, D. W., and Rathbun, R. E., 1976, Determination, storage, and preservation of low molecular weight hydrocarbon gases in aqueous solution: U.S. Geological Survey Journal of Research, v. 4, no. 2, p. 247-251.
- Stamer, J. K., Bennett, J. P., and McKenzie, S. W., 1983, Determination of ultimate carbonaceous BOD and the specific rate constant (K_1): U.S. Geological Survey Open-File Report 82-645, 21 p.
- Stephens, D. W., and Jennings, M. E., 1976, Determination of primary productivity and community metabolism in streams and lakes using diel oxygen measurements: U.S. Geological Survey Computer Program Documentation, 100 p.
- Terry, J. E., Morris, E. E., and Bryant, C. T., 1983, Water-quality assessment of White River between Lake Sequoyah and Beaver Reservoir, Washington County, Arkansas: U.S. Geological Survey Water-Resources Investigations Report 82-4063, 84 p.
- Terry, J. E., Morris, E. E., Petersen, J. C., and Darling, M. E., 1984, Water-quality assessment of Illinois River basin, Arkansas: U.S. Geological Survey Water-Resources Investigations Report 83-4092, 263 p.
- Tierney, G. F., and Young, G. K., 1974, Relationship of biological decay to stream morphology: Prepared by Meta Systems, Inc., Springfield, Virginia.
- Zison, S. W., Mills, W. B., Deimer, Dennis, and Chen, C. W., 1978, Rates, constants, and kinetics formulations in surface water quality modeling: U.S. Environmental Protection Agency Ecological Research Series, EPA-600 13-78-105, 317 p.

The Rate of Ferrous Iron Oxidation in a Stream Receiving Acid Mine Effluent

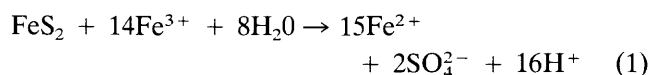
By D. Kirk Nordstrom

Abstract

The rate of ferrous iron oxidation has been measured during downstream transport of acid mine waters in a mountainous reach before and after a rainstorm of November–December 1975. The acid waters originate from the oxidation of a massive sulfide mineral deposit located in Shasta County, California. These waters contain 1,200 milligrams per liter of dissolved ferrous iron at a pH of 2.0 just before they join a larger stream. Below the confluence, the stream has no tributaries for about 540 meters. Water samples were collected, and stream velocities were measured at five stations within that reach and two downstream stations. Analyses of these samples showed that the rate of iron oxidation before the rainstorm ranged from 0.87 to 3.5 millimoles per hour with a mean of 2.4 millimoles per hour for a pH range of 2.40 to 2.62. These rates are five to eight orders of magnitude faster than the inorganic reaction rate and they can be caused only by bacterial catalysis. Selective enrichment for the iron-oxidizing bacterium, *Thiobacillus ferrooxidans*, gave positive results with an oxidation rate of 2.9 millimoles per hour in 9 K culture medium. After a moderate rainfall, the oxidation rate in the stream decreased to a mean value of 0.65 millimoles per hour at a pH of 2.9. This decrease reflects a flushing and dilution of the dissolved iron and the bacterial population by the rainstorm.

INTRODUCTION

Acid mine waters are produced by the oxidation of sulfide minerals, especially pyrite, in the presence of air and water, and this reaction is catalyzed by the iron-oxidizing bacterium, *Thiobacillus ferrooxidans* (Stumm and Morgan, 1981; Förstner and Wittman, 1979; Hiskey and Schlitt, 1982; Lawson, 1982; Nordstrom, 1982). An important step in the oxidation of pyrite is the oxidation of aqueous ferrous iron to ferric iron because the ferric ion oxidizes pyrite very rapidly at a low pH through the reaction



(Garrels and Thompson, 1960; Smith and others,

1968). Unless ferric iron is rapidly regenerated in solution, reaction 1 will quickly come to a halt. Because the inorganic oxidation of ferrous to ferric is very slow in acid solutions, Singer and Stumm (1970) called it the rate-determining step in pyrite oxidation. Below a pH of 3.5, the rate is independent of pH and follows the equation

$$\frac{-d\text{Fe}^{2+}}{dt} = k[\text{Fe}^{2+}]^2[\text{O}_2],$$

where the rate constant k equals 2.8×10^{-6} L/(mol atm s) at 30.5°C and in 1 M H₂SO₄, and t is time. However, this rate is so slow that, for time scales of practical value to both laboratory and field applications, Singer and Stumm (1968) have shown that the rate can be better treated as pseudo-first order. In phosphate and fluoride solutions, the rate can be well described by a first-order equation (Singer and Stumm, 1970). The first-order rate constant derived under conditions that most closely simulate acid mine waters is 1×10^{-7} /(atm min) (Singer and Stumm, 1968). The presence of *T. ferrooxidans* increases the oxidation rate to a nearly constant value of 3 mmol/h during the growth phase of the bacteria (Lacey and Lawson, 1970). The catalytic effects of trace metals, sulfate, pyrite, and clay particles have been found to be negligible in comparison to iron-oxidizing bacteria. Thus, *T. ferrooxidans* is the strongest known catalyst in promoting aqueous ferrous iron oxidation and, indirectly, pyrite oxidation. The occurrence of iron- and sulfur-oxidizing bacteria in acid mine waters is well known (Colmer and Hinkle, 1947; Joseph, 1953; Ehrlich, 1963; Dugan and others, 1970a, b; Scala and others, 1982), but no one has ever reported the *in situ* rate of ferrous-iron oxidation in a natural stream under field conditions. The purpose of this investigation was to determine the oxidation rate of dissolved ferrous iron in a mountain stream containing acid mine effluent. This investigation was begun in November 1975 as part of the author's Ph.D. Dissertation (Nordstrom, 1977).

Acknowledgments

This investigation was supported by cooperative funding between the California State Water Quality Control Board and the U.S. Geological Survey, Menlo Park. The encouragement of Everett Jenne and the assistance of Ray Hoffman in measuring streamflow is greatly appreciated. A review of an early draft of this manuscript by Ron James and reviews of the final draft by Vance Kennedy and Ken Bencala are greatly appreciated.

FIELD SITE

Weathering of massive sulfides in the West Shasta Mining District, Shasta County, California, has produced strongly acidic mine effluent (Nordstrom and others, 1977). The sulfides are composed predominantly of pyrite with lesser and variable amounts of chalcopyrite, sphalerite, galena, greenockite, chalcocite, covellite, tennantite-tetrahedrite, and pyrrhotite that occur as massive lenses and pods within the Balaklala Rhyolite of Devonian age (Kinkel and others, 1956). The largest and most seriously affected area is found at the Iron Mountain deposits, which is drained by Boulder and Slickrock Creeks, two main tributaries of Spring Creek (fig. 1). Acid waters ($\text{pH} \approx 1.0$) from the Hornet and Richmond portals flow through a 2-km-long stainless steel flume into a copper recovery plant before entering Boulder Creek. Effluent from the plant contains abundant microorganisms and high ferrous iron concentrations at a pH of about 1. After mixing with Boulder Creek, the total iron concentration of the effluent ranges from 400 to 2,000 mg/L. The combined portal and plant effluent is the dominant source of *T. ferrooxidans* and ferrous iron found downstream. Boulder Creek ($\text{pH} \approx 2$) empties into Spring Creek which flows another 4 km to a debris dam and finally enters Keswick Reservoir, on the Sacramento River, just south of Shasta Dam. Upstream from the Boulder Creek confluence, Spring Creek is a neutral pH mountain stream with only trace levels (< 1 mg/L) of heavy metals. Spring Creek usually has about twice the discharge of Boulder Creek at the confluence point. Spring Creek drains an area that is approximately twice the area drained by Boulder Creek.

Figure 1 shows the location of sampling stations for the iron-oxidation study along Spring Creek between the confluence of the two tributaries. Station L is located on Slickrock Creek just above its confluence with Spring Creek, and station K is located on Spring Creek just below its confluence with Slickrock. The last station, N, was chosen 4 km downstream at the mouth of the debris dam. The

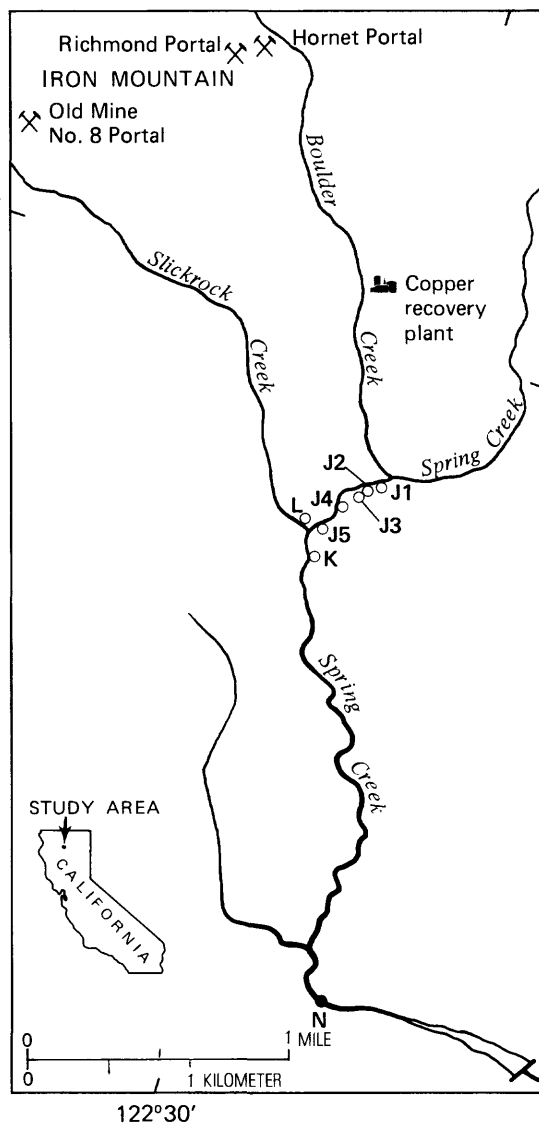


Figure 1. Sampling sites J1 through K along Spring Creek.

main reasons for choosing stations J1 to J5 are accessibility and negligible complications from base flow and tributary dilution. Stations J1 to K are roughly at 100-m intervals over a 540-m reach of the stream in a deep canyon carved through the granitic bedrock of the Mule Mountain intrusive stock (Kinkel and others, 1956). The stream gradient is 20 m/km, no tributaries enter Spring Creek between the Boulder and Slickrock confluences, and the low hydraulic conductivity typical of crystalline bedrock is expected to minimize base flow in the absence of major fault zones. Comparisons of stream discharges between station J1 and J5 confirm this assumption (Nordstrom, 1977). On November 26, 1975, during a period of relatively low flow (approximately $0.03 \text{ m}^3/\text{s}$), water samples were collected, and stream velocities were measured along Spring Creek. Eight

days later, a moderate rainfall began, lasting about 33 hours for a total precipitation of 50 mm. The discharge at station J1 peaked at about 10 a.m. on December 5. A second set of samples was collected on December 6 (about 12 hours after the rainfall ended) to investigate the effect of dilution and increased discharge on the oxidation rate. The postrainfall samples were collected long enough after the discharge had peaked that the stream discharge was constant (to within the uncertainty of the measurement, see below) during 1 day of sampling.

SAMPLING PROCEDURES AND ANALYTICAL METHODS

Water samples were filtered and acidified immediately on site. Samples were pumped through 0.1- μm pore-sized membranes. Three samples composed a set at each station. One sample was acidified with HNO_3 to a pH of less than or equal to 1.5 for metal analyses, another was acidified with HCl to a pH of less than or equal to 1.5 to preserve the oxidation state of the dissolved iron for ferrous and total iron analyses, and a third sample was left unpreserved for sulfate determination. Conductivity, pH, temperature, and stream velocity were measured on site. Ferrous iron and total iron were measured colorimetrically by the ferrozine method (Stookey, 1970; Gibbs, 1976; Gibbs, 1979). Other metals were analyzed by flame atomic absorption spectrophotometry, and sulfate was analyzed by the Thorin method (Skougstad and others, 1979, p. 615).

The largest source of uncertainty is the streamflow measurements. For prestorm data, velocities were estimated. Bed roughness, which is difficult to estimate for this stream, may affect the prestorm velocity. Poststorm measurements were made with a standard current meter. All streamflow measurements were consistent for the given stream conditions, but the error could be as high as 25 percent. However, this error is less than the scatter in the results.

As a basis of comparison with the field results, acid mine waters issuing from the Hornet portal were collected for a controlled oxidation rate study. These samples were unfiltered but were kept on ice or in the refrigerator for 1 month and were not allowed to warm until the beginning of the experiment. Only about 6 percent of the ferrous iron had oxidized during the month of storage. At the start of the experiment, separate samples were placed into Erlenmeyer flasks, the necks were stuffed with cotton wool, and the flasks were shaken continuously. One flask provided a sterile control by filtration through 0.1- μm pore-sized membranes. In addition, inocula from

Boulder Creek were enriched in the 9 K culture medium of Silverman and Lundgren (1959), which is selective for *T. ferrooxidans*. Ferrous iron oxidation rates also were obtained for 9 K culture medium, which should be near maximum growth because all the nutrients in 9 K culture medium have been optimized (Silverman and Lundgren, 1959).

CALCULATIONS AND RESULTS

The water analyses and stream velocities are shown in tables 1 and 2. From the ferrous iron analyses, the measurement of stream velocities, and the distances between stations, the rate of ferrous iron oxidation can be calculated from a simplified form of the reactive-convective transport equation,

$$\frac{\partial c}{\partial t} + \frac{v\partial c}{\partial x} = r,$$

where c is the solute concentration, t is time, x is distance, v is velocity, and r is reaction rate assuming no dispersion and no inputs. Assuming steady state conditions,

$$\frac{\partial c}{\partial t} = 0 \text{ and } \frac{v\partial c}{\partial x} = r,$$

or, by finite difference approximation,

$$\frac{v\Delta c}{\Delta x} = \frac{\Delta x}{\Delta t} \cdot \frac{\Delta c}{\Delta x} = \frac{\Delta c}{\Delta t} = r,$$

where Δc is the difference in ferrous iron concentrations between stations, Δx is the distance between stations, and Δt is the traveltime between stations. This procedure was applied to stations J1 to J5. For station K, a diluting correction was needed because of the confluence from Slickrock Creek, and, for station N, a diluting correction was needed because of the confluence of a small tributary downstream (South Fork Spring Creek). Because these tributaries carry such small amounts of ferrous iron, only a dilution effect can be seen. The effect of dilution at station K can be calculated from a mass balance equation on the load of ferrous iron above and below the Slickrock Creek confluence. As an example, consider first the mass balance for silica to check the behavior of a conservative constituent. The general equation

$$C_K Q_K = C_{J5} Q_{J5} + C_L Q_L$$

was applied, where C is concentration, Q is discharge, and the subscripts refer to each station number. Rearranging to solve for the concentration at station K results in

$$C_K = \frac{C_{J5} Q_{J5} + C_L Q_L}{Q_K} = 17.8 \text{ mg/L}$$

Table 1. Composition and velocity of Spring Creek at selected stations downstream before a rainstorm on November 26, 1975¹

[Data in milligrams per liter, except as indicated]

Parameters	Stations							
	J1	J2	J3	J4	J5	K	L	N
T (°C) - - - - -	8.3	8.2	8.4	9.5	6.8	6.5	7.2	7.0
Velocity (m/s) - - - - -		0.20	0.091	0.21	0.22	0.17	0.30	0.11
pH - - - - -	2.40	2.45	2.46	2.48	2.53	2.62	3.10	2.61
Conductivity (µm S/cm at 25°C) - - - - -	3,350	3,230	3,140	2,970	2,720	2,670	2,900	2,080
Fe ²⁺ - - - - -	300	278	267	234	182	140	7.2	4.9
Total Fe - - - - -	412	400	396	392	386	360	176	252
Na - - - - -	6.3	6.3	6.2	6.2	6.2	6.3	6.3	6.7
K - - - - -	4.0	4.0	4.0	4.0	3.9	3.4	.42	2.9
Al - - - - -	50	50	50	49	49	70	170	57
SO ₄ - - - - -	1,400	1,400	1,400	1,400	1,400	1,400	2,190	1,250
SiO ₂ - - - - -	26	26	26	26	26	32	69	33

¹Discharge at J5 estimated to be 0.11 m³/s, at K estimated to be 0.13 m³/s, and at N estimated to be 0.15 m³/s based on previous records.

Table 2. Composition and velocity of Spring Creek at selected stations downstream before a rainstorm on December 6, 1975¹

[Data in milligrams per liter, except as indicated]

Parameters	Stations							
	J1	J2	J4	J5	K	L	N	
T (°C) - - - - -	9.5	9.5	9.5	9.0	9.0	9.5	9.5	
Velocity (m/s) - - - - -		0.30	0.27	0.30	0.23	0.55	0.16	
Discharge (m ³ /s) - - - - -		.49	.50	.52	.57	.044	.53	
pH - - - - -	2.90	2.90	2.90	2.90	2.90	2.90	2.88	
Conductivity (µm S/cm at 25°C) - - - - -	1,110	1,148	1,102	1,040	1,038	1,630	1,040	
Fe ²⁺ - - - - -	55	52	49	42	31	9.5	18	
Total Fe - - - - -	100	102	100	93	84	75	77	
Na - - - - -	3.3	3.3	3.3	3.3	3.5	5.0	4.1	
K - - - - -	1.1	1.1	1.1	1.1	1.1	0.45	0.88	
Al - - - - -	17	17	17	17	22	80	21	
SO ₄ - - - - -	430	430	440	410	450	1,020	440	
SiO ₂ - - - - -	16	16	16	16	18	42	18	

¹Estimated by difference.

for the post-rainstorm data and compares excellently with the measured value of 18 mg/L. Having demonstrated the reliability of the mass balance calculation for a conservative constituent, the equation is then used for the nonconservative species of ferrous iron. This time, the calculation provides an estimate of the concentration of ferrous iron that would have

reached station K had there been no oxidation. The difference between that value and the actual value is a better estimate of the decrease in concentration due to oxidation. For the post-rainstorm data, the mass balance calculation results in ferrous iron equaling 39 mg/L compared to the analyzed value of 31 mg/L. Thus, after accounting for dilution, only 8 mg/L of

ferrous iron oxidized instead of 11 mg/L. Likewise, before the rainstorm, the calculated dilution decrease results in ferrous iron equaling 155 mg/L at station K compared to the actual value of 140 mg/L. The change in concentration due to oxidation is 15 mg/L. The distance over which this oxidation occurs is 73 m so that, before the rainstorm, the change in concentration with distance is 0.21 (mg/L)/m, and, after the rainstorm, it becomes 0.11 (mg/L)/m (table 3).

Because no discharge measurements were made to account for the dilution effect on station N by South Fork Spring Creek, element ratios were used. Decreases in specific conductance, aluminum, and sulfate fall in the range of 10 to 20 percent before the rainstorm. Using 15 percent as an average estimate, the undiluted ferrous iron should then be about 5.6 mg/L at station N.

No other effect is likely to change the oxidation rate from these dilutions; for example, the pH has not changed nearly enough to make any difference. After the rainstorm, the dilution effect is 5 percent or less, which makes the undiluted ferrous iron concentration 19 mg/L at station N.

The resulting ferrous iron oxidation rates are shown in table 3. The average rate decreased significantly after the storm.

Enrichment for *T. ferrooxidans* in 9 K culture medium gave a typical exponential growth rate curve

as reflected in the decrease of ferrous iron shown in figure 2. As pointed out by Brock (1974, p. 239), it is frequently difficult to distinguish between linear and exponential growth of microorganisms. From figure 2, one may determine that the most rapid growth occurred over a nearly linear portion of the curve. Likewise, Lacey and Lawson (1970), Silverman and Lundgren (1959), and Lundgren and others (1964) all had fairly constant growth rates of $3 \pm .7$, 2, and 1.5 mmol/h, respectively, in 9 K medium at 20°, 28°, and 28°C, respectively. Three experiments, such as the one shown in figure 2, gave rates of 3.4, 2.9, and 2.5 mmol/h at 25°C with an average of 2.9 mmol/h. The data of Silverman and Lundgren (1959), Lundgren and others (1964), and Lundgren and Schnaitman (1965) clearly show that the rate of ferrous iron oxidation is directly proportional to the concentration of *T. ferrooxidans* and not to the ferrous iron concentration. In this sense, the nearly constant (or quasi-linear) rates can be treated as zero order.

Nearly similar rates were obtained when unfiltered Hornet portal effluent was allowed to oxidize at 25°C. The ferrous iron oxidation curves are shown in figure 3. In flask A, two additional ferrous iron oxidation curves were obtained by adding $\text{FeSO}_4 \cdot 7\text{H}_2\text{O}$ to the solution at 271 and 344 hours. The four curves gave an average rate of 2.4 ± 0.5 mmol/h.

Microscopic examination of the oxidized Hornet mine portal waters and the 9 K culture medium

Table 3. Ferrous iron oxidation rates

Station intervals	$\frac{\Delta c}{\Delta x}$ [(mg/L)/m]	$\frac{\Delta x}{\Delta t}$ (m/s)	$\frac{\Delta c}{\Delta t}$ (mmol/hr)
Nov. 26, 1975:			
J1-J2	0.24	0.20	3.1
J2-J3	.18	.091	1.1
J3-J4	.26	.21	3.5
J4-J5	.23	.22	3.3
J5-K	.21	.17	2.3
K-N	.045	.30	.87
			Mean—2.4(± 1.1)
Dec. 6, 1975:			
J1-J2	.033	.30	.64
J2-J4	.015	.27	.26
J4-J5	.032	.30	.62
J5-K	.11	.23	1.6
K-N	.0042	.55	.15
			Mean—0.65(± .57)

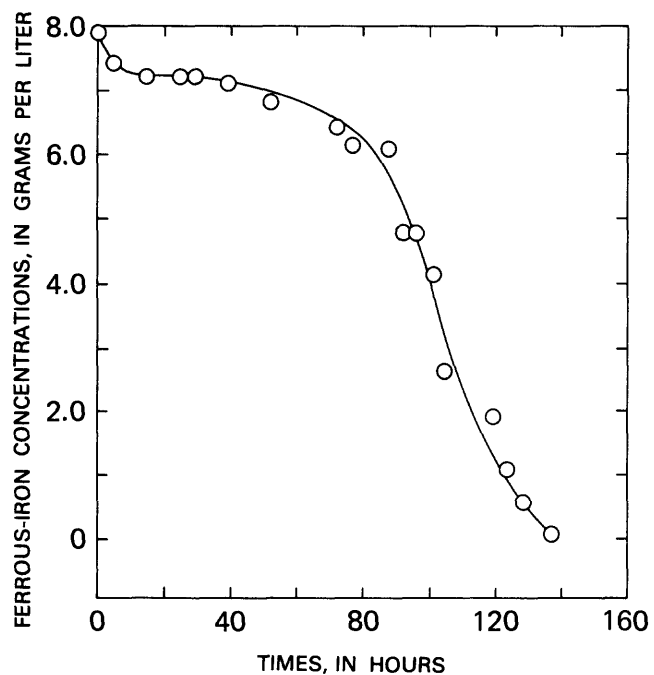


Figure 2. Oxidation of ferrous iron in 9 K culture medium inoculated with bacteria from Boulder Creek.

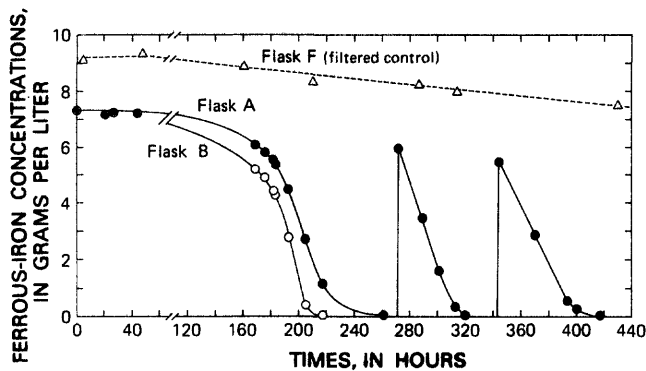


Figure 3. Oxidation of ferrous iron in acid mine waters from the Hornet portal. [See Nordstrom (1977) for complete analysis of original water.]

confirmed the presence of numerous bacilli, occasionally motile, which fit the description of *T. ferrooxidans* (Brock, 1974). They also were found to be gram-negative, another property of *T. ferrooxidans*.

DISCUSSION

The average rate of ferrous iron oxidation in a mountain stream receiving acid mine effluent was found to vary from 2.4 mmol/h before a rainstorm to 0.65 mmol/h after a rainstorm. These rates are very rapid compared to the inorganic oxidation rate which is several orders of magnitude less. For example, Singer and Stumm (1968) measured the inorganic oxidation rate at a pH of 2.9, a ferrous iron concentration of 55 mg/L, and sulfate concentration of 100 mg/L, which is similar to stations J1 to J5 on Spring Creek after the rainstorm. Their reaction rate was about 1×10^{-6} mmol/h nearly six orders of magnitude less. The positive results for enrichment of *T. ferrooxidans* and the excellent comparison of the rates in 9 K culture medium and in mine waters oxidized in the laboratory indicate that *T. ferrooxidans* appears to be the catalyzing agent and that, in an aerobic stream environment contaminated with mine drainage, the ferrous iron oxidation rate can occur at the maximum levels found under optimal laboratory conditions for bacterial growth.

The close similarity of rates in the laboratory and those in Spring Creek before the rainstorm indicate that nutrients were present in sufficient concentrations to allow maximum growth rate of bacteria in the stream. Doubling rates for bacterial growth has been estimated from the iron concentrations to be about four per day (Nordstrom, 1977). After the rainstorm a decrease in the rate by a factor of four suggests that the increase of streamflow may have diluted the concentration of bacteria. Because the stream discharge increased from about 0.11 to 0.51 m³/s af-

ter the rainstorm and the input load of bacteria is known to be nearly constant over the time period studied, it is quite likely that the bacterial population was simply diluted. Mine water outflow has been reported to take 2 to 3 days after a rainstorm to increase noticeably. Dissolved iron also would tend to be diluted by the same factor because the input load of iron is a constant, independent of the changing stream discharge. However, as shown above, the rate is a function of the bacterial population which is independent of ferrous iron concentrations.

The rate for station intervals between J2 and J3 and K and N for both pre- and post-rainstorm events consistently decreased. The station interval between J2 and J3 is geomorphologically different from the rest of the reach. The creek widens and deepens into a large pool in which the streamflow slows considerably, and a large amount of finely powdered pyrite can be seen covering the streambed. It is probable that the increased residence time in contact with an increased surface area of reactive pyrite is promoting reduction of some of the ferric iron by reaction 1. The rate of this reaction may be competing with the oxidation reaction of ferrous iron. Other possibilities such as reduction by dissolved organics, temperature changes, or changes in light intensity, seem much less likely. Dissolved organics are relatively ineffective at complexing iron at these low pH values. Temperature variations are negligible, and changes in light intensity are not significantly different for the various stream intervals.

The decreased rate for the station interval between K and N may reflect growth limitation due to reduced concentrations of nitrogen or phosphorous compounds or the inhibiting effect of bacterial excrement. The reach of the stream between K and N is much longer, and far less is known about its morphology so that it is difficult to say why a rate decrease was observed there. Dissolved oxygen concentrations have been measured along Spring Creek and have been found to be at or near saturation (Nordstrom and others, 1979) at all points measured, including both J1 and N. Therefore, oxygen is not a limiting factor.

CONCLUSIONS

In aerated stream environments containing high ferrous iron from acid mine effluent, the oxidation rate of iron tends to reach maximum levels under steady low flow conditions. These rates are comparable to measured laboratory rates where the oxidation of iron is catalyzed by the iron-oxidizing bacterium, *T. ferrooxidans*. Rainstorm events can decrease oxidation rates by diluting the bacterial popu-

lation, although rates are still several orders of magnitude greater than the rate of reaction in the absence of bacterial catalysis for the field site studied here. Considerable fluctuations can be expected in the iron oxidation rate during seasonal changes for natural stream environments.

REFERENCES CITED

- Brock, T. D., 1974, *Biology of microorganisms* (2d ed.): Prentice-Hall, Inc., 852 p.
- Colmer, A. R., and Hinkle, M. E., 1947, The role of microorganisms in acid mine drainage: A preliminary report: *Science*, v. 106, p. 253–256.
- Dugan, P. R., MacMillan, C. B., and Pfister, R. M., 1970a, Aerobic heterotrophic bacteria indigenous to pH 2.8 acid mine water: Microscopic examination of acid streamers: *Journal of Bacteriology*, v. 101, p. 973–981.
- 1970b, Aerobic heterotrophic bacteria indigenous to pH 2.8 acid mine water: Predominant slime-producing bacteria in acid streamers: *Journal of Bacteriology*, v. 101, p. 982–988.
- Ehrlich, H. L., 1963, Microorganisms in acid drainage from a copper mine: *Journal of Bacteriology*, v. 86, p. 350–352.
- Förstner, Ulrich, and Wittman, G. T. W., 1979, *Metal pollution in the aquatic environment*: Springer-Verlag, 486 p.
- Garrels, R. M., and Thompson, M. E., 1960, Oxidation of pyrite in ferric sulfate solution: *American Journal of Science*, v. 258, p. 57–67.
- Gibbs, C. R., 1976, Characterization and application of ferrozine iron reagent as a ferrous iron indicator: *Analytical Chemistry*, v. 48, p. 1197–1200.
- Gibbs, M. M., 1979, A simple method for the rapid determination of iron in natural waters: *Water Research*, v. 13, p. 295–297.
- Hiskey, J. B., and Schlitt, W. J., 1982, Aqueous oxidation of pyrite, in Schlitt, W. J., and Hiskey, J. B., eds., *Interfacing technologies in solution mining: Proceedings, Second International Solution Mining Symposium*, Society of Mining Engineers, Denver, CO, p. 55–74.
- Joseph, J. M., 1953, Microbiological study of acid mine waters: Preliminary Report, *Ohio Journal of Science*, v. 53, p. 123–127.
- Kinkel, A. R., Jr., Hall, W. E., and Albers, J. P., 1956, *Geology and base-metal deposits of West Shasta copper-zinc district, Shasta County, California*: U.S. Geological Survey Professional Paper 285, 156 p.
- Lacey, D. T., and Lawson, F., 1970, Kinetics of the liquid-phase oxidation of acid ferrous sulfate by the bacterium *Thiobacillus ferrooxidans*: *Biotechnology and Bioengineering*, v. 12, p. 29–50.
- Lowson, R. T., 1982, Aqueous oxidation of pyrite by molecular oxygen: *Chemical Reviews*, v. 82, p. 461–497.
- Lundgren, D. G., Andersen, K. J., Remsen, C. C., and Mahoney, R. P., 1964, Culture, structure, and physiology of the chemoautotroph *Ferrobacillus ferrooxidans*: *Developments in Industrial Microbiology*, v. 6, p. 250–259.
- Lundgren, D. G., and Schnaitman, C. A., 1965, The iron oxidizing bacteria—Culture and iron oxidation: *First Symposium Coal Mine Drainage Research*, Pittsburgh, PA, p. 14–22.
- Nordstrom, D. K., 1977, Hydrogeochemical and microbiological factors affecting the heavy metal chemistry of an acid mine drainage system: Stanford University, Ph.D. Dissertation, 210 p.
- 1982, Aqueous pyrite oxidation and the consequent formation of secondary iron minerals, in Kittrick, J. A., Fanning, D.S., and Hossner, L. R., eds., *Acid sulfate weathering*: Soil Science Society of America, p. 37–56.
- Nordstrom, D. K., Jenne, E. A., and Averett, R. C., 1977, Heavy metal discharges into Shasta Lake and Keswick Reservoirs on the Upper Sacramento River, California: A reconnaissance during low flow: U.S. Geological Survey Open-File Report 76–49, 25 p.
- Nordstrom, D. K., Jenne, E. A., and Ball, J. W., 1979, Redox equilibria of iron in acid mine waters, in Jenne, E. A., ed., *Chemical modeling in aqueous systems: Speciation, sorption, solubility, and kinetics*: American Chemical Society Symposium Series 93, p. 51–79.
- Scala, Gayle, Mills, A. L., Moses, C. O., and Nordstrom, D. K., 1982, Distribution of autotrophic Fe and S-oxidizing bacteria in mine drainage from sulfide deposits measured with the FAINT assay (abs): *Annual Meeting American Society of Microbiology*, Atlanta, GA, p. 189.
- Silverman, M. P., and Lundgren, D. G., 1959, Studies on the chemoautotrophic iron bacterium *Ferrobacillus ferrooxidans*, Part 1, An improved medium and a harvesting procedure for securing high cell yields: *Journal of Bacteriology*, v. 77, p. 642–647.
- Singer, P. C., and Stumm, Werner, 1968, Kinetics of the oxidation of ferrous iron: *Second Symposium Coal Mine Drainage Research*, Pittsburgh, PA, p. 12–34.
- 1970, Acid mine drainage: The rate determining step: *Science*, v. 167, p. 1121–1123.
- Skougstad, M. W., Fishman, M. J., Friedman, L. C., Erdmann, D. E., and Duncan, S. S., 1979, Methods for determination of inorganic substances in water and fluvial sediments: U.S. Geological Survey Techniques of Water-Resources Investigations, Book 5, Chapter A1, 626 p.
- Smith, E. E., Shumate, K. S., and Svanks, Karlis, 1968, Sulfide to sulfate reaction studies: *Second Symposium Coal Mine Drainage Research*, Pittsburgh, PA, 11 p.
- Stookey, L. L., 1970, Ferrozine—A new spectrophotometric reagent for iron: *Analytical Chemistry*, v. 42, p. 779–781.
- Stumm, Werner, and Morgan, J. J., 1981, *Aquatic chemistry* (2d ed.): Wiley-Interscience, 780 p.